Faculty of Sciences
GIGA-In Silico Medicine
Thermodynamics of Irreversible Processes

IN SILICO ANALYSIS OF THE FRANK-STARLING MECHANISM

Sarah Kosta

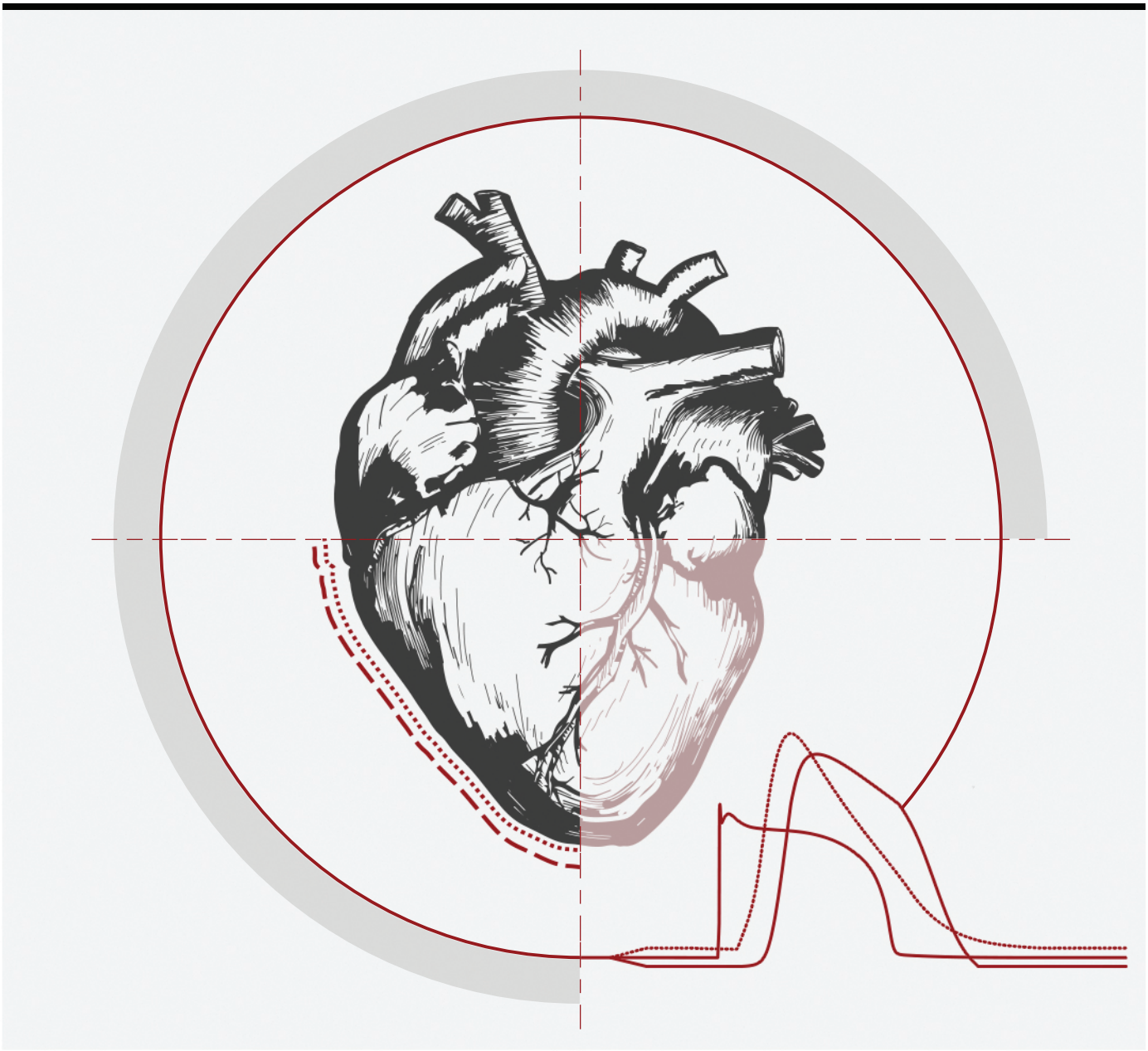

Thesis submitted in partial fulfilment of the requirements for the degree of Doctor of Science

Academic year 2019-2020

Faculty of Sciences
GIGA-In Silico Medicine
Thermodynamics of Irreversible Processes

IN SILICO ANALYSIS OF THE FRANK-STARLING MECHANISM

Sarah Kosta

October 2019

Thesis submitted in partial fulfilment of the requirements for the degree of Doctor of Science

Jury:

Prof. Alain SERET (Chairman)
Dr. Thomas DESAIVE (Secretary)
Dr. Joost LUMENS (Maastricht University, The Netherlands)
Prof. Jean BRAGARD (University of Navarra, Spain)
Prof. Vincent SEUTIN
Prof. Philippe KOLH
Prof. Pierre DAUBY (Advisor)
Prof. Maryse HOEBEKE (Co-advisor)

Academic year 2019-2020

This book was written using 100% recycled words.
— Terry Pratchett

RÉSUMÉ

L'effet Frank-Starling traduit une propriété essentielle du coeur qui permet de réguler le débit cardiaque en fonction des conditions hémodynamiques, et ce sur des échelles de temps de l'ordre d'un battement cardiaque. Il s'agit d'un mécanisme intrinsèque d'adapation du volume de sang éjecté à la précharge, et ce mécanisme tire ses origines dans les composants cellulaires qui forment le muscle cardiaque. Il est communément admis que la *"length-dependent activation"* (LDA), ou activation dépendant de la longueur, est la propriété cellulaire responsable du mécanisme de Frank-Starling observé à l'échelle du coeur. Cependant, la LDA est principalement mise en évidence lors d'expériences cellulaires ne reproduisant pas les conditions réelles, *in vivo*, d'un battement de coeur. Le lien supposé entre la LDA et l'effet Frank-Starling est en réalité difficile à établir expérimentalement, car deux échelles bien différentes (cellulaire et ventriculaire) sont mêlées.

Cette thèse a pour but d'analyser la corrélation entre un mécanisme cellulaire (la LDA), et la supposée manifestation de ce mécanisme à l'échelle cardiovasculaire (l'effet Frank-Starling). Cette analyse sera réalisée *in silico*, au moyen d'un modèle multi-échelle du système cardiovasculaire (SCV). Dans ce modèle, la contraction ventriculaire est décrite à l'échelle cellulaire. De tels modèles multi-échelles permettent de surpasser les difficultés expérimentales consistant à étudier deux échelles en même temps, tout en offrant un cadre rigoureux permettant d'intégrer les observations expérimentales provenant des deux échelles en question.

Ce modèle multi-échelle permet tout d'abord de réaliser une étude de la pertinence de divers indices de contractilité cardiaque. Ensuite, une analyse de l'effet Frank-Starling est proposée. Afin que la corrélation entre la LDA et l'effet Frank-Starling puisse être établie de la manière la plus rigoureuse possible, une attention toute particulière est portée aux définitions des divers concepts impliqués et à la mise en place de protocoles numériques pertinents. Les résultats obtenus montrent que la LDA est bien le mécanisme cellulaire qui sous-tend la réponse macroscopique (ventriculaire) à une variation de précharge. Mais cette réponse se fait de manière hautement dynamique, en mêlant des variables cellulaires et hémodynamiques, contrairement aux explication généralement trouvées dans la littérature. En plus de ces considérations physiologiques, le lien avec les thérapies cliniques est également abordé, car l'effet Frank-Starling est généralement présenté comme le principe de base du remplissage vasculaire. Cependant, nous remettons en question cette théorie et nous introduisons le concept de *"length-dependent fluid response"* (LDFR), ou réponse au remplissage dépendant de la longueur. Les résultats montrent que la LDA sous-tend la LDFV, mais que ce n'est pas le seul facteur qui dicte la réponse macroscopique (ventriculaire) à du remplissage vasculaire. La postcharge entre également en jeu, et la réponse globale du SCV provient en réalité d'une balance entre deux effets: un mécanisme cellulaire conduit par la LDA et une résistance hémodynamique à

l'éjection du sang. Enfin, le role de l'effet Frank-Starling dans l'équilibrage des volumes d'éjection ventriculaires est également abordé.

Le lien entre la LDA et l'effet Frank-Starling *in vivo* est ainsi démontré, mais l'analyse des résultats développés dans cette thèse montre que cette relation se traduit par des interactions complexes et dynamiques entre des variables cellulaires et des variables hémodynamiques. L'effet Frank-Starling est donc un effet profondément multi-échelle, au cours duquel des variables cellulaires et hémodynamiques interviennent et s'influencent mutuellement, tout au long du battement cardiaque. Le modèle multi-échelle présenté dans cette thèse fournit un outil d'analyse intéressant et qui peut être dévelopé davantage, ou utilisé dans le cadre d'autres études *in silico* destinées à étudier la corrélation entre variables cellulaires et hémodynamiques, dans des cas sains ou pathologiques.

ABSTRACT

The Frank-Starling mechanism (FS) is an essential feature of the heart, which allows for a beat-to-beat adaptation of cardiac output to hemodynamic conditions. This intrinsic adaptative mechanism to preload variations lies in the cellular components that make up the cardiac muscle. It is believed that length-dependent activation (LDA), a cardiac cellular property, is responsible for the FS mechanism observed at the heart scale. However, LDA is essentially highlighted in cellular experiments that do not reproduce the *in vivo* conditions of a beating heart. The connexion between LDA and the FS mechanism is actually difficult to unravel experimentally, as two very different scales (cellular and ventricular) are involved.

This thesis is devoted to the analysis of this connexion between a cellular mechanism (LDA) and its manifestation at the cardiovascular scale (FS mechanism). This analysis is performed *in silico* with a multiscale model of the cardiovascular system (CVS), where ventricular contraction is described at the cellular scale. Such models help overcome the experimental difficulties of linking two different scales, while providing a formal framework to integrate the experimental observations coming from both scales.

Our multiscale model is first used to study the relevance of some cardiac contractility indices. Then, an analysis of the FS mechanism is proposed. Attention is paid to providing rigorous definitions and numerical protocols so that the correlation between LDA and the FS can be established without any ambiguity. LDA is shown to underlie the macroscopic (ventricular) response to preload variations, but in a highly dynamical way, in contrast with what is generally presented in the literature. In addition to these physiological considerations, the relationship between the FS mechanism and clinical therapies is also addressed. The FS mechanism is commonly presented as the founding principle for vascular filling, but we challenge this theory and introduce the concept of length-dependent fluid response (LDFR). We show that LDA underlies LDFR, but it is not the only factor that drives the macroscopic (ventricular) response to fluid infusions. The afterload also comes into play and the global CVS response results from a balance between a cellular LDA-driven mechanism and a hemodynamic resistance to blood ejection. Finally, the role of the FS mechanism regarding stroke volumes equilibrium is also investigated.

We conclude that LDA indeed underlies the FS mechanism *in vivo*, but in a way that implies a complex dynamical interaction of cellular and hemodynamical variables. The FS mechanism is thus really a multiscale phenomenon, where the cellular variables and the hemodynamic variables influence each other during the whole heartbeat. It is hoped that our multiscale CVS model could be developed and used for further studies that aim at linking cellular properties and organ behaviors, either in healthy or in pathological conditions.

ACKNOWLEDGEMENTS

First of all, I would like to thank the AGO department for providing me with a teaching assistant position. I had the chance to do research, but also to discover the pleasure of teaching. Now there are several people who took part in my incredible journey as a PhD student, and I would like to thank them.

Many thanks to my advisor, Pierre Dauby, for giving me the opportunity to start a PhD in his research team. Since I discovered the modeling of biological systems, I knew this field would be rich in lessons and discoveries. Pierre helped me carry out my work from A, like actin, to Z, like the sarcomere Z-line, and eventually succeed in writing this manuscript. He is the living proof that an advisor can be rigorous and strict, while being incredibely nice and benevolent at the same time.

I also would like to thank to my co-advisor, Maryse Hoebeke, for welcoming me in her EPR laboratory. I especially want to acknowledge the help I also received from Philippe Kolh, Ange Mouithys, Nathalie Janssens, and Jean-Paul Cheramy when working with cardiac fibers. I never did experimental work on biological tissue before and all of them kindly devoted time in helping me and answering my (numerous) questions.

A special thank to Vincent Seutin, from my thesis comitee. Along with Philippe Kolh, they both helped me build my research project.

I gratefully thank Elena Lascano and Jorge Negroni, without whom this thesis would definitively not be the same, as many of their works and papers, and discussions we have had, served as a basis for my own studies.

Thanks to Thomas Desaive and Antoine Pironet for the discussions regarding cardiovascular modeling.

All the members of the Jury are also warmly acknowledged for accepting to read my thesis and for the time they have devoted to it.

Je me dois aussi de remercier tous mes collègues (et ex-collègues) du TPI qui m'ont accompagnée, par vagues, durant ce travail de doctorat. Un énorme merci tout d'abord à Sabine et Sophie, présentes lors de la glorieuse époque du Bureau des Filles. Merci pour l'accueil au sein de l'équipe, et merci pour les sorties et les pauses thé ! Evidemment je remercie aussi le Bureau des Garçons : Hatim, Arnaud, Antoine et Ramin. Un petit dab tout particulier à Antoine, vu notre amour mutuel pour les Dank Memes. Et puis merci aussi à Mona (et son talent de pâtissière) et à Simon, les locataires suivants du 2/50. Merci à Cécile pour sa présence pétillante dans l'équipe.

J'aimerais aussi remercier mes amis physiciens du DEPHY, ceux de la team « Self à 45 ». Ces pauses de midi devant des plats toujours suprenant gustativement parlant ont bien rythmé mes années de doctorat. Merci donc à Justine, François, Julien, Maxime, Marcus, Simon, Xavier et Antoine (et d'autres que j'oublie sûrement).

Xavier et Simon, je vous remercie une deuxième fois ici, parce qu'avec Mélanie vous faites partie d'un trio sans qui ma vie ne serait pas aussi fun. Méla, merci d'être toujours là, car tu m'es indispensable, mais tu le sais déjà.

Maintenant, j'aimerais également remercier mes Jets d'Ail adorés. Vous n'avez pas activement participé à ce travail de doctorat, mais votre présence tous les mardi soirs, et le plaisir pris en coaching avec vous m'ont vraiment aidée à passer ce cap de la thèse. Un merci tout particulier à Pierre et Marie, l'AKDT-team ! Pierre, tes petits soupers bios improvisés (huhu) m'ont fait beaucoup de bien, et les quelques soirées passées chez Marie étaient une vraie bulle de bonheur dans une phase de rédaction parfois chaotique. Merci évidement à tous les autres Jets d'Ail (Antoine, Alain, Ber', Virignie, Régis, Vincent, Tanguy, Jérômine, Romain, Vanie et Thierry P.) car sans vous je ne serais qu'une petit gousse isolée sans aucune maîtrise de la Farce.

Merci à mes proches, qui ne comprenaient pas toujours ce que je faisais dans ma vie professionnelle, mais qui sont restés présents et dévoués. Merci maman, papa, Ivana, Daniel, Baba, Dido, Teta, Christian, Pierre, Marie, Daniel, Jelica et les cousins !

Merci aussi à tous ceux qui, de près ou de loin, ont su m'apporter ce dont j'avais besoin pendant ce travail de doctorat. André, merci pour cette couverture qui respire le talent (et qui m'aura coûté mon âme et ta santé mentale). Alain, merci pour les petites impressions express de cet été. Sydney, merci pour les simulations numériques de dernière minute, et pour les moments de déconnexion totale dont j'avais aussi besoin. Margherita et Gauthier, merci pour ces séances de travail collectives, entrecoupées de (nombreuses) pauses bien méritées. Merci à Mme Dister pour la correction efficace de mes fautes d'anglais. Merci à Virginie pour les soirées papote et le soutien moral. Merci à maman pour les gougouilles.

Enfin, un immense merci à Vanie et Thierry, de la coloc' de l'Amour. Vous avez su amener du Soleil dans ma vie, même quand je croyais être au cœur d'un orage. Thierry, je ne trouve pas les mots pour te traduire ma gratitude. Tu as su m'épauler et me soutenir dans ce travail de rédaction, sans jamais cesser de croire en moi. Tu as été le calcium de mon crossbridge cycling (t'es obligé de lire ma thèse pour comprendre, maintenant).

CONTENTS

1 INTRODUCTION 1
1.1 General background . . . 1
1.2 Goal of this research . . . 2
1.3 Thesis organization . . . 3
2 PHYSIOLOGY OF THE CARDIOVASCULAR SYSTEM 5
2.1 Introduction . . . 5
2.2 The circulatory system . . . 6
2.3 The cardiac pump . . . 6
2.3.1 Anatomy . . . 6
2.3.2 Electrical activity . . . 8
2.3.3 The cardiac cycle . . . 8
2.3.4 Pressure and volume variations . . . 10
2.3.5 Important concepts . . . 11
2.4 Regulation of cardiac output . . . 13
2.4.1 Extrinsic regulatory mechanism . . . 13
2.4.2 Intrinsic regulatory mechanism . . . 13
2.5 The Frank-Starling mechanism . . . 14
2.5.1 Definition . . . 14
2.5.2 Historical background . . . 15
2.5.3 Vascular filling and fluid responsiveness . . . 20
3 PHYSIOLOGY OF THE CARDIAC CELL 23
3.1 Introduction . . . 23
3.2 Cardiomyocytes . . . 23
3.2.1 Excitability . . . 23
3.2.2 Contractility . . . 25
3.3 The excitation-contraction coupling . . . 28
3.4 Regulation of cardiac cell contraction . . . 29
3.4.1 Length-tension relationship . . . 31
3.4.2 Force-pCa relationship . . . 34
3.4.3 Length-dependent activation . . . 37
3.4.4 Force-velocity relationship . . . 39
3.4.5 Auxotonic contractions . . . 39
3.4.6 Positive effect of ejection . . . 41
3.4.7 Summary . . . 43
3.5 Cellular origins of the FS mechanism . . . 43
3.6 Summary . . . 45
4 MODELING THE CARDIOVASCULAR SYSTEM 47
4.1 The six-chamber model . . . 48
4.2 Passive elements . . . 50
4.2.1 Passive chambers . . . 50
4.2.2 Resistances . . . 51
4.2.3 Valves . . . 51
4.2.4 Volume variations . . . 52

4.3 Active elements . . . 53
4.4 Cardiac cell model . . . 54
4.4.1 Electrophysiology . . . 54
4.4.2 Sarcomere contraction . . . 60
4.4.3 Excitation-contraction coupling . . . 65
4.4.4 LDA in the cell model . . . 66
4.5 Ventricular model . . . 67
4.6 Model parameters . . . 71
4.6.1 Cellular parameters . . . 71
4.6.2 Hemodynamic parameters . . . 72
4.7 Simulations . . . 75
4.7.1 Baseline . . . 75
4.7.2 Heart failure . . . 76
4.7.3 Load variations . . . 79
4.8 Discussion . . . 80
4.8.1 CVS model . . . 80
4.8.2 Ventricular model . . . 81
5 COMPARISON OF CARDIAC CONTRACTILITY INDICES 83
5.1 Methods for inotropy and load variations . . . 83
5.1.1 Inotropy variations . . . 84
5.1.2 Load variations . . . 84
5.1.3 E_{ES} assessment . . . 84
5.2 Results . . . 84
5.3 Conclusion . . . 87
6 THEORETICAL ANALYSIS OF THE FRANK-STARLING MECHANISM 91
6.1 Influence map of the CVS model . . . 92
6.2 Instantaneous increase in preload . . . 94
6.2.1 Schematic PV loops during preload increase . . . 96
6.2.2 Simulated PV loops during preload increase . . . 96
6.3 Switching off the LDA . . . 98
6.4 Discussion . . . 100
6.4.1 Valves opening and closing . . . 100
6.4.2 Timing of contraction during IIP . . . 101
6.4.3 Dynamics of ejection . . . 104
6.5 The velocity dependence . . . 106
6.5.1 IIP with the NO VD model . . . 108
6.5.2 IIP with the FIXED BIOCH model . . . 110
6.6 The influence of t_0 . . . 112
6.7 Conclusions from the isolated ventricle model . . . 114
6.8 The FS mechanism *in vivo* . . . 115
6.9 Summary . . . 119
6.9.1 The FS curve . . . 120
6.10 Vascular filling . . . 122
6.10.1 Instantaneous versus stabilized behavior . . . 122
6.10.2 Stressed blood volume . . . 123
6.10.3 Vascular filling simulations . . . 123
6.10.4 Vascular filling without LDA . . . 126

6.10.5 Conclusion . . . 127
6.11 Note on stroke volume and stroke work . . . 129
6.12 SV equilibrium . . . 131
6.13 Link with other works . . . 132
7 CONCLUSION 135
7.1 Summary . . . 135
7.2 Main findings . . . 137
7.2.1 The model . . . 137
7.2.2 Cardiac contractility indices . . . 137
7.2.3 The FS mechanism . . . 138
7.2.4 The FS mechanism and vascular filling . . . 138
7.2.5 The FS mechanism and SV equilibrium . . . 139
7.3 Limitations and future work . . . 139
A EQUATIONS GOVERNING THE CELLULAR ELECTROPHYSIOLOGICAL MODEL 143
B EQUATIONS GOVERNING THE SARCOMERE CONTRACTION MODEL 151
C EQUATIONS GOVERNING THE HEMODYNAMIC (6-CHAMBER) MODEL 155
BIBLIOGRAPHY 159

LIST OF FIGURES

Figure 1 The cardiovascular system (CVS). 5
Figure 2 Blood vessels from the circulatory system. 6
Figure 3 Heart anatomy. 7
Figure 4 Cardiac valvular opening and closure mechanism. 7
Figure 5 Brief overview of the electrical conduction system of the heart. 8
Figure 6 The cardiac cycle. 9
Figure 7 Pressures and volume in the left heart during a cardiac cycle. 10
Figure 8 Typical maximal and minimal pressures in the ventricular chambers and in the main arteries. Mean pressure in the atrial chambers. 11
Figure 9 A theoretical left ventricular pressure-volume loop. . . . 12
Figure 10 End-diastolic volume (EDV), end-systolic volume (ESV), stroke volume (SV) and stroke work (SW). 13
Figure 11 Starling law of the heart. 14
Figure 12 Starling's heart-lung preparation. 15
Figure 13 Effect of increasing venous inflow in Starling's experiments. 16
Figure 14 Sarnoff's curves for the left and right heart. 17
Figure 15 A family of Starling curves. 17
Figure 16 Left ventricular systolic pressure as a function of the end-diastolic segment length. 18
Figure 17 Left ventricular stroke volume as a function of left ventricular end-diastolic volume. 19
Figure 18 Left ventricular stroke work (open circles) as a function of left ventricular end-diastolic pressure. 19
Figure 19 Typical FS curves found in cardiology books. 20
Figure 20 The Frank-Starling mechanism as a basis for fluid therapy. 21
Figure 21 Cardiac muscle as a syncytium. 23
Figure 22 Action potential of a ventricular cell. 24
Figure 23 K^+, Na^+ and Ca^{2+} typical concentrations inside and outside a cardiomyocyte at resting potential. 25
Figure 24 The striated cardiac muscle. 25
Figure 25 Internal structure of cardiomyocytes. 26
Figure 26 Thick and thin filaments composition. 26
Figure 27 Crossbridge cycling. 27
Figure 28 Sliding filament theory. 28
Figure 29 The excitation-contraction coupling. 29
Figure 30 Tetanization in skeletal muscle. 30
Figure 31 Typical twitch contractions of cardiac and skeletal cells. . 31
Figure 32 Length-tension relationship in skeletal muscle. 32
Figure 33 Length-tension relationship in skeletal and cardiac muscle. 33
Figure 34 Force-pCa relationship in cardiac muscle. 35

Figure 35 Force-pCa relationship for two different SLs. 36
Figure 36 Force-velocity relationship in cardiac muscle. 40
Figure 37 Isometric and auxotonic contractions. 40
Figure 38 Impact of preload on produced force during auxotonic contractions. 41
Figure 39 Positive effect of ejection. 42
Figure 40 Length-dependent activation and its link to the FS mechanism. 44
Figure 41 Multiscale model of a ventricle. 48
Figure 42 The six-chamber CVS model. 49
Figure 43 Pressure-volume relationship of a passive chamber in a LP model of the CVS. 50
Figure 44 Representation of a flow resistance. 51
Figure 45 Volume variation of a chamber. 52
Figure 46 End-systolic pressure-volume relationship (ESPVR). . . . 53
Figure 47 Illustration of the time-varying elastance model. 54
Figure 48 Electrical circuit model of the cell membrane. 55
Figure 49 Schematic representation of APs in epicardial, midmyocardial and endocardial cells. 56
Figure 50 Transmembrane currents involved in the Ten Tusscher and Panfilov model. 56
Figure 51 Stimulus current for the triggering of AP in the electrophysiological model. 57
Figure 52 Calcium dynamics in the electrophysiological model. . . 58
Figure 53 Equivalent CB model within the muscle unit. 61
Figure 54 Equivalent CB dynamics. 62
Figure 55 Calcium kinetics. 63
Figure 56 Length-tension relationship obtained with the cell model. 66
Figure 57 Force-pCa curves obtained with the cell model. 67
Figure 58 Spherical ventricle model. 67
Figure 59 Wall stress σ and its relationship to half-sarcomere units. 69
Figure 60 Hemodynamic parameters of the six-chamber model of the CVS. 73
Figure 61 Excitation-contraction coupling. 76
Figure 62 Pressures and flows evolution for the left and right side of the circulatory model. 77
Figure 63 Pressure-volume loops, left ventricular half-sarcomere length and left ventricular volume during one heartbeat. 78
Figure 64 Ventricular failure versus normal ventricle. 79
Figure 65 PV loops following a RV preload reduction maneuver. . . 80
Figure 66 Simulations of various inotropic states. 85
Figure 67 Transitory LV PV loops during a 20 % increase in R_{sys}. . . 86
Figure 68 Determination of E_{es}. 86
Figure 69 ESPVR for different loading conditions. 87
Figure 70 E_{es} assessment with different data sets. 88
Figure 71 Cardiac contractility indices variations under changes in inotropy. 89
Figure 72 Frank-Starling (FS) mechanism. 91

Figure 73 Influence map of the variables related to the left ventricle in the CVS model. 93
Figure 74 Input functions extracted from the whole CVS model. . . 94
Figure 75 Instantaneous increase in preload (IIP) protocol with the isolated ventricle model. 95
Figure 76 Schematic effect of an acute LV preload increase. 96
Figure 77 Instantaneous increase in preload. 97
Figure 78 Half-sarcomere length and biochemical rates during IIP. . 99
Figure 79 Instantaneous increase in preload with the NO LDA model.100
Figure 80 The four phases of ventricular contraction on P_{lv}. 101
Figure 81 Visual representation of variations in SV for the IIP protocols with and without LDA. 103
Figure 82 Influence map of the variables related to the isolated ventricle model. 104
Figure 83 Influence map for the NO LDA isolated ventricle model. 105
Figure 84 Influence maps of the different variables for the NO VD and FIXED BIOCH isolated ventricle models. 107
Figure 85 Instantaneous increase in preload with the NO VD model. 108
Figure 86 Visual representation of variations in SV for the IIP protocols with (red) and without (dashed blue) VD. 109
Figure 87 Instantaneous increase in preload with the FIXED BIOCH model. 110
Figure 88 Visual representation of variations in SV for the IIP and IIP FIXED BIOCH models. 111
Figure 89 IIP protocols for different t_0 values. 113
Figure 90 Influence of t_0 on the IIP protocol. 113
Figure 91 Comparison of the IIP and IIP bis protocols. 114
Figure 92 Instantaneous increase in LV preload in the whole CVS model. 116
Figure 93 Aortic flow, ventricular and aortic pressures during instantaneous increase in LV preload in the whole CVS model.118
Figure 94 Simulated FS curve with the CVS model. 121
Figure 95 Linearity of the FS curve. 122
Figure 96 Frank-Starling curve and fluid responsiveness. 123
Figure 97 Vascular filling simulations. Stroke volume and preload as a function of the stressed blood volume. 124
Figure 98 Vascular filling simulations. Stroke volume as a function of the preload. 125
Figure 99 Maximal active force, maximal pressure and ejection duration during vascular filling simulations. 125
Figure 100 Afterload and time of aortic valve opening during vascular filling simulations. 126
Figure 101 Analyze of the saturating part of the SV curve. 127
Figure 102 Vascular filling simulations with the NO LDA CVS model. Stroke volume, maximal force and maximal pressure as a function of SBV. 127
Figure 103 Vascular filling simulations with the NO LDA CVS model. 128
Figure 104 Comparison of the FS curve and the vascular filling curve. 129

Figure 105 Stroke work as a function of SBV obtained from vascular filling simulations. 130
Figure 106 Constant afterload protocol. Pressure, pressure-volume loop and aortic flow. 131
Figure 107 SV equilibrium restoration after a perturbation inside the CVS model. 132

Table 1	Cellular parameter adjustment.	72
Table 2	Identified parameters.	74
Table 3	Standard values for the thirteen parameter identification procedure.	74
Table 4	Standard values for the nine parameter identification procedure.	75
Table 5	Quantitative analysis of IIP protocol in the isolated ventricle model. The percentages show the relative variation with respect to the baseline case.	97
Table 6	Quantitative analysis of IIP protocol with the NO LDA model.	99
Table 7	Quantitative analysis of timing variations in IIP protocol.	102
Table 8	Quantitative analysis of IIP protocols. Comparison with the original IIP case.	112
Table 9	Quantitative analysis of timing variations in IIP protocols. Comparison with the original IIP case.	112
Table 10	Quantitative analysis of LV IIP protocol in the whole CVS model.	116
Table 11	Quantitative analysis of LV IIP protocol in the whole CVS model. Comparison with the original IIP protocol.	117
Table 12	Quantitative analysis of the constant afterload protocol.	130
Table 13	Electrophysiological parameters	150
Table 14	Mechanical parameters	153
Table 15	Hemodynamic parameters.	157

ACRONYMS

CVS Cardiovascular System

CO Cardiac Output

EDP End-Diastolic Pressure

EDV End-Diastolic Volume

EPVRV End-Systolic Pressure-Volume Relationship

ESV End-Systolic Volume

FS Frank-Starling

HR Heart Rate

IIP Instantaneous Increase in Preload

LDA Length-Dependent Activation

LDFR Length-Dependent Fluid Response

LV Left Ventricle

PV Pressure-Volume

RV Right Ventricle

SBV Stressed Blood Volume

SV Stroke Volume

SW Stroke Work

VD Velocity Dependence

1 INTRODUCTION

1.1 GENERAL BACKGROUND

The cardiovascular system (CVS) is the blood transportation network that allows for oxygen distribution and metabolites transport through the whole body. It consists of a circulatory system (the veins, arteries and capillaries) where blood circulation is powered by the heart, a double muscular pump composed of two atria and two ventricles. Due to extrinsic and intrinsic control mechanisms of heart rate and cardiac contractility, the heart is a fine-tuned pump that can regulate and adapt its output to varying hemodynamical conditions [1–3]. Among the intrinsic regulatory processes, the Frank-Starling (FS) mechanism is a fundamental cardiac property present in all vertebrates [4]. It operates as follows: if more blood returns to the heart, there is an increase in ventricular volume. This means that the cardiac fibers composing the cardiac muscle are more stretched. The preload, defined as the fibers length prior to contraction, is thus increased. And because of this preload increase, the amount of blood ejected by the ventricle, called the stroke volume (SV), increases. As a consequence, there is no "stagnant" amount of blood left in the ventricle after contraction. In other words, the heart ejects blood proportionnally to its initial filling. This is the commonly accepted defintion of the FS mechanism: an instantaneous increase in SV following an increase in preload, within the same heartbeat [1].

This mechanism has bee studied by physiologists since the late 19th century, and is called after the important work of Ernst Starling and Otto Frank [5–9]. Since the founding studies of Starling, Frank, and their predecessors [10, 11], many experimental studies were conducted across the 20th century in order to confirm the existence of this mechanism *in vivo*, also known today as the "Law of the Heart". At some point, it became clear that the origin of this rapid adaptation of the heart to loading variations lied in the mechanical properties of cardiac cells themselves. The cellular mechanism of muscular contraction was not elucidated before the second half of the 20th century [12, 13], after which numerous studies were performed on cardiac and skeletal cells to investigate their mechanical properties [14, and references therein]. Among them, the length-dependent activation (LDA), is of great importance. Experimentally highlighted in the 70s for the cardiac muscle [15], LDA is a cellular mechanism responsible for an increased produced force following an increase in length prior to contraction. The molecular mechanisms underlying LDA are not fully understood yet. Nevertheless, LDA is assumed to be the cellular basis for the FS mechanism [4, 16–21]. The most common explanation given in the literature is that, as preload increases, the length of cardiac fibers increases, and a greater force is generated during the cardiac beat. This leads to an increased produced pressure, and more blood is ejected, thus increasing the SV [1, 3, 18, 22].

In addition to these physiological considerations, the FS mechanism is also associated with clinical therapies in intensive care units. It is indeed considered as a basis for fluid therapy [23–26]. This therapy consists in intravenous fluid administrations to patients in clinics, in order to increase their cardiac output. The reasoning is that, as circulating blood volume is increased upon vascular filling, the preload increases. It is generally assumed that the FS mechanism takes action here and is responsible for the increased SV. The FS mechanism is also believed to regulate the SV equilibrium between both ventricles. As we see, this mechanism is an essential feature of the cardiac pump, and it forms the basis of commonly used therapies in intensive care units.

While the amount of biological experimental studies and data continues to grow, the field of mathematical modeling of biological systems is also expanding. Mathematical models aim at describing a system with equations, in order to analyze, interpret or predict the system behavior. When applied to biological systems, especially to the CVS, they become a powerful instrument, either for clinical purposes, or for broadening physiological knowledge [27, 28]. The state of the art in cardiac electromechanics modeling is quite advanced and vast, as a lot of subcellular, cellular, tissue and organ models are developed in the literature [28, 29, and references therein]. Since the heart is a multiphysics and multiscale system (microscopic events at the subcellular level generate emergent properties at the macroscopic tissue level [27, 28]), multiscale models of cardiac contraction are relevant tools to study the cardiac function. They allow to study the link between physiological observations across different spatial and temporal scales, a task not easy to perform experimentally. By providing a formal framework to link multiple experimental assays, cardiac modeling is becoming an important tool for the integration of knowledge of cardiac function in health and disease [27–29].

1.2 GOAL OF THIS RESEARCH

The FS mechanism is a global (macroscopic) response to an increase in preload. LDA, on the other hand, is essentially defined through cellular (microscopic) *isometric* experiments, where the cardiac cell length is fixed. This situation does not occur *in vivo*, or at least not during the whole time course of the beat, because cardiac cells shorten during blood ejection, and lengthen during blood filling. Hence, a direct relationship between the FS mechanism and LDA cannot be straighforwardly made. It is of course very difficult to investigate this relationship experimentally, as two very different scales are involved. In this case, mathematical models of biological system help overcome the experimental limitations. In this work, we propose an original *in silico* analysis of the FS mechanism to investigate the contribution of LDA, based on a multiscale model of the CVS, where ventricular contraction is described at the cellular scale. Attention is paid to providing rigorous definitions and numerical protocols so that the correlation between LDA and the FS can be established without any ambiguity, a precaution not always found in the literature and in textbooks. After this physioliogical analysis, we also perform vascular filling simulations to investigate the supposed role of the FS mechanism in clinical applications.

1.3 THESIS ORGANIZATION

Chapter 2 presents an overview of the CVS, along with some essential cardiac physiology concepts, necessary to understand this work. The FS mechanism is introduced with a brief history of the experimental researches. The principle of vascular filling therapy is also described.

Chapter 3 provides a physiological background for cardiac cell contraction. Important notions and properties are described. LDA is presented in details, and a theoretical discussion about its link with the FS mechanism is provided.

Chapter 4 presents the multiscale model we built in order to perform an analysis of cardiac contraction at both scales, cellular and ventricular.

Chapter 5 presents an original study of cardiac contractility indices. Since cardiac contractility is a property intrinsically related to the cellular scale, and needs to be assessed with reliable indices at the organ scale in clinics, our model allows for an *in silico* study of the contractility-dependence of four cardiac contractility indices.

Chapter 6 presents the core study of this thesis: an *in silico* analysis of the FS mechanism and its relationship with the cellular LDA. We challenge the correlation that is generally admitted between vascular filling therapy and the FS mechanism. We also analyze the role of the FS mechanism in regulating the SV equilibrium between both ventricles.

Chapter 7 presents conclusions and future work perspectives.

2 PHYSIOLOGY OF THE CARDIOVASCULAR SYSTEM

2.1 INTRODUCTION

In this chapter, a brief description of the cardiovascular system (CVS) and elements of cardiac physiology will be addressed. This will provide a basis for understanding CVS modelling and the results presented in the following chapters.

The cardiovascular system is the blood transportation network that allows for oxygen distribution and metabolites transport through the whole body. As can be seen in Fig. 1, oxygenated blood leaves the pulmonary circulation and enters the left atrium, then the left ventricle. It is ejected into the systemic circulation and visits all the organs except the lungs. Finally it comes back deoxygenated into the right atrium, then into the right ventricle. It is finally sent through the pulmonary circulation to be oxygenated again, and the cycle restarts.

The CVS mainly consists of two components:

- The circulatory system, composed of veins, arteries and capillaries.
- The cardiac pump, composed of two atria and two ventricles.

Both components will be more detailed in the next sections.

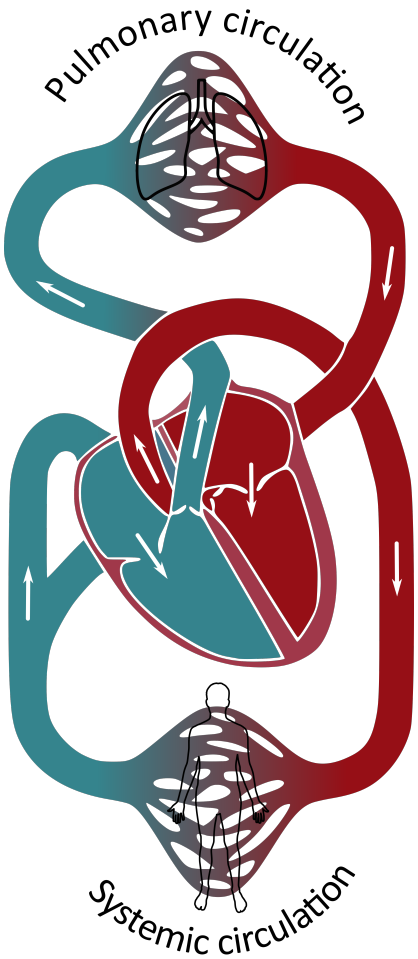

Figure 1: The cardiovascular system (CVS).

2.2 THE CIRCULATORY SYSTEM

The systemic and pulmonary circulations form the circulatory system. They enable the distribution of blood to all organs, where exchanges of fluids, gases and nutrients occur between blood and tissues [1]. Blood leaves the heart trough the arterial system. The arteries branch into smaller arteries, which in turn branche into arterioles, and finally the arterioles supply the capillaries. The capillary system is a parallel network of small porous vessels where the exchanges mentionned earlier take place. The capillary system connects the arterial and the venous system. Blood returns to the heart via the venous sytem, a converging network of veins. A schematic representation of the circulatory system is presented in Fig. 2.

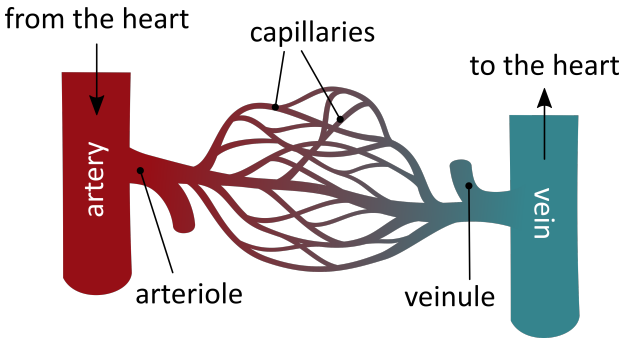

Figure 2: Blood vessels from the circulatory system.

The main arteries are the aorta and the pulmonary artery. The former connects the left ventricle to the beginning of the systemic circulation and contains oxygenated blood. The latter connects the right ventricle to the beginning of the pulmonary circulation and contains de-oxygenated blood. The main arteries are large, elastic and oppose almost no resistance to blood flow. Once they subdivise into arterioles and capillaries, resistance to blood flow increases and becomes considerable.

The main veins are the inferior and superior *venae cavae* and the pulmonary veins. The *venae cavae* connect the end of systemic circulation to the right atrium and contain de-oxygenated blood. The pulmonary veins connect the end of the pulmonary circulation to the left atrium and contain oxygenated blood. Veins are compliant vessels that can act as blood reservoirs and regulate blood flow and pressures distribution [1].

2.3 THE CARDIAC PUMP

2.3.1 *Anatomy*

The heart is a double muscular pump: the *right heart*, which propels blood through the pulmonary circulation, and the *left heart*, which propels blood through the systemic circulation [3]. Each pump is composed of two chambers: an atrium and a ventricle, as schematised in Fig. 3. Four cardiac valves, also presented in Fig. 3, prevent the blood from flowing backwards and ensure an efficient

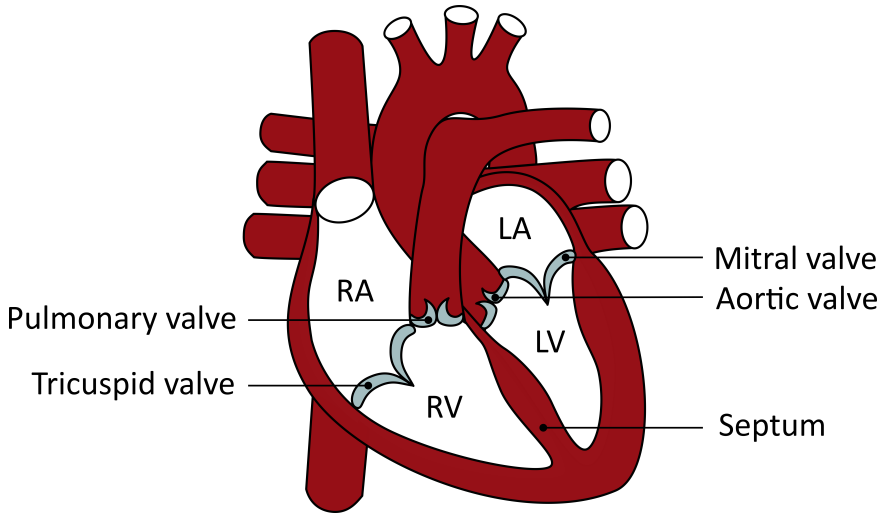

Figure 3: Heart anatomy. The left heart is composed of the left atrium (LA) and the left ventricle (LV). The right heart is composed of the right atrium (RA) and the right ventricle (RV). The common ventricular wall is called the septum. The four valves ensure the unidirectionnality of blood flow.

pumping during the cardiac cycle. The tricuspid valve is located between the right atrium and the right ventricle. The mitral valve is lovated between the left atrium and the left ventricle. These two valves are called the atrio-ventricular (AV) valves. The pulmonary valve is located between the right ventricle and the pulmonary artery. Finally, the aortic valve is located bewteen the left ventricle and the aorta. These two valves are called the ventriculo-arterial (VA) valves. Cardiac valves work in such a way that if the uptream pressure is greater than the downstream pressure, the valve gets opened. If the pressure gradient reverses, the valve closes. A schematic representation of this passive mechanism is shown in Fig. 4.

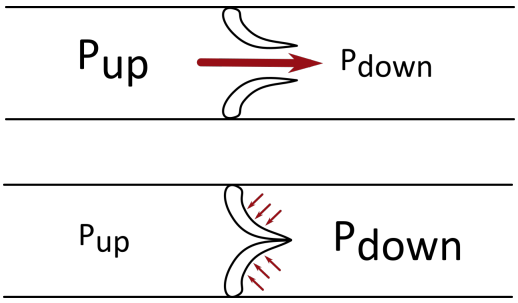

Figure 4: Cardiac valvular opening and closure mechanism. When the upstream pressure is greater than the downstream pressure, the valve is opened and blood flows according to the pressure gradient. If the pressure gradient is reversed, the valve gets closed because of its leaflet structure, thus preventing the blood from flowing backwards. This is a passive mechanism that does not require active contraction from the valve [3].

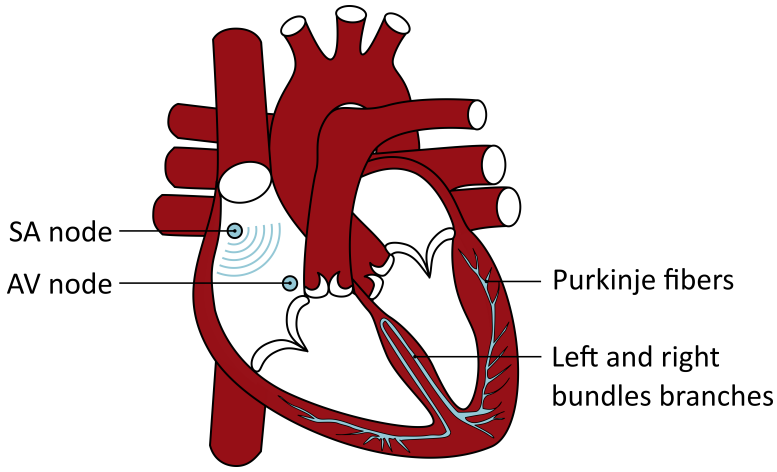

Figure 5: Brief overview of the electrical conduction system of the heart. Starting from the sino-atrial (SA) node, action potentials (APs) propagate across the atria. At the atrio-ventricular (AV) node, APs are able to activate ventricular tissue by following the bundle branches located in the septum. Finally, the Purkinje fibers system guides the electrical activation accross the whole ventricle.

2.3.2 *Electrical activity*

Electrical waves propagate periodically through the cardiac muscle, called the myocard, and initiate mechanical contraction[1]. The primary source for the electrical activation are the pacemaker cells located in the sino-atrial (SA) node, as shown in Fig. 5. These cells are able to initiate electrical impulses (called "action potentials", AP) that spread accross the atrial tissue first and then accross the ventricular walls. There is a conduction delay at the atrio-ventricular (AV) node (Fig. 5), which means that ventricular contraction is activated later than atrial contraction. This limits the risk of high ventricular rates in case of atrial fibrillation and allows an appropriate ventricular filling before contraction, thus optimizing cardiac contraction [1].

2.3.3 *The cardiac cycle*

A cardiac cycle is initiated and maintained by the electrical impulses born in the SA node, as mentionned in the previous section. The cardiac cycle is charaterized by successions of two events: diastole and systole [1, 3]. Diastole is associated with atrial/ventricular relaxation and blood filling, while systole is associated with active contraction and blood ejection through the main arteries.

The four phases of the cardiac cycle are presented in Fig. 6 and discussed now.

Ventricular filling

The AV valves open and blood flows spontaneously from the atria into the ventricles. Ventricular filling is mostly passive, but the atrial systole is

[1]The electrical and mechanical activity of the cells that compose the myocard will be detailed in Chapter 3.

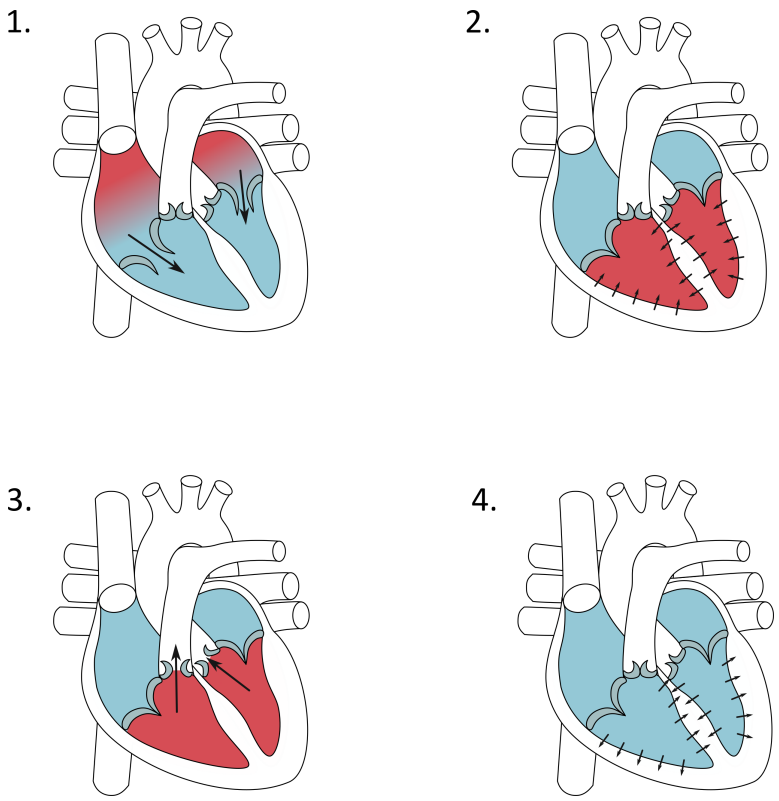

Figure 6: The cardiac cycle. Ventricular filling (1), isovolumic contraction (2), blood ejection (3), and isovolumic relaxation (4).

responsible for a supplementary *kick* of blood which enhances ventricular loading in the late filling phase [1, 3].

Isovolumic contraction

After the atrial kick, atrial pressure falls while ventricular pressure rises with blood filling. The AV valves close, according to the mechanism described earlier (see Fig. 4). Ventricular contraction begins, which causes a rapid increase in pressure inside the ventricular cavities. Because all the valves are closed, there is no variation in blood volume[2] and this phase is called *isovolumic contraction*.

Blood ejection

Pressure rises in both ventricles and exceeds aortic and pulmonary arteries pressures. Thus, the VA valves open and blood ejection begins. The active contraction of ventricular fibers progressively comes to an end. Pressure inside ventricular cavities start decreasing and it slows down ventricular emptying. When ventricular pressure drops down below the aortic and pulmonary pressures, the corresponding valves close. It is the end of ventricular systole.

[2]Ventricular geometry changes, however, and the heart shape becomes more spheroidal [1].

Isovolumic relaxation

Ventricular relaxation begins, and provided that all the valves are closed, it is an isovolumic phase. Since atria keep receiving blood from the venous side of both circulations during ventricular systole, atrial pressure rises and once it exceeds ventricular pressure, the AV valves open and the cardiac cycle starts again.

2.3.4 *Pressure and volume variations*

Blood flows in the opposite direction of the pressures gradients, and the cardiac valves opening and closing mechanism also relies on pressure differences. A diagram of pressure variations in the left heart during one heartbeat is shown in Fig. 7, where the four phases described earlier are also indicated. Pressures in the right heart are not represented, but they are quantitavely similar. Volume variations are also plotted.

Left ventricular pressure rises slowly during ventricular filling, then sharply during isovolumic contraction. Maximal pressure (systolic pressure) is achieved during blood ejection. Then the pressure drops considerably during isovolumic relaxation.

Left atrial pressure varies to a much smaller extent compared to ventricular pressure. It is often approximated as a constant, but actually the atrial pressure curve is rather complex in shape, as the events taking place during atrial diastole and systole are numerous and varied [1, 3].

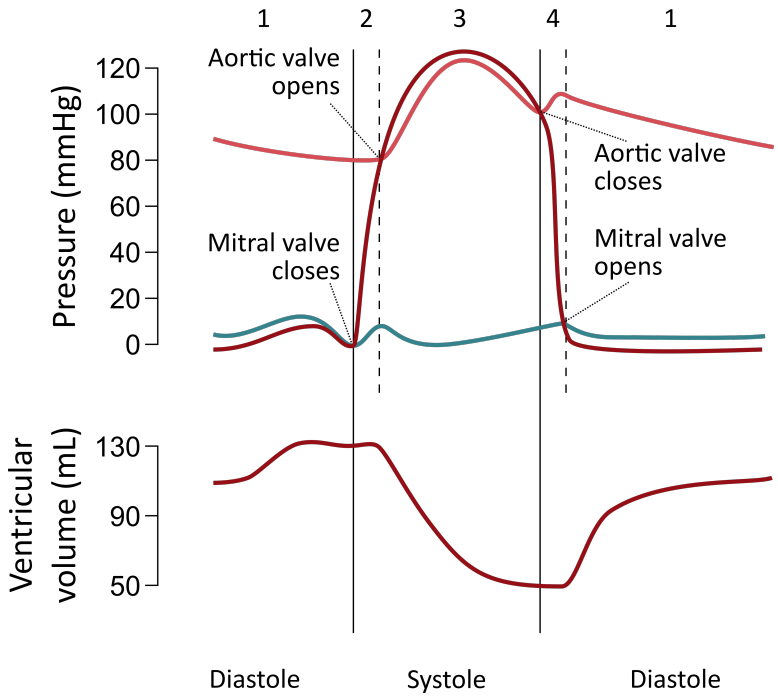

Figure 7: Pressures and volume in the left heart during a cardiac cycle. Adapted from [30].

Aortic pressure increases during blood ejection, as it fills with the blood coming from the left ventricle. When the aortic valve closes, aortic pressure starts declining as blood flows into the systemic circulation.

The typical pressure range inside the four cardiac cavities and main arteries is shown in Fig. 8. These pressures are expressed in millimetres of mercury[3] (mmHg) above atmospheric pressure.

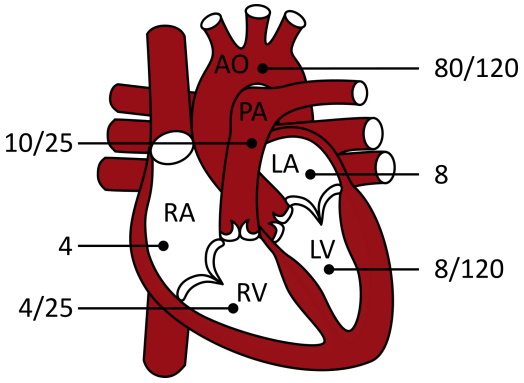

Figure 8: Typical maximal and minimal pressure values in the ventricular chambers and in the main arteries. Mean pressure in the atrial chambers. All values are in mmHg. AO: aorta, PA: pulmonary artery.

Ventricular blood volume increases during diastolic filling. Then it is kept constant during the isovolumic contraction. As the ejection phase starts, ventricular volume decreases. Some blood remains inside the ventricle at the end of the ejection phase, and this blood volume is kept constant during the isovolumic relaxation. It increases again during the next filling phase, etc ...

A useful tool to present the pressure and volume of the cardiac chambers is the pressure-volume loop (PV loop). These curves are commonly used in cardiac physiology, as they provide insights into heart passive and active properties. Ventricular pressure is plotted as a function of ventricular volume. One PV loop corresponds to one heartbeat (or one cardiac cycle). A typical left ventricular PV loop[4] is depicted in Fig. 9.

Finally, it is worth noticing than the left heart is a high-pressure pump, while the right heart is a low-pressure pump, as can be seen from the typical pressure values depicted in Fig. 8. Those two pumps, arranged in series, eject the same amount of blood during a heartbeat. This ensures that blood does not accumulate in one of the two circulations.

2.3.5 *Important concepts*

Stroke volume

The stroke volume (SV) is the amount of blood ejected by a ventricle during a heartbeat. It is equal to the difference between the end-diastolic volume (EDV) and the end-systolic volume (ESV). The former is the ventricular volume at the

[3] 1 mmHg $\approx$ 133.3 Pa.

[4] For a normal heart at a resting beating rate.

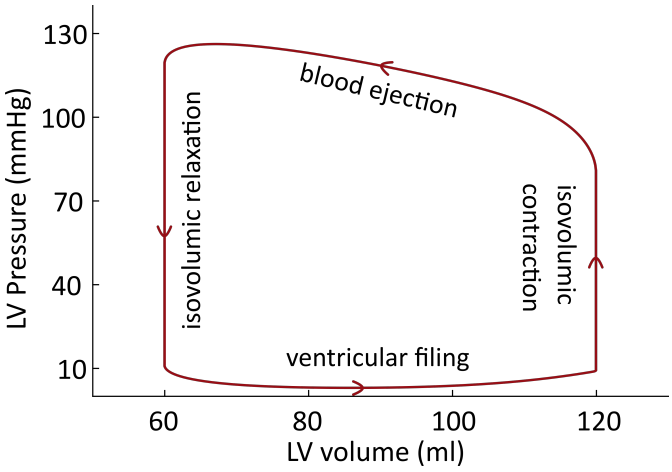

Figure 9: A theoretical left ventricular pressure-volume loop.

end of the filling phase and the latter is the volume at the end of the ejection phase. These concepts can be easily seen in a PV loop, as in Fig. 10.

Cardiac output

The cardiac output (CO) is the volume of blood being pumped by the heart per unit of time. It is given by the product of ventricular SV and heart rate (HR):

$$CO = HR \times SV \tag{2.1}$$

Stroke work

Stroke work is the mechanical work performed by the ventricle during a heartbeat. It is given by the area enclosed by the PV loop (see Fig. 10).

Preload

Preload is the initial stretching of the cardiac myocytes prior to contraction [1]. It is related to the maximal length of cardiac fibers at the end of diastole. The more blood returns to the heart, the more stretched the fibers are. Ventricular preload has an important effect on SV, as described in the next section.

Afterload

Afterload is the "load" against which the heart must contract to eject blood [1]. For the left ventricle, it is especially related to the aortic pressure, that the ventricle has to overcome in order to eject blood. It is also related to the ventricular wall stress: the greater the wall stress, the greater the tension cardiac fibers have to develop in order to shorten against the intraventricular pressure.

Inotropy

Cardiac inotropy, or contractility, is related to the intrinsic ability of the heart muscle to actively contract. An increase in inotropy leads to an increase in the

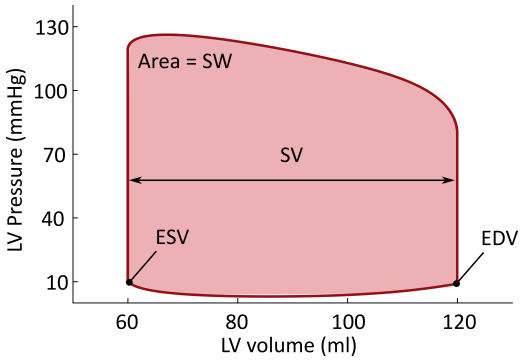

Figure 10: End-diastolic volume (EDV), end-systolic volume (ESV), stroke volume (SV) and stroke work (SW) are easily measurable with a PV loop.

force of contraction. Cardiac contractility is associated with calcium handling at the cellular scale, and will be further described in the next chapter.

2.4 REGULATION OF CARDIAC OUTPUT

Since CO is the product of HR and SV, it can be controlled via HR and/or SV regulation. A distinction is often made between *intrinsic* and *extrinsic* CO regulatory mechanisms. The former are associated with regulatory mechanisms inherent in the cardiac pump itself, while the latter refer to external influences on cardiac electromechanics.

2.4.1 *Extrinsic regulatory mechanism*

Heart rate is mainly controlled via neuronal (sympathetic and parasympathetic stimulations) and humoral (e.g., epinephrine, or thyroid hormones) regulatory mechanisms, and it can also be altered with temperature or kalemia variations [1, 31]. Inotropy (or contractility) can be altered via neuro-hormonal factors as well [18, 31, 32]. Extrinsic control is exerted primarily through phosphorylation of specific regulatory proteins [33], and it will not be addressed in detail in this work.

2.4.2 *Intrinsic regulatory mechanism*

An increase in HR can lead to an intrinsic positive inotropic effect, called the Bowditch effect[5]: as the frequency of contraction increases, more calcium is present in the intracellular compartment, which increases the contractile force [1, 34]. The link bewteen calcium and inotropy will be analyzed in the next chapter.

Variation in ventricular loading also induces inotropic responses: an increase in EDV, either because of increased aortic resistance or venous return[6], immediately leads to an more powerful ventricular contraction. This rapid response is called the Frank-Starling mechanism (FS mechanism). A second inotropic re-

[5]Sometimes also refered as the "frequency-dependent activation" or the "positive staircase effect".
[6]Venous return is defined as the amount of blood coming back to the heart.

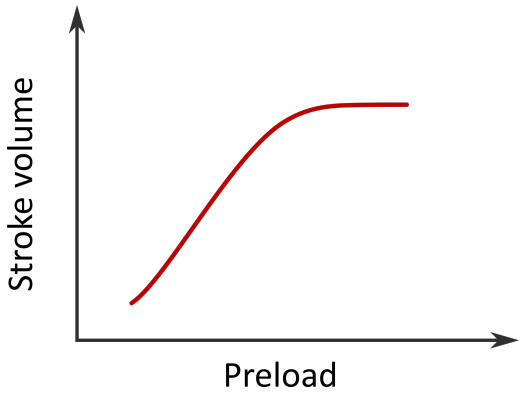

Figure 11: Starling law of the heart. An increase in preload leads to an increase in stroke volume.

sponse, occuring typically several minutes later, further increases myocardial contractility. This slower response, named the Anrep effect, is a mechanism by which the heart adapts to an abrupt increase in afterload, occurring after the FS mechanism takes place [35, 36]. It is related to alteration in calcium handling, contrary to the FS mechanism.

Since this work focuses on the instantaneous response to ventricular loading variations, the FS mechanism is described in the next section, while the Anrep effect will be set aside.

2.5 THE FRANK-STARLING MECHANISM

2.5.1 *Definition*

During ventricular or atrial blood filling, cardiac fibers are extended and become ready to contract. This initial stretch of the fibers, the preload, is modulated by the amount of blood entering the cavity, among other things. For instance, if the blood flow arriving in the right atrium (the venous return) increases, right ventricular preload increases. And as a result, the stroke volume increases. This is called the "Frank-Starling mechanism" (FS mechanism), a mechanism studied for more than a century since the work of Otto Frank [5] and Ernest Starling [6–9]. The FS mechanism implies that the heart is able to adapt the stroke volume to the venous return. If more blood enters a ventricle, more blood will be ejected during this beat, so no "stagnant" amount of blood will accumulate inside the cavity. Furthermore, this extra volume of ejected blood will soon reach the other ventricle, where it will also be ejected thanks to the FS mechanism. Therefore the ouputs of both ventricles are matched over time, and no blood volume accumulates in one circulation [1, 37–39]. This intrinsic ability of the heart to adapt its output in response to changes in ventricular filling is also called the "Starling law of the heart" [3, 20, 21]. A schematic "Starling's curve" is represented on Fig. 11.

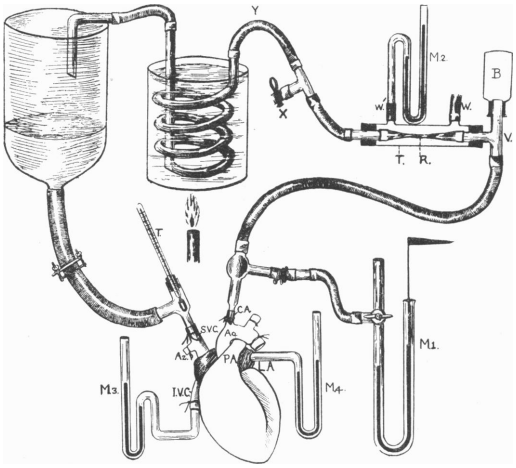

Figure 12: Starling's heart-lung preparation [6]. The systemic circulation is bypassed. The systemic blood flow is diverted from the aorta into an adjustable resistance (the "arterial resistance"), then into an elevated blood reservoir. Blood return from this reservoir to the vena cava is controlled by a screw. Then blood flows into the intact pulmonary circulation (not shown) and back to the left heart.

2.5.2 *Historical background*

The correlation between diastolic filling and cardiac output had already been brought to light before the work of Frank and Starling [10, 11]. However, Starling's study is most remembered because of his elaborate experimental procedures on "heart-lung preparations", as reproduced in Fig. 12.

After a thoracotomy on anesthetized dogs, Starling cut the aorta and diverted the blood flow into an extracorporal circuit, so that systemic circulation was cut through. Instead, the systemic flow passed through an artificial resistance (called "the arterial resistance"), then through an elevated blood reservoir. This blood reservoir was then connected to the vena cava and blood could flow into the pulmonary circulation, which was kept intact. The opening of the reservoir was controlled by a screw. Since the blood flow leaving the reservoir matched the blood flow ejected in the aorta, Starling called them both "cardiac output". The degree of opening of the screw determined the amount of blood volume coming back into the right atrium, allowing modifications of the preload. The arterial resistance could also be varied, allowing modifications of the afterload.

Starling observed that the degree of diastolic filling had a direct impact on cardiac output. For instance, if the arterial pressure rose, the heart was able to maintain a constant output: at the first beat, it could not eject as much blood as before, since the pressure it was contracting against had increased. So at the end of the systole there was more blood left inside the heart. The following diastolic (filling) phase then led to an increased end-diastolic volume, because the venous return added to the remaining blood volume from the preceeding beat. A greater fiber length meant more energy set free in the next beat, and the heart, after several beat, would be able to eject the same amount of blood as before. When this stabilized state was reached, the heart output was still the same but the heart was now operating with a permanent increased end-diastolic volume, as long

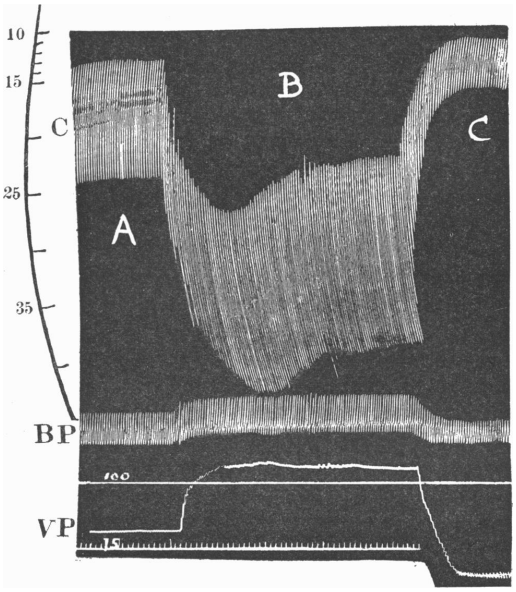

Figure 13: Effect of increasing venous inflow in Starling's experiments (phase "B") [7]. Ventricular volume (in ml, upper recording) increase is characterized by a downward deflection of the curve (see the scale on the left). Note also that the amplitude of the volume oscillations are increased with increased venous return, meaning that more blood is ejected on each beat. BP: arterial pressure. VP: venous pressure.

as the arterial pressure keeps its new and higher value. Starling also studied the impact of venous return on cardiac output. By varying the opening of the screw or the height of the blood reservoir, right ventricular filling could be altered. Fig. 13 shows the results obtained. When venous inflow was increased, venous pressure (VP) and ventricular volume increased. The important result is that the cardiac output also increased.

In his famous Linacre Lecture on the *Law of the heart*, Starling wrote: "The energy of contraction is a function of the length of the muscle fibers" [9]. At that time the physiology of muscle contraction at the cellular scale was not understood yet but Starling had already perceived that the ability of the heart to accomodate different loading conditions lied in the muscle fibers length-dependent properties. In other words, an increase in ventricular filling increases the cardiac cells length, which promotes an increase in developed systolic force and pressure. Starling focused a lot on cardiac work and the "mechanical energy set free at each contraction", as thermodynamics had a dominant role in the field of physiology at this time [40].

To further develop Starling's findings, many experimental studies were conducted to clarify the relationship between fibers length and cardiac output. As fiber length is not directly measurable *in vivo*, the end-diastolic volume (EDV) was generally considered as a good preload index. *In vivo* volume assessment is still arduous and for this reason the end-diastolic pressure (EDP) was usually prefered. However, it was shown that EDP does not correlate well with fiber length [41, 42], and Starling himself emphasized the importance of diastolic length and not diastolic pressure [7].

[7] "It is length rather than tension which determines the energy of contraction" [7].

Sarnoff and Berglund explored the validity of the *Law of the heart* in open-chest anesthetized dogs with an intact systemic circulation [43]. They connected a blood reservoir to the left or right atrium and varied the atrial pressure by elevating or lowering the reservoir, thus impacting the amount of blood flowing into the atria, then into the ventricles. Then they recorded ventricular stroke work (SW) as a function of mean atrial pressure, as presented in Fig. 14. Atrial pressure is a major determinant of ventricular filling, so mean right (left) atrial pressure was considered as an index of right (left) ventricular preload.

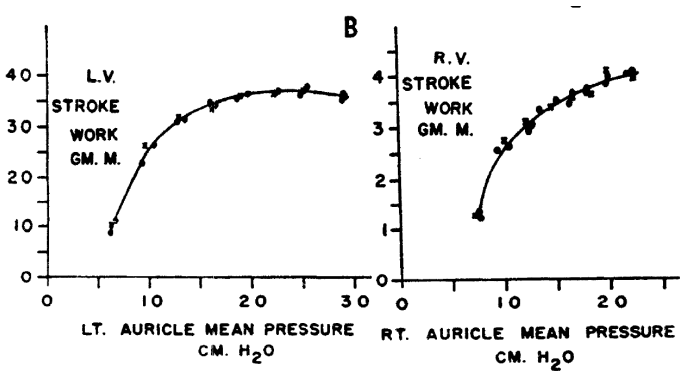

Figure 14: Sarnoff's curves for the left and right heart [43]. Mean atrial pressure is taken as a preload index. Stroke work is measured for varying venous inflows, controled by the height of a blood reservoir.

Sarnoff and Berglund also came up with the idea of a "family of Starling curves". For instance, a pharmacological agent such as epinephrine has an impact on ventricular inotropic state, which may alter SW without any variation in atrial pressure. So for each heart, there is a serie of curves, and shifting from one curve to another may occur with inotropic variations, as schematized in Fig. 15.

With this view, a change in filling pressure in one direction may be associated with a change in SW in the opposite direction. This does not question the FS relationship, it is rather the sign of a curve shift, because of physiological or pharmacological alterations. The point is that, under these new conditions, a

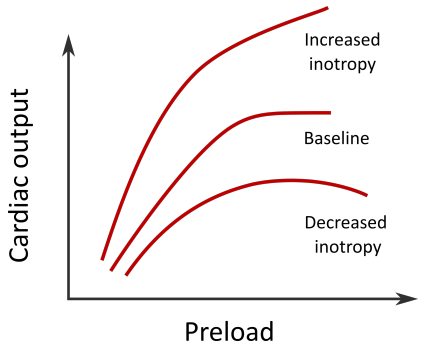

Figure 15: A family of Starling curves. An increase in preload may be associated with a decrease in cardiac output if the inotropy decreases. This does not mean that the FS mechanism has vanished.

consistent relationship betweeen filling pressure and stroke work is always obtained, namely an increased SW for increasing atrial pressures, with a plateau phase for the highest filling pressures [43, 44].

Braunwald and colleagues studied the FS mechanism in human patients [45–49]. They worked with a variety of protocols and measurements methods.

In one of their study [45], they could measure the length of a muscle segment between the points of attachment of a gauge sealed to the left ventricule of anaesthetized patients undergoing open-chest operations. The length of the segment at the end of the diastolic phase was taken as an index of preload. They also recorded the maximal systolic pressure and obtained graphs as the one presented in Fig. 16. They came to the conclusion that the left ventricular end-diastolic fiber length was a fundamental determinant of the force of ventricular contraction.

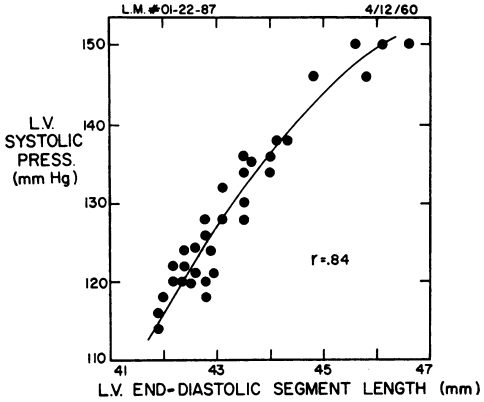

Figure 16: Left ventricular systolic pressure as a function of the end-diastolic segment length [45]. These segments were attached to the left ventricle of anaesthetized patients undergoing open-chest operations. The longer the segment length, the higher the developed pressure.

Braunwald and colleagues also worked with intact unanaesthetized patients. They measured end-diastolic volume and stroke volume by a biplane angiocardiographic technique [47]. They showed that beat-to-beat variations in EDV were correlated with the SV of the subsequent beat, as showed in Fig. 17.

Another set of experiments were conducted in the intact heart of human patients, where rapid blood transfusions were used to simulate an increase in venous return, thus an increase in preload [46]. After inhibiting the activity of the autonomic nervous system[8], the transfusion increased the central blood volume, stroke volume and stroke work (see Fig. 18). Demontrating that, in response to a preload increase, the normal human heart reacted in a manner similar to that of the heart-lung preparations, Braunwald and colleagues concluded that the Starling law of the heart is applicable to man [48].

They also adressed the issue of the adrenergic nervous system, whose activity regulates myocardial contractility. They presented the FS mechanism as an

[8]Intravenous fluid infusions may trigger the activity of the autonomic nervous system and hinder the increase in blood volume, thus interfering with the venous return and the FS mechanism. This was not a problem for Starling experiments since he worked on heart-lung preparations, disconnected form the nervous sytem.

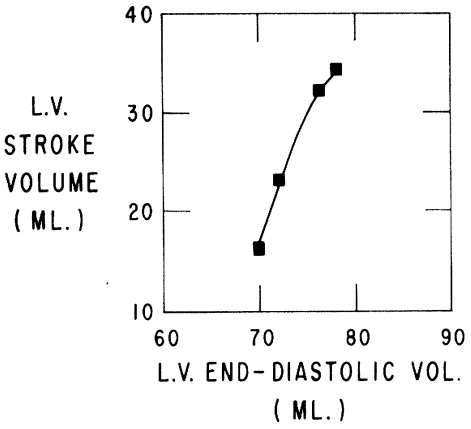

Figure 17: Left ventricular stroke volume as a function of left ventricular end-diastolic volume [47]. Volumes were measured by a biplane angiocardiographic technique on intact unanaesthetized patients.

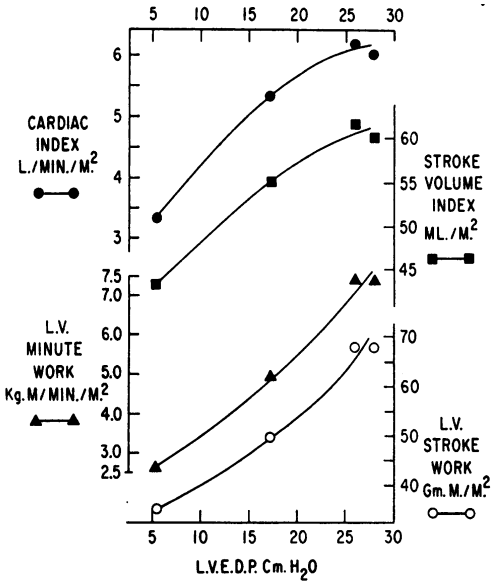

Figure 18: Left ventricular stroke work (open circles) as a function of left ventricular end-diastolic pressure [46]. Rapid blood infusions were performed on human patients to simulate an increase in venous return.

intrinsic regulatory mechanism of cardiac performance, determined to a major extent by the fibers length at the onset of ventricular contraction [48]. On the other hand, the action of the sympathetic nervous system was presented as an extrinsic control mechanism of cardiac contractility that does not depend on fiber length. The former will be thoroughly examined in this thesis but the extrinsic effect of the nervous system will be set aside.

To conclude, many studies confirmed this intrinsic ability of the heart to accommodate changes in preload [40], thus corroborating the early findings of Starling: "Within wide limits the heart is able to increase its output in direct proportion to the inflow." [7].

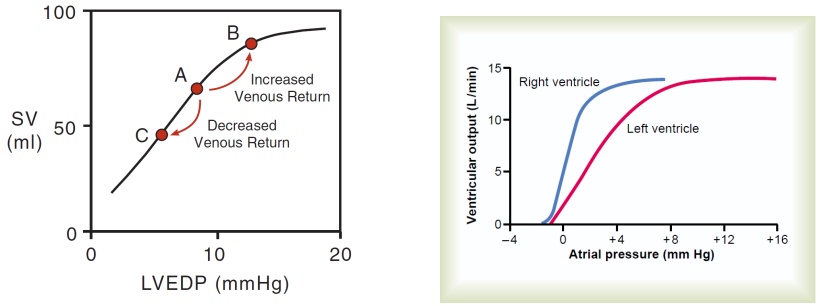

(a) (b)

Figure 19: Typical FS curves found in cardiology books [1, 3]. The preload is often replaced by end-diastolic volume, end-diastolic pressure or right atrial pressure. Cardiac (or ventricular) output is sometimes substituted for stroke volume. The curves in (b) are often called "ventricular function curves" [3].

Let us note that the FS mechanism is addressed in every cardiology book today. The Starling curves are generally presented as in Fig. 19. Ventricular preload is often assimilated with the end-diastolic volume, the end-diastolic pressure, or the right atrial pressure. Cardiac output is sometimes substitued for SV. SW, on the other hand, is rarely represented. The most common description of the FS mechanism goes as follows: "The greater the heart muscle is stretched during filling, the greater is the force of contraction and the greater the quantity of blood pumped into the aorta" [3]. There have been a debate about the existence of a descending part of the curve for very high preloads, but it is generally admitted that in physiological conditions the heart operates on the ascending part of the curve, because the passive tensions in cardiac fibers prevent them to extend excessively [43, 50]. The shape of the curve is presented as curvilinear, with a steep portion for low preloads and a plateau region for high preloads [23, 51].

2.5.3 *Vascular filling and fluid responsiveness*

Among the experiments described in the previous section, the rapid blood transfusions performed by Braunwald and colleagues on human patients [46] are particularly interesting, because they showed an increase in stroke volume after the transfusion. This experimental protocol actually forms the basis of *vascular filling* (or fluid therapy, or fluid resuscitation), a frequently used therapy to manage critically ill patients with hemodynamic instability [23–26]. Basically, fluid is administrated intravenously in order to restore cardiac output[9]. The patient will be declared *fluid-responsive* if the cardiac output substantially increases with the fluid injection. Predicting the hemodynamic response to fluid administration is essential, as excessive fluid infusion may result in volume overloading and promote pulmonary edema or right ventricular dysfunction [24, 25].

The FS mechanism is often cited as the basis for vascular filling therapy [23–26]. As fluid injection increases the circulating blood volume, ventricular preload increases. The basis for fluid therapy is summarized in Fig. 20, where fluid-responsiveness is assumed to be correlated with the Frank-Starling curve. If the

[9]The type and amount of fluid injected may vary, as well as the duration of the infusion.

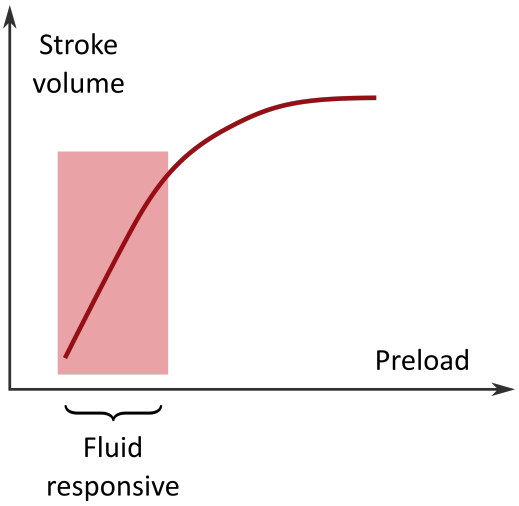

Figure 20: The Frank-Starling mechanism as a basis for fluid therapy. Increasing ventricular preload through fluid injection may lead to an increase in stroke volume if the patient operates on the ascending part of the FS curve.

patient is operating on the steep part of the curve, an increase in preload will induce a substantial increase in stroke volume. On the other hand, if the patient is operating on the flat portion of the curve, fluid injection will not lead to a significant increase in stroke volume. Clinicians are thus left with this basic question: on which portion of his/her curve is the patient operating? A definite answer is nonetheless hard to obtain.

Following this reasoning, the determination of preload alone should be enough to predict fluid responsiveness. However, as mentionned earlier, the length of cardiac fibers is not available *in vivo*. So other ventricular preload indices are required, especially in clinics where fluid responsiveness assessment is coupled with the need for minimally invasive measurements. Fiber length is often substituted with ventricular volume. Surprisingly, EDV measurements lead to conflicting results regarding fluid responsiveness prediction. This may be related to the difficulty of accurate volume measurement *in vivo*, an issue that is still relevant to this day [52], or to the influence of intrathoracic pressure on preload, afterload and contractility [24]. Other markers of preload exist that are more commonly used in clinics, like central venous pressure (CVP) or right atrial pressure (Pra). The latter clearly impacts right ventricular filling, which in turn impacts left ventricular filling. CVP is often considered as a good approximation of Pra, and as a consequence it is frequently used as an index of right or left ventricular preload [26]. However, Bakker and Berlin [40] highlighted the ambivalence of CVP as a preload index. Provided that "CVP depends on cardiac output as much as it determines it", such static markers of preload are partly unreliable and studies have shown their irrelevance in the context of fluid responsiveness [24, 25]. Dynamic indices of fluid responsiveness have been proposed. They are based on cardio-pulmonary interactions during mechanical ventilation [53]. The latter impact the overall functioning of the heart over a respiratory cycle, especially ventricular filling (thus preload). For instance, during forced inspiration, lung pressure increases and the overall pressure acting on the heart and pulmonary

circulation increases as well. This impedes right atrial and ventricular filling, thus decreasing right ventricular preload. According to the FS mechanism, this will impact SV, and to a greater extent if the patient is operating on the steep portion of the FS curve. By tracking SV variations (SVV) within a respiratory cycle, one can assess fluid responsiveness. If the patient is operating on the steep portion of the FS curve, SVV will be greater than for a non-responsive patient. Systolic pressure variation (SPV) or arterial pulse pressure variations (PPV) are generally prefered as they are more easily availaible on a beat-to-beat basis in clinics. These indices are only convenient for mechanically ventilated patients, but they also suffer from limitations regarding fluid responsiveness predictions [53]. Another method proposed by Taboul and colleague consists in raising the legs of the patient, thus altering temporarily the preload and challenging the FS mechanism [26].

No ideal predictor of fluid-responsiveness has emerged yet. In intensive care units, only half of the patients responds positively to vascular filling therapy [50, 54], so the question of fluid responsiveness prediction remains crucial.

In this work, vascular filling therapy will be addressed with a mathematical model of the CVS, and its link with the FS mechanism will be investigated. Before that, elements of cardiac cell physiology will be addressed in Chapter 3, as they are essential to understand the basis of the mathematical model described in Chapter 4. This model will be used for a study of cardiac contractility indices in Chapter 5 and for an analysis of the FS mechanism and vascular filling procedures in Chapter 6.

3

PHYSIOLOGY OF THE CARDIAC CELL

3.1 INTRODUCTION

In this chapter, the cardiac muscle physiology will be described. Attention will be paid to the cardiac muscle cells, commonly referred to as cardiomyocytes. It is essential to understand the features of such cells in order to apprehend the cardiac properties at the heart scale.

3.2 CARDIOMYOCYTES

Cardiomyocytes are long (about 100 µm) and roughly cylindrical (about 25 µm in diameter) cells. The cardiac muscle is a functional syncytium of cardiac cells, which is schematized in Fig.21. Cardiomyocytes are connected to each other through specialized membranes called intercalated discs. These intercellular regions provide an electrical coupling and a mechanical link between adjacent cells. This structure allows the heart to contract as a unit when action potentials propagate along the muscle tissue [1].

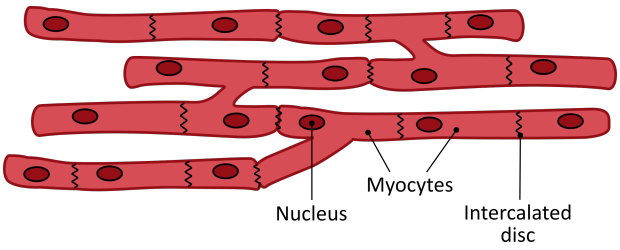

Figure 21: Cardiac muscle as a syncytium. The intercalated discs allow for the transmission of action potential from one cell to another. This structure provides rapid and coordinated contractions of the cardiac cells.

Cardiomoycytes are excitable and contractile. This means that they are able to propagate action potentials (AP) and those APs cause the cells to contract. *In fine*, the whole cardiac muscle is able to pump blood in response to the electrical propagating waves. The excitability and contractility properties of cardiomyocytes will be portrayed in the following sections.

3.2.1 *Excitability*

An action potential (AP) can be defined as an intense electrical activity across a cell membrane. It is characterized by wide variations of the membrane potential, defined as the electric potential difference between the interior and the

exterior of a cell. Ionic channels, distributed along the cell membrane, may open and close in response to voltage or chemical signals, and induce ionic currents across the membrane. Contrary to pacemaker cells, cardiomyocytes cannot spontaneously generate APs. However, the depolarization currents from adjacent cells can trigger an AP propogation through the cardiomyocyte membrane. A typical AP from a ventricular cell is shown in Fig.22, and can be divided into five phases.

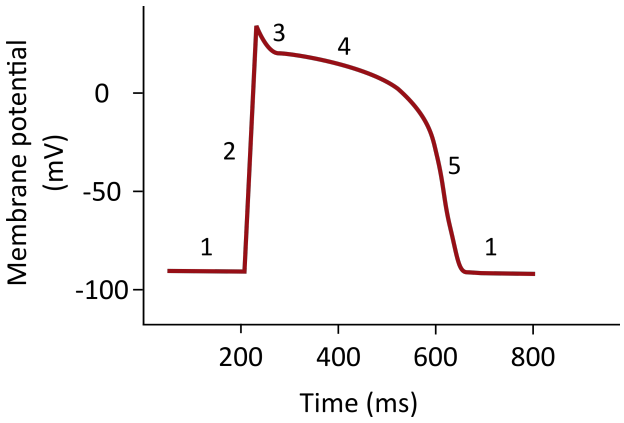

Figure 22: Action potential of a ventricular cell. See description in the text.

PHASE 1 There is always a potential difference across the cardiomyocyte membrane. If we take the extracellular potential as 0 V, the internal potential of a cardiac cell is about -90 mV. This is the resting potential of a cardiac cell. It is negative because there is a non uniform distribution of ions (K^+, Na^+ and Ca^{2+}, primarily) on both sides of the membrane [1], as schematized in Fig. 23. At rest, the cell membrane is permeable to K^+ ions and there is a net outward flow of those ions outside the cell. This low ions leak is corrected by an ionic channel that brings back the K^+ inside the cell. On the other hand, the membrane permeability to Na^+ and Ca^{2+} ions is very low and there is almost no diffusion of those ions across the membrane at rest.

PHASE 2 If the cell membrane is depolarized and reaches a threshold of about -70 mV, a rapid depolarization phase arises. Sodium channels open and there is a massive entry of Na^+ ions inside the cell. The membrane potential rises sharply and reaches a maximum positive value.

PHASE 3 Sodium channels are inactivated while potassium channel open. This lead to an outward flow of K^+ ions that tends to repolarize the cell membrane.

PHASE 4 While there is a net outward flow of K^+ ions, a net inward flow of Ca^{2+} is also initiated because calcium channels were opened in response to the membrane depolarization. This counterbalances the repolarization and leads to a plateau phase for the potential.

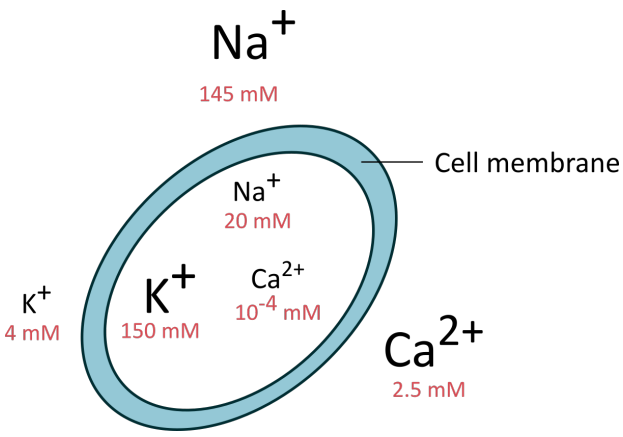

Figure 23: K^+, Na^+ and Ca^{2+} typical concentrations inside and outside a cardiomyocyte at resting potential.

PHASE 5 The repolarization finally occurs when the calcium channels close and more potassium channels open. The membrane potential reaches its initial resting value. However, active ionic pumps and ionic exchanger are required for the cell to get back to the initial ionic distribution (see Fig.23): the Na^+ /K^+ ATP-ase pump, the Na^+/Ca^{2+} exhanger and the Ca^{2+} pump.

3.2.2 *Contractility*

The cardiac muscle is a type of striated muscle (like skeletal muscle), which is named after the striated appearance observed under a microscope (Fig.24). This reveals an organized structure that goes as follows (see Fig. 25): cardiomyocytes contain bundles of myofibrils, which are composed of successive sarcomeres. A sarcomere is the segment between two neighbouring Z-lines, and the basic contractile units of the myocyte [1]. Each sarcomere is mainly composed of two myofilaments: the thick and thin filaments.

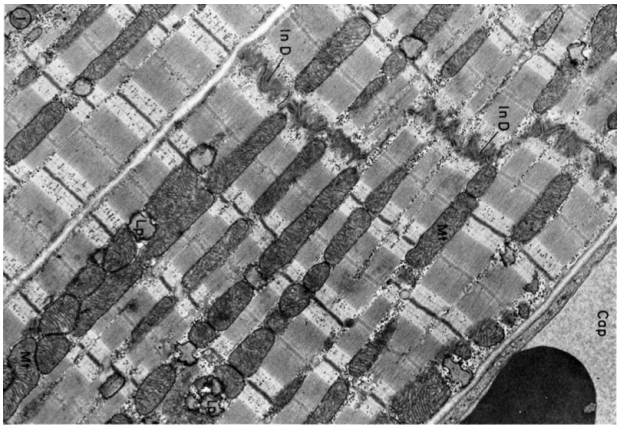

Figure 24: The striated cardiac muscle [55]. The striated appearance observed under an electron microscope shows the organized structure of myofibrils.

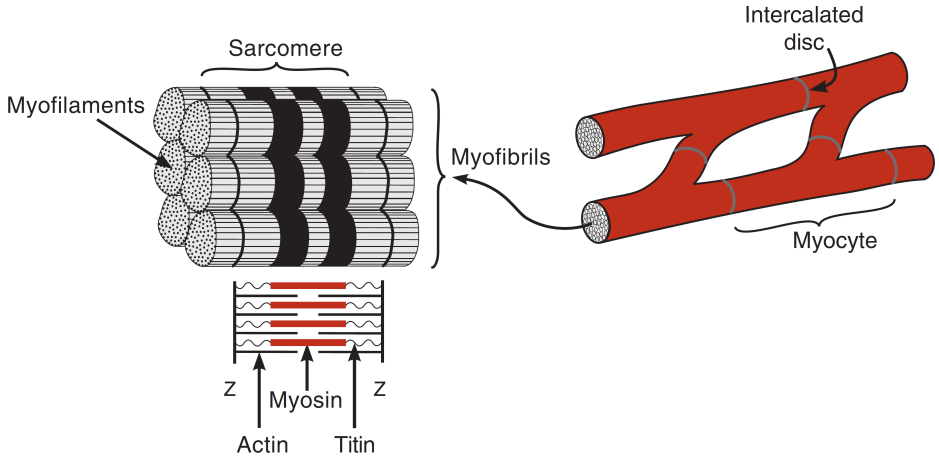

Figure 25: Internal structure of cardiomyocytes [1]. Cardiomyocytes are composed of bundles of myofibrils. Each myofibril is made of a regular succession of sarcomeres, defined as the segment between two adjacent Z-lines. Sarcomeres are composed of myofilaments, essentially myosin (thick) and actin (thin) filaments.

The thin filaments are essentially made of actin molecules, organized in double helix strands (see Fig.26). Tropomyosin molecules surround the actin filaments, and troponin complexes are associated with each tropomyosin. A *regulatory unit* (RU) is a repeating structure along the thin filament, composed of one troponin complex, one tropomyosin molecule and seven actin monomers.

The thick filaments are made of myosin molecules (Fig.26). Each myosin contains two globular heads with two important properties: they are able to hydrolyze ATP molecules and to bind to an actin molecule. These heads are commonly referred to as "crossbridges" (CBs), that are able to form bonds with the thin filaments and initiate mechanical contractions.

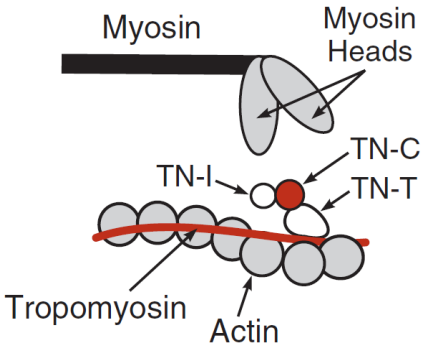

Figure 26: Thick and thin filaments composition [1]. The thick filaments are composed of myosin molecules, which possess two globular heads able to hydrolyse ATP molecules and to attach to actin. Thin filaments are composed of actin, tropomyosin and troponin complexes. Each troponin complex contains three subunits: troponin T, troponin I and troponin C. The latter contains a binding site for calcium ions. A regulatory unit (RU) contains one troponin complex, one tropomyosin molecule and seven actin monomers.

In the absence of calcium, the actin binding site is hidden by the tropomyosin. If a calcium ion binds to the troponin complex, a conformational change occurs in the troponin-tropomyosin complex and the binding sites become available. If the calcium ion is released, the complex recovers its initial position and the myosin head is no longer able to reach the actin binding sites.

Introduced in 1954, the sliding filament theory shed light on the molecular basis of muscle contraction [12, 13]). In the presence of calcium ions, crossbridges (CBs) can undergo a serie of ATP hydrolysis and conformational changes that generate a force pulling the thin filaments. This crossbridge cycle is represented in Fig.27. Once an ATP molecule is dissociated into ADP and Pi (inorganic phosphate), the crossbridge attaches to the actin binding site. When the Pi is released, a conformational change occurs and the crossbridge pulls the actin filament along the thick filament (= *the power stroke*). Then the ADP is released and replaced by another ATP molecule, lowering the affinity for the actin. The crossbridge detaches, and the cycle starts all over again [56]. At the sarcomere scale, this cycle leads to a sliding of the thin filament relative to the thick filaments, thus to a global contraction of the cell, as depicted in Fig.28.

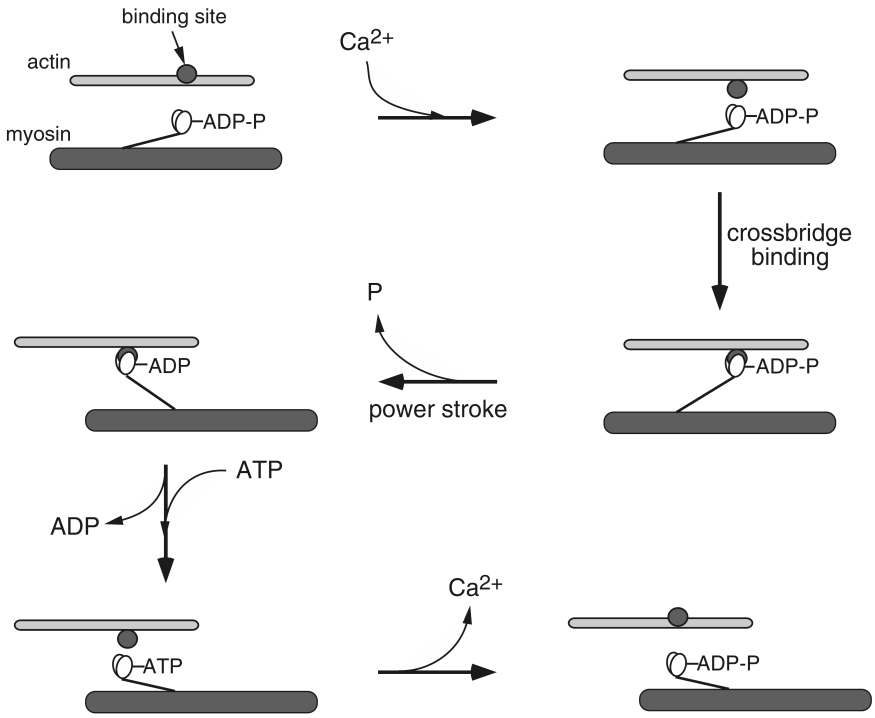

Figure 27: Crossbridge cycling [56]. In the presence of calcium ions, the actin binding site is available for crossbridge formation. Following ATP hydrolysis, a crossbridge binds to actin. Once the inorganic phosphate is released, the crossbridge moves to a new configuration. This movement, called the power stroke, pulls the actin filament along the thick filament. The remaining ADP is then replaced by a new ATP molecule. The affinity for actin is lowered and the crossbridge detaches from the thin filament. Hydrolysis of ATP occurs again, but if calcium ions are removed, the cycle ends because the actin binding site is henceforth unavailable.

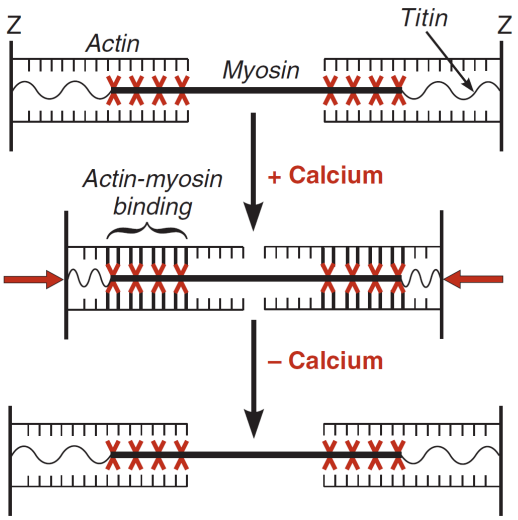

Figure 28: Sliding filament theory [1]. In the presence of calcium ions, crossbridges are able to bind to actin and pull the thin filaments, leading to a relative sliding of the filaments. Thus, a shortening of the sarcomere occurs upon crossbridge cycling. If calcium ions are removed, crossbridge binding is prevented and the contraction ends. The sarcomere gets back to its relaxed length because of the passive forces, exerted primarly by the titin molecule.

A third important protein, the titin, connects the thick filaments to the Z line (Fig. 25 and Fig. 28) and keeps them centered within the sarcomere [1]. This protein is also responsible for the elastic properties of the sarcomeres, wich are related to the passive mechanical properties of the cardiac muscle.

The force produced by sarcomeres during contraction can be split into two contributions: the *active* force, produced by active crossbridges cycling, wich requires calcium ions and ATP activation, and the *passive* elastic force, mainly produced by titin.

3.3 THE EXCITATION-CONTRACTION COUPLING

The coupling between myocyte action potentials and contraction is called excitation–contraction coupling (ECC) [1, 57]. The mediator fo this coupling is the intracellular calcium. During an AP, intracellular calcium concentration increases and the calcium ions migrate to the sarcomeres where they allow the binding between myosin and actin molecules, as explained earlier.

Inside the cardiac cell is a structure called the sarcoplasmic reticulum (SR) that surrounds the sarcomeres and acts as a reserve for Ca^{2+} ions. When intracellular calcium levels rise during an AP (phase 3 from Fig.22), this rise is "sensed" by the ryanodine-sensitive calcium-release channels (RyR channels), located in the SR membrane, which release the calcium ions stored in the SR. At the end of the AP, intracellular calcium is pumped back into the SR through the SERCA pump (sarcoendoplasmic reticulum calcium ATPase). As intracellular calcium levels decrease, calcium ions leave the troponin-tropomyosin complexes and the myosin heads detach from the actin filaments, thus ending the contraction.

It is worth noticing the importance of calcium in muscle contraction. Any alteration in cellular calcium handling will lead to change in contraction, referred to as inotropic changes. Thus, the inotropy (or contractility) defined in the previous chapter is deeply related to the cellular management of the following calcium ions fluxes: the membrane calcium channels (L-type channels), the calcium release and uptake from the SR, the calcium affinity for troponin, the Na^+/Ca^{2+} exchanger and the Ca^{2+} pump. The role of calcium in excitation-contraction coupling is schematized in Fig.29.

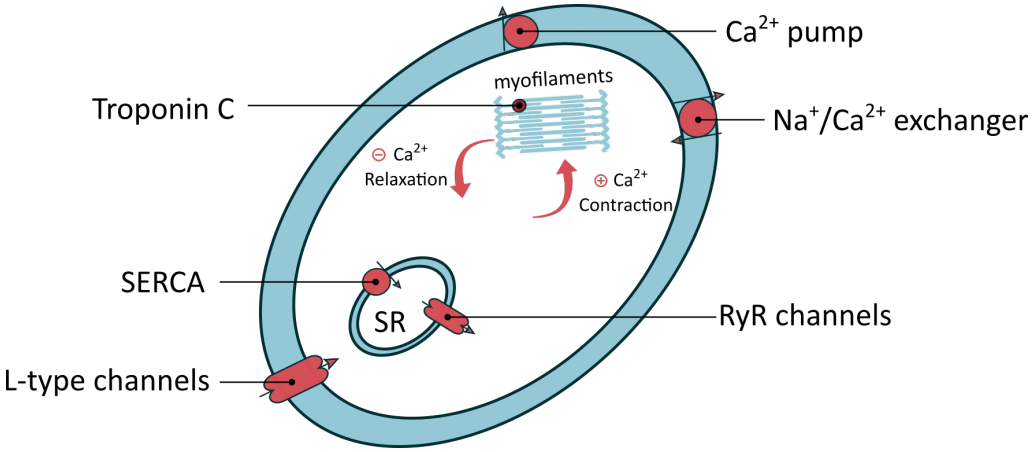

Figure 29: The excitation-contraction coupling. Calcium is the mediator for cardiac cells contration. Alterations in calcium handling lead to inotropy variations and may occur through the alteration of different calcium fluxes: calcium entry in the cell though L-type channels, calcium release and uptake from the SR, calcium binding to troponin C, calcium extrusion of the cell through the Na^+/Ca^{2+} exchanger and the Ca^{2+} pump.

3.4 REGULATION OF CARDIAC CELL CONTRACTION

Calcium is the physiological activator of the contractile machinery of cardiac cells. It induces activation of the thin filament which, in turn, allows for cross-bridge formation, ATP hydrolysis, and force development. There is a direct relationship between the amplitude of the calcium transient and the cellular contractile state. Thus the heart inotropic state can be controlled by modifications of calcium homeostasis, via neuro-humoral mechanisms or pharmaceutical agents [32, 58]. These are extrinsic mechanisms, already cited in Chapter 2, that alter contractility, and they will not be addressed in details here. On the other hand, muscle cells also have an intrinsic ability to alter their contractile state, a property shared by skeletal and cardiac cells, but which is particularly crucial for cardiac cells *in vivo*.

Skeletal and cardiac cells are both excitable and contractile, and they undergo similar events at the cellular and sub-cellular scales during contraction. However, despite their similar behaviors, mechanical output regulation of both muscle types is different, as cardiac and skeletal cells are designed for different purpose [33, 34]. In skeletal muscle, neurons are responsible for the electrical activa-

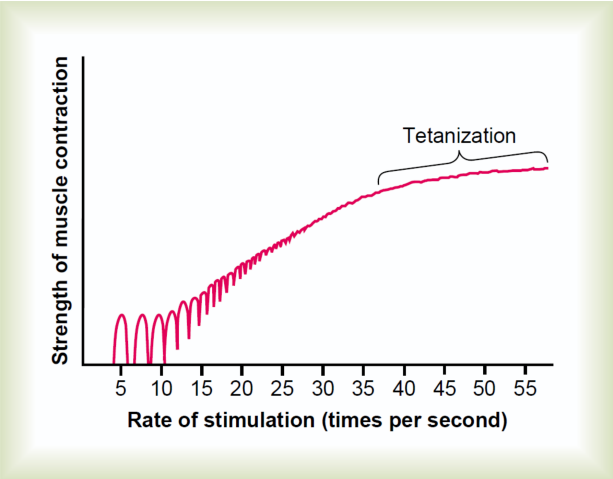

Figure 30: Tetanization in skeletal muscle [3]. By increasing the frequency of twitch contractions, produced force increases, as the new contraction is added partially to the previous one. When frequency gets high enough, a full contractile state is achieved and sustained, which is called tetanization: enough calcium ions are maintained in the cytoplasm and no relaxation occurs anymore.

tion of muscle fibers. A motor unit is the combination of a motor neuron and the muscle fibers innervated by this neuron. The force produced by a muscle can be modulated by controlling the recruitment of motor units: the greater the number of activated motor units, the greater the force. Besides, increasing the frequency of neural excitation increases the produced force, as shown in Fig. 30. A *twitch* contraction is an electrical stimulation that leads to the generation of a single AP. By increasing the frequency of twitch contractions, skeletal muscle can undergo *tetanic* contractions, which are sustained muscle contractions where the produced force is maximal and constant over time (Fig. 30). This happens because calcium ions accumulate in the cytoplasm, as a new excitation takes place before the previous one is over.

Typical twitch contractions of cardiac and skeletal cells are shown in Fig. 31 for comparison. It can be observed that the AP of cardiac muscle is longer than for skeletal muscle, and so is the effective refractory period, which means that normally relaxation always occurs before a new excitation can take place. This is why cardiac muscle cannot undergo tetanic contractions [1, 32, 34]. Furthermore, all the cardiac cells are activated at each heartbeat. No gradation of force through recruitment modulation is conceivable since there is 100% recruitment every time [34]. Another difference lies in the ECC mechanism. SR of skeletal muscle normally releases enough calcium to saturate the troponin C sites during tetanic contraction, while in cardiac muscle the raise in intracellular $[Ca^{2+}]$ is not high enough for troponin C saturation. Thus not all the CBs can be recruited and this leads to a submaximal activation of the cardiac muscle *in vivo* [33, 34]. Unlike the skeletal muscle, which is *fully activated* during contraction, the cardiac muscle is said to be *partially activated*.

These differences in activation and regulation between the two muscle types lead to functionnal differences. Since all cardiomyocytes participate in the heart contraction at each beat, cardiac output has to be regulated at the cellular level,

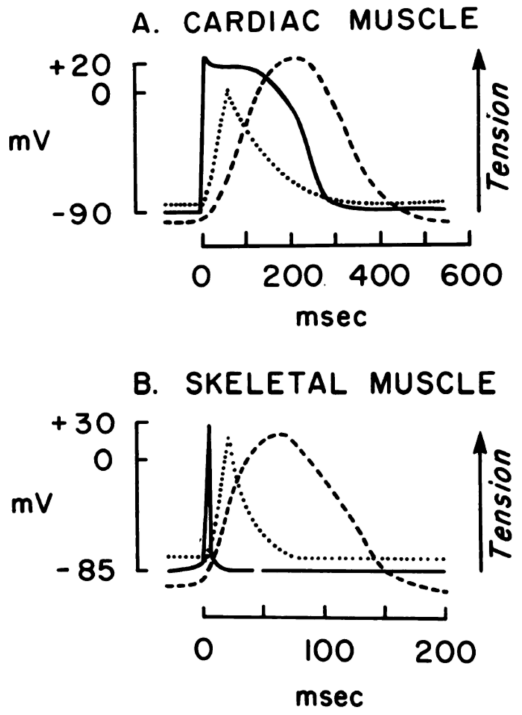

Figure 31: Typical twitch contractions of cardiac and skeletal cells [60]. The cell are electrically stimulated to elicit the generation of one AP (normal line). Intracellular calcium (dotted line) and produced tension (dashed line) are recorded. Cell extremities are attached, so that sarcomere length does not vary during contraction (*isometric* contraction). Note the different scales on the two horizontal axis.

as each cell must be able to vary its activity [33, 59]. In particular, the length-dependent properties of cardiac cells appear to be essential for intrinsic cardiac output modulation, and those properties are described below.

3.4.1 *Length-tension relationship*

LENGTH-TENSION RELATIONSHIP IN SKELETAL MUSCLE

A famous study on skeletal muscle by Gordon *et al.* [61] led to new insights regarding the length-dependent properties of contractile fibers. Isolated fibers from frog skeletal muscle were attached to both ends and stimulated electrically (*isometric* tetanic contractions). The active[1] tetanic force (or tension) was recorded as a function of sarcomere length (SL). A schematic summary of their results is shown in Fig. 32. The isometric tension increases with increasing SL, then saturates to a plateau, and finally decreases to zero. The sliding filament theory can admirably well explain the shape of this length-tension relationship. For the greatest SL values, the force is zero because there is no overlap between the thick and thin filaments. Reducing SL leads to a progressive and linear increase in force, as more and more CBs can be formed. Once the optimal overlap

[1]The active force is the difference between total recorded force and passive force, the latter being associated with the passive elastic properties of muscle, as explained previously.

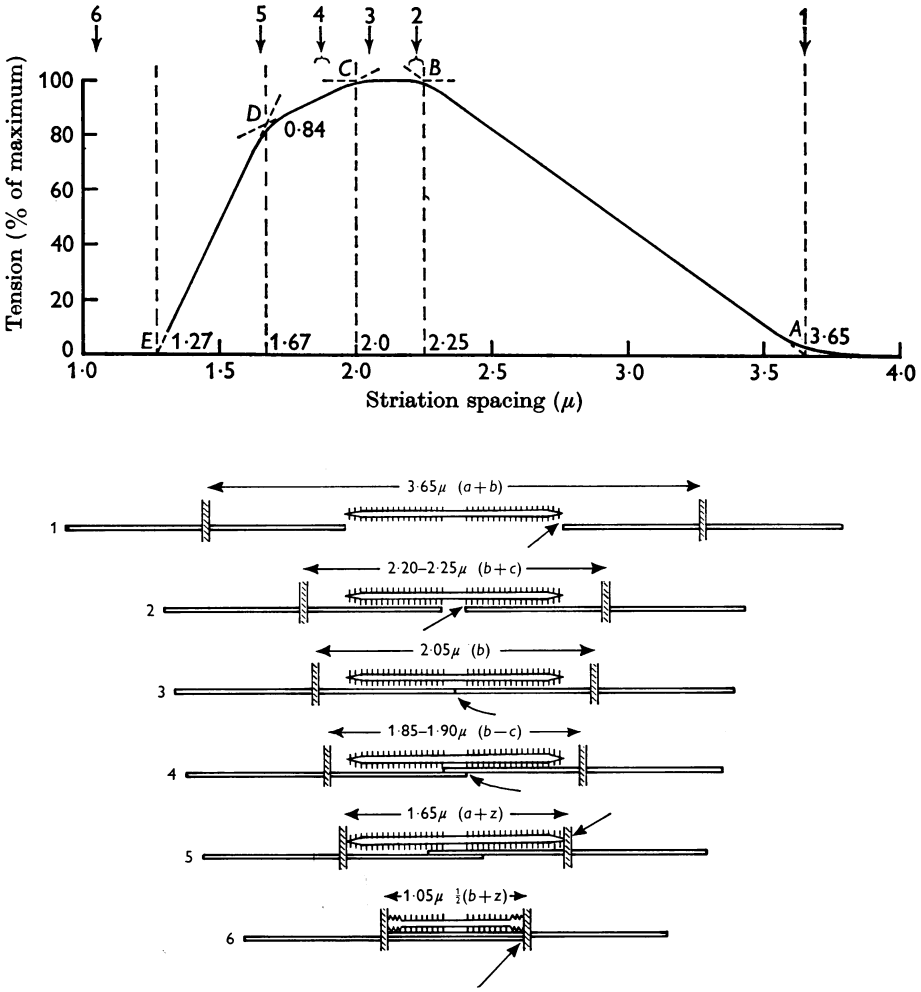

Figure 32: Length-tension relationship in skeletal muscle [61]. The active tetanic isometric force is recorded as a function of sarcomere length (top). The degree of myofilament overlap, along with the sliding filament theory (bottom), can explain the shape of the curve. See description in the text.

is reached (all the myosin heads are facing the thin filaments), there is a plateau. At shorter SLs there is a double overlap between the left and right thin filaments. These thin filaments can slide past each other and interfere, but by doing so they prevent some CB formation, which decreases the active force. When thick filaments run into the Z-line, there is a further decrease in force with decreasing SL, as thick filaments become "crumpled" and CB formation is hindered (see Fig. 32).

LENGTH-TENSION RELATIONSHIP IN CARDIAC MUSCLE

Other methods must be implemented to obtain the length-tension relationship for cardiac muscle. As cardiac cells cannot undergo tetanic contractions, the *peak* active force, F_{peak} for an isometric *twitch* contraction (similar to Fig. 31) is recorded instead. Here the fibers are only partially activated, with a transient

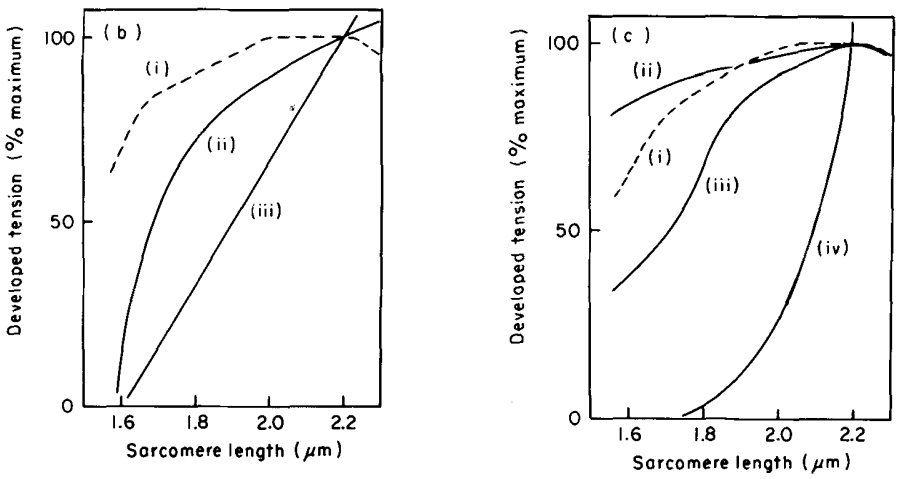

(a) (b)

Figure 33: Length-tension relationship in skeletal and cardiac muscle [62]. (a) Sarcomere length-tension relationship of intact muscle. (i) Tetanic tension from skeletal muscle. (ii) Peak active tension in twitch of intact cardiac muscle with an extracellular calcium concentration $[Ca^{2+}]_o$ = 2.5 mM. (iii) identical to (ii) but with $[Ca^{2+}]_o$ = 0.5 mM. (b) Sarcomere length-tension relationship of skinned muscle. (i) Maximal calcium-activated tension for skinned skeletal muscle. (ii) Maximal calcium-activated tension for skinned cardiac muscle. (iii) Tension for skinned cardiac muscle with low calcium concentration ($[Ca^{2+}]$ = 40 nM) and phasic contractions induced by calcium release from the SR. (iv) Tension for skinned cardiac muscle with an intermediate calcium concentration ($[Ca^{2+}]$ = 2.7 μM).

calcium flow. The results are plotted in Fig. 33a, and show a much steeper curve for cardiac than for skeletal fibers. Note that, if the extracellular calcium concentration is increased, so that intracellular calcium flow is increased, the cardiac length-tension curve gets closer to the skeletal curve.

To get completely rid of the partial activation, and induce *maximal calcium-activated* contractions in cardiac cells, one can work with skinned cells. Skinned cells have their membrane chemically removed, so that calcium concentrations can be fixed to any value. For a fixed calcium concentration, a constant isometric force is produced. For fully activated skinned cells, the cardiac length-tension curve gets really close to the skeletal smoother curve (Fig. 33b(i) and (ii)). The steepness of the length-tension curve of cardiac cells thus varies with the degree of activation. Furthermore, for intact cardiac cells (Fig. 33a(ii) and (iii)) we observe a considerable increase in peak isometric force between 2.0 and 2.2 μm. However the change in myofilament overlap is totally negligeable for this sarcomere length range (see Fig. 32). This means that the degree of myofilament overlap cannot solely explain the shape of the length-tension curve for the intact cardiac muscle during a twitch contraction. Actually, the myofilament overlap explanation is only adequate for fully-activated fibers length-tension curves (Fig. 33a(i), Fig.33b(i) and (ii)). For partially-actived fibers, such as cardiac muscle *in vivo*, the steep increase in peak isometric force with increasing length (Fig. 33a(ii) and (iii)) must highlight a length-dependent property which completes the myofilament overlap explanation. However, considering the nar-

row SL range for cardiac muscle *in vivo* (1.8 - 2.2 μm^2), myofilament overlap only makes minor contributions to the increase in isometric force upon length stretch in cardiac muscle [18, 62–64] (see Fig. 32). This really confirms that another length-dependent mechanism must come into play.

Note also that the length-tension relationship in not essential in skeletal muscles contraction because these muscles operate normally on the (optimal) flat part of the curve and the length variations occuring during contraction are moderate, so that sarcomere length remains always near the optimum. As explained previously [33, 34, 65], skeletal muscle force is instead controlled through recruitment and frequency modulation. The cardiac muscle, on the other hand, operates *in vivo* on the ascending part of the length-tension relationship, and the observed modulation of activation by length is worth being investigated precisely.

3.4.2 *Force-pCa relationship*

Another interesting experimental procedure, performed on cardiac skinned cells, completes the description of the length-tension relationship by providing the "force-pCa" curve. Here the constant isometric force of skinned cardiac cells is reported as a function of the fixed calcium concentration $[Ca^{2+}]$, with a semi-logarithmic scale ($pCa = -\log [Ca^{2+}]$). A typical force-pCa curve is shown in Fig. 34. The corresponding sigmoidal-shaped curve can be described by a Hill equation [66]:

$$\text{Relative Force} = \frac{\text{Force}}{\text{Force}_{\text{max}}} = \frac{[Ca^{2+}]^n}{EC_{50}^n + [Ca^{2+}]^n} \tag{3.1}$$

where n is the Hill coefficient and EC_{50} is the calcium concentration needed to reach to half the maximal force, $\text{Force}_{\text{max}}$. This maximal force, produced at full activation (corresponding to $pCa < 5$), is identical to the maximal calcium-activated tension from skinned cardiac cell reported for different sarcomere length in Fig. 33b(ii).

(3.2) can also be rewritten as:

$$\frac{\text{Force}}{\text{Force}_{\text{max}}} = \frac{1}{1 + 10^{n \cdot (pCa - pCa_{50})}} \tag{3.2}$$

where $pCa = -\log [Ca^{2+}]$ and $pCa_{50} = -\log EC_{50}$. Because of the semi-logarithmic scale, this equation is more appropriate to fit the parameters n pCa_{50}. Note that an increase in calcium concentration corresponds to a decrease in pCa value, but not in a linear trend because of the logarithmic relationship.

The Hill coefficient, which assesses the steepness of the force-Ca relationship, is typically around 3-4 for cardiac fibers [67], indicating a cooperative mechanism: binding of one calcium ion to a RU[3] promotes either calcium or CB binding to adjacent RUs. That is, one calcium-activated RU may activate other RUs

[2]The passive force of cardiac muscle increases greatly with SL and prevents the cardiac fibers to extend beyond 2.2 μm.

[3]Regulatory unit, composed of one troponin complex, one tropomyosin molecule and seven actin monomers, as defined in a previous section.

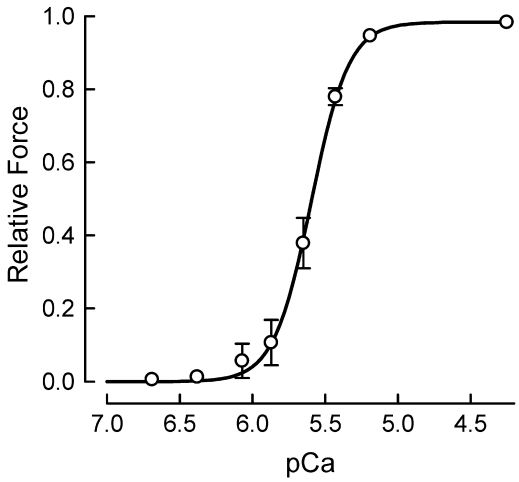

Figure 34: Force-pCa relationship in cardiac muscle. [67]. The sigmoidal shape of the curve indicates a cooperative mechanism. Note that the calcium concentration increases from left to right on the horizontal axis.

[20], otherwise the fitting procedure would give $n = 1$, and the curve slope from Fig. 34 would be less abrupt[4]. Thus, for cardiac muscle at intermediate levels of activation, small variations in pCa produce more than proportional changes in active force [37, 67].

The force-pCa curves also describes the *calcium sensitivity* of cardiac muscle. This concept of calcium sensitivity "reflects the contractile response of the myofilaments to a given calcium concentration at steady state. Thus this sensitivity plays a major role in determining the contractile response to the intracellular calcium transient" [68]. It can quantified by determination of EC_{50} or pCa_{50} values [69], which define the calcium concentration around which a steep change in force occurs.

The force-pCa curves for two different SLs are compared in Fig. 35. Note that both curves are normalized to their respective $Force_{max}$, the maximal produced force at full activation (pCa < 5). Those maximal values depend on myofilament overlap (see Fig. 33b) but since the force-pCa curves are normalized, the overlap effect is cleared out here. Still, at intermediate levels of activation, the produced force depends on length: for a fixed calcium concentration, a greater force is obtained at higher SLs. The curve corresponding to the highest SL value is indeed shifted to the left, which corresponds to an increase in the pCa_{50} value, which means that the calcium concentration needed to reach half the maximal force is reduced in a longer sarcomere. Thus the calcium sensitivity of cardiac muscle appears to be altered by length.

It is important to emphasize here that $Force_{max}$ is fundamentally different from (and greater than) the peak force F_{peak} obtained in the isometric twitch experiments from intact cardiac muscle reported in Fig. 33a(ii) and (iii). The reason is that, during a twitch experiment, and also during *in vivo* contractions, there is a transient intracellular calcium flow, with $[Ca^{2+}]$ ranging typically from 0.1 μM

[4] $n = 1$ corresponds to the case where calcium binding to one RU controls activation and force production of this RU alone, independently from the others RUs.

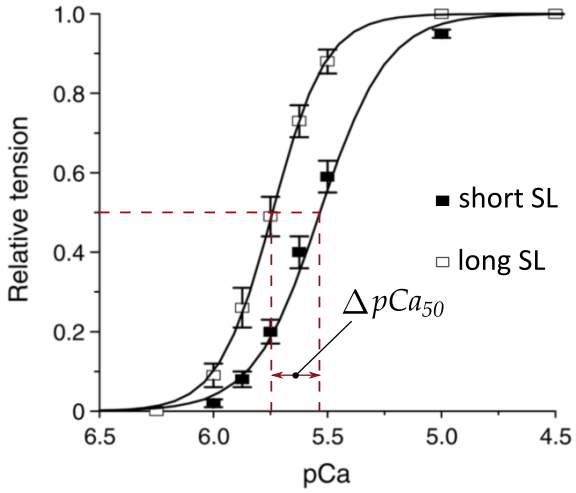

Figure 35: Force-pCa relationship for two different SLs (adapted from [70]). For a fixed intracellular calcium concentration, the active isometric produced force increase with increasing SL. Thus calcium sensitivity is increased with increasing SL, a phenomenon that can be quantified with ΔpCa_{50}.

(pCa = 7) to 1 μM (pCa = 6) [32, 67], and not a constant calcium supply. Moreover, the time of peak calcium actually precedes the time of peak force in isometric twitches, as observed in Fig. 31. One must thus consider that the instantaneous force-calcium relationship varies during the time course of the twitch contraction [67]. The process of calcium activation and force production is thus highly dynamical *in vivo*[5], and the argument presented in the present section only allows understanding partially the role of length in the dynamics. Furthermore, it is worth mentionning that skinning procedures alter the intracellular composition and myofilament geometry. Thus their physiological signifiance must be handled carefully [69, 71]. Interestingly, it is also possible to get force-pCa relationships for intact cardiac muscle. The experimental procedures and calcium concentration assessements are less manageable[6] and do not correspond to physiological conditions either, but the results still show a similar sigmoidal curve, albeit with a higher calcium sensitivity compared to skinned muscle [68, 71]. Even if this relationship between isometric force and free calcium concentration is not sufficient to characterize the dynamic contraction of cardiac muscle *in vivo*, this reductionist approach reveals significant mechanical properties of myofila-

[5] "... the level of myofilament activation is by no means a simple proportional function of cytosolic calcium concentration. Rather, it constitutes a complex and dynamic signal transduction process that itself is also subject to regulation and modulation by both intrinsic (mechanical loading, sarcomere length) and extrinsic (neuro-hormonal) factors." [18]

"The control of the myofilaments by [Ca] and other factors is very complex. [...] One must retain the perspective that the relationship between $[Ca]_i$ and contraction is not fixed and it is contraction which is the physiological function of cardiac muscle cells." [32]

[6] By immersing intact cardiac fibers in highly concentrated potassium solutions, a slow increase in intracellular calcium occurs in parallel with a slow increase in produced twitch force. Intracellular calcium concentration is monitored with a fluorescent dye. Force and calcium are considered in equilibrium, and recording force and the fluorescence signal at different times results in a force-pCa curve similar to Fig. 34 [68].

ments, such as cooperativity and calcium sensitivity [71]. It also demonstrates the length-dependence of calcium activation, an important property described in the next section.

To close this section, it is finally interesting to mention that force-pCa curves can also be obtained with skinned skeletal cells, and reveal the same sigmoidal shape and length-dependence of pCa_{50} [14, 72]. However, as already stressed for the length-tension relationship, skeletal muscle is able to deliver maximally-activated produced forces, and the length-dependency of activation is of less importance for force modulation *in vivo*. Cardiac muscle, on the other hand, works under partial activation, with typical SLs and calcium concentrations located in the steep region of the length-tension and force-pCa relationships, respectively. Both curves seem to indicate that an intrisic length-dependent mechanism exists to control force development in cardiac cells and adapt their mechanical output. This mechanism is described in the following section.

3.4.3 *Length-dependent activation*

Since cardiac fibers normally operate under partial-activation conditions (not all the troponin C sites are saturated with calcium), it is clear from the results presented above that force can be increased at the cellular levels via two possible mechanisms [34]:

- an increase in the calcium supply, or
- an increase in *calcium sensitivity*.

The former can be achieved via autonomic nervous control or pharmaceutical agents, as it represents an *extrinsic* control of cardiac contractile state[7] (inotropy) [33]. The latter can be modulated by extrinsic factors as well [32, 69] but it can also be modulated via sarcomere length, as explained in the previous section: for a fixed calcium concentration, more force is generated at a longer sarcomere length. This increase in contractile state following a stretch is not related to an increase in calcium transient, but is due to an increase in the myofilament sensitivity for calcium [62, 73]. This *intrinsic* control of cardiac contractile state is referred to as *length-dependent activation* (LDA).

LDA is defined in the literature as the increase in calcium sensitivity upon sarcomere stretch. It is considered as the subcellular basis for the sharp ascending limb of the length-tension relationship in cardiac muscle undergoing isometric twitch contractions [1, 16–18, 20, 21, 34, 62, 74, 75]. This increase in active peak force is related to an increase in the number of active cycling crossbridges in the cardiac sarcomere when SL is increased [16, 18, 34, 76, 77][8]. The magnitude of LDA can be quantified using the ΔEC_{50} (or ΔpCa_{50}) value, which corresponds

[7] Extrinsic variations of contractile state and the efficiency of cardiac contractility indices will be studied in Chapter 5.

[8] "... evidence has been accumulating that sarcomere length modulates the level of Ca^{2+} sensitivity through variation in the number of strong-binding actin-myosin interactions. The basic idea is that with increase in sarcomere length along the ascending limb of the force-length curve there is a more favorable disposition of the myosin heads relative to actin, thereby increasing the probability of strong-binding actin-myosin interactions taking place." [16]

to the difference between two EC_{50} (or pCa_{50}) values obtained for two different SLs (see Fig. 35) [78].

The molecular basis for LDA have been extensively investigated and reviewed [14, 17, 18, 21, 64, 79]. The interfilament spacing (or lattice spacing) was proposed as an essential factor for LDA. As cardiac fibers keep their volume constant over mechanical contraction, an increase in length leads to a decrease in lattice spacing. The myofilaments are thus brought closer and this increases the probability of crossbridge formation [16, 80]. This increased probability is expected to lead to an increased rate of crossbridge formation, such that more crossbridges are in a force-generating state during the contraction, resulting in a greater force at a given submaximal calcium concentration[9] [69].

However, many studies indicate that lattice spacing seems to only play a secondary role in LDA [17, 18, 64]. The essential role of titin as a "length-sensor", was proposed instead [17, 18, 63]. Titin interacts and binds locally to the thick and thin filaments, and this giant elastic protein extends upon sarcomere stretching. Seiquera and van der Velden [20, 21] reviewed the proposed mechanisms for LDA and concluded that stretch-effects promote titin strain-induced effects, which could regulate LDA as follows:

- Production of radial forces that reduce lattice spacing;
- Increased strong-binding crossbridges[10] formation and troponin C alterations;
- Increased calcium cooperativity.

Protein isoforms may also partially account for disparity between skeletal and cardiac cooperative activation and length-dependent properties [14, 33, 74, 78]. For instance, skeletal troponin C presents two calcium binding sites, while cardiac troponin C only contains one [81, 82]. Thus, although their sarcometric structures are similar, the different contractile and regulatory protein isoforms between muscle types give rise to functional differences [33]. For example, cardiac muscle exhibits shallower force-pCa curves (thus less cooperativity) and smaller pCa_{50} value (thus less calcium sensitivity), but a greater length-dependence of calcium sensitivity [14, 78]. Experiments have shown that exchanging skeletal troponin C for cardiac troponin C in skeletal muscle (or the opposite procedure) alters cooperativity and calcium sensitivity [83–85]. Myosin and titin isoforms also play a role in species or regional variations of cardiac cell length-dependent properties [4, 70, 75, 86].

Some experimental studies also suggest that the degree of myofilament protein phosphorylation, an extrinsic modulator of cardiac performance [33], may play a role in regulating LDA [18, 20, 74, 75, 85, 87].

The origins of calcium cooperativity are still not completely understood either. It may originate from RU-RU, CB-CB, and/or RU-CB interactions[11] [14, 37, 88–

[9] This mechanism is less significant for skeletal muscle, as skeletal SR normally releases enough calcium to fully saturate all of the troponin in the fiber, which leads to a maximal crossbridge recruitment [34].

[10] "Strong-binding" crossbridges correspond to attached myosin heads without any nucleotides or with ADP. They have a high affinity for actin, as opposed to the "weak-binding" crossbridges, corresponding to attached myosin heads with ATP or with ADP and Pi.

[11] RU-RU interaction: calcium binding to a RU promotes calcium binding to adjacent RUs.

90]. According to experiments conducted by Dobesh and colleagues [91], cooperativity (whose magnitude is quantified with the Hill coefficient) does not seem to be length-dependent, but the debate remains open on that point [18, 20, 37].

De facto, LDA appears to be a composite of several molecular mechanisms, but no categorical explanation prevails to date, despite the extensive number of studies [21, 37, and references therein]. What is certain is that calcium sensitivity is length-dependent, which means that for a fixed calcium concentration, a greater isometric twitch force is generated at longer SL because of an increase in the number of attached CBs. This is the widely accepted definition of LDA in the literature.

Finally, it is worth noticing that LDA is essentially studied and highlighted in isometric experiments, as the ones presented in this section. Fixing SL facilitates the study of length-dependent phenomena. However, cardiac cells do not undergo isometric contractions *in vivo*, as they are able to shorten during blood ejection. Thus, experiments where cells are allowed to shorten may provide additional insights regarding the influence of length on cardiac cell output. Some important experiments on shortening cardiac fibers are described in the following sections.

3.4.4 *Force-velocity relationship*

Since cardiac cells are allowed to contract during contraction, their velocity of shortening can be recorded during *isotonic* contractions. In this experimental setup, cardiac fibers are submitted to a certain load and allowed to shorten during a twitch contraction, against the (fixed) load. The shortening velocity is measured as a function of the imposed load, and a typical result is shown in Fig. 36. The load corresponding to zero velocity (no shortening) is the isometric force, while the maximal velocity (at zero load) corresponds to the unloaded contraction case. If the same experiments are reiterated with an increased initial SL (increased preload but same afterload), the velocity of shortening increases for a fixed load (see Fig. 36). Thus preload (or SL) also affects the dynamics of isotonic contractions.

3.4.5 *Auxotonic contractions*

In vivo, cardiac cells do not undergo isometric nor isotonic contractions. Sarcomere length is not kept constant during the cardiac cycle: SL increases during blood filling, then is almost constant during the isovolumic contraction and finally decreases during blood ejection. On the other hand, the load against which the fibers are contracting (the afterload) also varies during the blood ejection phase, so they do not undergo isotonic contraction either. Instead, cardiac cells experience *auxotonic* contractions *in vivo*, where they are able to shorten and produce tension.

CB-CB interaction: attached CBs promote the binding of other CBs, either inside the same RU or in adjacent RUs.

CB-RU interaction: attached CBs in a RU promote calcium binding in that same RU or in adjacent RUs.

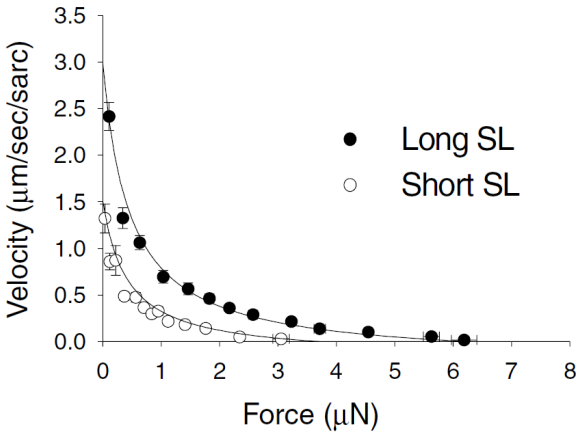

Figure 36: Force-velocity relationship in cardiac muscle [86]. Velocity of isotonic contractions of skinned cardiac fibers as a function of the imposed load. The initial SL before contraction has an impact on the shortening velocity: at longer sarcomere length, the shortening velocity increases for a fixed load.

It has been observed experimentally than the maximal isometric twitch force at a sarcomere length L_0 is always greater than the developed force when the cell is allowed to shorten from L_0 (see Fig. 37) [92, 93].

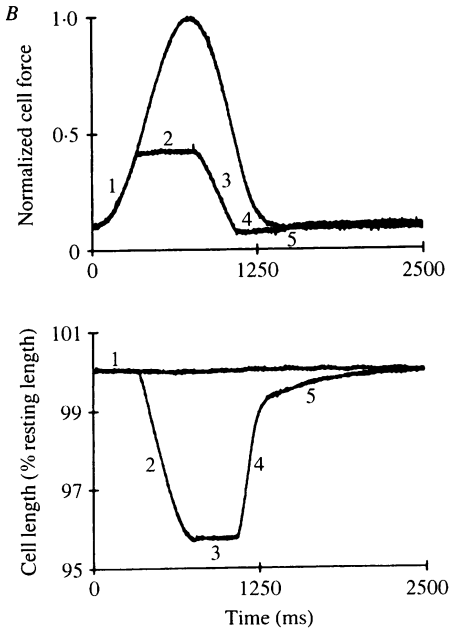

Figure 37: Isometric and auxotonic contractions [92]. Top: developed force for an isometric (normal curve) and an auxotonic (numbered curve) contractions. Bottom: cell length for the isometric (normal curve) and auxotonic curve (numbered curve). The length variations for the auxotonic contraction are close to a physiological contraction. Experimentally, both cell ends are attached to the compliant tips of micropipettes, and the bending of these tips upon cell shortening allows for force calculation. Force or length clamps can be imposed by externally controling the micropipettes tips positions.

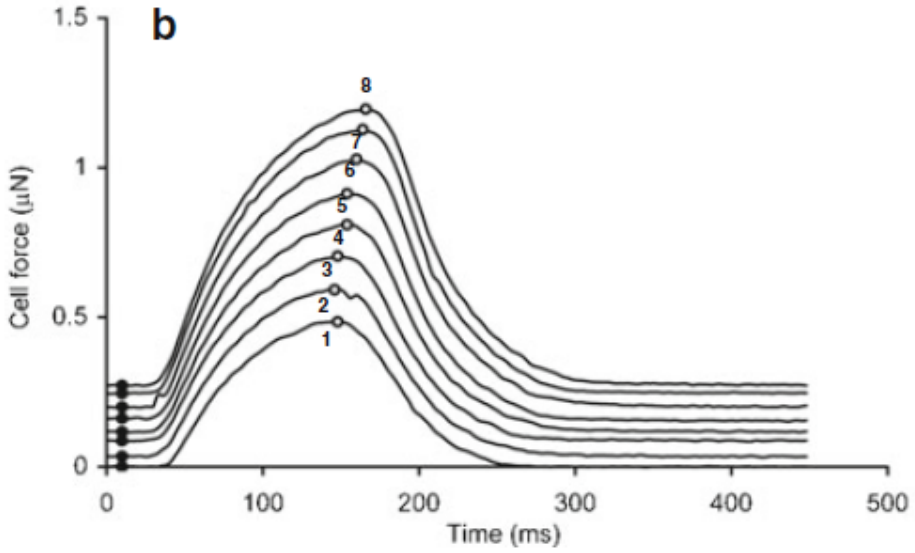

Figure 38: Impact of preload on produced force during auxotonic contractions [96]. Initial stretch of cardiac cells (preload) is varied and the produced forced during a twitch auxotonic contraction is recorded (1: lowest preload, 8: greatest preload). The peak force and whole dynamic of contraction appear to be altered by preload. Experimentally, both cell ends are attached to compliant carbon fibers (CF). Produced force can be determined by measuring CFs bending, knowing their compliance.

In other experiments, starting from a sarcomere length $L > L_0$, the produced force when reaching the length L_0 during shortening has been shown to be smaller than the force that would have been produced by an isometric contraction at L_0 [94]. This effect is termed *shortening deactivation* and, as cardiac cells shortens during the blood ejection phase, this property may a role in regulating cardiac contraction[12] [14, 75]. How SL affects this degree of deactivation remains however unclear.

Under auxotonic contractions, preload affects the timing and magnitude of contraction [95, 96], as shown in Fig. 38. Even if these are not isometric twitch contractions, the maximal produced force still increases with increasing preloads.

3.4.6 *Positive effect of ejection*

The experiments presented in the previous section show that the magnitude of force is decreased under auxotonic contraction compared to the isometric case. The work of De Tombe and Little [97] led to suprising results that seem to be in conflict with these obserations. These authors worked on cardiac cell auxotonic contractions that mimicked an ejecting beat and observed that, under certain loading conditions, the maximal developed force was greater than the

[12] "This mechanism may, in fact, provide an important myofibrillar brake system, which could be important in preventing excessive pressure development in the face of diminishing chamber size during ejection. In addition, shortening-induced cooperative deactivation is likely a major factor for [...] control of ventricular relaxation." [75]

isometric force (see Fig. 39a). This "positive effect of ejection" is also observed at the heart scale (Fig. 39b) [98, 99]. In a recent editorial, De Tombe and Tyberg [19] mentionned the "ejection-history dependence" of cardiac muscle: depending on loading conditions, the ejection (cell shortening) phase may actually lead to increased force development compared to the isometric case. Thus, under certain physiological conditions, a positive effect of ejection occurs [19, 97] which is modulated, among other parameters, by preload[13].

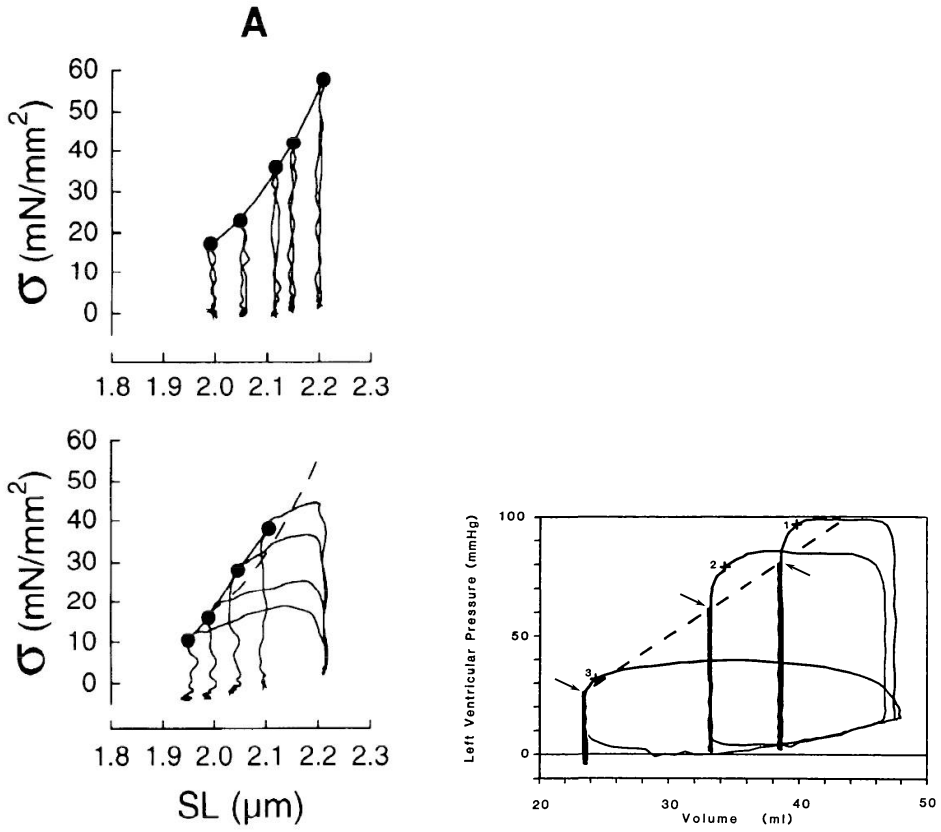

(a) (b)

Figure 39: Positive effect of ejection. (a) Top: Stress (force divided by muscle cross-sectionnal area) as a function of length in isometric twitch contractions. Bottom: Stress as a function of length in auxotonic (physiological) contractions. The dotted line corresponds to the maximal isometric forces reported from the upper panel. For high SLs, the maximal auxotonic force is greater than the maximal isometric force. This is termed the "positive effect of ejection": shortening of cardiac cells has led to a produced force greater than expected from the isometric value [97]. (b) Three LV PV loops from a canine heart, corresponding to different loading conditions (adapted from [98]). The "+" marks correspond to the end-systolic pressure. The arrows indicate the maximal isovolumic pressure for three isovolumic (non ejecting) beats. For PV loops 1 and 2, there is a clear "positive effect of ejection", as maximal developed pressure overcome maximal isovolumic pressure.

[13] "... conditions set up early in the contraction at the end-diastolic volume may determine contractile state throughout the entire contraction and thus constitute a short-term memory mechanism." [97]

3.4.7 *Summary*

We have seen that SL definitely modulates cardiac cell behavior. For an isometric twitch contraction, an increase in length leads to an increased calcium sensitivity and an increased developed force. This property is termed LDA. Although its underlying molecular mechanisms are not fully understood yet, LDA certainly modulates cardiac cell output *in vivo*. However, as physiological (auxotonic) contractions are different from isometric contractions, the exact way LDA affects cellular contraction is not easy to demonstrate. It is worth noticing that cardiac contraction starts with an isovolumic phase, where cardiac cell length is almost kept constant, so the beginning of contraction is probably modulated by LDA as highlighted in the isometric experiments. But during the blood ejection phase, cardiac cells shorten, and shortening deactivation and/or positive effect of ejection come into play. As proposed by Hanft *et al.* [75], the initial SL (preload) could modulate the number of active CBs during the isovolumic contraction (through the LDA mechanism), which would then affect the shortening capacity during the ejection phase.

3.5 CELLULAR ORIGINS OF THE FS MECHANISM

As all cardiac cells are recruited on each beat, it is the mechanical output of each cell that has to be modulated in order to modulate the whole cardiac output (CO). As explained above, this mechanical output can be modulated with extrinsic mechanisms that alter contractility (e.g., neuro-humoral control), but there is also an intrinsic modulation mechanism of contractile state by length: LDA.

On the other hand, the FS mechanism, described in Chapter 2, "is an intrinsic property of all vertebrate cardiac tissue" [4] that allows for the modulation of CO on a beat-to-beat basis. This property must be inherent to the cardiac cells themselves, and do not depend on extrinsic control of cell contractility. For this reason, LDA, namely a calcium sensitivity change upon change in SL, is often considered as the cellular basis of the FS mechanism [16–21]. As already mentionned in Section 2.5, the commonly given explanation is that, as preload increases, sarcomere length increases, so does the peak produced force during contraction. At the heart scale, the produced pressure rises and more blood can be ejected, hence the increased stroke volume [1, 3, 18, 22]. Here the isometric experiments highlighting LDA are directly linked to the "preload-adaptability" of the beating heart. In other words, the increase in produced force upon SL increase, for a fixed calcium concentration, obtained from the force-pCa curves, is often associated with the increase in produced pressure when the end-diastolic volume (or preload) is increased, as shown in Fig. 40. However, both results are obtained with crucial differences in the experimental setup. Force-pCa curves are obtained with fixed SL and fixed calcium concentrations, while cardiac cells *in vivo* undergo auxotonic contractions with a transient calcium, which results in the PV loops from Fig. 40. A similar parallel between PV loops under varying preload conditions and cardiac cells experiments under isometric conditions is regularly drawn (see Fig. (5) from [18] or Fig. (1) from [17]). We see that the length-dependence of the peak force in isometric condition is usually directly as-

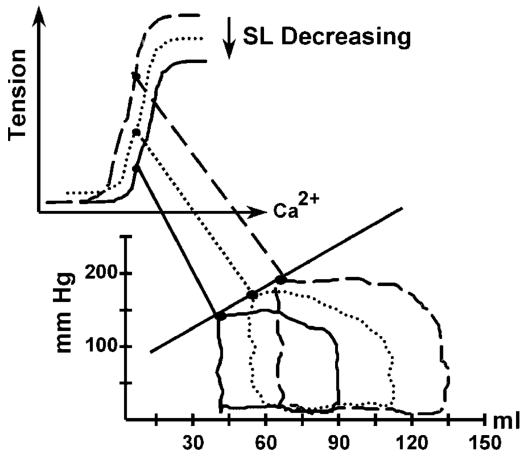

Figure 40: Length-dependent activation and its link to the FS mechanism (Figure (6) from [59]). Left ventricular PV loops for different EDVs (or preload). The increase in systolic pressure following an increase in EDV is directly associated with the increase in force (or tension) upon SL stretch observed in force-pCa curves, for a fixed calcium value.

sociated with the diastolic (or preload) dependence of the ventricular pressure-volume loop in a beating heart. This reasoning is, at least, insufficient to explain the FS mechanism, as it uses "static" cellular experiments (fixed length, fixed calcium) to describe a highly dynamical effect of increased preload on cardiac contraction.

It has already been underlined that the length-tension relationship and the Starling Law could not directly be put in parallel [62, 100–102]. As Allen and Kentish stated, "... the length-tension relationship in isolated muscle should be regarded as a simple way of investigating one aspect of the range of length-dependent properties that are involved in the Frank-Starling mechanism in the intact heart. These properties include the length-dependence of tension development, of velocity of shortening, of total shortening and of work output[14]" [62]. More recently, McDonald and colleagues [86, 103] also emphasized on the SL influence on shortening, and not only on the force-generating capacity.

As shown in the previous sections, preload affects the velocity of shortening in isotonic experiments [86], and the timing and magnitude of contraction in auxotonic conditions [95, 96]. Finally, the "positive effect of ejection" shows how preload, among other parameters, may affect the whole dynamic of an ejecting beat [19, 97, 98]. These properties are rarely cited when discussing the cellular basis for the FS mechanism. The latter is somehow always associated with an increase in peak force following an increase in fiber length. The impact of preload on the whole dynamics of heart contraction is more rarely discussed.

[14]The cellular work output is the aera under the force-length loop during a contraction, similar to the stroke work for the pressure-volume loop.

3.6 SUMMARY

The heart mechanical properties arise from the biochemical properties of cardiac sarcomeres [18, 28, 59]. Thus single cell experiments provide useful insight into our understanding of cardiac function [92, 96]. However, a direct correlation between microscopic and macroscopic properties should be handled carefuly. There is a variety of cellular experimental protocols (isometric/isotonic/auxotonic contraction, skinned or intact cells, sarcomere length control and measurement techniques, ...), but a replication of the beating heart conditions is almost never found. For this reason, there is an intrinsic limit in what can be derived from cellular experiments and applied at the heart scale [18, 62, 76].

In the literature, LDA (cellular scale) is always associated with the FS mechanism (organ scale) [16–21]. The given explanation is generally related to the increase in force-generating capacity upon preload increase [1, 3, 18, 22], and more rarely to the ejection dynamics alterations [86, 103]. LDA certainly plays a role in physiological contractions, but this role may not exclusively be related to the increase in produced force. This relationship between LDA and the FS mechanism lies at the heart of this thesis.

LDA and the FS mechanism being often presented as interchangeable concepts, we use the following definitions in order to avoid any ambiguity:

- FS mechanism: an increase in SV following an increase in preload, within the same heartbeat. Observed at the (ventricular) macroscopic scale.
- LDA: an increase in F_{peak} when cardiac cells are activated at a longer length. Observed at the (sub-cellular) microscopic scale.

Now we can ask ourselves the following question: is the FS mechanism only mediated through LDA? In other words, is the increase in maximal developed force following an increase in preload the only factor accounting for the increase in SV? Does preload only impacts SV through maximal force modulation?

This question is hard to answer experimentally, as both scales are involved. In this case mathematical models of the CVS can be very useful, as they allow to overcome the experimental difficulty of altering only one parameter (the preload) while measuring microscopic variables (such as sarcomere length). In the next chapter, a multiscale model of the human CVS will be presented, that will allow an *in silico* analysis of the FS mechanism.

4

MODELING THE CARDIOVASCULAR SYSTEM

The previous chapters concisely covered the physiology of the cardiovascular system (CVS), with a focus on the cellular level. The CVS is a complex structure whose internal mechanisms are not fully elucidated yet. Experimental studies are sometimes difficult to implement because many parameters are not easily manageable, e.g., the intrinsic variablity across studied subjects, measurements replicability and measurements precision, efficient control of all the involved parameters, to name but a few. Mathematical modeling of biological systems has become a powerful tool to overcome the experimental limitations. As stated by Niederer and Smith [27]: " ... computational physiology has a significant role to play in rationalising data, linking observations to function and translating laboratory results into clinical contexts". Computational modeling may be used in clinics to assist physicians or used as explorative device to broaden physiological knowledge. A mathematical model has to reliably reproduce experimental observations, but a balance has to be found between accuracy and computational tractability. To cite Rice *et al.* [104]: "In all modeling efforts, some level of abstraction is chosen as a compromise between parsimony and complexity". Indeed, a simple model may sometimes be preferred to a time-consuming model, filled with numerous parameters to identify, depending on the aim of the study.

In this chapter, a model of the human CVS system is presented. Particular attention is paid in building the heart model. The aim is to relate the cellular properties to the organ behavior, with a reasonable computational cost. Then this heart model is inserted in a lumped-parameter model of the CVS to finally obtain a multiscale model of the human CVS. Such integrative models help in understanding the influences of the various sub-systems on whole system behavior [105]. In our case, sarcomere length influence at the organ and CVS scales is at the center of our study.

The heart being a multiphysics and multiscale system, different approaches may be followed to build a cardiac pump model [28, 29]. On the one hand, three-dimensionnal descriptions of the whole heart electromechanics can be obtained with finite-element models [106–112]. Such models are however complex, time-consuming and require a large amount of imaging data to build the model geometry. On the other hand, *ad hoc* models, that rely on phenomenological approaches, may also be used [113]. These are less sophisticated, as they are not built on strictly physiological considerations. They are rather developed to reproduce macroscopical observations. A third approach, that we will follow, consists in building mathematical models of the heart that only require ordinary differential equations, and still provide a link between the cellular level and the organ scale. Basically, a single sarcomere model is associated with a simple ventricular model: the force and length of a sarcomere are converted into pressure and volume inside the ventricular cavity (see Fig. 41). Such multiscale models

[114–123] offer a better link between the microscopic properties of the cardiac tissue and the macroscopic observations at the CVS scale while providing a reasonable computational cost.

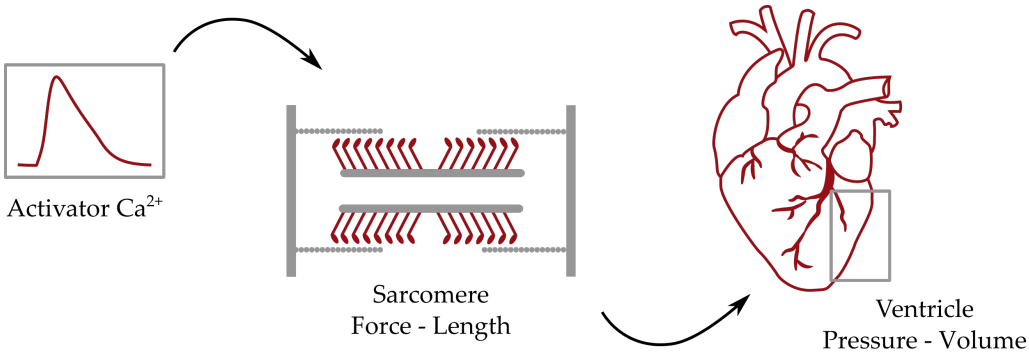

Figure 41: Multiscale model of a ventricle. The force and length obtained from a sarcomere model of contraction are linked to the pressure and volume variation of a ventricle model. The calcium transient may be used as an input function or extracted from an electrophysiological model.

In the following, we will first describe the CVS model at the macroscopic scale, and focus on the so-called passive elements (which do not actively generate pressure). Then the two active elements (left and right ventricles) will be introduced. A cellular model of contraction is presented afterwards, and the microscopic variables (sarcomere force and length) are linked to the macroscopic variables (ventricular pressure and volume) to obtain a multiscale model of the human CVS.

4.1 THE SIX-CHAMBER MODEL

A model of the whole human CVS requires a mathematical description of the following two components :

- The vascular network (veins, arteries, capillaries, ...);
- The cardiac pump, namely two atria and two ventricles.

Following the approach of others [114, 115, 124–128], a lumped-parameter (LP) model is chosen to describe the CVS. Such models are based on the discretization of the system, where the variables of interest (like pressures and volumes) are considered only at specific points. Some parts of the CVS are represented as "elastic chambers" while other are represented as "resistive vessels" or "diodes". A schematic representation of the CVS model that we use is depicted in Fig 42. Six compartments represent the left (LV) and right (RV) ventricles (active elements), the pulmonary artery (PA) and pulmonary vein (PV), the aorta (AO) and the vena cava (VC) (*passive* elements). The atria are not taken into account in this model. The systemic and pulmonary circulations are depicted as resistances while the four cardiac valves (mitral, tricuspid, aortic and pulmonary) are represented as diodes associated with a resistance. The electrical analogy with diodes is proposed because cardiac valves ensure the unidirectionnality of blood flow.

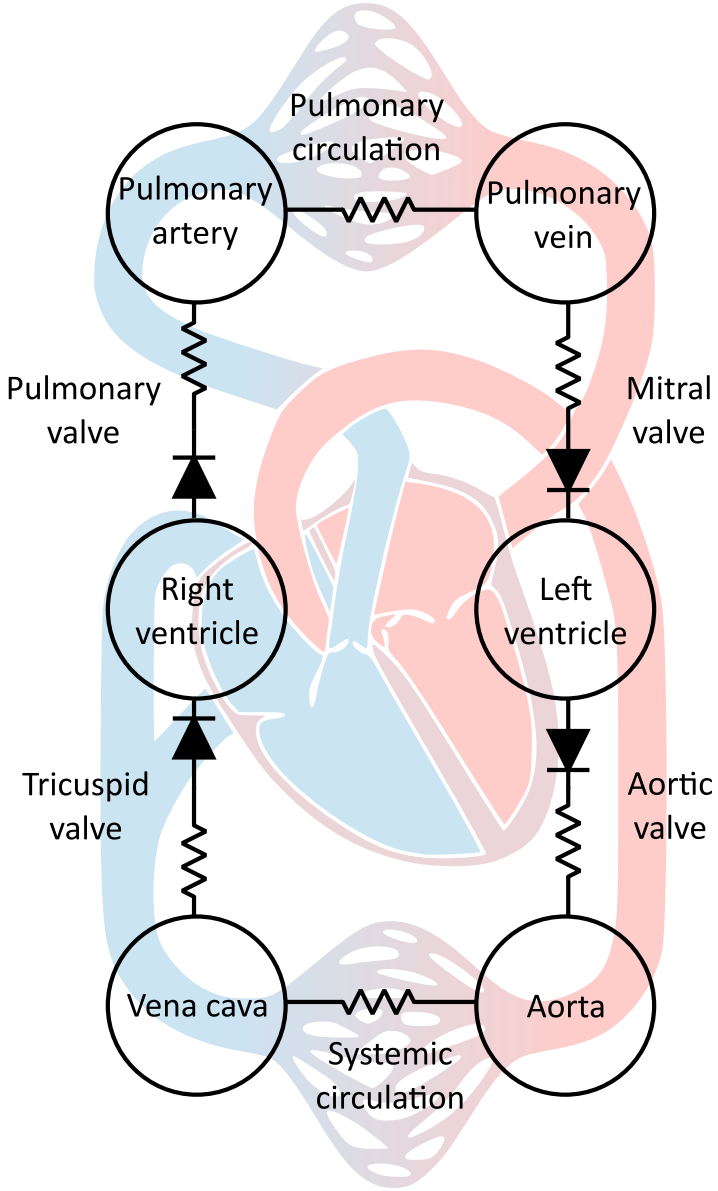

Figure 42: The six-chamber CVS model. Passive chambers: the aorta, the vena cava, the pulmonary vein and artery. Active chambers: the left and right ventricles. The atria are not accounted for in this model. The four cardiac valves are depicted as electrical diodes.

4.2 PASSIVE ELEMENTS

4.2.1 *Passive chambers*

The pressure of a passive chamber, such as an artery or vein, increases with its volume. The pressure-volume curve is generally convex [129, 130], and the local slope of the curve, $\Delta P/\Delta V$, is called the *elastance* E (see Fig. 43). A common first-order approximation leads to the following expression for the pressure-volume relationship in a passive chamber [53, 129]:

$$P(t) = E \cdot (V(t) - V_u) \tag{4.1}$$

where t is time, E is the (constant) elastance of the chamber, around a chosen working point (see Fig. 43) and V_u is the unstressed volume, the volume at which pressure is equal to zero.

By defining the *stressed* volume V_s as $V_s = V - V_u$, the relationship becomes :

$$P(t) = E \cdot V_s(t) \tag{4.2}$$

This *stressed* blood volume is the portion of blood volume that generates pressure inside the chamber. A passive chamber is represented in Fig. 43.

The pressure-volume relationship of arteries and veins may vary due to several factors (reflex constrictions, viscoelastic properties, ... [53]). This means that E and V_u are not strictly constant over time. It is worth mentionning that the compliance C is sometimes adressed instead of the elastance. The latter is just the inverse of the former ($C = \Delta V/\Delta P = E^{-1}$). The more compliant the vessel, the lesser the pressure variations in response to a volume change.

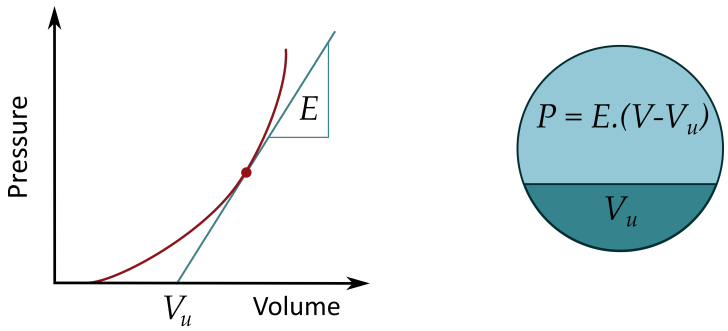

Figure 43: Pressure-volume relationship of a passive chamber in a LP model of the CVS. The pressure-volume curve (left), albeit convex, is assumed linear around a working point. The pressure inside the passive chamber (schematized on the right) then linearly increases with the volume V of the chamber, and is proportional to the (constant) elastance E of the chamber. The unstressed volume, V_u, is the chamber volume at which pressure is equal to zero. The difference between V and V_u gives V_s, the stressed volume.

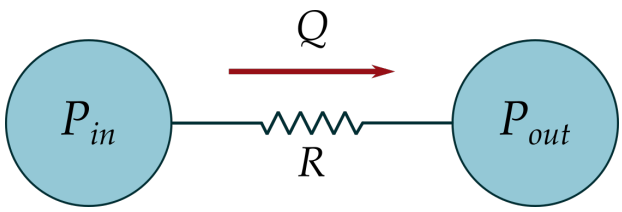

Figure 44: Representation of a flow resistance. The blood flows through the resistive vessels is modelized with a Poiseuille-like equation.

4.2.2 *Resistances*

The systemic and pulmonary circulation networks are modeled with flow resistances, like the one depicted in Fig 44. When traveling across the blood vessels (arteries and veins), there is a drop in pressure, that can be mathematically described as follows:

$$Q(t) = \frac{P_{in} - P_{out}}{R} \tag{4.3}$$

where Q is the blood flow and R is the hydraulic resistance. Eq. (4.3) is actually similar to Poiseuille's law where the hydraulic resistance is given by:

$$R = \frac{8\eta l}{\pi r^4} \tag{4.4}$$

where η is the fluid viscosity, l the length of the vessel and r its radius. Note however that the systemic and pulmonary resistances, R_{sys} and R_{pul}, cannot be computed from this equation, as the hypotheses formulated for Poiseuille's equation[1] are not valid here. However, the linear relationship between blood flow and pressure gradient is still assumed and the resistance is experimentally determined.

It is worth noticing that the inertia of blood has been neglected so far: blood flow suddenly stops if the pressure gradient reaches zero. A more realistic equation for blood flow would take into account an inertance parameter L [124, 126, 131] such that:

$$Q(t) = \frac{P_{in} - P_{out}}{R} - \frac{L}{R}\frac{\mathrm{d}Q}{\mathrm{d}t} \tag{4.5}$$

Here blood flow will not immediatly reach zero once the pressure gradient cancels. Note that this model will not be considered in our work.

4.2.3 *Valves*

As described in Chapter 2, cardiac valves ensure the unidirectionnality of blood flow. They only open if the upstream pressure is greater than the downstream one.

[1] Steady and laminar flow in a rigid cylindrical vessel.

Thus, assuming Poiseuille's law for the blood flow through the valve, we can write:

$$Q(t) = \begin{cases} \dfrac{P_{in} - P_{out}}{R} & \text{if } P_{in} > P_{out} \\ 0 & \text{otherwise} \end{cases} \tag{4.6}$$

In Fig 42, the four cardiac valves are symbolized as a combination of a resistance and a diode.

Blood inertia can also be taken into account for blood flow across valves [126, 127]. Such models are able to reproduce the fact that valves open when the pressure gradient is positive, and close when blood flow becomes negative. However, this more realistic description makes the simulations more computationnaly intensive, as the blood flow equation has to be solved *a priori* to know when Q becomes negative [53]. This modeling approach will not be followed in our work.

4.2.4 *Volume variations*

The volume variation of a chamber depends on the blood flows coming in (Q_{in}) and going out (Q_{out}), as represented in Fig 45. Thus we can write :

$$\frac{\mathrm{d}V(t)}{\mathrm{d}t} = Q_{in}(t) - Q_{out}(t) \tag{4.7}$$

Assuming that the unstressed volume remains constant, we can also write:

$$\frac{\mathrm{d}V_s(t)}{\mathrm{d}t} = Q_{in}(t) - Q_{out}(t) \tag{4.8}$$

Since the CVS is a closed loop, the total blood volume variation is equal to zero and so is the total stressed blood volume variation. In other words, the total amount of blood responsible for a non-zero pressure inside the CVS, named the *stressed blood volume* (SBV), is kept constant. However, this assumption is only valid for short periods of time, as SBV may vary through sympathetic nervous actions, haemorrhage, fluid exchanges and other mechanisms [53].

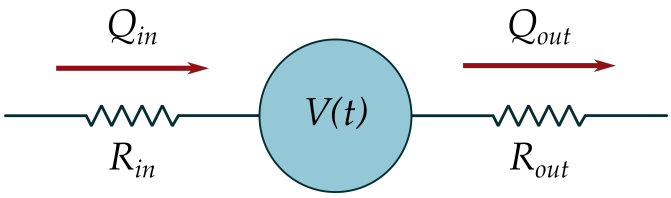

Figure 45: Volume variation of a chamber. Blood flows coming in (resp. going out) the chamber contribute positively (resp. negatively) to blood volume variations inside the chamber.

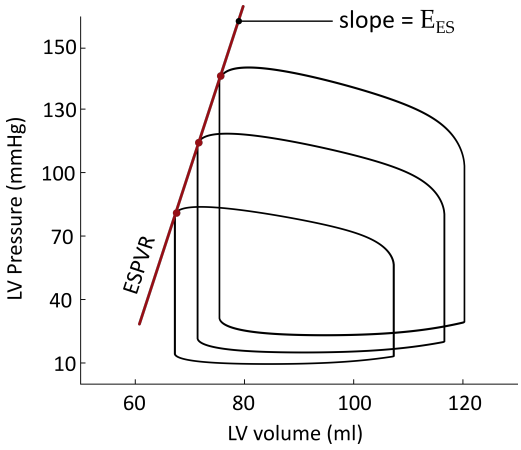

Figure 46: End-systolic pressure-volume relationship (ESPVR). The work of Suga *et al.* [113] showed that the end-systolic points of every PV loops are aligned on a straight line. The slope of this curve is called the end-systolic elastance (E_{ES}). It depends on contractility.

4.3 ACTIVE ELEMENTS

The two active elements of our model are the left and right ventricles. Since these chambers are able to actively contract and generate pressure, a linear pressure-volume relationship like Eq. (4.2) cannot accurately portray the pressure development in a beating ventricle. Other models are required to describe the cardiac pump. The time-varying elastance model, for instance, is commonly used in CVS modeling. In this model, developed by Suga *et al.* [113], a ventricular pressure-volume relationship similar to Eq. (4.1) is proposed:

$$P(t) = E(t) \cdot (V_c(t) - V_u) \tag{4.9}$$

where $E(t)$ is a non-linear, time-varying elastance. This model was proposed based on the following observations: the top left point of all PV loops were always located on an almost straight line, called the end-systolic pressure-volume relationship (ESPVR), as represented in Fig. 46. The slope of this curve, the end-systolic elastance E_{ES}, was found constant even when preload or afterload were varied. In the time-varying elastance theory proposed by Suga *et al.*, $E(t)$ is an input function that can be written as:

$$E(t) = E_{ES} \cdot e(t) \tag{4.10}$$

where $e(t)$ is a normalized function (varying from $e_{min} = 0$ to $e_{max} = 1$) used as an input of the model and called *the activation function*. This function was empirically built to obtain proper PV loops, as illustrated in Fig. 47.

As already mentionned, E_{ES}, the slope of the ESPVR, is assumed to be independent of preload or afterload [113], but it changes with the inotropic (or contractile) state of the ventricle, making E_{ES} a good candidate for monitoring cardiac contractility.

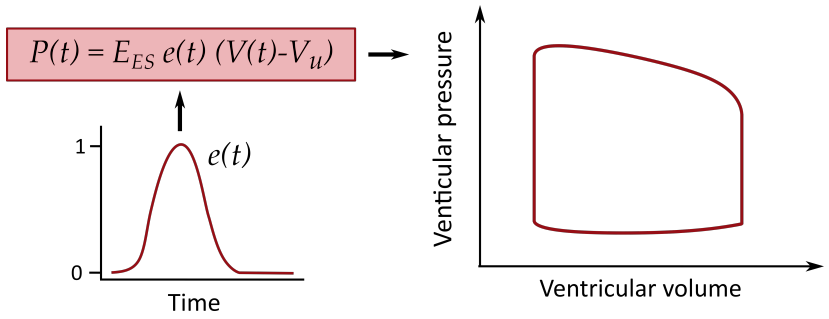

Figure 47: Illustration of the time-varying elastance model. The activation function, $e(t)$, is built to obtain proper PV loops. The ventricular pressure also depends on ventricular volume and E_{ES}.

Despite the time-varying elastance theory provided a very simple and functional model, criticisms have been adressed to this approach. The ESPVR has been shown to be in fact more parabolic than linear in shape [120, 129, 132–134] and also load-dependent [99, 135]. Moreover, the ventricular pressure was shown to be also negatively dependent on the blood flow out of the ventricle [136, 137]. In other words, the ventricle presents an "internal resistance" to blood ejection, as its developed pressure tends to decrease with greater ejection flows. Eq. (4.9) can be modified to take some of these observations into account [134, 137–139] but these *ad hoc* corrections do not compensate for the main drawback of this model: the absence of any physiological background. Cardiac contraction originates in fact at the cellular and sub-cellular scale, a perspective completely ignored here. Thus one cannot expect such a model to capture the complex properties of cardiac muscle and their consequences on the CVS performance.

As our aim is to keep a link between the cellular level and the organ scale in our mathematical model of the ventricle, we follow the third approach described in the introduction of this Chapter (see 41) and we consider a cellular model of contraction. This cellular model and the link to the ventricular scale will be thoroughly described in the following sections.

4.4 CARDIAC CELL MODEL

A single-cell electromechanical model is the combination of an electrical model and a mechanical model of contraction [28]. The electrical model describes the electrophysiology and the calcium handling within the cell, while the mechanical model describes myofilaments sliding and force production upon calcium activation. In our cell model, we couple an electrophysiological model of a human ventricular cell [140, 141] to a mechanical contraction model of a half-sarcomere [142–144]. Those two models are described below.

4.4.1 *Electrophysiology*

Cellular electrophysiology can be modeled assuming the cell membrane is a capacitor in parallel with several variable resistors [145], as schematized in Fig. 48.

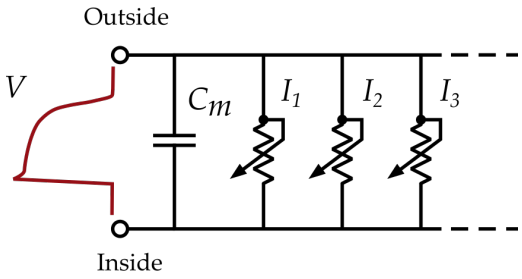

Figure 48: Electrical circuit model of the cell membrane. The membrane is assimilated to a capacitor C_m in paralell with variable resistors. Ionic currents across the membrane occur during an AP, and are responsible for the variation in the potential difference V across the membrane. The typical time variation of V during an AP in a ventricular cell is shown in red.

There is an electrical potential difference between the outside and the inside of the cell, noted V. During an action potential (AP), V varies due to ions penetrating or leaving the cell through ionic channels, as described in Chapter 3. If we note I_i the electrical current carried by ion i through the cell membrane, we have:

$$C_m \frac{\mathrm{d}V}{\mathrm{dt}} + \sum_i I_i + I_{\text{stim}} = 0 \tag{4.11}$$

where C_m is the membrane capacitance and I_{stim} is a possible stimulation current that triggers the AP.

C_m is generally expressed as a capacitance per unit area, and the ionic currents are expressed in Amperes per unit area (current densities). If Eq. (4.11) is normalized with respect to the membrane capacitance, we obtain:

$$\frac{\mathrm{d}V}{\mathrm{dt}} + \sum_i I_i + I_{\text{stim}} = 0 \tag{4.12}$$

where the current densities are now expressed in Amperes per Farad.

From these ionic currents densities, we can also obtain the time evolution of the intracellular concentrations for each type of ions. If $[\text{Ion}]_i$ denotes the concentration of ion i, we have:

$$\frac{\mathrm{d}[\text{Ion}]_i}{\mathrm{dt}} = \frac{C_{m0}(I_{in,i} - I_{out,i})}{z_{ion} V_c F} \tag{4.13}$$

where I_{in} (resp I_{out}) is the global electrical current density due to the ions entering (resp. exiting) the intracellular compartment of volume V_c, z_{ion} is the valence of the ion, and F is the Faraday constant. The C_{m0} factor is the membrane capacitance of the cell (expressed in Farad), required to obtain proper concentration units when working with the normalized current densities from Eq. (4.12).

Since we want a human CVS model, we use the model of Ten Tusscher and Panfilov (TTP) [140, 141], which describes the transmembrane ionic currents

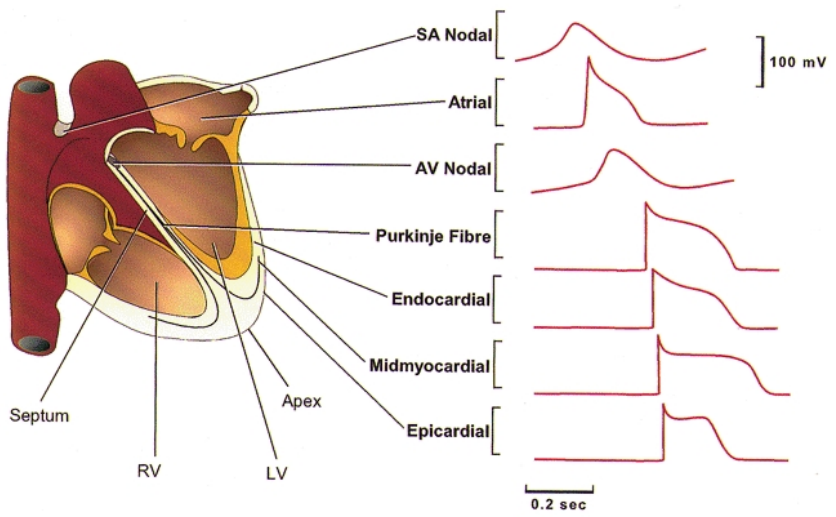

Figure 49: Schematic representation of AP variability in epicardial, midmyocardial (M) and endocardial cells [146]. The APs in other locations are also represented.

(K^+, Na^+ and Ca^{2+} currents) for three types of human ventricular cells: endocardial, midmyocardial, and epicardial cells. Those cells are located at different depths across the ventricular wall, and undergo slightly different APs, as shematized in Fig. 49.

A representation of all the transmembrane ionic currents involved in the TTP model is shown in Fig. 50. A few equations from this model will be detailed in the following sections, but for the sake of clarity, the complete set of equations and parameters of the electrophysiological model for the midmyocardial cells, which we choose for our cellular model, are listed in Appendix A.

The stimulation current I_{stim}, which allows the AP trigger, is plotted in Fig. 51. It is assimilated to a brief inward (thus, negative) potassium current. The

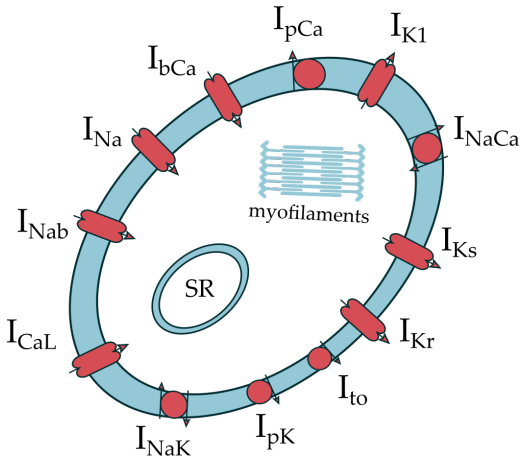

Figure 50: Transmembrane currents involved in the Ten Tusscher and Panfilov model [140, 141].

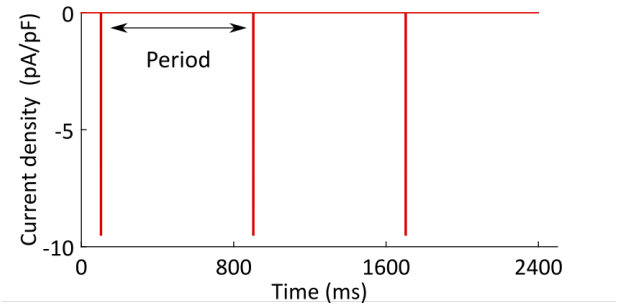

Figure 51: Stimulus current for the triggering of AP in the electrophysiological model. A brief negative current is applied periodically to generate and sustain APs production. The chosen period (800 ms) sets the HR (75 bpm).

stimulation period sets the heart rate (HR), which is 75 beats per minute (bpm) in our model, a normal resting HR for an adult human [1].

From the transmembrane currents pictured in Fig. 50, we can adapt Eq. (4.13) for the K^+ and Na^+ intracellular concentrations:

$$\frac{d[K]_i}{dt} = -C_{m0}\frac{-2I_{NaK} + I_{Ks} + I_{K1} + I_{to} + I_{pK} - I_{stim}}{V_c F} \tag{4.14}$$

$$\frac{d[Na]_i}{dt} = -C_{m0}\frac{3I_{NaK} + 3I_{NaCa} + I_{Na} + I_{bNa}}{V_c F} \tag{4.15}$$

where V_c is the cytoplasmic volume. Note that the Na^+/K^+ pump (I_{NaK}) exchanges three Na^+ for two K^+, and the Na^+/Ca^{2+} exchanger (I_{NaCa}) exchanges three Na^+ for one Ca^{2+}.

This electrophysiological model also describes calcium (Ca) dynamics, which is essential to represent the cardiac excitation-contraction coupling. A more detailed description of calcium currents is presented here. As schematized in Fig. 52. The intracellular space is divided into three compartments: the diadic space (SS), the sarcoplasmic reticulum (SR) and the cytoplasm (CYTO). Ca concentrations in those three subspaces may vary due to entering or exiting calcium currents. Ca buffers are also present, such as calsequestrin in the SR, or calmodulin and troponin in the CYTO space [32], which modulate the amount of free Ca ions. A mathematical description of Ca buffers is provided below, then Ca currents are listed to finally obtain the differential equations that govern Ca concentration.

4.4.1.1 *Calcium buffers*

The chemical reaction for calcium buffering is given by:

$$[Ca] + [Buf] \rightleftharpoons [CaBuf] \tag{4.16}$$

where [Ca], [Buf], and [CaBuf] are the concentration of free Ca, free buffer, and Ca-buffer complex, respectively.

The equilibrium constant K_{buf} of reaction (4.16) is given by:

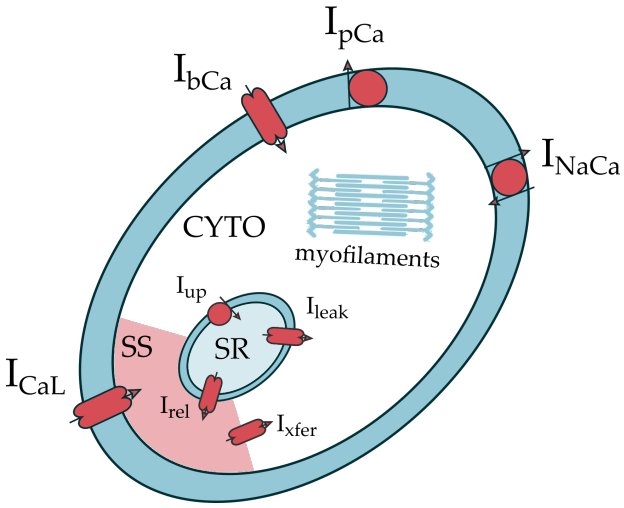

Figure 52: Calcium dynamics in the electrophysiological model. Three compartments are involved: cytoplasm (CYTO), sarcoplasmic reticulum (SR), and diadic space (SS). Explanations in the text.

$$K_{\text{buf}} = \frac{[\text{Ca}]\,[\text{Buf}]}{[\text{CaBuf}]} \tag{4.17}$$

If we note Buf_t the (constant) total buffer concentration, we naturally have:

$$[\text{Buf}] = \text{Buf}_\text{t} - [\text{CaBuf}] \tag{4.18}$$

A common approximation is the Rapid Buffer Approximation (RBA) [147]. Assuming a steady-state is reached for reaction (4.16), we can combine Eq. (4.17) and Eq. (4.19) to get the concentration of Ca-buffer complex:

$$[\text{CaBuf}] = \frac{[\text{Ca}]\,\text{Buf}_\text{t}}{[\text{Ca}] + K_{\text{buf}}} \tag{4.19}$$

We can apply the reasoning above for Ca buffers concentrations in the CYTO, SS and SR compartments. Total Ca, free Ca, and Ca-buffer complex concentrations in the CYTO compartment are noted $[\text{Ca}]_{\text{itot}}$, $[\text{Ca}]_\text{i}$, and $[\text{CaBuf}]_\text{i}$ respectively. With similar notations for the SS and SR compartments, we have:

$$[\text{Ca}]_{\text{itot}} = [\text{Ca}]_\text{i} + [\text{CaBuf}]_\text{i} \tag{4.20}$$
$$[\text{Ca}]_{\text{SStot}} = [\text{Ca}]_{\text{SS}} + [\text{CaBuf}]_{\text{SS}} \tag{4.21}$$
$$[\text{Ca}]_{\text{SRtot}} = [\text{Ca}]_{\text{SR}} + [\text{CaBuf}]_{\text{SR}} \tag{4.22}$$

With the RBA, we can write [140, 141]:

$$[\text{CaBuf}]_\text{i} = \frac{[\text{Ca}]_\text{i}\,\text{Buf}_\text{i}}{[\text{Ca}]_\text{i} + K_\text{bufi}} \tag{4.23}$$

$$[\text{CaBuf}]_\text{SS} = \frac{[\text{Ca}]_\text{SS}\,\text{Buf}_\text{SS}}{[\text{Ca}]_\text{SS} + K_\text{bufSS}} \tag{4.24}$$

$$[\text{CaBuf}]_\text{SR} = \frac{[\text{Ca}]_\text{SR}\,\text{Buf}_\text{SR}}{[\text{Ca}]_\text{SR} + K_\text{bufSR}} \tag{4.25}$$

where Buf_i, Buf_SS, and Buf_SR are the total buffer concentrations for the CYTO, SS and SR compartments, respectively. K_bufi, K_bufSS, and K_bufSR are the associated equilibrium constants.

4.4.1.2 *Calcium currents*

Ca currents are schematized in Fig. 52. Ca ions enter the SS compartment from the extracellular space through L-type calcium channels (I_CaL). The increase in SS Ca concentration triggers the release of Ca ions from the SR (I_rel) into the SS, by the process of Ca-induced Ca release (CICR). Then these Ca ions diffuse through the CYTO space (I_xfer), where they can promote myofilaments activation and contraction. I_leak, on the other hand, describes the passive leak of Ca ions from the SR into the CYTO compartment. At the end of contraction, Ca ions are pumped back from the CYTO space into the SR via the SERCA pump (I_up) or outside the cell by the $\text{Na}^+/\text{Ca}^{2+}$ exchanger ($I_\text{Na/Ca}$) and the sarcolemnal calcium pump (I_pCa). Finally, an additonal transmembrane calcium current, I_bCa, also plays a role in intracellular Ca fluxes during an AP.

4.4.1.3 *Free calcium concentrations*

With the ionic currents from the previous section, it is possible to write equations for total Ca concentrations in the CYTO compartment:

$$\begin{aligned}\frac{\text{d}[\text{Ca}]_\text{itot}}{\text{dt}} &= -C_m\,\frac{I_\text{bCa} + I_\text{pCa} - 2I_\text{NaCa}}{2V_cF} + \frac{V_\text{sr}}{V_c}(I_\text{leak} - I_\text{up}) + I_\text{xfer} \\ &= \frac{\text{d}[\text{Ca}]_\text{i}}{\text{dt}} + \frac{\text{d}[\text{CaBuf}]_\text{i}}{\text{dt}}\end{aligned} \tag{4.26}$$

where V_c is the CYTO volume, and V_{sr} the SR volume. Note that the transmembrane currents are expressed in Amperes per Farad (see Eq. (4.12)), while the SR and diffusive currents are expressed in units of concentration per time[2].

By differentiating Eq. (4.23) and combining the result with Eq. (4.26), we obtain the equation governing $[\text{Ca}]_\text{i}$:

$$\begin{aligned}\frac{\text{d}[\text{Ca}]_\text{i}}{\text{dt}} = -\frac{1}{1 + \dfrac{K_\text{bufi}\,\text{Buf}_\text{i}}{[\text{Ca}]_\text{i} + K_\text{bufi}}}\Bigg(&C_m\,\frac{I_\text{bCa} + I_\text{pCa} - 2I_\text{NaCa}}{2V_cF} \\ &+ \frac{V_\text{sr}}{V_c}(I_\text{leak} - I_\text{up}) + I_\text{xfer}\Bigg)\end{aligned} \tag{4.27}$$

[2]The volume ratio is present because I_up, I_rel and I_leak are expressed in mole per liter of *SR* volume.

Solving this differential equation provides the intracelluler free Ca concentration required for the sarcometric contraction model, described in the next section. Similar equations are obtained for free Ca concentrations in the SS and SR compartments, and they can be found in Appendix A, along with the detailed currents description and parameters values.

4.4.2 *Sarcomere contraction*

We use the model of Negroni and Lascano [143, 144] to describe the mechanical contraction. Here, the cardiac muscle is assimilated to a series arrangement of muscle units. Each muscle unit is defined by the half-sarcomere length (L) and the muscle cross-sectionnal area. Whithin the muscle unit, the half-sarcomere is composed of inextensible thick and thin filaments, in parallel with an elastic element. This parallel elastic element accounts for the other intracellular components responsible for the passive force, that will be described later. The thick and thin filaments can slide past each other and crossbridges (CBs) can attach to the thin filament in the overlap region.

According to the CB theory [148], attached CBs act as independent force generators that occupy different states in the CB cycle. Here each attached CB, numbered by an index i, is assimilated to a linear spring, generating a force $f_i = a \cdot h_i$ where a is the elastic constant and h_i is CB elongation. So the total CB force F_t exerted by the pool of attached CBs within a half-sarcomere is:

$$F_t = \sum_i f_i = \sum_i a \cdot h_i = N \cdot a \cdot h \tag{4.28}$$

where N is the total number of attached CBs, and h is the mean CB elongation. F_t can be seen as N times the produced force of an *equivalent CB*, which represents all the attached CBs, with h the length of the equivalent CB.

If [CB] is the concentration of attached CBs, Vol the myoplasmic volume containing the contractile elements, and N_a the Avogadro's number, we can write:

$$N = N_A \cdot \text{Vol} \cdot [\text{CB}] \tag{4.29}$$

Muscle force is proportional to muscle size [149, 150]. This is why experimental force measurements are generally normalized with respect to muscle cross-sectionnal area and expressed as stress (typically in mN/mm^2). In the model considered here, produced force is normalized with respect to muscle cross-sectional area measured at a defined reference state, area_r. Assuming that muscle units keep their volume constant during contraction, we have $\text{Vol} = L_r \cdot \text{area}_\text{r}$ where L_r is the reference half-sarcomere length where the muscle cross-sectional area is measured. The normalized produced force F_a, *i.e.*, the total force created by a muscle unit divided by the reference cross-sectional area of this unit is then given by:

$$F_a = \frac{F_t}{\text{area}_r} \tag{4.30}$$

$$= \frac{N_A \cdot \text{Vol} \cdot [\text{CB}] \cdot a \cdot h}{\text{area}_r} \tag{4.31}$$

$$= A_e \cdot [\text{CB}] \cdot h \tag{4.32}$$

where A_e contains all the constants of the problem, [CB] is the concentration of attached CBs, and h is the equivalent CB elongation.

The equivalent CB model is represented in Fig. 53a. It is situated at the free end of an "equivalent" half-thick filament, so that the half-sarcomere length L of the muscle unit is the sum of two components:

$$L = X + h \tag{4.33}$$

where X is an inextensible length (thick filament length plus the non-overlapping part of the thin filament).

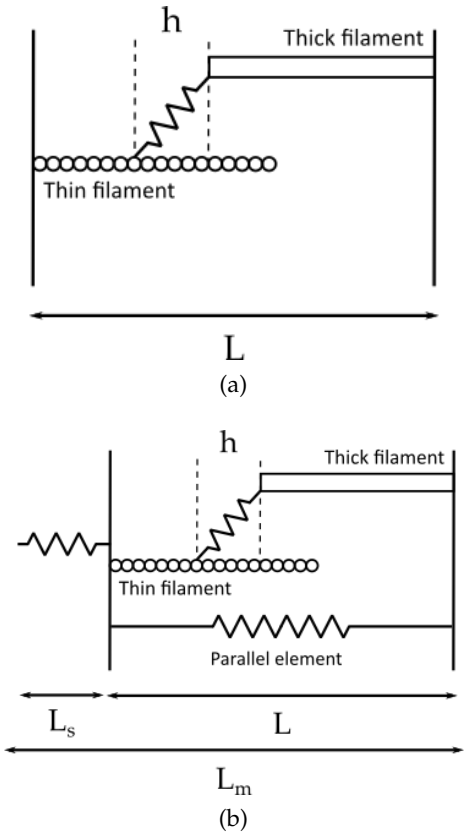

Figure 53: Equivalent CB model within the muscle unit. (a) The equivalent CB is assumed to be situated at the end of an equivalent inextensible half-thick filament, facing an equivalent inextensible thin filament. L is the half-sarcomere length, h is the equivalent CB elongation (see description in the text). (b) The contractile elements are in parallel with an elastic element that accounts for the passive properties of the muscle. There is also a series elastic element of length L_s (see description in the text). L_m is the total half-sarcomere length.

The equivalent CB dynamics is schematized in Fig. 54. At any steady length L, the equivalent CB has a constant elongation h_r (a) If a sudden shortening ΔL of the muscle unit occurs, h absorbs this shortening and the equivalent CB length becomes $h = h_r - \Delta L$. (b) Normally, CBs attach and detach cyclically from the thin filament during muscle contraction. Here the equivalent CB cannot detach and reattach to another position on the thin filament to recover the steady elongation h_r, otherwise the force would abruptly fall to zero. Instead, the equivalent CB remains attached as long as there is at least one attached CB. The asynchronous CBs attachment/reattachment dynamics is represented by a sliding of the equivalent CB attachment point along the thin filament (c). Thus, once shortening ends at a new length $L - \Delta L$, the equivalent CB regains its steady state elongation h_r by sliding its point of attachment. The return to h_r is assumed to produce a change in X as follows:

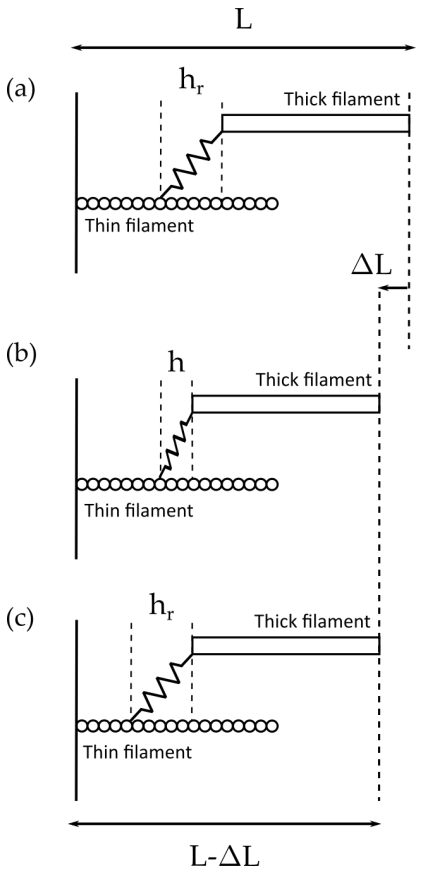

Figure 54: Equivalent CB dynamics.

$$\frac{dX}{dt} = B \cdot (h - h_r) \tag{4.34}$$

where $\frac{dX}{dt}$ is the velocity of motion of the mobile equivalent CB end.

In the model used in our approach, two attached CB states are proposed: a weak (w) and a power (p) state. This leads to two equivalent CBs: CB_w, with elongation h_w, a state in which the equivalent CB has not developed the power stroke yet, and CB_p, with elongation h_p, a state in which the equivalent CB can develop the power stroke. Using the model consisting of Eqs. (4.33) and (4.34) for the two types of CB states, we have:

$$L = X_p + h_p \tag{4.35}$$
$$L = X_w + h_w \tag{4.36}$$
$$\frac{dX_p}{dt} = B_p \cdot (h_p - h_{pr}) \tag{4.37}$$
$$\frac{dX_w}{dt} = B_w \cdot (h_w - h_{wr}) \tag{4.38}$$

Eq. (4.32) must also be adaptated and becomes:

$$F_a = A_w \cdot [\mathrm{CB_w}] \cdot h_w + A_p \cdot [\mathrm{CB_p}] \cdot h_p \tag{4.39}$$

CB concentrations are obtained with the following calcium kinetics model. A five-state troponin system (TS) is represented in Fig. 55. A TS is defined as three adjacent troponin–tropomyosin regulatory units (RU). Each RU can fix one calcium ion, and since calcium binding is a cooperative mechanism, it is assumed that three calcium ions bind in one step to the troponin system[3]. CB attachment occurs once the three RUs are "calcium-activated". Thus the five states of the model are: free TS (TS), calcium bound to TS ($\mathrm{TSCa_3}$), calcium bound to TS with three attached CBs in the weak state ($\mathrm{TSCa_3^{\sim}}$), calcium bound to TS with attached CBs in the power state ($\mathrm{TSCa_3^*}$), TS without calcium and with attached CBs in the power state ($\mathrm{TS^*}$).

In this context, Eq. (4.39) becomes:

$$F_a = A_w \cdot 3[\mathrm{TSCa_3^{\sim}}] \cdot h_w + A_p(3[\mathrm{TSCa_3^*}] + 3[\mathrm{TS^*}]) \cdot h_p \tag{4.40}$$

If we redefine A_w and A_p to include the common factor "3", we finally have:

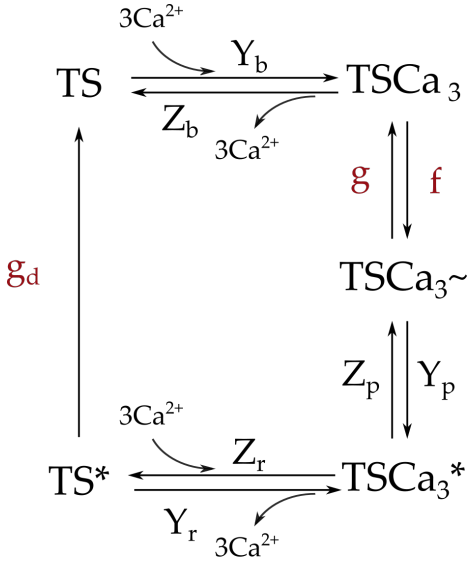

Figure 55: Calcium kinetics. A troponin system TS consists of three adjacent troponin-tropomyosin units. Three calcium ions can bind to a troponin system to form $\mathrm{TSCa_3}$. Then, three CBs can attach in a weak state denoted $\mathrm{TSCa_3^{\sim}}$ and shift into a power state $\mathrm{TSCa_3^*}$. The calcium ions can leave the troponin system while the CBs are still attached, this state being denoted $\mathrm{TS^*}$. Finally the CBs detach in an irreversible manner. The colored rate constants are length or CB-elongation-dependent (see text for details).

[3]Since the Hill coefficient n for cardiac muscle is around 3-4 [67], a possible explanatory mechanism is that the binding of one calcium ion to a RU facilitates the binding of a second calcium ion to the adjacent RU. This promotes the binding of a third calcium ion as well. A single binding step of three calcium ions to three adjacent RUs is assumed for simplicity.

$$F_a = A_w \cdot [\mathrm{TSCa}_3^{\sim}] \cdot h_w + A_p([\mathrm{TSCa}_3^{*}] + [\mathrm{TS}^{*}]) \cdot h_p \tag{4.41}$$

The parallel elastic element from Fig. 53b is present to account for the passive elastic properties of the muscle. The corresponding normalized passive force is written:

$$F_p = K_e \cdot (L - L_0)^5 + L_e \cdot (L - L_0) \tag{4.42}$$

where L_0 is the half-sarcomere "slack" length and K_e and L_e respectively represent titin and cellular element elasticities [144]. This passive force exists even if there is no attached CB, provided that it originates from the other (passive) cellular components.

The total normalized muscle force F is finally given by the sum of the active and passive forces:

$$F = F_a + F_p \tag{4.43}$$

There is also a series elastic element in the muscle unit model (Fig 53b). This element describes the compliant muscle ends and produce a force F_s, which is always equal to F given the series arrangement, and which is expressed as:

$$F_s = F = \alpha(\exp(\beta L_s) - 1) \tag{4.44}$$

where α and β are fixed parameters and L_s is the series element length [144].

The total half-sarcomere length is noted L_m:

$$L_m = L + L_s \tag{4.45}$$

The equations for the concentrations of the different troponin system states can be derived from the biochemical cycle (Fig. 55):

$$\begin{cases} \dfrac{\mathrm{d}[\mathrm{TSCa_3}]}{\mathrm{dt}} = \mathrm{Y_b}\,[\mathrm{TS}]\,[\mathrm{Ca}]_\mathrm{i}^3 - \mathrm{Z_b}\,[\mathrm{TSCa_3}] + \mathrm{g}\,[\mathrm{TSCa}_3^{\sim}] - \mathrm{f}\,[\mathrm{TSCa_3}] \\ \dfrac{\mathrm{d}[\mathrm{TSCa}_3^{\sim}]}{\mathrm{dt}} = \mathrm{f}\,[\mathrm{TSCa_3}] - \mathrm{g}\,[\mathrm{TSCa}_3^{\sim}] + \mathrm{Z_p}\,[\mathrm{TSCa}_3^{*}] - \mathrm{Y_p}\,[\mathrm{TSCa}_3^{\sim}] \\ \dfrac{\mathrm{d}[\mathrm{TSCa}_3^{*}]}{\mathrm{dt}} = \mathrm{Y_p}\,[\mathrm{TSCa}_3^{\sim}] - \mathrm{Z_p}\,[\mathrm{TSCa}_3^{*}] + \mathrm{Z_r}\,[\mathrm{TS}^{*}]\,[\mathrm{Ca}]_\mathrm{i}^3 - \mathrm{Y_r}\,[\mathrm{TSCa}_3^{*}] \\ \dfrac{\mathrm{d}[\mathrm{TS}^{*}]}{\mathrm{dt}} = \mathrm{Y_r}\,[\mathrm{TSCa}_3^{*}] - \mathrm{Z_r}\,[\mathrm{TS}^{*}]\,[\mathrm{Ca}]_\mathrm{i}^3 - \mathrm{g_d}\,[\mathrm{TS}^{*}] \end{cases} \tag{4.46}$$

where $[\mathrm{Ca}]_\mathrm{i}$ is the intracellular free calcium ions concentration. Since the total troponin system concentration, $[\mathrm{TS}]_\mathrm{t}$, is constant (and equal to 70 μM [143, 144]), we have:

$$[\mathrm{TS}] = [\mathrm{TS}]_\mathrm{t} - [\mathrm{TSCa_3}] - [\mathrm{TSCa}_3^{\sim}] - [\mathrm{TSCa}_3^{*}] - [\mathrm{TS}^{*}] \tag{4.47}$$

The rate constants Y_b, Z_b, Y_p, Z_p, Y_r and Z_r defined by Fig. 55 are constant parameters of the model. On the other hand, f, g and g_d (colored in Eq. (4.46) and in Fig. 55) depend on sarcomere length or CB elongation. Explicitly, we have:

- $f = Y_a \exp(-R(L - L_a)^2)$

  This biochemical rate describes CB attachment in the zone of overlap between thick and thin filaments, where L_a is the optimal overlap length. In other words, the term "f $[TSCa_3]$" can be seen as the effective $TSCa_3$ concentration to which CBs can attach, determined by the zone of overlap between the thick and thin filaments [143]. L_a, R, and Y_a were adjusted to reproduce the length-tension relationship[4] [142].

- $g_d = Y_d \exp(-Y_c(L - L_c))$

  This biochemical rate describes CB irreversible detachment from TS^* to TS. This equation represents the lattice spacing effect on the rate of CB detachment: gd decreases at larger length, where lattice spacing is reduced [144].

- $g = Z_a + F_h\ Y_v\ (1 - e^{-\gamma(h_w - h_{wr})^2})$ where

$$F_h = \begin{cases} 0.1 & \text{if } h_w > h_{wr} \\ 1 & \text{if } h_w < h_{wr} \end{cases} \tag{4.48}$$

  This biochemical rate describes the asymetrical CB detachment from $TSCa_3^{\sim}$ to $TSCa_3$. The term $(h_w - h_{wr})$ describes in fact a contraction velocity dependence since:

$$h_w - h_{wr} = \frac{1}{B_w}\left(\frac{dX}{dt}\right) \tag{4.49}$$

  This asymetrical mathematical description of g_d was proposed in the last version of the model, to get improved simulation of afterloaded contractions [144].

All the equations of the mechanical model of contraction are summarized in Appendix B, along with the parameters values.

4.4.3 *Excitation-contraction coupling*

As discussed in Chapter 3, calcium is a key element of cardiac electrophysiology, and it is also the direct activator of the myofilaments and cell contraction. The coupling between the electrophysiological model and the mechanical contraction model is carried out as follows: the intracellular calcium concentration $[Ca]_i$ obtained from the electrophysiological model is used as an input for the calcium kinetics. A feedback pathway is also implemented. Indeed, the following three "troponin currents":

[4] Described in Chapter 3.

$$I_{trop} = 3\,(\frac{\mathrm{d}[\mathrm{TSCa_3}]}{\mathrm{dt}} + \frac{\mathrm{d}[\mathrm{TSCa_3^{\sim}}]}{\mathrm{dt}} + \frac{\mathrm{d}[\mathrm{TSCa_3^{*}}]}{\mathrm{dt}}) \tag{4.50}$$

extracted from Eq. (4.46) participate in the modulation of $[\mathrm{Ca}]_\mathrm{i}$. That is why we add those currents in Eq. (4.27):

$$\begin{aligned}\frac{\mathrm{d}[\mathrm{Ca}]_\mathrm{i}}{\mathrm{dt}} = & -\frac{1}{1+\frac{K_{\mathrm{buf_i}}\,\mathrm{Buf_i}}{([\mathrm{Ca}]_\mathrm{i}+K_{\mathrm{buf_i}})^2}}\Bigg(C_{m0}\frac{I_{\mathrm{bCa}}+I_{\mathrm{pCa}}-2I_{\mathrm{NaCa}}}{2V_cF} \\ & +\frac{V_{\mathrm{sr}}}{V_c}(I_{\mathrm{leak}}-I_{\mathrm{up}})+I_{\mathrm{xfer}} \\ & -3\,(\frac{\mathrm{d}[\mathrm{TSCa_3}]}{\mathrm{dt}}+\frac{\mathrm{d}[\mathrm{TSCa_3^{\sim}}]}{\mathrm{dt}}+\frac{\mathrm{d}[\mathrm{TSCa_3^{*}}]}{\mathrm{dt}})\Bigg)\end{aligned} \tag{4.51}$$

The factor "3" is present because three calcium ions bind to a TS. With this new equation, the calcium buffering by troponin molecules in the CYTO compartment is explicitely considered. However, troponin buffering was already implicitely taken into account in Eq. (4.23). For this reason, the $\mathrm{Buf_i}$ value have to be reduced, otherwise the troponin buffering would be account for twice. As the total troponin concentration is equal to 70 μM, $\mathrm{Buf_i}$ is thus reduced by 70 μM.

4.4.4 *LDA in the cell model*

The length and CB elongation dependences of the rate constants described above are implemented to reproduce a vast range of experimental results [143, 144]. To illustrate some of these experimental results, the length-tension and the force-pCa curves (defined in Chapter 3), which highlight LDA in cardiac muscle, can be reproduced with the cell model [143]. They are presented in Fig. 56 and Fig. 57. Note that the cooperativity mechanism is also well reproduced (see the sigmoidal shape of the curves in 57), as it was assumed that three calcium ions bind in one step to three adjacent RUs.

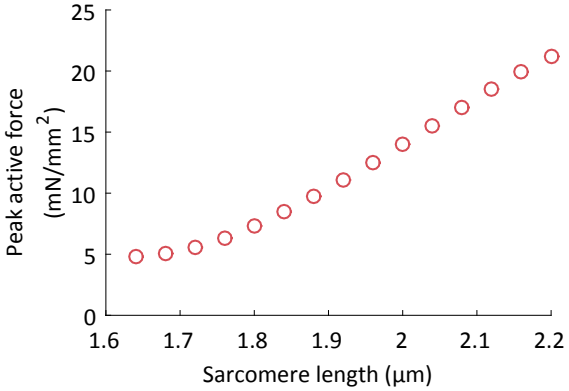

Figure 56: Length-tension relationship obtained with the cell model. Peak active force F_a as a function of sarcomere length ($2 \cdot L_m$) for isometric twitch contractions (L_m fixed).

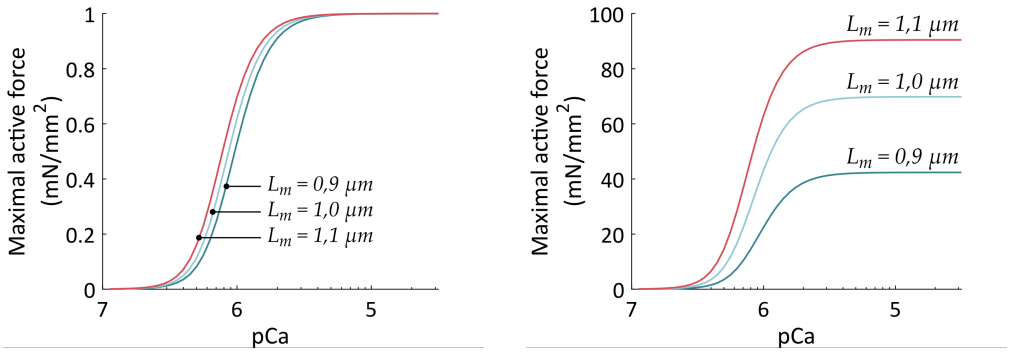

Figure 57: Force-pCa curves obtained with the cell model. (a) Normalized active force $F_a / F_{a,max}$ as a function of pCa. The left shift for higher SL is the distinguishing feature of LDA. (b) Active force (F_a) as a function of pCa. The greater force obtained at full activation (pCa < 5) for higher SLs is due to the myofilament overlap effect.

4.5 VENTRICULAR MODEL

The cell model described above allows computing the action potential, the developed force and the contraction of a single muscle unit. At the ventricular scale, the action potential propagation across cardiac tissues leads to a global contraction of the ventricle. Thus, there is a link between the force produced by the cardiac cells and the global pressure inside ventricular cavities. Likewise, length variations of cardiac cells are related to volume variations of ventricular cavity. Connecting microscopic variables (force and length) to macroscopic variables (pressure and volume) results in a multiscale model of heart contraction.

To connect the force F_m and total length L_m of the half-sarcomere to the pressure and volume of the active chamber, both ventricles are simply considered as thick-walled spheres, as shown in Fig. 58.

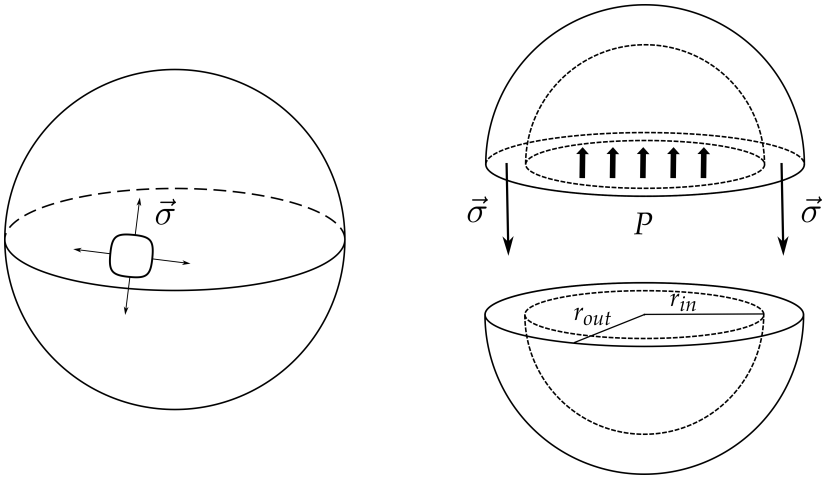

Figure 58: Spherical ventricle model. *Left*: Ventricles are both assimilated to a thick-walled sphere, and σ is the (uniform) wall stress. *Right*: Pressure inside the ventricular chamber, P, is related to σ (see text).

We assume that many contractile units are distributed homogeneously in all directions on the ventricular wall, an assumption already made by others [121, 128, 151–153], so that wall stress can be considered uniform. With this constant wall stress σ, the equilibrium of the two hemispheres of the ventricle (see Fig. 58) gives:

$$P\,\pi {r_{in}}^2 = \sigma\,\pi({r_{out}}^2 - {r_{in}}^2) \tag{4.52}$$

which leads to the following expression for the pressure inside the active chambers:

$$P = \sigma(\frac{{r_{out}}^2}{{r_{in}}^2} - 1) \tag{4.53}$$

Now we have to connect σ to the force produced by the cardiac cells. We follow the approach of Shim *et al.* [128] and assume that N half-sarcomeres of variable length L_m are aligned along a circle of variable radius R inside the ventricular wall, as illustrated in Fig. 59. We naturally have:

$$N \cdot L_m = 2\pi R \tag{4.54}$$

During ventricular diastole and systole, L_m vary between a maximal ($L_{m,max}$) and a minimal ($L_{m,min}$) value. The (constant) number of contractile units N was carefully chosen so that $L_{m,min}$ and $L_{m,max}$ correspond to physiological relevant values. To do so, we write the relationships between length, radius and volume for the minimal (systolic) V_{min} and maximal (diastolic) V_{max} ventricular blood volumes (V_r is defined in Fig. 59):

$$N \cdot L_{m,min} = 2\pi R_{min} \tag{4.55}$$
$$N \cdot L_{m,max} = 2\pi R_{max} \tag{4.56}$$
$$\frac{4}{3}\pi {R_{min}}^3 = V_{min} + V_r \tag{4.57}$$
$$\frac{4}{3}\pi {R_{max}}^3 = V_{max} + V_r \tag{4.58}$$

Taking the difference between Eq. (4.58) and Eq. (4.57) gives:

$$\begin{aligned} \frac{4}{3}\pi({R_{max}}^3 - {R_{min}}^3) &= SV \\ \iff \frac{4}{3}\pi {R_{min}}^3(\frac{{R_{max}}^3}{{R_{min}}^3} - 1) &= SV \\ \iff R_{min} &= \sqrt[3]{\frac{SV}{\frac{4}{3}\pi(\frac{L_{max}^3}{L_{min}^3} - 1)}} \end{aligned} \tag{4.59}$$

where SV is the stroke volume ($V_{max} - V_{min}$). To get a numerical value for R_{min}, we see that SV, L_{min}, and L_{max} must be known parameters. As explained earlier in this work, length-dependent properties at the cellular scale are connected

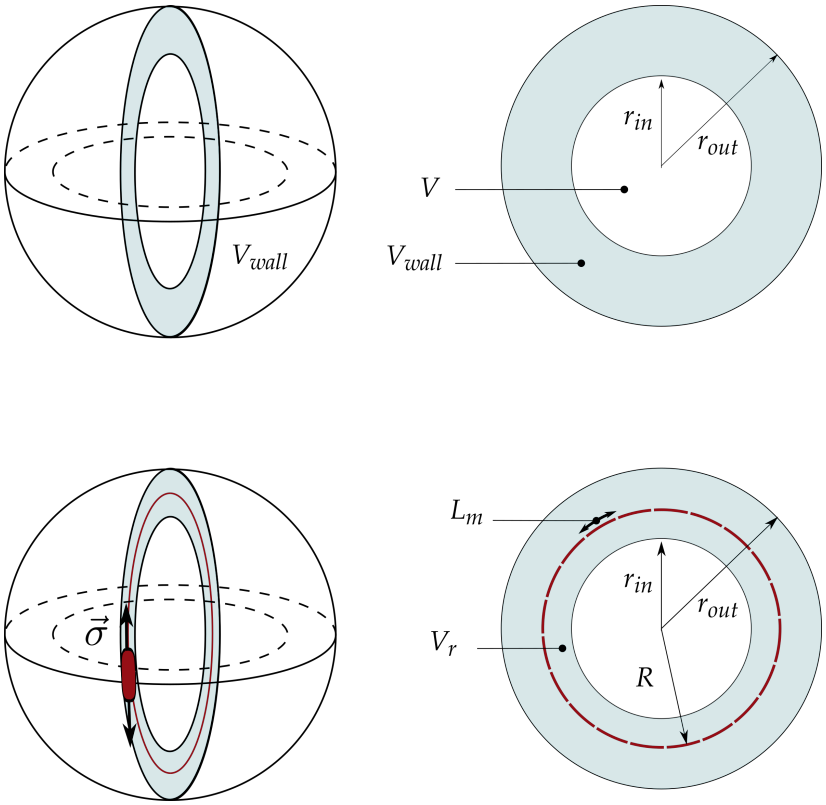

Figure 59: Wall stress σ and its relation to the half-sarcomere units. Top: thick-walled sphere model. V_{wall} is the (incompressible) volume of the ventricular wall included between r_{in} and r_{out}. It corresponds to the (constant) volume occupied by the cardiac muscle. V corresponds to the volume of the chamber, which is actually the ventricular blood volume. This volume varies during diastole and systole, as well as r_{in} and r_{out}. Bottom: A circle of N half-sarcomeres of length L_m is located inside the ventricular wall, at a certain radius R (red line) to be determined (see text). The force produced by this series arrangement of half-sarcomeres is responsible for the wall stress σ. The muscle volume included between r_{in} and R is the reference volume V_r.

to macroscopic properties of the heart. Thus it was essential to get the correct interval of variation for L_m in our multiscale model. We choose $L_{min} = 0.93$ μm and $L_{max} = 1.08$ μm, both values being physiologically relevant extremes for half-sarcomere lengths *in vivo* [154, 155]. We also imposed $SV = 60$ ml, a normal hemodynamic value [156]. Once a numerical value for R_{min} is obtained, Eqs. (4.55) and (4.57) allow the determination of N and V_r, which are constant parameters of the model.

Those N half-sarcomeres arranged in series all produce the same force, F, obtained from the sarcometric model described in the previous section. As explained earlier, this is a normalized muscle force over a reference cross-sectionnal area:

$$F = \frac{F_m}{\text{area}_\text{r}} \tag{4.60}$$

On the other hand, the wall stress σ is expressed as a force per unit area:

$$\sigma = \frac{F_m}{\text{area}} \tag{4.61}$$

Assuming again that muscle units keep constant volume, we also have:

$$L_r \cdot \text{area}_\text{r} = L_m \cdot \text{area} \tag{4.62}$$

where L_r is the half-sarcomere length at the reference area A_r.

From Eq. (4.60) - (4.62), we get:

$$\sigma = F \frac{L_m}{L_r} \tag{4.63}$$

Substituting Eq. (4.63) into Eq. (4.53), we get:

$$P = 7,5\, F \frac{L_m}{L_r} (\frac{{r_{out}}^2}{{r_{in}}^2} - 1) \tag{4.64}$$

The $7,5$ factor stands for the unit changes in Eq. (4.64) (pressure is expressed in mmHg while the normalized force F is expressed in mN/mm^2).

We finally obtain the pressure-force relationship of our multiscale model by adding a passive pressure term that accounts globally for the elastic properties of the tissue surrounding the ventricle [118]:

$$P = 7,5\, F \frac{L_m}{L_r} (\frac{{r_{out}}^2}{{r_{in}}^2} - 1) + \lambda (V - V_0)^3 \tag{4.65}$$

where λ is related to the stiffness and V_0 is the unstressed volume [118].

To reduce computationnal cost, both ventricles in our heart model are assumed to have the same electrophysiology even if the mechanical behavior can be different. This is a plausible assumption, as both ventricles are activated synchronously (see Fig. 49) and contract evenly [157]. On the other hand, as explained in Chapter 2, each ventricle pumps blood through a different circulation: one through the higher pressurized systemic circulation, the other through the lower pressurized pulmonary circulation. This is why, in our model, both ventricles share the same "activation" process, but not the same contractile process. The troponin currents from Eq. (4.50) that were added in Eq. (4.51) depend however on the troponin concentrations from the mechanical model. They are averaged (and approximated) as follows:

$$\begin{aligned} I_{trop} = \frac{1}{2}\, 3\, (\frac{\text{d}[\text{TSCa}_3]}{\text{dt}} + \frac{\text{d}[\text{TSCa}_3^{\sim}]}{\text{dt}} + \frac{\text{d}[\text{TSCa}_3^{*}]}{\text{dt}})_{\text{LV}} \\ + \frac{1}{2}\, 3\, (\frac{\text{d}[\text{TSCa}_3]}{\text{dt}} + \frac{\text{d}[\text{TSCa}_3^{\sim}]}{\text{dt}} + \frac{\text{d}[\text{TSCa}_3^{*}]}{\text{dt}})_{\text{RV}} \end{aligned} \tag{4.66}$$

where the indices "LV" and "RV" refer respectively to the left and right ventricles.

4.6 MODEL PARAMETERS

The multiscale model presented above depends on many parameters, which can be split into microscopic (or cellular) parameters and macroscopic (or hemodynamic) parameters.

4.6.1 *Cellular parameters*

The complete set of equations and parameters used in the cell model can be found in Appendix A and Appendix B. Most of them come from the original articles [141, 144], but some of them had to be modified to improve the multiscale model outputs or for other reasons. These are listed below and summarized in Table 1.

Calcium buffer and troponin currents

As explained previously, troponin buffering in the CYTO compartment is taken into account with the troponin currents (Eq. (4.50)). For this reason, total CYTO buffer concentration, (Buf_i in Eq. (4.23)) is reduced from 200 μM (original value from [141]) to 130 μM, since total troponin concentration is 70 μM [142].

Calcium release from the SR

The $[\text{Ca}]_\text{i}$ increase obtained with the ten Tusscher and Panfilov model [141] is rather sharp and leads to a slight increase of the elongation h_w (from the mechanical model, see Eq. (4.36)) at the beginning of sarcomere contraction. This behavior does not impact significantly the global hemodynamic results, but a smoother increase of $[\text{Ca}]_\text{i}$ would ensure a more physiological behavior of the equivalent crossbridge elongation h_w. To this end, we follow the approach of Lascano *et al.* [158] who modified the equations governing calcium liberation by the sarcoplasmic reticulum (CICR). These equations are detailed in Appendix A.

Sliding velocity of the equivalent crossbridge

The sliding velocities of the two equivalent crossbridges along the thin filament is characterized by the parameters B_w and B_p from Eqs. (4.38) and (4.37). These parameters have to be increased by a factor of 3.5. Otherwise, the produced force is not able to increase fast enough compared to $[\text{Ca}]_\text{i}$ increase during an AP. It should be stated that the parameter governing the sliding dynamics of the equivalent crossbridge cannot be unequivocally connected to the underlying molecular mechanisms of filament sliding. Several values have been proposed [128, 142–144]. In [144], different values are given to B_p and B_w, and those values are artificially increased (by a factor 3,5) to simulate the inotropic effect of isoproterenol and the following increase in CB cycling rate. In our case, increase in sliding velocity can be seen as the price to pay in order to get physiological values for the developed force and the resulting ventricular pressure. A similar approach was followed by Land *et al.* [159] when inserting their cellular model of contraction inside a whole organ model, although their models are different from ours. They "manually" increased the rate of cross-bridge cycling to obtain

Parameter	Original value	Modified value	Units
Buf_c	200	130	μM
B_p	0,5	1,75	ms^{-1}
B_w	0,35	1,225	ms^{-1}
K_e	$10,5 \cdot 10^4$	$3,15 \cdot 10^4$	$\text{mN}/\text{mm}^2/\mu\text{m}^5$
L_e	10	3,00	$\text{mN}/\text{mm}^2/\mu\text{m}$

Table 1: Cellular parameter adjustment.

physiological ejection fraction[5]. Eventually, note that the B_p and B_w adjusted values remain close (in term of order of magnitude) to the initial values from [144].

Passive force

Finally, the parameters characterizing the passive force (K_e and L_e from Eq.(4.42)) in the mechanical model have to be modified. A more detailed explanation is provided in the next section, since this adjustement is related to the pressure development in the ventricular model.

4.6.2 *Hemodynamic parameters*

The CVS model is schematized in Fig. 60. Thirteen hemodynamic parameters have to be identified, and they are listed in Table 2: the four valves resistances, the two circulation resistances, the four passive chambers compliances, wall volume of both ventricles, and stressed blood volume. The parameters are identified using the *fminsearch* algorithm from MATLAB (The MathWorks, Natick, MA, USA) in order to minimize an objective function defined as the absolute relative error between a chosen set of reference variables and their corresponding calculated values. Since we do not have any experimental data, the value for the reference data were chosen in order to correspond to standard healthy values [1, 156, 160].

Valve resistances are practically difficult to identify, and they are generally excluded from the identification procedure [53, 161, 162]. Since we do not have any experimental data, we cannot determine their value *a priori*, so we perform a first identification procedure with the thirteen hemodynamic parameters from Fig. 60 and use the reference data from Table 3 to compute the objective function to minimize. This set of thirteen reference variables includes: the stroke volume, the maximal left and right ventricular pressures, the minimal left and right ventricular volumes, the maximal value and amplitude of the aortic, pulmonary artery, pulmonary vein and vena cava pressuress. Then we fix the obtained valve resistance values, and we perform a second identification procedure with the remaining nine parameters and the reference data from Table 4. This set of reference variables includes: the stroke volume, the left and right mean ventricular pressures, the minimal left and right ventricular volumes, the mean aortic and

[5] The ejection fraction is the stroke volume divided by the end-diastolic volume.

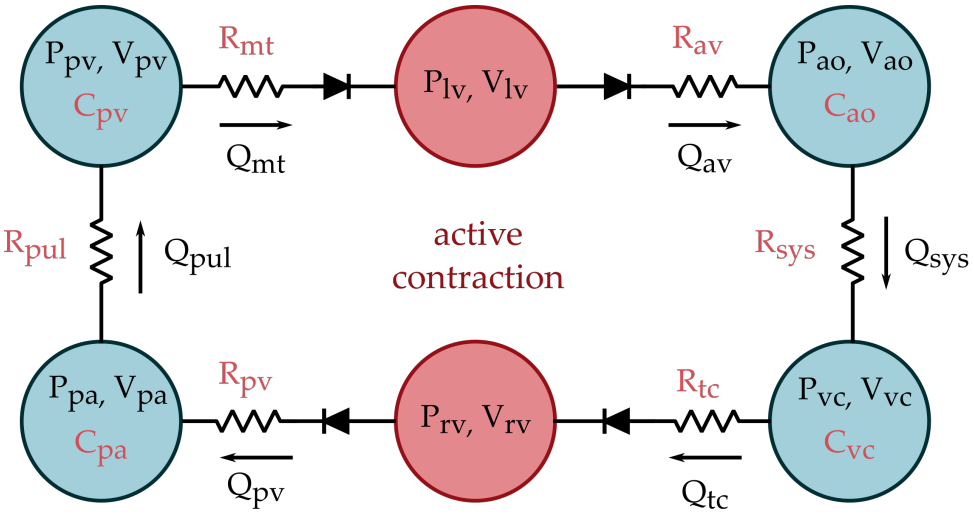

Figure 60: Hemodynamic parameters of the six-chamber model of the CVS. Twelve adjusted parameters are colored in red. Total stressed blood volume (SBV), the thirteenth parameter, is given by: $V_{lv} + V_{ao} + V_{vc} + V_{rv} + V_{pa} + V_{pv}$. Passive chambers (blue) are characterized by their constant compliance while active chambers (red) contraction is described at the cellular scale.

pulmonary artery pressures, and the amplitude of vena cava and pulmonary pressures.

With the set of cellular parameters described above, the model always produces high end-diastolic pressures and low end-systolic pressures compared to physiological values. This difficulty originates from the too simple geometrical description of the ventricles, which are here considered as spheres. In a real heart, bundles of cardiac fibers are actually wrapped around the ventricular cavity so that the ventricle is also twisted in a very complex way during contraction [108, 155, 163]. Of course the spherical model of the ventricles presented above cannot take into account this aspect of contraction and an adaptation of the values of some parameters was necessary to compensate for the simplicity of the model.

From Eq. (4.53), it is easy to understand that systolic pressure, which is related to the maximum active force generated in the sarcomeres, can be increased by increasing the ventricular wall volume V_{wall}. However, since the diastolic pressure, which is related to the passive force in the myocytes, also increases with the wall thickness, we had to reduce the intensity of the sarcomere passive force by 70 % in order to recover physiological diastolic pressures. Note that Shim *et al.* [128] also modified the passive force expression in order to preserve the ventricular ejection fraction. In summary, the price to pay for the spherical model of the ventricles is a reduction factor to apply to the cellular parameter measuring the passive force of the sarcomere (see Table 1).

The complete set of equations and parameters used in the hemodynamic model can be found in Appendix C.

Parameter	Value	Units
SBV	940.86	ml
R_{sys}	1.38	10^3 mmHg $\cdot$ ms/ml
R_{pul}	109,57	mmHg $\cdot$ ms/ml
R_{mt}	22.09	mmHg $\cdot$ ms/ml
R_{tc}	11.56	mmHg $\cdot$ ms/ml
R_{av}	47.96	mmHg $\cdot$ ms/ml
R_{pv}	3.51	mmHg $\cdot$ ms/ml
C_{ao}	0.9550	mmHg/ml
C_{vc}	79.10	mmHg/ml
C_{pa}	2.43	mmHg/ml
C_{pv}	23.34	mmHg/ml
V_{lvw}	334.86	ml
V_{rvw}	48.31	ml

Table 2: Identified parameters.

	Standard value	Units
Stroke volume	60	ml
Maximal LV pressure	120	mmHg
Maximal RV pressure	21,5	mmHg
Maximal aortic pressure	113	mmHg
Amplitude of aortic pressure	35	mmHg
Maximal pulmonary artery pressure	21	mmHg
Amplitude of pulmonary artery pressure	13	mmHg
Maximal pulmonary vein pressure	7,5	mmHg
Amplitude of pulmonary vein pressure	2	mmHg
Maximal vena cava pressure	7	mmHg
Amplitude of vena cava pressure	1,5	mmHg
Minimal LV volume	60	ml
Minimal RV volume	60	ml

Table 3: Standard values for the thirteen parameter identification procedure.

	Standard value	Units
Stroke volume	60	ml
Mean LV pressure	59	mmHg
Mean RV pressure	12	mmHg
Mean aortic pressure	108	mmHg
Mean pulmonary artery pressure	19	mmHg
Amplitude of pulmonary vein pressure	2	mmHg
Amplitude of vena cava pressure	0.5	mmHg
Minimal LV volume	60	ml
Minimal RV volume	60	ml

Table 4: Standard values for the nine parameter identification procedure.

4.7 SIMULATIONS

In this section, we will present some results obtained with our CVS model, that agree well with experimental observations and thus validate our modeling approach. The baseline (healthy) behavior is correctly reproduced, as well as a heart failure (HF) situation. Besides, our model correctly portrays the typical shift in the ventricular PV loops following a variation in loading conditions. These results are detailed below.

4.7.1 *Baseline*

Results from a simulation of the CVS model are shown in Fig. 61-63. Heart beat is fixed at 75 bpm, and only one heartbeat is depicted. This simulation is a "converged" simulation: several beats were computed in a row to achieve SV equilibrium between both ventricles.

Fig. 61 illustrates the excitation-contraction coupling: following the AP generation, there is a raise in intracellular calcium, which promotes sarcomere force production. The time of peak force is delayed compared to the time of peak intracellular calcium, as observed *in vitro* [60].

Fig. 62a and 62b show the left and right pressures evolution within one heartbeat. LV (resp. RV) pressures increase during filling. Once it exceeds pulmonary vein (vena cava) pressure, mitral (tricuspid) valve closes and isovolumic contraction begins. When it exceeds aortic (pulmonary artery) pressure, aortic (pulmonary) valve opens and ejection starts. This phase is followed by isovolumic relaxation, which starts when LV (RV) pressure falls under aortic (pulmonary artery) pressure, and aortic (pulmonary) valve closes. A new filling phase starts once LV pressure is lower than pulmonary vein (vena cava) pressure and mitral (tricuspid) valve opens again. RV pressure is significantly lower than LV pressure, as the typical pressure levels in the pulmonary circulation are lower than in the systemic circulation [1, 3].

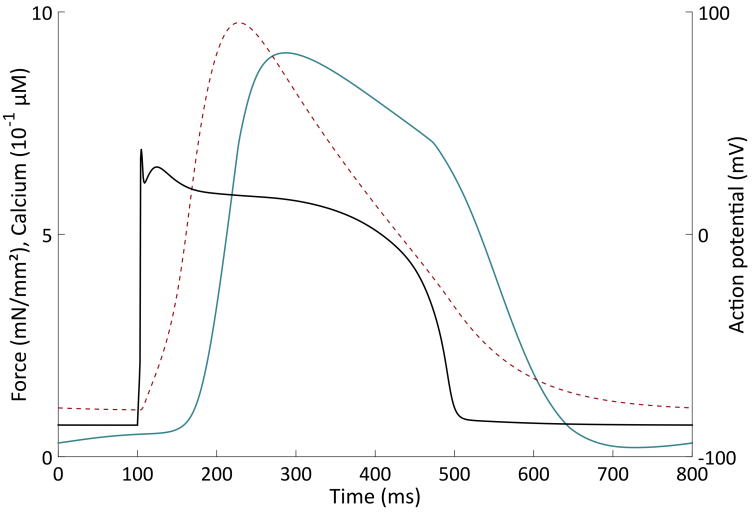

Figure 61: Excitation-contraction coupling. Within one AP (black), intracellular calcium concentation increases (dotted red). This promotes sarcomere contraction and force developement (blue). The time of peak force is delayed compared to the time of peak intracellular calcium. Heart rate is fixed at 75 bpm, so the period of a single heartbeat is 800 ms.

Fig. 62c and 62d show the flows evolution within one heartbeat. Mitral (tricuspid) flow is non-zero during the filling phase, while aortic (pulmonary vein) flow is non-zero during the ejection phase. Systemic (pulmonary) flow is never zero but fluctuates due to the pumping action of LV (RV).

Fig. 63a shows LV and RV pressure-volume loops, where the four phases of the cardiac cycle are easily identifiable: filling, isovolumic contraction, ejection and isovolumic relaxation. SV equilibrium is easily observable.

Fig. 63b shows the LV half-sarcomere length evolution and the LV volume changes (the equivalent RV curves, not represented, are similar). The minimal (systolic) and maximal (diastolic) corresponding values are physiologically relevant.

4.7.2 *Heart failure*

Heart failure (HF) occurs when the heart is not able to provide sufficient cardiac output to meet the metabolic demand [1, 32]. This depressed contractile function of the heart originates at the cellular scale, where changes in cellular signal transduction mechanisms and excitation–contraction coupling impair inotropy [32, 164–166]. The cellular basis for HF are still not fully understood, but in most HF model studies, the following observations are consistently made:

- A reduction in twitch force amplitude,
- A reduction in intracellular calcium amplitude and rate of relaxation,
- A prolongation of the AP duration.

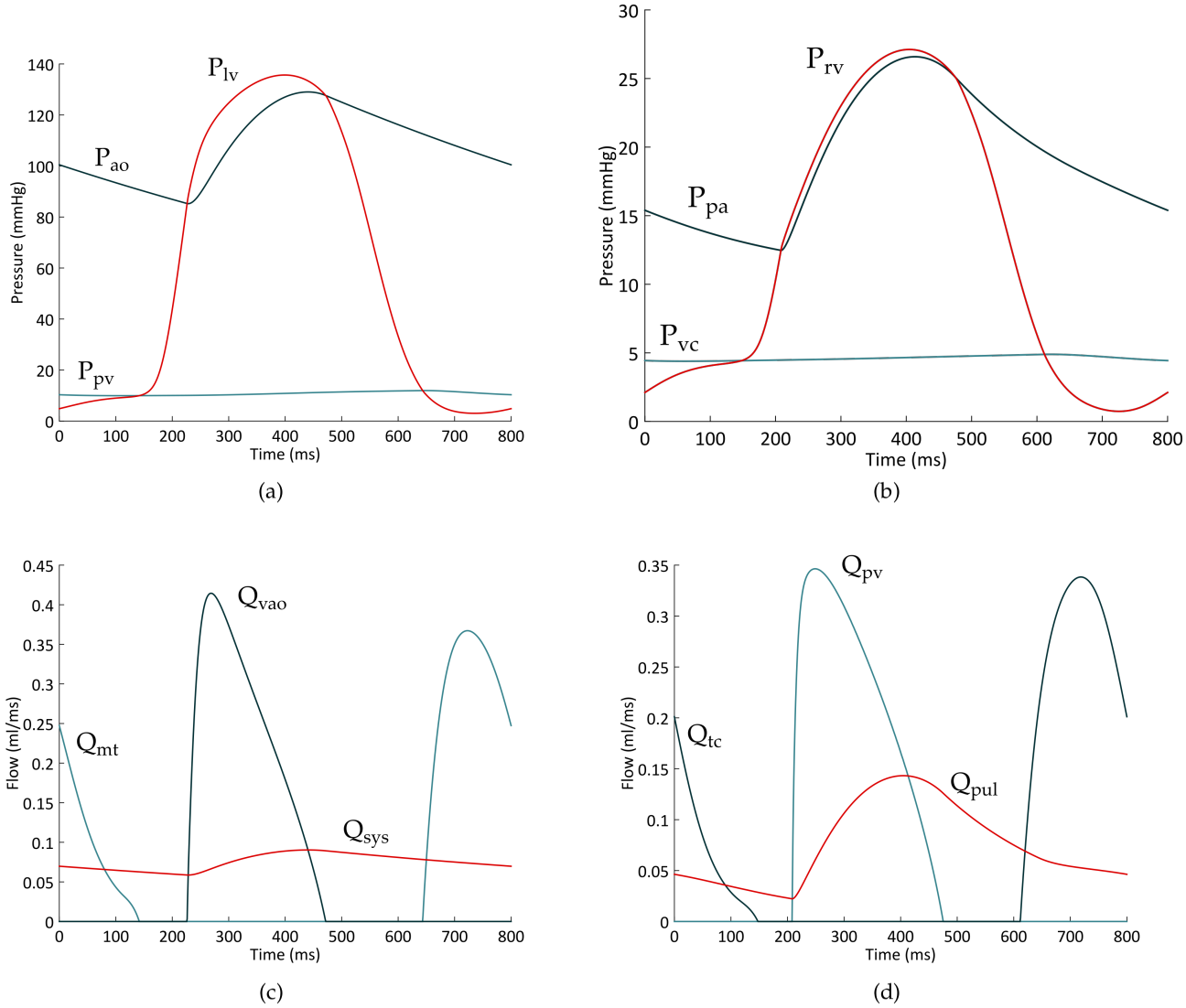

Figure 62: Pressures evolution for the left (a) and right (b) side of the circulatory model. Flows evolution for the left (c) and right (d) side of the circulatory model.

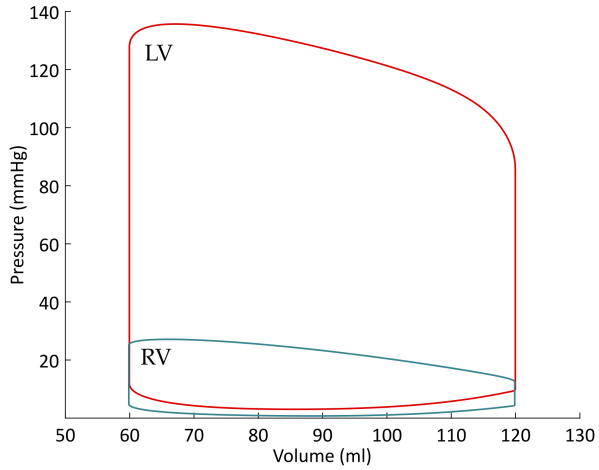

(a)

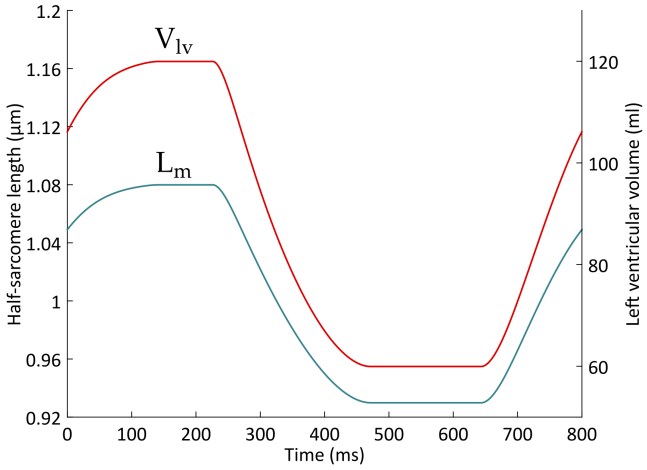

(b)

Figure 63: Pressure-volume loops (a), half-sarcomere length and left ventricular volume (b) during one heartbeat. Stroke volumes are identical for the left and right ventricle, but the right ventricle generates less pressure, as the pressure levels in the pulmonary circulation are lower than in the systemic circulation. LV half-sarcomere length variations belong to a physiological interval, and they are linked to ventricular volume variations during the cardiac cycle.

Some ionic currents are altered in HF, especially the potassium currents I_{to}, I_{K1} and I_{Ks}, which are reduced in HF conditions. Increased activity of the Na/Ca exchanger ($I_{\text{Na/Ca}}$) and a reduced calcium sequestration capacity by the SR are also commonly observed [32, 164–166].

Following these experimental observations, HF can be implemented in our model by decreasing G_{to}, G_{K1} and G_{Ks} by 20 %, increasing k_{NaCa} by 20 % and decreasing V_{up} by 10 %, with respect to their original values from Appendix A [116]. Our multiscale model is then able to connect these cellular altered properties to the hemodynamics variables, as shown in Fig. 64.

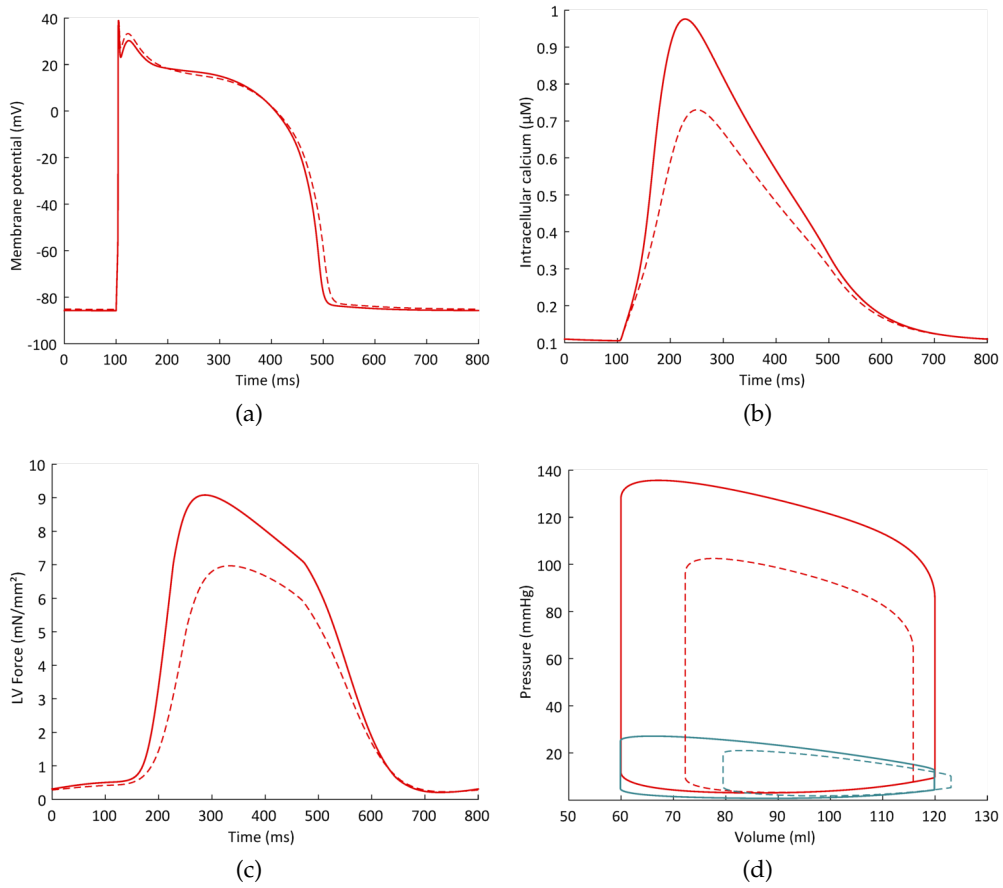

Figure 64: Ventricular failure (dashed line) versus normal ventricle (full line). From (a) Action potential. (b) Intracellular calcium. (c) LV normalized force. (d) LV (red) and RV (blue) PV loops. Prolongation of AP duration, reduced calcium and force amplitudes are correctly reproduced. The resulting PV loops present the depressed contractile function typical of HF.

4.7.3 *Load variations*

The results presented in the previous two sections are stabilized behaviors, obtained after several beats, during which LV and RV stroke volumes equilibrate. Transient behaviors can also be observed, following preload or afterload variations, for instance. Such alterations during the cardiac cycle may happen for numerous reasons: a change in the venous return, a change in the arterial pressure, a pathological condition, *etc*.

The inflation of a Fogarty balloon inserted in the vena cava is a current way of reducing RV preload experimentally. To mimic the inflation of this balloon, we increase the tricuspid valve resistance (R_{tc} from Fig. 60) tenfold, thus allowing less blood to enter the right ventricle. The consequences on the pressure-volume loops on both ventricles are presented in Fig. 65, and are consistent with experimental observations. It is worth emphasizing that the upper left corners of the PV-loops, which constitute the ESPVR, are not exactly located on a straight line, as often postulated when time-varying elastance models of contraction are used. This question will be discussed in further details in Chapter 5.

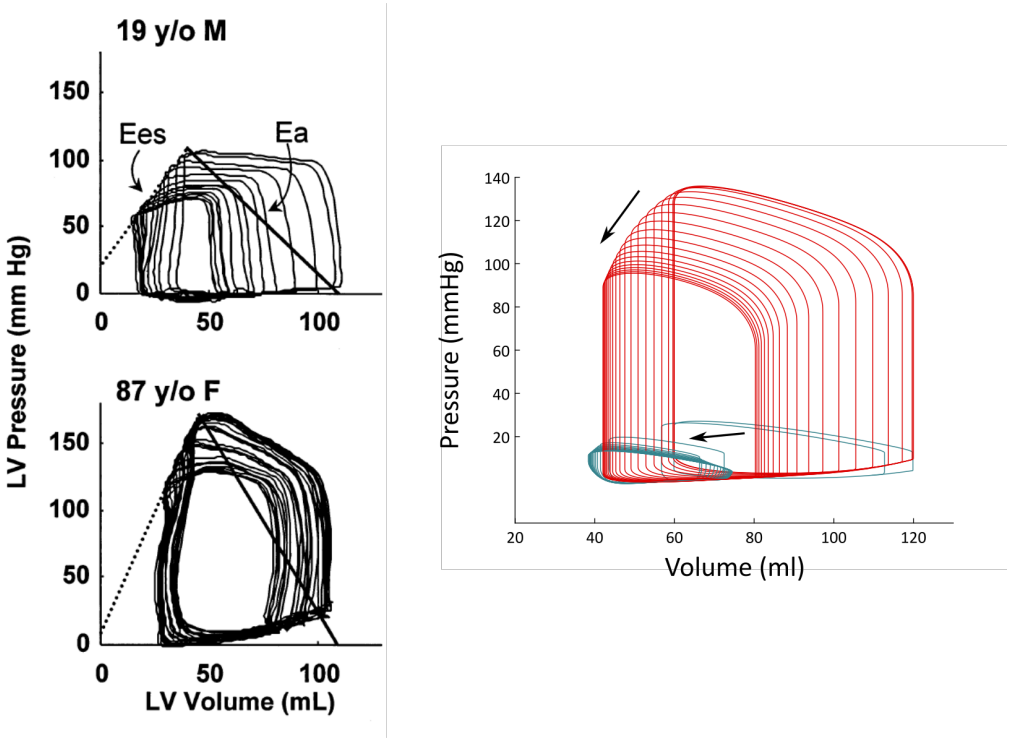

Figure 65: Left: Experimental LV PV loops during a RV preload reduction maneuver, for a young (top) and elder (bottom) patient [167]. Right: Simulated LV (red) and RV (blue) PV loops following a tenfold increase in R_{tc}.

4.8 DISCUSSION

4.8.1 *CVS model*

The 6-chamber lumped-parameter (LP) model is undoubtely a very simple approach to describe the complexity of the whole human CVS, and it is built under many assumptions, as explained in the previous sections. In order to depict the systemic and pulmonary circulations, with their respective venous and arterial components, the minimal requirement is a 6-chamber model: the left and right cardiac pumps, the aorta and pulmonary artery, the vena cava and the pulmonary vein. Although this is a very simple representation of a much more complex circulatory system, the main idea is to obtain realistic ventricular filling and ventricular-vascular coupling [105]. As demonstrated in Fig 62-63, this model is able to capture the fundamental dynamics of the CVS. Indeed, LP models are able to reproduce and capture trends in the CVS dynamics, which make them relevant tools for assisting health professionals in their diagnosis and therapy selection [126, 168]. In the litterature, other models of cardiac contraction exist, that are not based on the varying-elastance model, and are also coupled with LP models of the whole CVS [117, 169], or parts of the CVS [159, 170, 171].

Note that the atria are not present in this model. Thus ventricular filling is only achieved through a passive filling mechanism, while in reality atrial contraction accounts for about 20 % of ventricular filling [3]. Since, in our model, ventricular filling occurs through the upstream valves, we can expect the identi-

fied valve resistances to be lower than in reality. But this still leads to an accurate reproduction of the ventricular filling phase (see Fig. 62). Ventricular interaction is not modeled in this work. However, ventricles share a common wall, the septum (Fig. 3), and they are enclosed in the rigid pericardium. Thus volume variations in one ventricle actually exert influence on the other, a phenomenon not addressed in this study.

4.8.2 *Ventricular model*

The time-varying elastance model, commonly used in combination with lumped-parameter models of the CVS, was not considered in this study. The aim here is to link the microscopic properties of cardiac tissue to the macroscopic behaviors observed at the organ scale. As explained earlier, the time-varying elastance model fails to offer this framework. The heart being a multiscale system by itself [28, 29], multiscale models are more appropriate to study the influence of a sub-system on the whole system behavior [105]. Our ventricular contraction model is quite simple compared to 3D modeling approaches that also rely on cardiac fibers mechanics to describe global ventricular contraction [112, 169, 171–174]. The zero-dimension (0D) approaches to model the ventricle that we adopt, which only require ordinary differential equations and drastically reduce computational cost, are however also used [117, 118, 120–123, 128, 175]. As Caruel *et al.* [122] demonstrated in their study, such "0D" models of a cardiac chamber are still relevant, as they are "meant to provide a straigthforward translation of local properties to the organ level without incorporating anatonomical details". It is worth mentionning that cardiac 3D models, given their complexity, require elaborate calibration and validation [27, 122]. Compared to the complex 3D ventricular modeling, based on finite-element methods, our 0D ventricular model thus provides computational efficiency, as it allows for the processing of many heartbeats in a row with a very small computational cost (one beat computed in a few seconds). This means that we are able to track instantaneous behaviors following a perturbation in the CVS dynamics, but also that we can observe the model reaching a new steady-state following the perturbation.

Particular attention was paid to the sarcomere contraction model and length-dependent properties implementation. Many cardiac sarcomere contraction models have been proposed [29, and references therein]. Contrary to cardiac electrophysiological modeling, "there is a lack of consensus on the best modelling framework to simulate the biophysics of the sarcomere" [29]. Among other things, model implementation is limited by the incomplete understanding of cardiac cell physiology, such as the molecular basis for LDA. This leads to a partially phenomenological description of sarcomere contraction. We chose the model developed by Negroni and Lascano because it is able to reproduce a wide range of cellular mechanical experiments, with the same set of parameters. In particular, length-tension relationship and force-pCa curves are well reproduced (see Fig. 56 and 57). Other results, such as shortening deactivation or force-velocity relationship, are also portrayed with this model. It is worth mentionning that Negroni and Lascano used the first version of their model [142] as a basis for a simple "0D" ventricle model [118] that could accurately depict the positive ef-

fect of ejection observed experimentally by Hunter *et al.* [98] and discussed in Chapter 3. They also built a similar "0D" ventricle model with the most recent version of their contraction model to study cardiac contractile dysfunction at different scales, and their results were in good agreement with experimental data [119]. As shown in section 4.7, a couple of situations (healthy and HF case, load variations) are well reproduced with our model, which validates our modeling approach.

In Chapter 5, an analysis of cardiac contractility indices is conducted. Since contractility is a cellular feature that translates at the heart scale, our model is able to link the cellular contractile state to CVS outputs. In Chapter 6, an analysis of the FS mechanism is addressed with our model, in order to determine the relative contribution of LDA and other factors to the CVS response to preload increase.

5

COMPARISON OF CARDIAC CONTRACTILITY INDICES

Contractility is a measure of cardiac pump function, of its inherent ability to generate force [3, 22, 176]. At the ventricular scale, an increase in contractility leads to an increase in the amount of ejected blood, thus an increase in SV (or CO, if HR is kept constant). This cardiac property originates at the cellular scale. As explained in Chapter 3, contractility (or inotropy) is mainly regulated via the cellular calcium handling mechanisms [1]. In this chapter, we focus on the ventricular contractile state, that we will unequivocally refer to as *inotropy* from now on.

In clinics, it is essential to evaluate the functional ability of the heart, its intrinsic contractile function. For instance, if a patient with a valvular disease presents an abnormally low CO, clinicians have to determine if this is because inotropy is reduced, or because of the hemodynamic conditions, in this case an outflow obstruction due to a valvular disease. Thus there is a need for contractility indices (CIs). These clinical indices of inotropy must be assessable in clinics and deeply correlated with the inotropic state of the ventricles, but independent of preload and afterload conditions. Several CIs have been proposed:

- E_{ES}, the slope of the ESPVR curve, is still considered as the gold standard for inotropy assessment [2, 51, 129, 177]. It was however shown to be load-dependent [99, 129, 135], and the ESPVR is not always linear in shape [52, 120, 129, 132–134]. We also showed the non linearity of the ESPVR in Fig. 65.
- The peak first derivative of left ventricular pressure, $(dP_{lv}/dt)_{max}$, is another proposed CI with a relatively weak load-dependence [2, 51, 129, 178].
- The peak first derivative of arterial pressure, $(dP_a/dt)_{max}$, was also proposed, as it is easier to assess the arterial pressure than the ventricular pressure in clinics [177].
- In case of catheterization of the patient, the time T_d from onset of contraction to $(dP_{lv}/dt)_{max}$ was proposed as a reliable CI [179].

In this chapter, we simulate ventricular inotropy changes and hemodynamical load variations. Then we evaluate the load and inotropy sensitivity of the four CIs proposed above.

5.1 METHODS FOR INOTROPY AND LOAD VARIATIONS

An ideal contractility index would display little load dependence in the physiologic range, but would also show a sensitive response to inotropic variations [178]. With our model, we can generate both inotropy and load variations, as described below, in order to assess the inotropy-dependence as well as the load-dependence of the proposed CIs.

5.1.1 *Inotropy variations*

Since our multiscale model of the CVS has an explicit cellular description, it is easy to reproduce different inotropic states. For instance, during beta-adrenergic stimulation, which is an extrinsic control of cardiac cell activation that results in increased inotropy, SR Ca release and uptake is increased [1]. In our model, we simply increased (reduced) I_{rel} and I_{up} (see Fig. 52) amplitude to obtain increased (depressed) inotropic states. More precisely, we increased or decreased V_{rel} and V_{up} from the mathematical expressions in Appendix A. Three increased (depressed) inotropic states were obtained by a 10, 20 and 30 % increase (decrease) in V_{rel} and V_{up}.

5.1.2 *Load variations*

In order to evaluate the possible load-dependency of the CIs, six load variations are induced by changing some hemodynamic parameters: R_{sys} increased and decreased by 20 %, all the hemodynamic resistances increased and decreased by 10 %, all the elastances of the passive chambers increased and decreased by 10 %.

5.1.3 E_{ES} *assessment*

After a change in load or inotropy, the end-systolic elastance cannot be calculated with the last PV loop only, since a linear regression between at least two end-systolic points is required to calculate E_{ES}. Once the system has reached a stabilized behavior, a Fogarty protocol (described in Chapter 4) is induced in order to get more than one PV loop. The end-systolic points are defined as the points where ventricular pressure becomes inferior to aortic pressure. Indeed, when the condition $P_{lv} < P_{ao}$ is reached, the aortic valve closes, which signifies the end of systole. The ESPVR is defined with these end-diastolic points and a linear regression is performed to assess E_{ES}.

5.2 RESULTS

Intracellular Ca, normalized LV force and LV PV loops for the seven different inotropic states are shown in Fig. 66. Each load variation protocol is performed for each of the seven inotropic states. As an example, LV PV loops obtained after a 20 % R_{sys} increase in the baseline inotropic state are shown in Fig. 67. Simulations end when the system reaches a new steady-state, where LV and RV SV are identical again.

For each load variation, $(\mathrm{dP_{lv}/dt})_{\max}$ and $(\mathrm{dP_a/dt})_{\max}$ are calculated over the last PV loop, once the system has reached its stabilized behavior. In our model, arterial pressure is assimilated with the aorta pressure, so $(\mathrm{dP_a/dt})_{\max}$ is rather noted $(\mathrm{dP_{ao}/dt})_{\max}$. T_d, being defined as the time from onset of contraction to time of $(\mathrm{dP_{lv}/dt})_{\max}$, is also calculated over the last PV loop. The time of onset of contraction is taken as the time of mitral valve closure, once the filling phase ends and the isovolumic contraction starts.

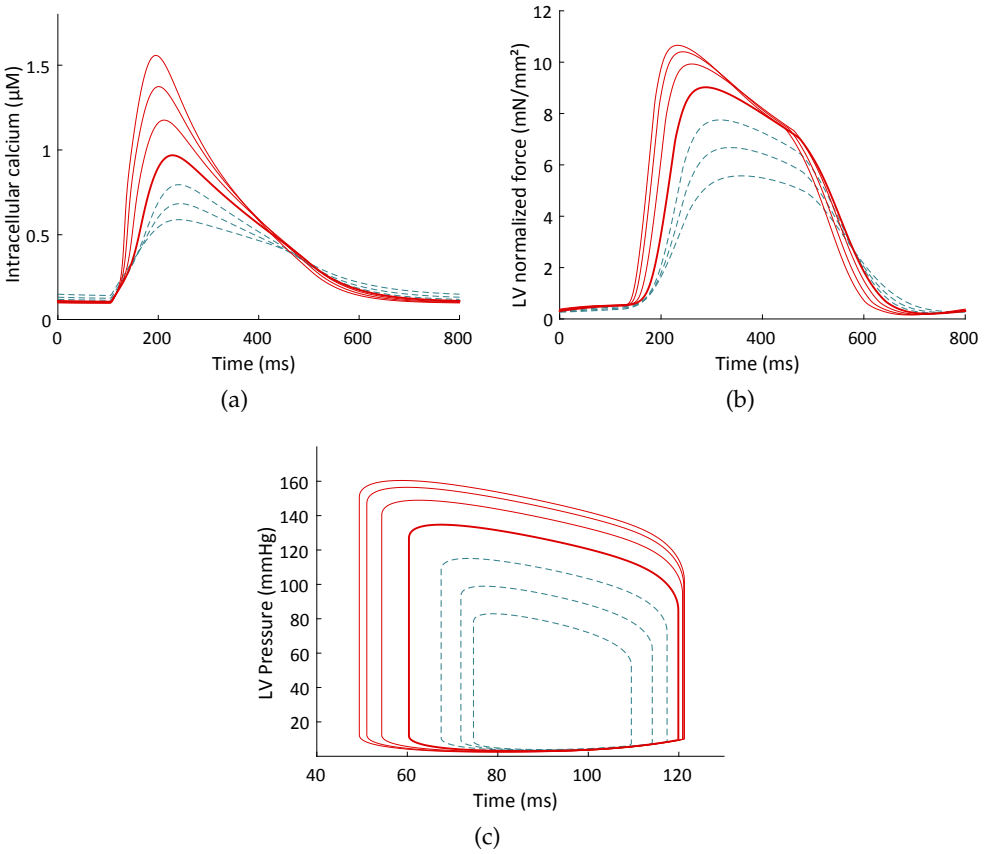

Figure 66: Simulations of various inotropic states. Intracellular calcium (a), LV normalized force (b) and LV PV loop (c) corresponding to seven different inotropic states. Bold red line: baseline case. Normal red lines: increase in inotropy, corresponding to 10, 20 and 30 % increase in V_{rel} and V_{up}. Dotted blue lines: decreased inotropy, corresponding to 10, 20 and 30 % decrease in V_{rel} and V_{up}.

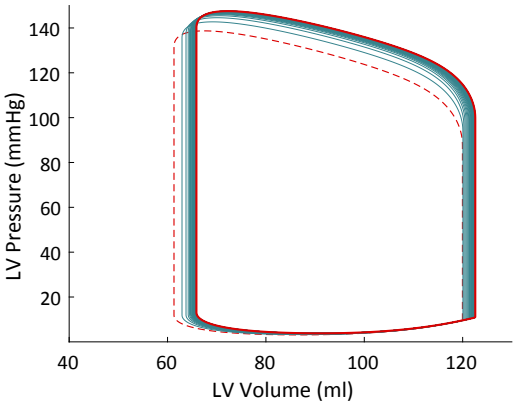

Figure 67: Transitory LV PV loops during a 20 % increase in R_{sys}. Dotted red line: initial CVS steady-state preceding R_{sys} increase. Normal red line: final CVS steady-state. Blue lines: transitory PV loops.

A supplementary Fogarty protocol is applied to calculate E_{ES}, as explained in the previous section. The slope of the ESPVR is calculated over the last fourteen end-systolic points from twenty-four consecutive PV loops, as shown in Fig. 68. Note that, as observed experimentally [99, 120, 129, 132–135] and reproduced numerically [115, 116], the ESPVR is more convex than linear in shape, and appears to be load-dependent. This can also be observed in Fig. 69, where only the end-systolic points are depicted for different loading conditions. Determining E_{es} with a linear regression is thus delicate.

The results are summarized in Fig. 71, where each CI is represented as a function of the seven inotropic states. Since six load variation protocols were applied, there is six CI values associated with each inotropic state, along with the CI value corresponding to the baseline case (no load variation).

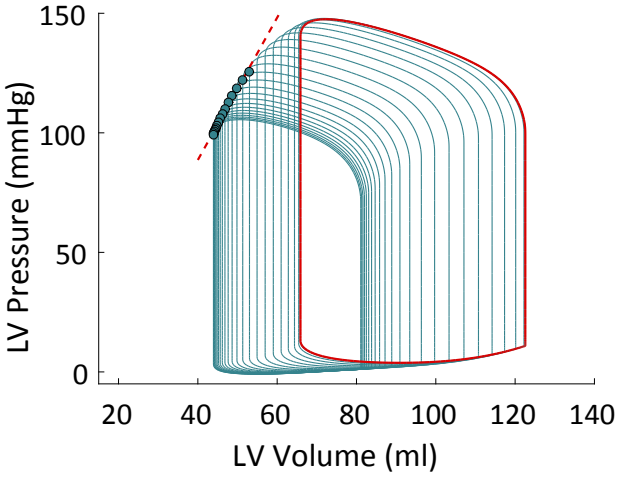

Figure 68: Determination of E_{es}. Once a new steady-state is reached after load variation (bold red line), a Fogarty protocol is induced. A linear regression is established over fourteen end-systolic points (blue markers) in order to calculate E_{ES}, the slope of the ESPVR.

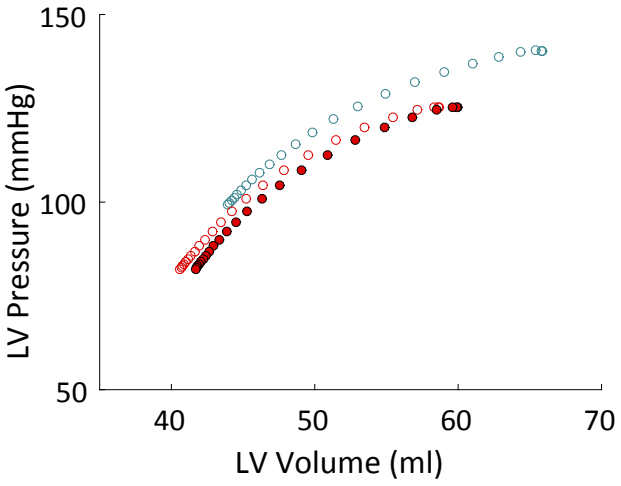

Figure 69: ESPVR for different loading conditions. The end-systolic points correspond to aortic valve closure. Filled markers correspond to a basic Fogarty protocol, with a baseline inotropy. Open markers correspond to two load variation protocols followed by a Fogarty protocol, with the same baseline inotropy.

The first two indices are increasing functions of inotropy while T_d is a decreasing funtion of inotropy. For each inotropic state, we can calculate the standard deviation relative to the baseline case (no load variation). For the load variations simulations we have considered, $(dP_{lv}/dt)_{max}$ standard deviation with respect to the baseline case is less than 2 %, while for $(dP_{ao}/dt)_{max}$ it ranges from 4 to 10 % and for T_d it ranges from 1 to 5 %. In the case of $(dP_{lv}/dt)_{max}$, the standard error is very small, which allows us to conclude that this quantity can actually be considered as a reliable CI, truly independent of the load and increasing with inotropy, a conlusion also drawn experimentally by Drake-Holland *et al.* [180]. The quantities $(dP_{ao}/dt)_{max}$ and T_d have larger standard deviations, which indicates that those indices are slightly load-dependent. E_{es} is an increasing function of inotropy and presents the highest standard deviations, ranging from from 4 to 25 %. Moreover, the way E_{es} is calculated also has an impact on the results from Fig. 71d, as the ESPVR is more parabolic than linear in shape [52]. Depending on the end-systolic points chosen for the linear regression (in our case, the last fourteen points from twenty-four PV loops), calculated E_{es} may vary, as shown in Fig. 70, where three ESPVRs are obtained with three different data sets.

5.3 CONCLUSION

In clinics, there is a need for assessing the intrinsic ventricular contractile state, independently of the loading conditions. Several CIs were proposed,and the present chapter is an original analysis of four of them [116]. We show that all of them are monotonic functions of inotropy. However, only $(dP_{lv}/dt)_{max}$ can be considered as a true index of contractility since it is actually load-independent. The load-dependency of T_d, and to a lesser extent, of $(dP_{ao}/dt)_{max}$ remains rather small and these two measures are thus reasonably good indices of cardiac contractility. The load-dependency of E_{es} is larger and even if E_{es} increases

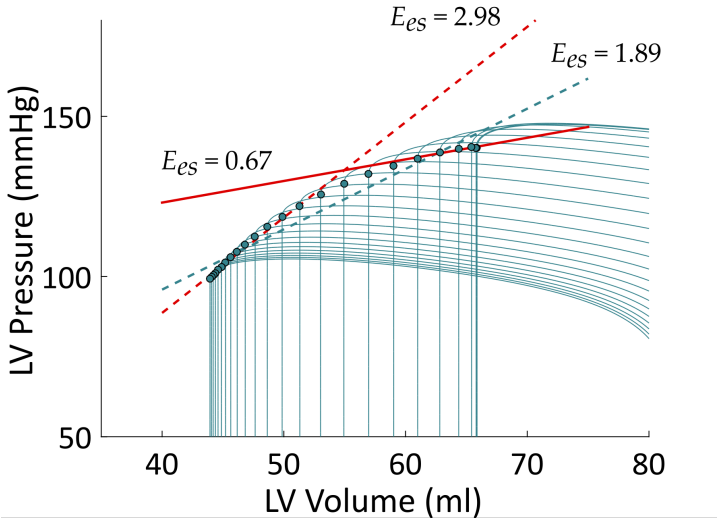

Figure 70: E_{es} assessment with different data sets. Linear regression over the last fourteen end-systolic points (dashed red), linear regression over twenty-four (all) end-systolic points (dashed blue), linear regression over the first six end-systolic points (normal red).

with inotropy, it cannot be considered as an absolute index of contractility, especially with an unreliable linear regression of a convex ESPVR. These conclusions about E_{es} were also drawn experimentally [133, 178] and with another multiscale model [115], which really questions the gold standard status of end-systolic elastance as a reliable contractility index.

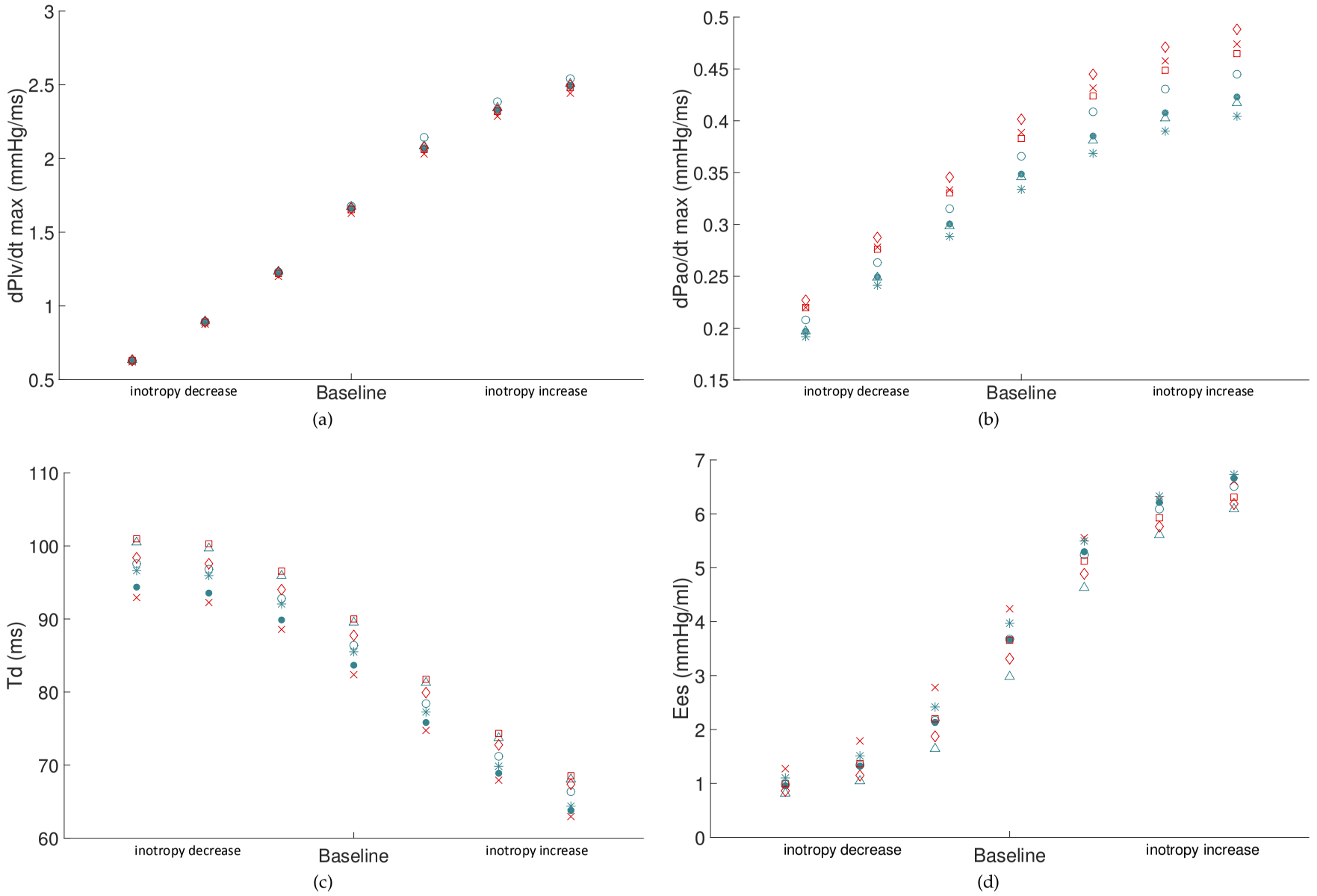

Figure 71: Cardiac contractility indices variations under changes in inotropy. No load variation (○), R_{sys} increase (△), R_{sys} decrease (×), global R increase (●), global R decrease (□), global E increase (∗), global E decrease (⋄).

6

THEORETICAL ANALYSIS OF THE FRANK-STARLING MECHANISM

As already detailed in Chapter 2, the Frank-Starling (FS) mechanism describes the intrinsic ability of the heart to adapt its output to variations in ventricular filling, on a beat-to-beat basis. This correlation between diastolic filling and cardiac output is generally schematized with Starling curves, like the one depicted in Fig. 72.

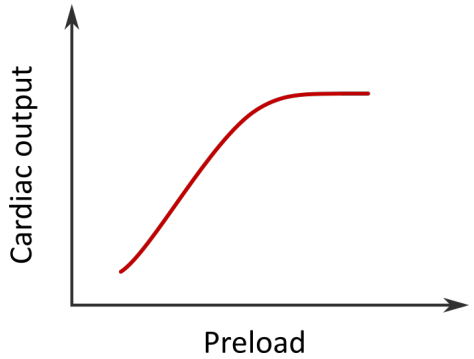

Figure 72: Frank-Starling (FS) mechanism. As the preload increases, the cardiac output (or stroke volume) increases, up to a certain limit. This relationship allows for beat-to-beat adjustment of cardiac output in response to changes in venous return.

Experimental studies on the FS mechanism at the CVS scale are numerous, and some of them were described in Chapter 2. Basically, the aim of such studies is to confirm the correlation between preload and cardiac output and to obtain experimental curves similar to Fig. 72. On the vertical axis, cardiac output is sometimes replaced by stroke volume[1](SV), or stroke work[2](SW). On the horizontal axis, preload is associated with the cardiac fibers length at the end-diastolic phase, prior to ventricular contraction. Other preload indices are used, as it is not possible to assess cardiac fibers length *in vivo*: end-diastolic volume (EDV), end-diastolic pressure (EDP), mean atrial pressure and central venous pressure are the most common preload measurements. As already discussed in Chapter 2, all these preload indices have their limitations and can lead to results misinterpretation. Moreover, linking preload indices from the right side of the circulation, such as right atrial pressure, with outputs from the left circulation, such as left ventricular stroke volume, may also lead to misleading results [43]. Even if a variety of studies at the heart scale explored the FS mechanism, they are difficult to interpret because of the intrinsic complexity of the CVS system. Variations in heart rate, inotropy or hemodynamic conditions, *e.g.*, via extrinsic regulatory mechanisms or via the Anrep effect, can overshadow the FS mechanism, and complicate its study *in vivo*. Moreover, the variability across experimental methods prevents a direct comparison between the diverse studies.

[1]With a constant heart rate, both notions are interchangeable.
[2]As explained in Chapter 2, stroke work is given by the area enclosed within the PV loop.

Preload alteration can occur naturally on a beat-to-beat basis [47], due to atrial fibrillation [181], or be induced via *vena cava* occlusion [39, 48, 182], vascular filling procedures [39, 46, 183, 184], or by elevating the patients legs for a certain amount of time [185]. Once LDA (length-dependent activation) was proposed as the cellular basis for the FS mechanism, as explained in Chapter 3, studies at the cellular and subcellular scales allowed for the reduction in the complexity of interfering factors and controlling parameters [96]. But these studies are mostly conducted in isometric conditions, which toughens the extrapolation to physiological conditions. Moreover, even if ventricular pressure is directly associated with cellular force, it also depends on ventricular volume, so the myocardial effects at the heart scale are mixed up with the "geometrical" effects of the ventricular chamber[3].

Multiscale mathematical models represent a convenient tool to overcome all these experimental obstacles. In this chapter, we propose an *in silico* study of the FS mechanism, with a particular attention paid to the phenomena taking place at the cellular scale, as the LDA is assumed to be the cellular origin of the FS mechanism. The aim is to explore the various factors involved in the increase in stroke volume when left ventricular preload is increased. Since the cardiac fibers undergo a complex, fundamentally *dynamic* behavior during a hearbeat, it is not hazardous to suppose that LDA, which is most often highlighted in isometric contractions, will not be the only mechanism controlling the increase in stroke volume following an increase in preload. This theoretical analysis of the FS mechanism is first performed with an isolated left ventricle model, which ensures that only the left ventricular preload is varied. Then, this procedure of increased left ventricular preload is also applied to the whole CVS model. Then this study of the FS mechanism is extended to vascular filling and SV equilibrium simulations. Eventually, other modeling studies related to cardiac output regulation and the FS mechanism are presented and compared with our results.

6.1 INFLUENCE MAP OF THE CVS MODEL

Before we start studying the effect of preload increase on the left ventricle, we introduce a useful tool to analyze the different variables that have an influence on the left ventricular SV. In Fig. 73, a schematic representation of the CVS model is built as follows: the important variables associated with the left ventricle are depicted and connected with arrows in order to express the influence they have on each other. Note that this "map of influences" is actually shaped as a complex system of connected loops. For instance, the aortic pressure determines (partially) the aortic flow. This aortic flow in turn determines (partially) the aortic chamber volume. And this chamber volume determines aortic pressure. We see that the variables are linked in a circular way, and it is not possible to chose a "starting point" for the diagram of influences. However, the diagram is easier to read by looking first at the mitral flow Q_{mt} along with the main equations on the right side of the figure. We see that Q_{mt}, together with the aortic flow

[3]For instance, in case of a thin sphere of radius r and thickness h, pressure P is related to the wall stress σ by the Law of Laplace: $P = \frac{2\sigma \cdot h}{r}$. We see that even is σ is constant, pressure can decrease if the chamber volume increases.

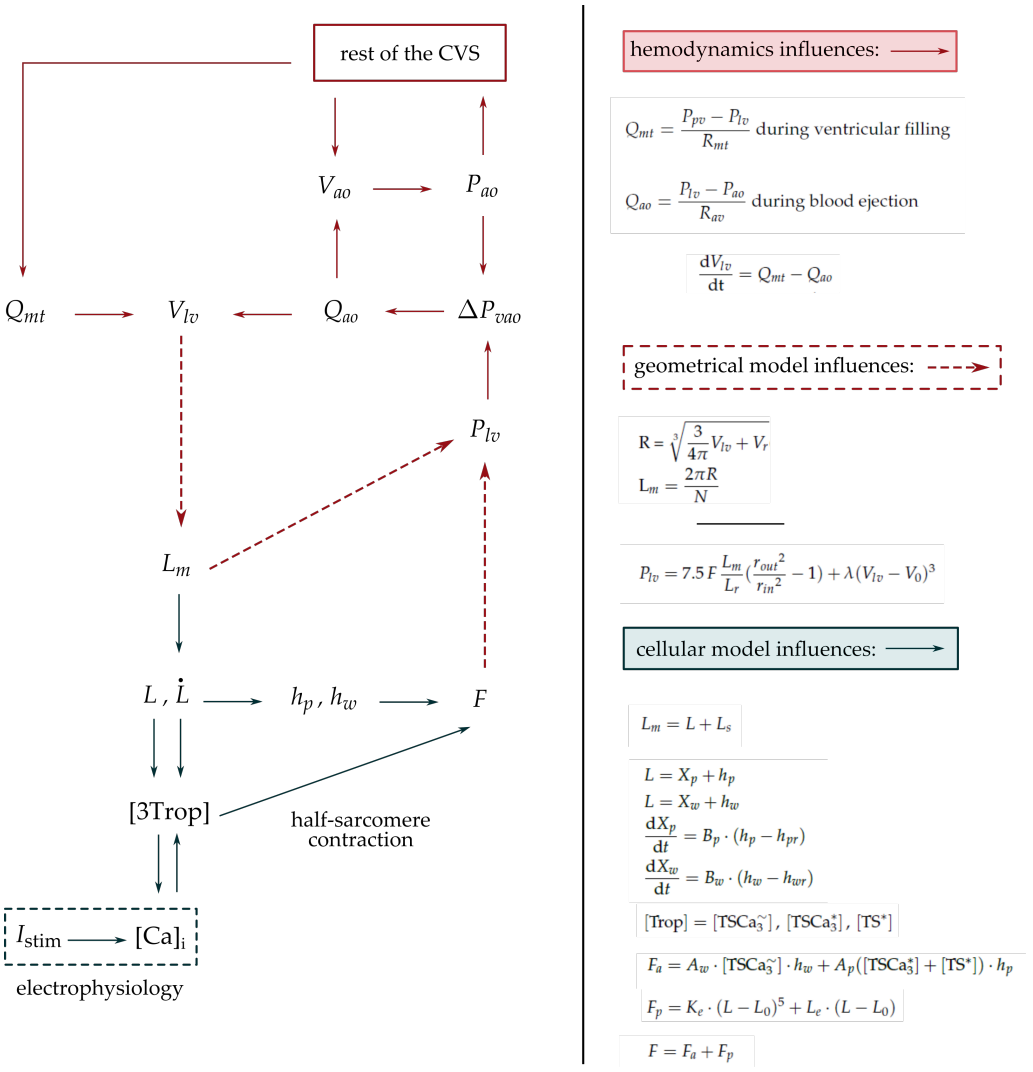

Figure 73: Influence map of the variables related to the left ventricle in the CVS model ($\Delta P_{vao} = P_{lv} - P_{ao}$). Left panel: schematic overview of the involved variables. The arrows indicate the direction of influence. Right: associated equations describing the influence between the different variables. Explanations in text.

Q_{ao}, defines V_{lv}. V_{lv} in turn affects L_m, because they are linked with the spherical ventricle model (geometrical model). Then, L_m in turn influences L and its time derivative, $\dot{L}$. The three concentrations describing the troponin system and involved in force production are represented by the short notation [3Trop]. They depend on L via the rate constants f and g_d, and on $\dot{L}$ via the rate constant g (from the CB biochemical cycle described in Section 4.4.2). [3Trop] also depend on calcium concentration $[Ca]_i$. The latter is dictated by the electrophysiological model equations, where the AP is triggered by a stimulus current I_{stim}. Note that [3Trop] also influence $[Ca]_i$ with the feeback mechanism described in Section 4.4.3. L also dictates the equivalent CBs elongations h_p and h_w (from the equivalent CB dynamics). *In fine*, the force F is computed from these cellular variables ([3Trop], h_p and h_w), and is related to the pressure P_{lv} via the geometrical model. An important point to make here is that P_{lv} does not only depend on developed force, but it also depends explicitely on L_m because of the geometrical model. So

force and pressure cannot be considered as equivalent and exchangeable notions, or expected to vary exactly in the same way. P_{lv} also depends on ventricular dimensions, and for a fixed force, increases with a decreasing L_m. Eventually, P_{lv}, along with P_{ao}, dictates the pressure gradient $\Delta P_{vao} = P_{lv} - P_{ao}$ and thus the aortic flow. This aortic flow is associated with the volume and pressure of the aortic chamber, that will play a role in the rest of the CVS, and finally affect Q_{mt}. V_{lv} is computed from Q_{ao} and Q_{mt}, and SV is finally obtained by taking the difference between $V_{lv}^{\max}$ and $V_{lv}^{\min}$.

6.2 INSTANTANEOUS INCREASE IN PRELOAD

There is a general consensus for considering the FS mechanism as an *instantaneous* effect: preload variations directly alter the cardiac output within the same heartbeat. For this reason, only the transient effect of a sudden LV preload increase within one heartbeart will be investigated in this section. It is thus necessary to design a simulation protocol where only the preload can be varied, all other variables remaining unchanged, especially inotropy and afterload. To remove the circulatory influence, the left ventricle is extracted from the CVS model. Then, the pulmonary vein and aortic pressures, P_{pv} and P_{ao}, are used as input functions, as well as the intracellular calcium concentration $[\mathrm{Ca}]_\mathrm{i}$. This ensures a control of ventricular preload, afterload and inotropy, respectively. These three input functions are extracted from the baseline simulation of the whole CVS model presented in Chapter 4, and reproduced schematically in Fig. 74. This forms the *isolated ventricle* model, represented in Fig. 75.

An instantaneous increase in preload (IIP) is achieved by suddenly increasing P_{pv} by 9 mmHg between t_0 and t_0 + 60 ms during left ventricular filling, with t_0 = 50 ms. In the whole CVS model, the stimulus current is applied at t_{stim} = 100 ms, so this sudden increase in P_{pv} is applied 50 ms before activation, during the ventricular filling phase. The influence of the starting time t_0 will be discussed later, but unless stated otherwise it will always be fixed at 50 ms for all the simulations.

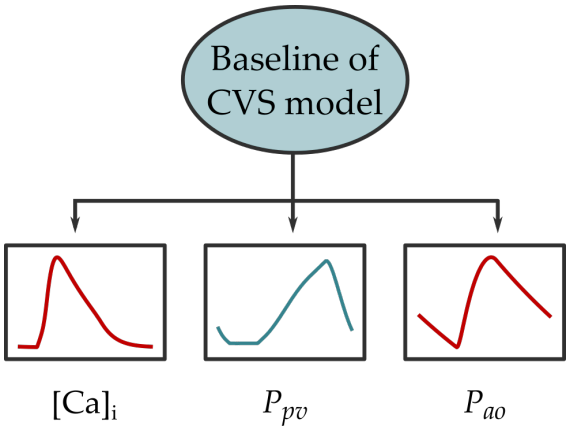

Figure 74: Input functions extracted from the CVS model. Intracellular calcium concentration, aortic and pulmonary vein pressures are extracted from a baseline simulation of the CVS model presented in Chapter 4.

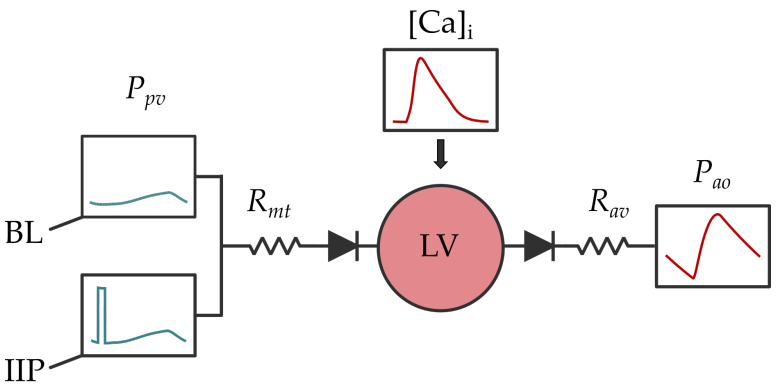

Figure 75: Instantaneous increase in preload (IIP) protocol with the isolated ventricle model. Aortic (red) and pulmonary (blue) pressures are used as input functions, as well as the intracellular calcium contration $[Ca]_i$. The superior pulmonary pressure curve corresponds to the baseline (BL) case extracted from the whole CVS model. The inferior curve corresponds to the IIP protocol. The pulmonary pressure is artifically increased by 9 mmHg for 60 ms to generate a sudden increase in preload. Note that different scales are used for the aortic and pulmonary vein pressure curves.

This sudden increase in P_{pv} increases the mitral flow and thus ventricular volume. Eventually, this increases sarcomere length prior to contraction (namely, the preload). The IIP protocol is depicted in Fig. 75.

The case of unchanged afterload is worth discussing. Unlike preload, the definition of ventricular afterload is more tricky [186]. Indeed, at the cardiac fiber scale, it is unequivocally defined as the force opposing fiber shortening during contraction [2, 129, 187]. For instance, the isotonic contractions described in Chapter 3 correspond to constant afterload contractions, because the load against which the fibers are contracting is kept constant. At the heart scale, afterload is similarly described as the "load" against which the heart must contract to eject blood [1, 186, 187]. From this definition, it is often assumed that aortic pressure is a major determinant of LV afterload, as it represents the pressure that the LV must overcome to eject blood into the systemic circulation [1, 3, 186]. The greater the aortic pressure, the greater the afterload on the left ventricle. However, LV afterload should not simply be equated with aortic pressure. Indeed, afterload could better be described as the ventricular wall stress during ejection [1, 2, 187]. This wall stress does not only depend on developed pressure, but also on ventricular size[4], which varies during ejection. Because of changing size and pressures, afterload varies continuously during ventricular ejection [2, 129]. A more rigorous afterload definition should be "... all the factors that contribute to total myocardial wall stress (or tension) during systolic ejection" [186]. But for practical reasons, LV afterload is often equated with aortic pressure and, although it is not a perfect definition, it allows for a simple and reasonable afterload assessment. For the rest of this work, we will associate LV afterload with aortic pressure. In case of an IIP protocol performed with the isolated ventricle model, P_{ao} will thus be considered as an input function, as we only want preload to vary. Of course, this protocol is not completely physiological, as aortic pres-

[4]Recalling the Law of Laplace for a thin sphere ($\sigma = \frac{P \cdot r}{2h}$), we see that, for a fixed pressure, σ increases with increasing chamber size.

sure is mainly determined by the upstream ventricular blood ejection. Later in this chapter, an IIP protocol will also be applied to the left ventricle inside the whole CVS model, with no need for an afterload input function. To avoid any ambiguity, we use the following definitions:

- **Unchanged afterload**: P_{ao} is an input function of time, extracted from the baseline case.
- **Physiological afterload**: P_{ao} is not an input function, it is determined by Eq. (C.1) from the CVS model.

6.2.1 *Schematic PV loops during preload increase*

PV loops are useful tools to visualize the preload influence. In Fig. 76, schematic PV loops are drawn to show the acute effect of preload increase, all other variables remaining constant, especially inotropy and afterload. These PV loops present an increase in preload (increased EDV), which naturally leads to an increased SV. Note that these PV loops are not extracted from experimental data, as it is experimentally challenging to only vary the preload. For this reason, the schematic PV loops upon a single preload increase may vary in the literature (see Fig. (5.8.4) in [22] or Fig. (1) in [188]), but they all present an increase in SV.

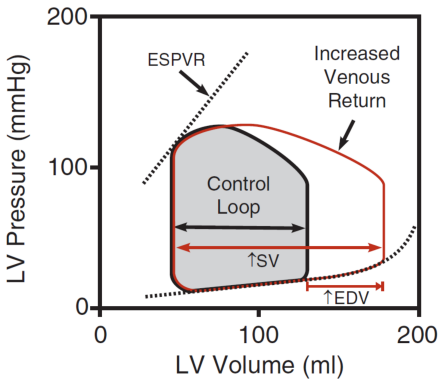

Figure 76: Schematic effect of an acute LV preload increase [1]. As venous return increases, more blood enters the LV during diastole, and LV preload increases. As a result, SV increases. This is the signature of the FS mechanism. These schematic PV loops are constructed assuming constant afterload and constant inotropy.

6.2.2 *Simulated PV loops during preload increase*

The LV total half-sarcomere length (L_m), active force and PV loop obtained with the IIP protocol in the isolated ventricle are depicted in Fig. 77. These quantities are also compared to the baseline (BL) case. Since the three input functions from Fig. 74 were extracted from the baseline case presented in Chapter 4, the baseline curves for the isolated LV model are of course identical to those presented in Fig. 61 and 63. Regarding the IIP case, since the preload has increased, the sarcomere length prior to contraction is greater and we observe that the max-

imal produced force increases. This is the signature of length-dependent activation (LDA). It can be seen from the PV loops that the stroke volume is greater with IIP. A quantitative analysis of the IIP case relative to the BL case is shown in Table 5. A 5 % increase in maximal force is observed, along with a 13 % increase in SV following preload increase. Note that the increase in maximal produced pressure is less than 1 %.

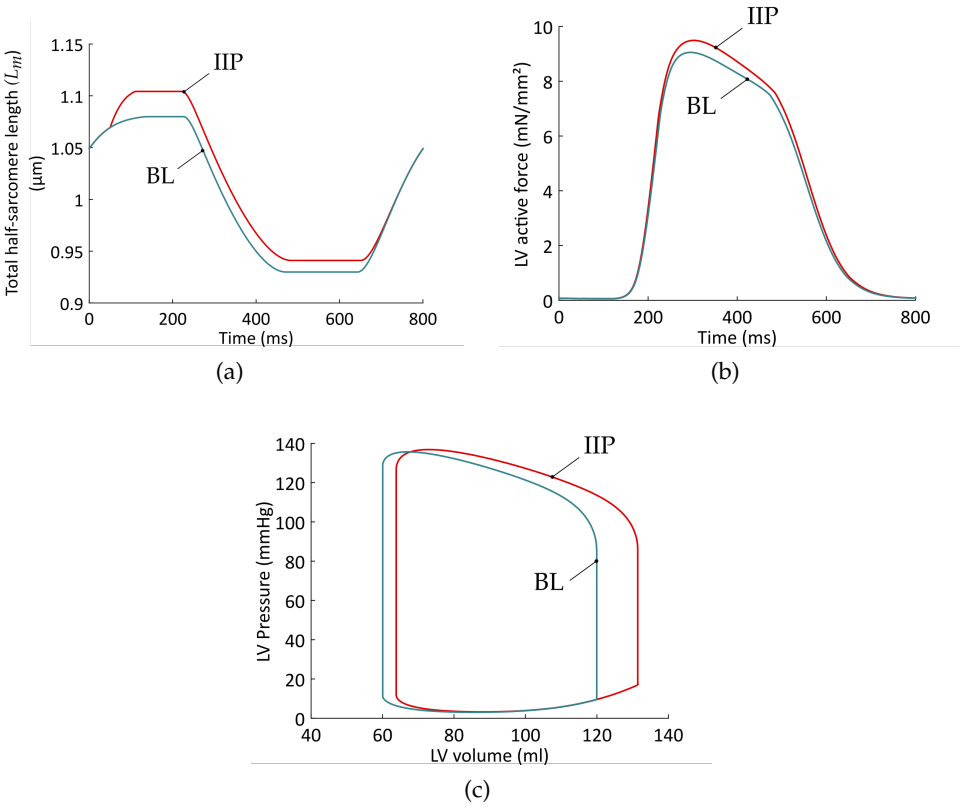

Figure 77: Instantaneous increase in preload. (a) Total half-sarcomere length (L_m). (b) Normalized active force. (c) PV loop. Comparison between the baseline (BL) case (blue line) and the IIP case (red line).

	End-diastolic volume (ml)	Stroke volume (ml)	Maximal active force (mN/mm²)	Maximal pressure (mmHg)
BL	119,96	60	9,05	135,65
IIP	131,43 (+ 9,57 %)	67,61 (+ 12,68 %)	9,49 (+ 4,85 %)	136,82 (+ 0,86 %)

Table 5: Quantitative analysis of IIP protocol in the isolated ventricle model. The percentages show the relative variation with respect to the baseline case.

Now, we may ask ourselves if the increased force, driven by LDA, is solely responsible for the increase in stroke volume. Furthermore, we see in Fig. 77c that the ESV from the IIP is greater than for the baseline case, contrary to what is observed on the schematic PV loop from Fig. 76. This means that the increase in

preload has somehow influenced the ejection dynamics so that the ESV is also altered. All these questions will be discussed further in the following sections.

6.3 SWITCHING OFF THE LDA

In our model, LDA is implemented via the rate constants from the biochemical cycle described in Chapter 4 and schematized in Fig. 55. The length-dependence of the attachment rate f and the irreversible detachment rate g_d is expressed as follows:

$$f = Y_a \exp(-R(L - L_a)^2) \tag{6.1}$$
$$g_d = Y_d \exp(-Y_c(L - L_c)) \tag{6.2}$$

Here L is the half-sarcomere length (total half-sarcomere length L_m minus the series element length L_s, see Fig. 53). L changes during the contraction: it increases with ventricular filling, and decreases during ejection, as observed in Fig. 78a. Thus, f and g_d vary with time, which dictates the force and pressure development. As can be observed in Fig. 78b and 78c, the attachment rate f increases while the irreversible detachment rate g_d decreases upon IIP. This naturally leads to an increased produced force (see Fig. 77b), since CBs attachment (resp. detachment) got promoted (resp. depressed).

This explicit length-dependence of f and g_d can now be removed by using an input function L_{in} instead of the "real" length L:

$$f = Y_a \exp(-R(L - L_a)^2) \quad \longrightarrow \quad Y_a \exp(-R(L_{in} - L_a)^2) \tag{6.3}$$
$$g_d = Y_d \exp(Y_c(-L - L_c)) \quad \longrightarrow \quad Y_d \exp(-Y_c(L_{in} - L_c)) \tag{6.4}$$

This input function is chosen so that the model produces the same results for the baseline case. To do so, the input function L_{in} is the half-sarcomere length extracted from the baseline case (see Fig. 78a). In other words, f and g_d are now fixed functions of time (blue curves from Fig. 78b and 78c) and do not depend on the true length of the half-sarcomere anymore. More precisely, they do not depend on length variations relative to the BL case. In other words, if $L(t)$ happens to change with respect to the BL case, f and g_d will not vary accordingly. This modified ventricle model where the length-dependence is "switched off" will be further referred to as the "NO LDA" model. When no increase in preload is imposed on the LV, the NO LDA ventricular model obvioulsy leads to the baseline case results. When the IIP protocol is applied, it yields however different outputs than those shown in Fig. 77. These outputs are presented in Fig. 79.

The stroke volume for the NO LDA model following IIP has decreased compared to the IIP case, while the maximal active forces are similar. A quantitative comparison between the three presented cases (baseline case, IIP and IIP NO LDA) is presented in Table 6. We see that, when LDA is turned off, there is no increase in SV upon IIP (- 1,05 % compared to + 12,68 % with LDA). This observation indicates that LDA is responsible for the SV increase upon IIP. But when LDA is turned off, the maximal produced force still increases upon IIP (+ 5,50 %

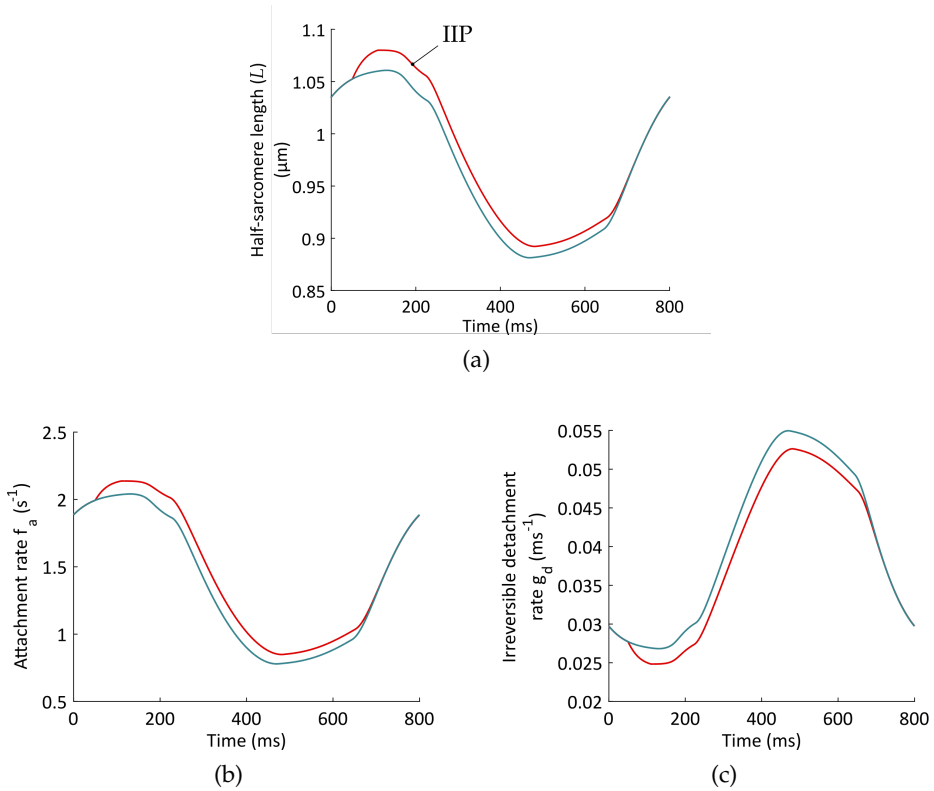

Figure 78: Half-sarcomere length and biochemical rates during IIP. (a) Half-sarcomere length for the BL case (blue) and IIP protocol (red). (b) Attachment rate f. (c) Irreversible detachment rate g_d.

compared to + 4,85 % with LDA), while the SV slightly decreases. This surprising result suggests that the SV increase following IIP when LDA is present is not directly mediated through an increase in generating force capacity. In other words, *the presence of LDA does not involve an increase in maximal force which is straightforwardly responsible for an increase in SV*. Furthermore, it is worth noticing that the maximal pressure did not change significantly (+ 0,86 % with LDA and - 0,05 % without LDA). This suggests that *maximal force and/or pressure may not be relevant indices when studying preload effects and SV variations*.

	End-diastolic volume (ml)	Stroke volume (ml)	Maximal active force (mN/mm²)	Maximal pressure (mmHg)
BL	119,96	60	9,05	135,65
IIP	131,43 (+ 9,57 %)	67,61 (+ 12,68 %)	9,49 (+ 4,85 %)	136,82 (+ 0,86 %)
IIP NO LDA	131,45 (+ 9,58 %)	59,37 (- 1,05 %)	9,55 (+ 5,50 %)	135,59 (- 0,05 %)

Table 6: Quantitative analysis of IIP protocol with the NO LDA model.

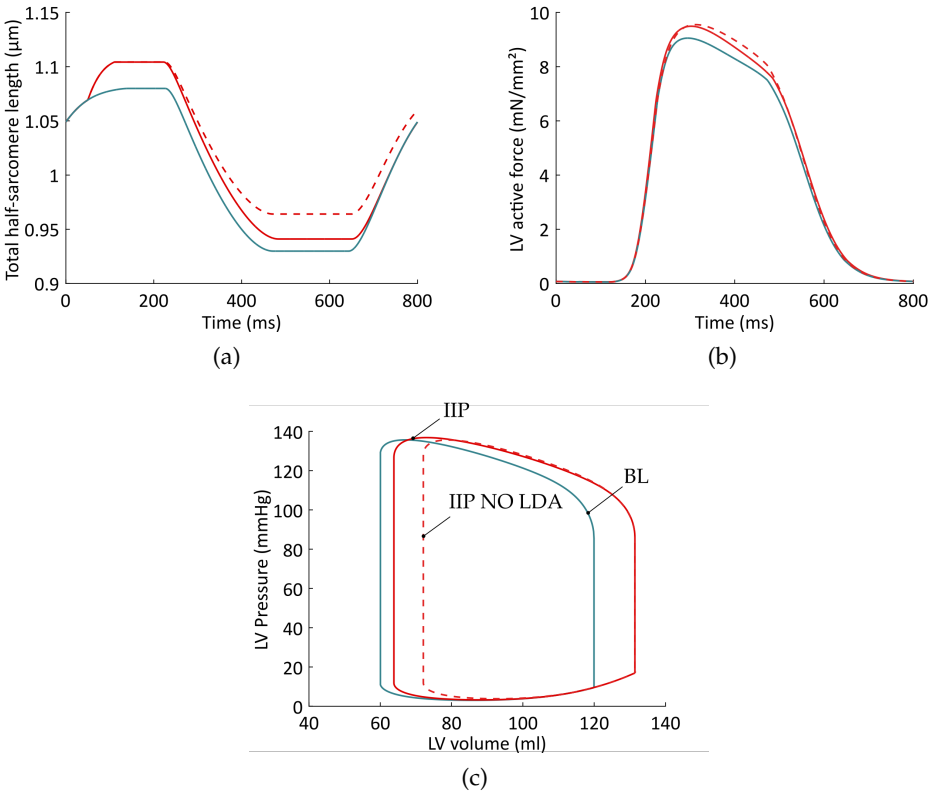

Figure 79: Instantaneous increase in preload with the NO LDA model. Comparison between BL (blue), IIP (normal red) and IIP NO LDA (dashed red). (a) Total half-sarcomere length (L_m).(b) normalized active force. (c) PV loop.

Moreover, as will be discussed in the next section, the temporal dynamics of contraction is also altered upon preload increase.

6.4 DISCUSSION

We observed in the previous section that an increase in preload leads to an increase in force and SV in the presence of LDA. This is the common explanation for the FS mechanism *in vivo*. However, an increase in force was also observed with the NO LDA model, and it did not lead to an increased SV. It is worth analyzing the whole dynamics of contraction to better understand the SV variations following preload alterations. This is discussed in the following subsections.

6.4.1 *Valves opening and closing*

In our left ventricle model, the mitral valve closes when $P_{lv} > P_{pv}$, at a time noted t_{mtC}. Then the isovolumic contraction starts and it ends when $P_{lv} > P_{ao}$. This defines the isovolumic contraction duration Δt_{isoV}. The aortic valve opens at a time noted t_{aoO}, and blood is ejected into the systemic circulation until $P_{lv} < P_{ao}$. At this point the aortic valve closes. This defines the ejection duration Δt_{ej}. The isovolumic and ejection phases are represented in Fig. 80.

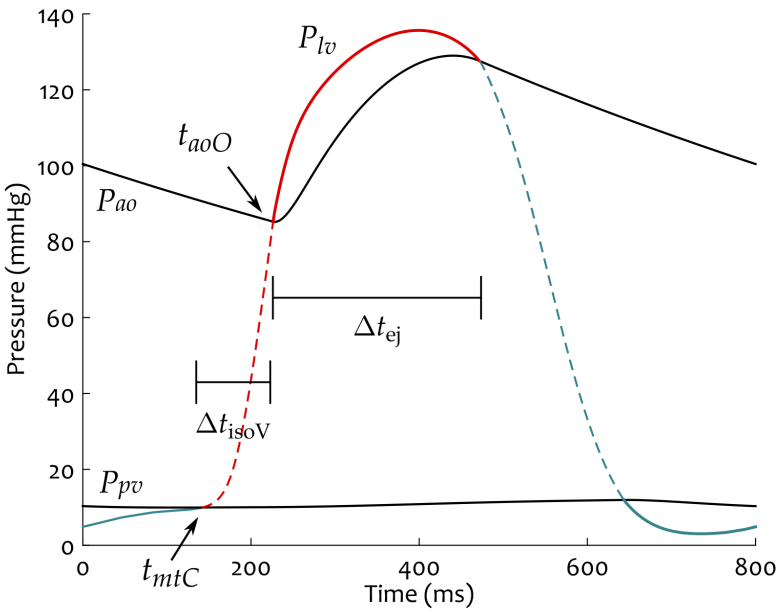

Figure 80: The four phases of ventricular contraction on P_{lv}: ventricular filling (blue line), isovolumic contraction (dashed red line), blood ejection (red line), ventricular relaxation (dashed blue line). t_{mtC} is the time of mitral valve closing, Δt_{isoV} is the isovolumic contraction duration, t_{aoO} is the time of aortic valve opening, and Δt_{ej} is the blood ejection duration.

6.4.2 *Timing of contraction during IIP*

The start of the isovolumic contraction phase t_{mtC}, the start of the ejection phase t_{aoO}, the isovolumic contraction duration Δt_{isoV} and the blood ejection duration Δt_{ej} are calculated for the BL, IIP and IIP NO LDA simulations. The results are presented in Table 7. We first see that t_{mtC} decreases following IIP compared to the BL case. This is not surprising since, during IIP, a sudden increase in P_{pv} is induced. This allows for an increase in the mitral flow, ventricular volume, and thus in ventricular (passive) pressure. When this sudden P_{pv} increase ends (at a time t_0 + 60 ms = 110 ms), we naturally have $P_{lv} > P_{pv}$ and the isovolumic contraction phase starts. So this phase begins earlier than in the BL case, because the IIP has generated a faster ventricular filling process. We also see from Table 7 that the isovolumic contraction duration increases for IIP and IIP NO LDA. On the other hand, there is no substantial differences in t_{aoO} between the BL case and the two IIP cases. This means that, although the timing of contraction is altered from the very beginning of contraction (t_{mtC} decreases and Δt_{isoV} increases), the dynamics during IIP somehow "slows down" during the isovolumic contraction and ends up with an aortic valve opening time t_{aoO} that is similar to the BL case. Eventually, the ejection duration Δt_{ej} is significantly increased only for the IIP case (+ 6,35 %).

	t_{mtC} (ms)	t_{aoO} (ms)	Δt_{isoV} (ms)	Δt_{ej} (ms)	Stroke volume (ml)
BL	141,60	226,32	84,72	245,31	60
IIP	110 (- 22,32 %)	222,32 (- 1,77 %)	112,32 (+ 32,58 %)	260,88 (+ 6,35 %)	67,61 (+ 12,68 %)
IIP NO LDA	110 (- 22,32 %)	225,04 (- 0,57 %)	115,04 (+ 35,79%)	246,48 (+ 0,48 %)	59,37 (- 1,05 %)

Table 7: Quantitative analysis of timing variations in IIP protocol.

The data indicate that an increased ejection duration is correlated with an increase in SV. This result is not surprising since the stroke volume can be written as:

$$SV = \int_{\Delta t_{\text{ej}}} Q_{ao}(t)\,\mathrm{d}t \tag{6.5}$$

where the aortic flow Q_{ao} during ejection is given by:

$$Q_{ao}(t) = \frac{P_{lv} - P_{ao}}{R_{av}} = \frac{\Delta P_{vao}}{R_{av}} \tag{6.6}$$

where $P_{lv} - P_{ao}$ is the aortic valve pressure gradient, noted ΔP_{vao}. Essentially, SV is the area under the $Q_{ao}(t)$ curve, and $Q_{ao}(t)$ is determined by ΔP_{vao} during ejection.

Since P_{ao} is an input function in the isolated ventricle model, we can see that it is the left ventricular pressure developement alone which drives the aortic flow. During IIP, the dynamics of pressure development has changed in such a way that ΔP_{vao} is greater during the ejection phase. As a consequence, a higher aortic flow is reached, along with a prolonged ejection duration, as can be seen in Fig. 81a, and this results naturally in a higher SV, because SV is given by the area under the $Q_{ao}(t)$ curve. We see that, even if the maximal produced pressure does not increase considerably upon IIP, the slight increase in pressure observed *during the whole ejection phase* is ultimately responsible for the increased SV. For the NO LDA model, on the other hand, the dynamics of pressure development during ejection leads to a lower aortic flow, and the ejection duration is similar to the BL case (see Table 7). No substantial SV variation is thus observed. This phenomenon is also well illustrated in Fig. 81b. Here both the aortic and ventricular pressures are drawn for the IIP and IIP NO LDA cases. We see that ventricular pressure is slightly lowered in the IIP NO LDA case and that the ejection duration is shorter (black arrows). In the next subsection, we discuss the origin of this altered contraction dynamics, and its relationship with stroke volume variations.

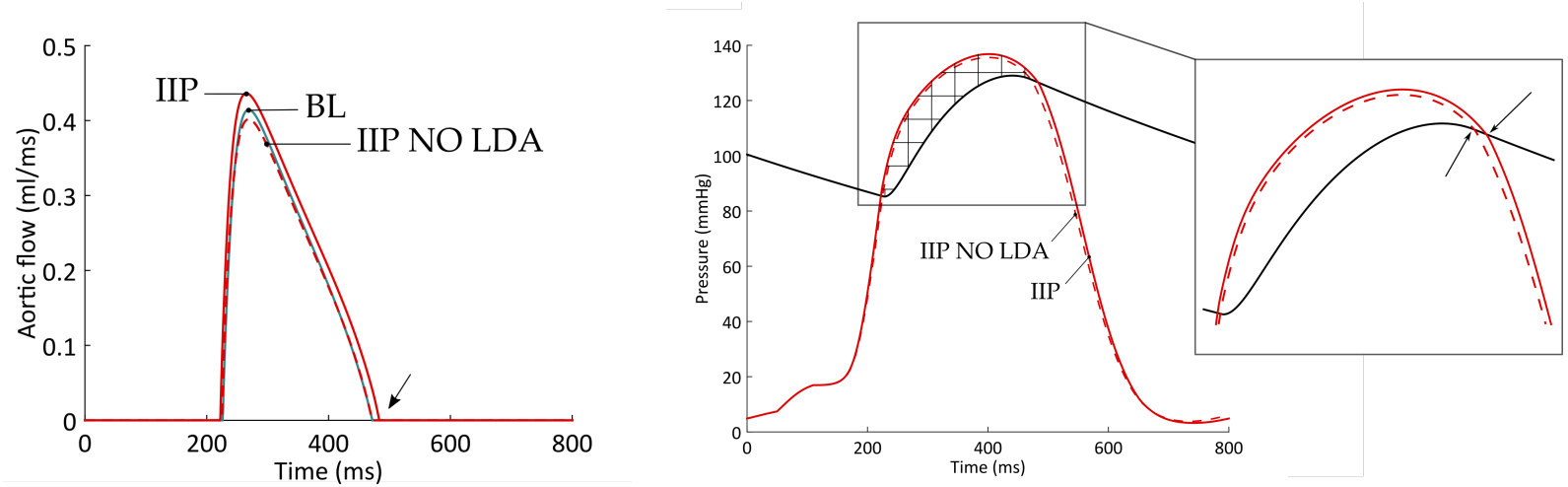

Figure 81: Visual representation of variations in SV for the IIP protocols with and without LDA. (a) Aortic flow for the BL (blue), the IIP (red) and the IIP NO LDA (dashed red) cases. The stroke volumes are given by the areas under the curves. The arrow indicates the longer ejection duration for the IIP case. (b) Ventricular and aortic pressures time evolution. The hatched aera enclosed between the ventricular pressure (red and dashed red) and the aortic pressure (black) is related to the SV. We see that there is a slight difference in ventricular pressure amplitudes between the IIP and IIP NO LDA which accounts partially for the difference in SV. Besides, there is also a difference in the ejection duration. The arrows indicate that the aortic valve closes earlier for the NO LDA case, resulting in a lower SV.

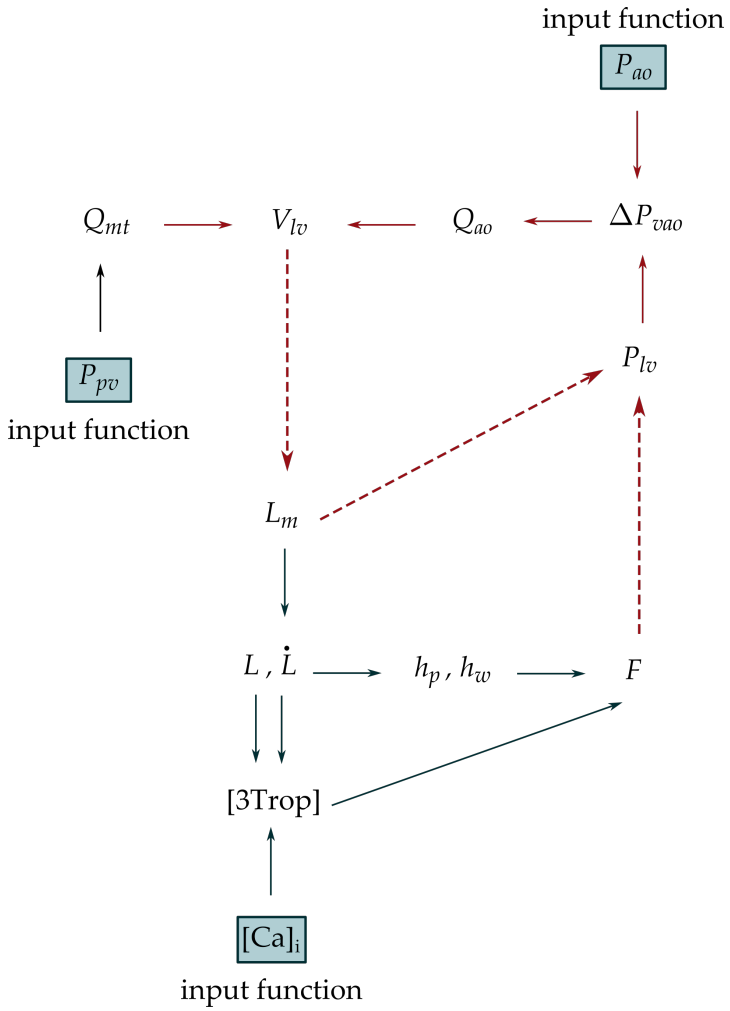

Figure 82: Influence map of the variables related to the isolated ventricle model.

6.4.3 *Dynamics of ejection*

From the results listed in Table 6 and 7, we can conclude that the length-dependence of force development is required to obtain an increase in SV following preload increase. Indeed, the IIP case leads to an increased SV while the IIP NO LDA leads to a SV that is even slightly lower than the BL case. We showed in the previous section that the aortic flow amplitude has increased following IIP, as well as the ejection duration. This was not observed with the IIP NO LDA. Thus, we may ask ourselves and try to explain how the length-dependence of the isolated ventricle model, triggered by the preload increase, drives these increases. To do so, an influence map for the isolated left ventricle model is proposed in Fig. 82. This map is extracted from the whole CVS influence map presented at the begining of this Chapter and P_{pv}, P_{ao} and $[\mathrm{Ca}]_\mathrm{i}$ are replaced with input functions (see section 6.2).

From this map, we can see that preload alteration via an increase in P_{pv} (IIP protocol) affects L_m, which direclty alters P_{lv} (see the red dotted arrows from Fig. 82). L_m also impacts L and the produced force F, which also influences the pressure (red dotted arrow). Of course, these alterations occurs continuously within

the heartbeat. In other words, a sudden increase in P_{pv} modifies the whole $L_m(t)$ and $L(t)$ functions, as seen in Fig. 78a. This in turns modifies the whole $F(t)$ and $P(t)$ functions. The exact way these alterations occur through time is hard to clarify, as all the involved variables (length, [3Trop], force , ...) are deeply interconnected. Besides, the map of influences proposed in Fig. 82 is a loop, so it is not conceivable to extract one independent variable that influence the others. It can be however be stated that the IIP sets up new initial conditions for the contraction, which ultimately affects the whole dynamics of pressure development. And it is this altered dynamics that is responsible for the SV increase.

Regarding the IIP NO LDA case, another influence map is presented in Fig. 83, where the length-dependence of [3Trop] is removed as explained in section 6.3. Here, L still influences the produced force through h_p and h_w (see Fig. 83), and its time-derivative still affects [3Trop]. This (partial) remaining length-dependence is enough to obtain a greater produced force, even greater than in the IIP case (see Fig. 79b). However, the whole temporal dynamics of force developement is affected differently than in the IIP case, and this leads to a different $L_m(t)$ evolution (see Fig. 79a). Since L_m also influences the developed pressure, we observe

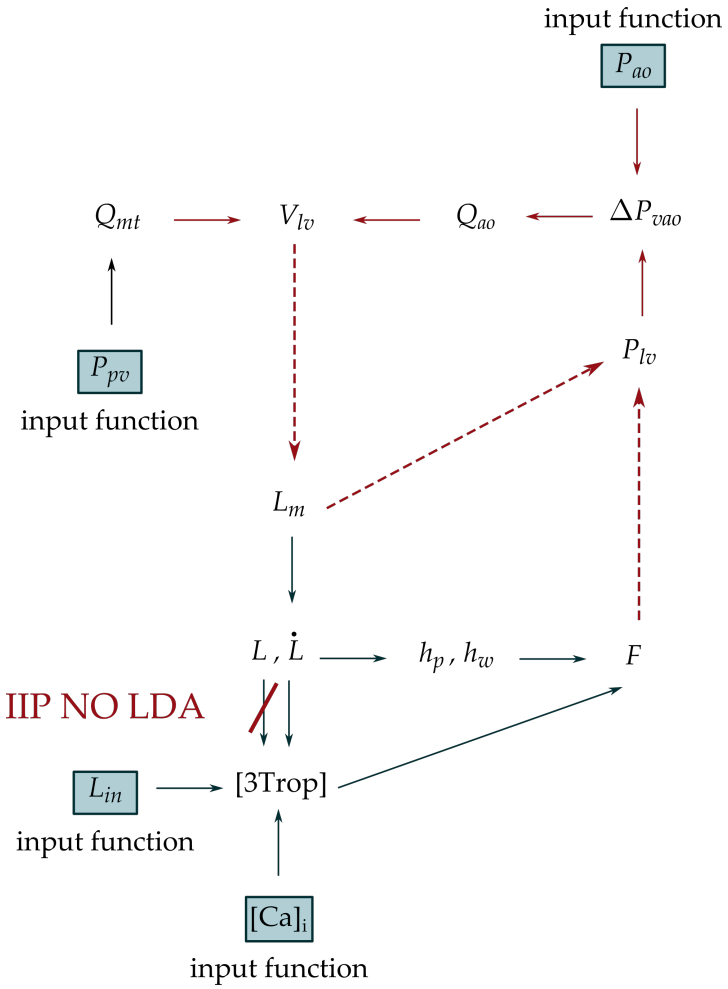

Figure 83: Influence map for the NO LDA isolated ventricle model. The length-dependence of [3Trop] is switched off by the procedure described in Section 6.3. Note that L still influences the produced force because it also affects h_p and h_w.

an increase in produced force without any substantial increase in pressure (see Fig. 81a). The pressure gradient and aortic flow are thus similar to the BL case (see Fig. 81b) and a similar SV is obtained.

To conclude, we showed in this section that LDA is responsible for an increase in SV following preload alteration. The IIP protocol leads to an increase in maximal produced pressure. This increase cannot be directly associated with an increase in maximal produced pressure, as pressure also explicitely depends on L_m. It is the combination of an increased force development and an altered L_m time evolution that leads to an increase produced pressure *throughout the whole ejection period*. This ventricular pressure drives the pressure gradient ΔP_{vao} during ejection, which thus increases, and the aortic flow reaches higher values. ΔP_{vao} is also the determinant of the aortic valve opening and closing, and since the ventricle is developing a higher pressure, it is now able to eject for a longer period. This secondary effect of pressure increase also participates in the increase in SV. When the length-dependence is turned off (NO LDA), the IIP protocol sets new initial conditions that do not affect the force and pressure time development in the same way. Indeed, we observed that, even if the developed force increases, the developed pressure remains close the BL case, as well as the pressure gradient and the ejection duration. The SV does not vary substantially in this case.

6.5 THE VELOCITY DEPENDENCE

In the previous section, we switched off the length-dependence of the isolated ventricle model by removing the length-dependence of two biochemical rate constants, f and g_d. We called this model where the length-dependence was bypassed the NO LDA model. However, a length-dependence remains in the NO LDA model. More precisely, a velocity dependence, because of the detachement rate g, expressed as follows:

$$\begin{aligned} g &= Z_a + F_h\, Y_v\, (1 - e^{-\gamma (h_w - h_{wr})^2}) && (6.7)\\ &= Z_a + F_h\, Y_v\, (1 - e^{-\gamma \frac{1}{B_w} (\dot{L} - \dot{h_w})^2}) && (6.8) \end{aligned}$$

where $\dot{L}$ appears explicitely because $\frac{dX_w}{dt} = B_w(h_w - h_{wr})$ and $L = X_w + h_w$ (see Eqs. (4.36) and (4.38)).

This rate constant is partially responsible for the correct reproduction of shortening deactivation, which occurs in the beating heart during ejection. So if we want to analyze the cellular length effects and their link with the FS mechanism, a more rigorous approach would be to cut completely any form of length-dependence in the sarcometric contraction model. We actually defines two new models, the NO VD and FIXED BIOCH model. The basis of the NO VD model is that LDA is still present (f and g_d are left unchanged), and only the velocity dependence is switched off:

$$\begin{aligned} g &= Z_a + F_h\, Y_v\, (1 - e^{-\gamma \frac{1}{B_w}(\dot{L} - \dot{h_w})^2}) \\ &\longrightarrow Z_a + F_h\, Y_v\, (1 - e^{-\gamma \frac{1}{B_w}(\dot{L_{in}} - \dot{h_w})^2}) \end{aligned} \tag{6.9}$$

where $\dot{L_{in}}$ is an input function, extracted from the baseline simulations of the CVS model.

The basis of the FIXED BIOCH model is to remove all length and velocity dependences of the CB biochemical cycle: the three procedures described by Eqs. (6.3), (6.4) and (6.9) are thus applied to the isolated ventricle model.

The influence maps of the different variables for the NO VD and FIXED BIOCH models are presented in Fig. 84. We see that [3Trop] are still influenced by L for the NO VD model, while [3Trop] act as if they were input functions for the FIXED BIOCH model since all the length and velocity dependences were removed.

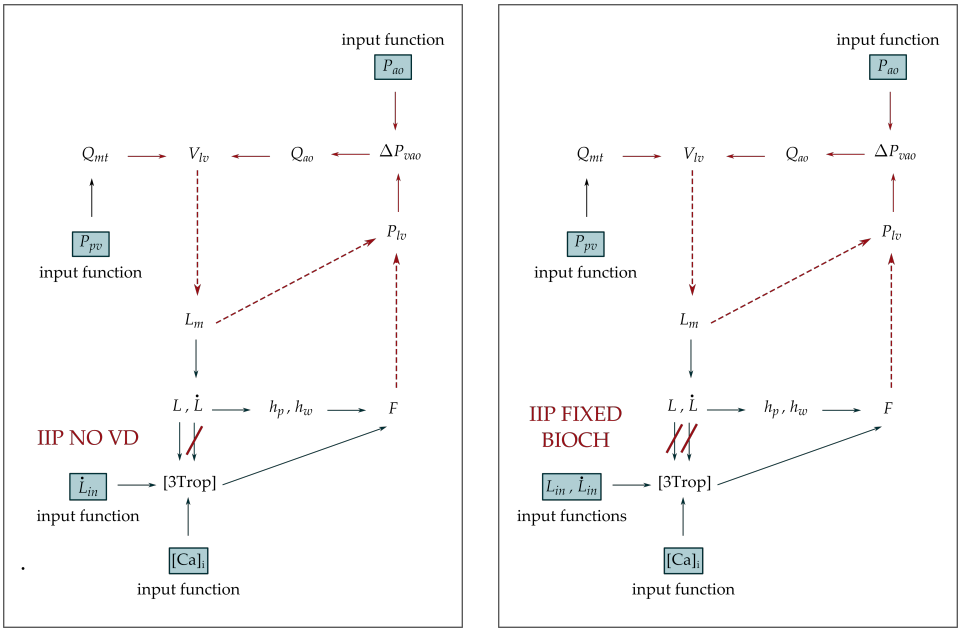

Figure 84: Influence maps of the different variables for the NO VD and FIXED BIOCH isolated ventricle models. (a) In the NO VD model, the velocity-dependence of [3Trop] is switched off, but the length-dependence is preserved. (b) In the FIXED BIOCH model, both length and velocity dependences are removed, and [3Trop] can thus be seen as input functions of the model.

We want to emphasize now that, whether talking about the NO LDA, NO VD or FIXED BIOCH model, the produced force does not only depend on [3Trop], but it also depends on h_p and h_w, which are both altered by length variations. As a reminder, h_p and h_w are the elongations of two equivalent CBs described in Chapter 4. The dynamics of h_p and h_w is related to the equivalent CBs dynamics, which are themselves related to the mechanics of sarcomere shortening (see Fig.

54 and Eqs. (4.35)-(4.38)). These dynamics are phenomenological descriptions which connect the sarcomere length variations to the equivalent CBs elongation. So, even for the FIXED BIOCH model, an inevitable length-dependence remains. Still, the biochemistry of sarcomere contraction, described by the biochemical CB cycle, is rendered completely length-independent with the FIXED BIOCH model.

6.5.1 *IIP with the NO VD model*

An IIP protocol is applied with the NO VD isolated ventricle model presented in Fig. 84a. The resulting half-sarcomere length, produced force and PV loop are shown in Fig. 85 and compared quantitavely with the IIP case in Tables 8 and 9.

We see that there is a strong increase in SV with the NO VD model (+ 16,92 % compared to the IIP case). Once again, a closer look at the aortic flow facilitates the understanding. Indeed, as can be observed in Fig. 86a, a higher aortic flow means that a higher ΔP_{vao} is obtained when the VD is turned off. This result suggests that removing the shortening deactivation helps reaching a higher pressure during the whole ejection period (see Fig. 86b). However, this ejection period does not last longer compared to the IIP case (+ 0,09 %).

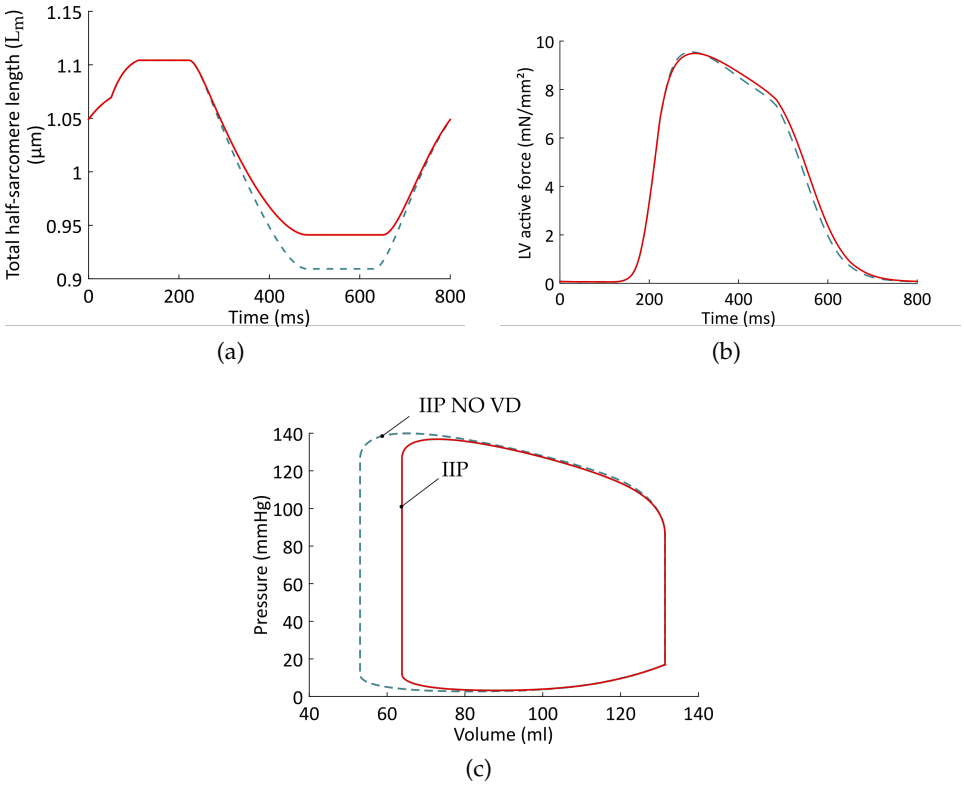

Figure 85: Instantaneous increase in preload with the NO VD model. (a) Total half-sarcomere length (L_m). (b) Normalized active force. (c) PV loop. Comparison of the IIP NO VD case (dashed blue line) versus the IIP case (red line).

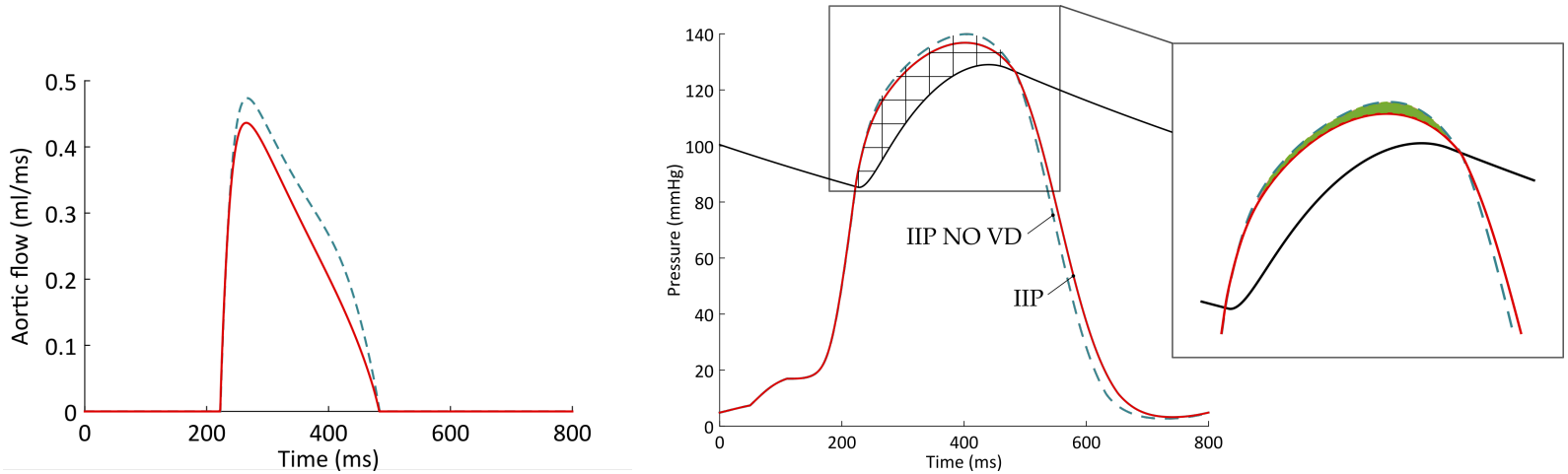

Figure 86: Visual representation of variations in SV for the IIP protocols with (red) and without (dashed blue) VD. (a) Aortic flow the IIP (red) and the IIP NO VD (dashed blue) cases. The ejection durations are similar for both models but the aortic flow amplitude is higher for the IIP case. (b) Ventricular and aortic pressures time evolution. The hatched aera enclosed between the ventricular pressure (red and dashed blue) and the aortic pressure (black) is proportional to the SV. We see that there is a difference in ventricular pressure amplitudes between the IIP and IIP NO VD models (green area), which accounts for the difference in SV.

In the NO VD model, the dynamics of contraction following preload increase has changed in such a way that only the amplitude of the aortic flow increases, while the ejection period is similar to the IIP case.

6.5.2 *IIP with the FIXED BIOCH model*

An IIP protocol is also applied with the FIXED BIOCH model presented in Fig. 84b. The resulting half-sarcomere length, produced force and PV loop are shown in Fig. 87 and compared quantitavely with the IIP case in Tables 8 and 9.

We see that there is a strong decrease in SV with the FIXED BIOCH model (-46,09 % compared to the IIP case). This occurs because the aortic flow is lower and the ejection period is greatly reduced (Fig. 88a). In this case, the dynamics of pressure development has changed in such a way that a lower pressure is obtained through the whole ejection period (Fig. 88b), hence a lower ΔP_{vao}, which leads to a lower aortic flow and a shortened ejection period (- 38,95 % compared to the IIP case). This results suggest that removing the length and velocity dependences of the CB biochemical cycle hinders the positive adaptation of SV to preload increase.

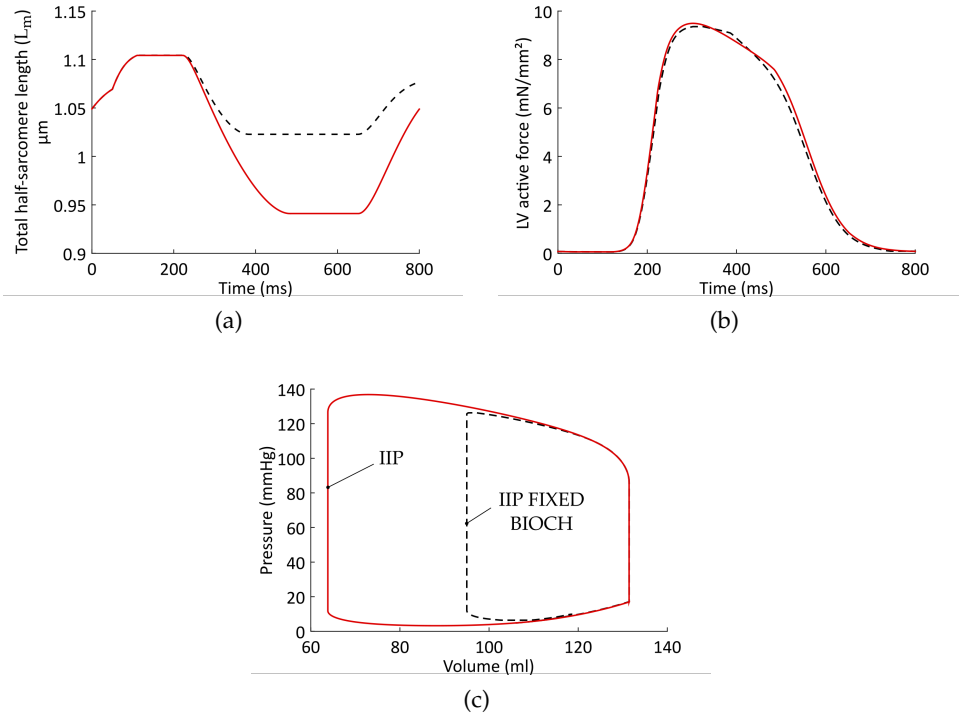

Figure 87: Instantaneous increase in preload with the FIXED BIOCH model. (a) Total half-sarcomere length (L_m). (b) Normalized active force. (c) PV loop. Comparison of the FIXED BIOCH case (dashed black line) versus the IIP case (red line).

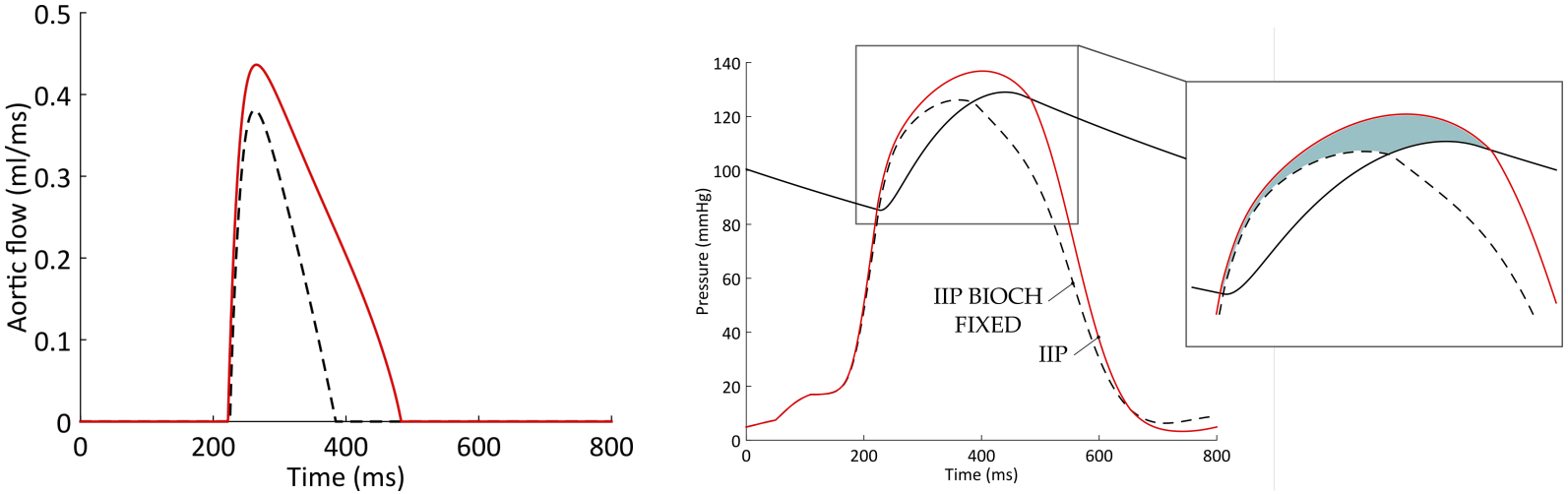

Figure 88: Visual representation of variations in SV for the IIP (red) and IIP FIXED BIOCH (dashed black) models. (a) Aortic flow for the IIP (red) and the IIP FIXED BIOCH (dashed black) cases. The amplitude of the aortic flow is reduced for the FIXED BIOCH model, as well as the ejection duration. (b) Ventricular and aortic pressures time evolution. We see that there is a difference in ventricular pressure amplitudes between the IIP and IIP FIXED BIOCH models. Besides, there is also a difference in the ejection duration. Both effects contributes to the decreased SV observed for the IIP FIXED BIOCH case. The relative SV difference between both models is related to the colored area.

	Stroke volume (ml)	Maximal active force (mN/mm²)	Maximal pressure (mmHg)
IIP	67,61	9,49	136,82
IIP NO LDA	59,37 (- 12,19 %)	9,55 (+ 0,62 %)	135,59 (- 0,90 %)
IIP NO VD	78,37 (+ 15,92 %)	9,55 (+ 0,59 %)	139,91 (+ 2,26 %)
IIP FIXED BIOCH	36,44 (- 46,09 %)	9,36 (- 1,38 %)	126,31 (- 7,82 %)

Table 8: Quantitative analysis of IIP protocols. Comparison with the original IIP case.

	t_{mtC} (ms)	t_{aoO} (ms)	Δt_{isoV} (ms)	Δt_{ej} (ms)
IIP	110	222,32	112,32	260,88
IIP NO LDA	110 (+ 0 %)	225,04 (+ 1,22 %)	115,04 (+ 2,42 %)	246,48 (- 5,52 %)
IIP NO VD	110 (+ 0 %)	222,64 (+ 0,14 %)	112,64 (+ 0,28 %)	261,12 (+ 0,09 %)
IIP FIXED BIOCH	110 (+ 0 %)	225,36 (+ 1,37 %)	115,36 (+ 2,71 %)	159,28 (- 38,95 %)

Table 9: Quantitative analysis of timing variations in IIP protocols. Comparison with the original IIP case.

6.6 THE INFLUENCE OF t_0

The IIP protocol analyzed in the previous sections is performed with a fixed t_0 value (see beginning of section 6.2), which dictates the beginning of the sudden P_{pv} increase. Since the results presented above suggest that the whole timing of contraction is altered following IIP, it is worth examining the influence of t_0.

To this end, we perform an IIP protocol for eight t_0 values ranging between 0 and 140 ms. In Fig. 89, the first, fourth and last IIP simulations are portrayed. The different P_{pv} curves are shown, along with the associated P_{lv} curves and the input P_{ao} curve.

SV as a function of t_0 is shown in Fig. 90a. We see that SV increases and reaches an optimal value at t_0^{opt} = 80 ms, then decreases. The maximal relative SV variation is less than 5 %. The shape of the SV curve can be explained by looking at the EDV curve shown in Fig. 90b. EDV starts decreasing once t_0 is greater than 80 ms, because the P_{pv} increase occurs too late in the contraction process compared to the optimal t_0^{opt} case, and a less effective preload increase is thus

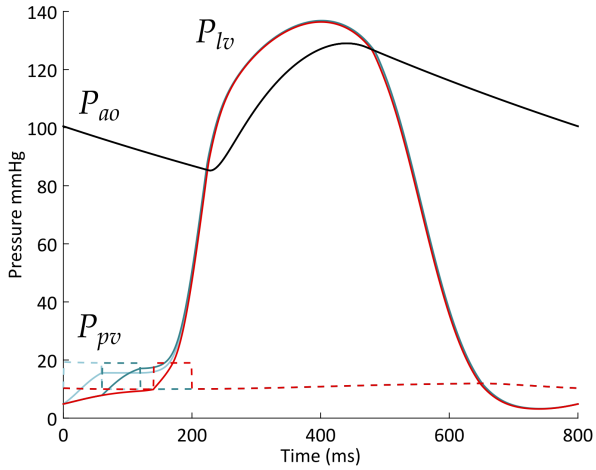

Figure 89: IIP protocols for different t_0 values. P_{pv} curves (dashed) and Plv curve (full line) for $t_0 = 0$ (light blue), 60 (dark blue) and 140 (red) ms. The input function P_{ao} is also represented.

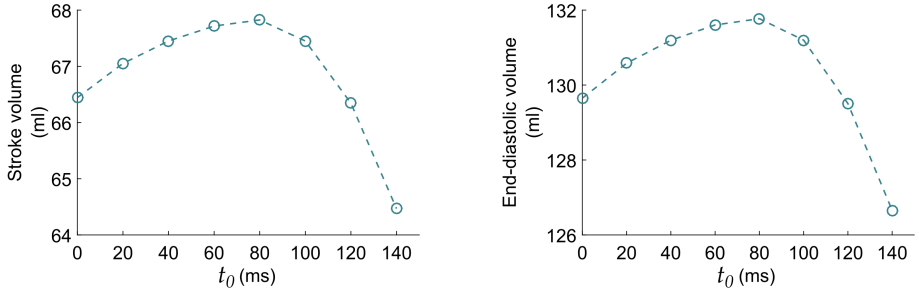

(a) (b)

Figure 90: Influence of t_0 on the IIP protocol. (a) SV as a function of t_0. An optimum is reached at $t_0 = 80$ ms. (b) EDV as a function of t_0. An optimum is also reached at $t_0 = 80$ ms, which means that there is an optimal preload increase at $t_0 = 80$ ms, responsible for the optimal SV.

achieved. In other words, an efficient preload increase is achieved only is t_0 is not to high, and this preload increase is optimal for $t_0^{\text{opt}} = 80$ ms.

The aim of the IIP protocol is simply to obtain an increase in preload. We choose to work with an suddent P_{pv} increase starting at $t_0 = 50$ ms and lasting 60 ms, which leads to an EDV equal to 131,43 ml. This corresponds to an increase in preload compared to the BL case (see Table 5). We can however decide to work with other values for t_0 and the P_{pv} increase duration, as long as the same EDV is achieved. For instance, if we use $t_0 = 0$ ms and a duration of 80 ms (IIP bis), we obtain the same EDV (131,85 ml), and the same global behavior of the system, as observed in Fig. 91 where the obtained PV loops are identical for the IIP and IIP bis protocols. These results confirm that the IIP protocol may be set up with different t_0 and duration values, as long as the same EDV is achieved if a comparison needs to be made.

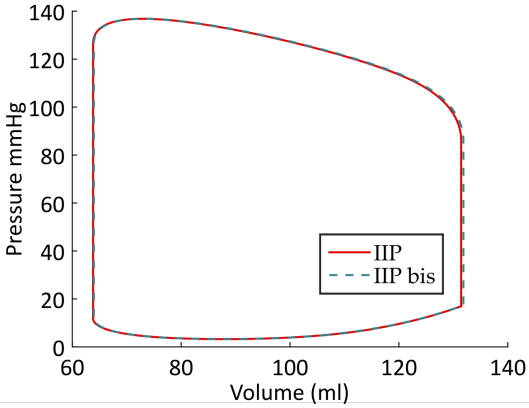

Figure 91: Comparison of the IIP and IIP bis protocols. The IIP protocol corresponds to $t_0 = 50$ ms and lasts 60 ms. The IIP bis protocol corresponds to $t_0 = 0$ ms and lasts 80 ms. Both protocols lead to almost the same EDV, hence the same preload. As a result, they lead to the same global behavior of the system, as observed on the PV loops, which are almost identical.

6.7 CONCLUSIONS FROM THE ISOLATED VENTRICLE MODEL

The results presented in the previous sections were obtained with an isolated ventricle submitted to an instantaneous increase in preload (IIP). This isolated ventricle model was extracted from the CVS model presented in Chapter 4 and adapted so that only the preload could be varied, all other variables remaining unchanged.

We first observed that an increased SV was obtained following preload increase, which is the definition of the FS mechanism. The maximal developed force increased, as well as the maximal developed pressure (but to a lesser extent). With the NO LDA model, no substantial increase in SV was observed, indicating that LDA is indeed required for the FS mechanism to be observed. However, an increase in maximal force still occured with the NO LDA model. This shows that maximal force and pressure may not be relevant indices when studying the preload effect on SV. Indeed, we first clarified the relationship between force and pressure, and showed that pressure is also determined by sarcomere length L_m, which is also affected by preload variations. For instance, in the NO LDA model, we observed an increased maximal force, but no increase in maximal pressure. This is why no increase in SV occured.

Secondly, we showed that it is actually the whole time development of pressure during the ejection period that is ultimately responsible for the SV variations upon preload increase. By looking at the aortic flow, we showed that Q_{ao} increased in IIP, both in amplitude and duration. This resulted in an increased SV (SV being the area under the aortic flow curve). Since the aortic flow is determined by the pressure gradient $\Delta P_{vao} = P_{lv} - P_{ao}$, and since P_{ao} is an input of the isolated ventricle model, it is the ventricular pressure development during the whole ejection period that dictates both ΔP_{vao} and the ejection duration period. This pressure development is altered following IIP.

From these observations, we can deduce that the increase in SV following IIP is not only mediated through an increase in maximal produced force at the

cellular scale. This suggests that the FS mechanism is a length-dependent effect that is not only related to the maximal produced force. From what we saw above, this length-dependent effect rather impacts the whole dynamics of contraction and ejection at the organ and CVS scales. In other words, we can say that preload variation sets up new initial conditions at the beginning of the cardiac cycle, which in turn alter the whole dynamics of length and pressure development. We see that FS mechanism is really a *multiscale* phenomenon, where the cellular variables and the hemodynamic variables influence each other during the whole heartbeat. It is not an easy task to dissociate all the variables involved in this altered dynamics of contraction in IIP. The influence map presented in Fig. 82 shows the complex correlations between the different variables (length, force, pressure, ...) and the impossibility to extract one independent variable which could command all the others. However, it is now possible to "track" markers of preload alterations, such as an increased ΔP_{vao} and an increased Δt_{ej}.

Finally, we also worked with the NO VD and FIXED BIOCH models. The first allowed to partially shut down shortening deactivation, and the second allowed to work with a complete length-independent CB biochemistry. We observed that, following IIP:

- A great increase in SV is observed with the NO VD model. This suggests that shortening deactivation is actually detrimental to pressure and force developement.
- A great decrease in SV is observed with the FIXED BIOCH model, as SV actually reaches a value inferior to the BL case. This suggests that the length and velocity dependences of the biochemical cycle are required for the system to adapt properly to preload variations.

To close this section, let us emphasize again that all the above conclusions are drawn for an isolated ventricle model. This model helped to build an IIP protocol where only the preload could be varied. But the obtained results have limitations regarding the results translation to the whole CVS model, mainly because the afterload was modelized as a given $P_{ao}(t)$. In the next section, the IIP protocol is adapted to the whole CVS model.

6.8 THE FS MECHANISM *in vivo*

We have studied before the FS mechanism in an isolated ventricle model but it is very important to extend the analysis in the *in vivo* situation described by the whole CVS model. To reproduce an instantaneous increase in LV preload with the whole CVS model, the mitral flow, Q_{mt} is artificially increased by 0,43 ml/ms during 60 ms during the left ventricular filling phase. This value was chosen so that the EDV following IIP is equal to the EDV from the isolated ventricle model. This IIP protocol is also performed with a NO LDA CVS model, where the biochemical rates f and g_d were adapted in the same way as in Eqs. (6.3) and (6.4) for both ventricles. The resulting developed LV force, PV loop and timing of contraction are shown in Fig. 92, and the values of relevant variables are summarized in Table 10.

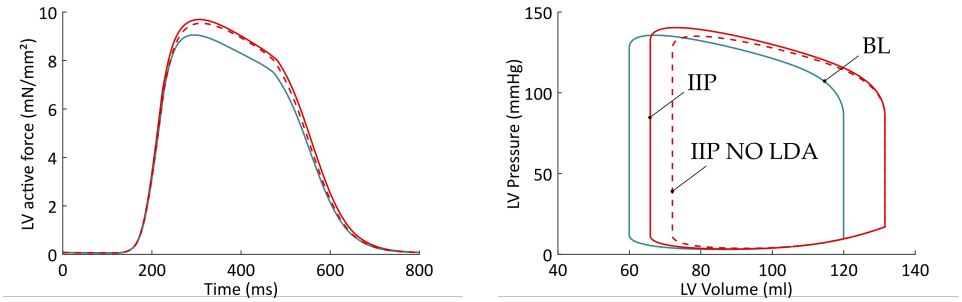

(a) (b)

Figure 92: Instantaneous increase in LV preload in the whole CVS model. (a) Normalized active force. (b) PV loop. Comparison of the baseline case (blue line) versus the IIP case (red line) and the IIP NO LDA case (dashed red line).

	End-diastolic volume (ml)	Stroke volume (ml)	Maximal active force (mN/mm²)	Maximal pressure (mmHg)	Δt_{ej} (ms)
BL	119,96	60	9,05	135,65	245,28
IIP	131,53 (+ 9,65 %)	65,68 (+ 9,47 %)	9,69 (+ 7,07 %)	140,37 (+ 3,48 %)	257,44 (+ 4,96 %)
IIP NO LDA	131,54 (+ 9,66 %)	59,50 (- 0,84 %)	9,54 (+ 5,34 %)	135,06 (- 0,44 %)	246,40 (+ 0,96 %)

Table 10: Quantitative analysis of LV IIP protocol in the whole CVS model.

First of all, we observe that SV increases in the IIP case (+ 9,47 %) while it does not change significantly with the NO LDA model. The maximal force increases in the IIP case (+ 7,07 %) and also, to a lesser extent, in the IIP NO LDA case (+ 5,34 %). The dynamics of contraction is also altered by the IIP protocol. Δt_{ej} increases for the IIP model, while it does not vary significantly for the NO LDA model. These observations are qualitatively similar to the results obtained with the isolated ventricle model. This justifies our initial procedure of extracting the ventricle from the CVS model to study only the preload effect, and allows relating the the conclusions drawn for the isolated ventricle model to the observations made with the whole CVS model. The only difference is that the maximal force for the IIP case is now greater than for the IIP NO LDA.

As with the isolated ventricle model, we can also conclude here that LDA is the mechanism responsible for the SV increase upon preload alteration, but the increase in maximal cellular force is not enough to explain this SV increase. The dynamics of contraction is actually globally affected by the preload increase, which sets new initial conditions for length, force and pressure development. The altered pressure developement leads to an increased amplitude of the pressure gradient ΔP_{vao}, which also induces a longer ejection duration. Both effects explain the SV increase, and these effects arise from a *multiscale* interaction between cellular and hemodynamic variables. Regarding the NO LDA CVS model,

preload also affects the dynamics of pressure development but the absence of LDA means that this altered dynamics does not lead to an increased ΔP_{vao}, hence the absence of any SV increase.

A NO VD and a NO BIOCH CVS models were also built following the same procedure than for the isolated ventricle model. The quantitative results are summarized in Table 11. We observe:

- An increased SV and maximal pressure for the IIP NO VD model compared to the IIP case,
- A decreased SV, maximal pressure and ejection duration for the IIP FIXED BIOCH compared to the IIP case.

	End-diastolic volume (ml)	Stroke volume (ml)	Maximal active force (mN/mm²)	Maximal pressure (mmHg)	Δt_{ej} (ms)
IIP	131,53	65,68	9,69	140,37	257,44
IIP NO LDA	131,54 (+ 0,01 %)	59,50 (- 9,41 %)	9,54 (- 1,62 %)	135,06 (- 3,78 %)	246,40 (- 4,29 %)
IIP NO VD	131,53 (+ 0 %)	68 (+ 3,53 %)	9,73 (+ 0,36 %)	142,08 (+ 1,21 %)	260,56 (+ 1,21 %)
IIP FIXED BIOCH	131,54 (+ 0,01 %)	46,88 (- 28,63 %)	9,28 (- 4,26 %)	124,69 (- 11,17 %)	223,68 (- 13,11 %)

Table 11: Quantitative analysis of LV IIP protocol in the whole CVS model. Comparison with the original IIP protocol.

These results are qualitatively similar to what was observed with the isolated ventricle model, thus validating again our previous approach.

In the present protocol describing the *in vivo* situation, a physiological afterload is used (P_{ao} is not an input function anymore) and the LV pressure development during ejection modifies this aortic pressure. Indeed, the pressure gradient $\Delta P_{vao} = P_{lv} - P_{ao}$ dictates the aortic flow and thus the aortic volume and pressure evolutions (see the influence map in Fig. 73). Actually, the afterload increases following IIP, as shown in Fig. 93a. This increased afterload will in turn dictate the ejection resistance and the LV pressure development. So here there is a competition between an increased ventricular pressure, which tends to increase the ejecting capacity by increasing ΔP_{vao}, and an increased afterload, which tends to oppose SV increase by decreasing ΔP_{vao}. By looking at the aortic flow (Fig. 93b), a quantity that is proportional to ΔP_{vao}, we can deduce immediately which effect takes over. Since the aortic flow amplitude increases for the IIP case compared to the BL case, this means that the increased ventricular pressure developement counterbalances the afterload increase and leads to an increased ΔP_{vao}. This increased ΔP_{vao} also induces a prolonged ejection duration. Finally, the SV is indeed increased, although this increase is lower than what was observed with the unchanged afterload case.

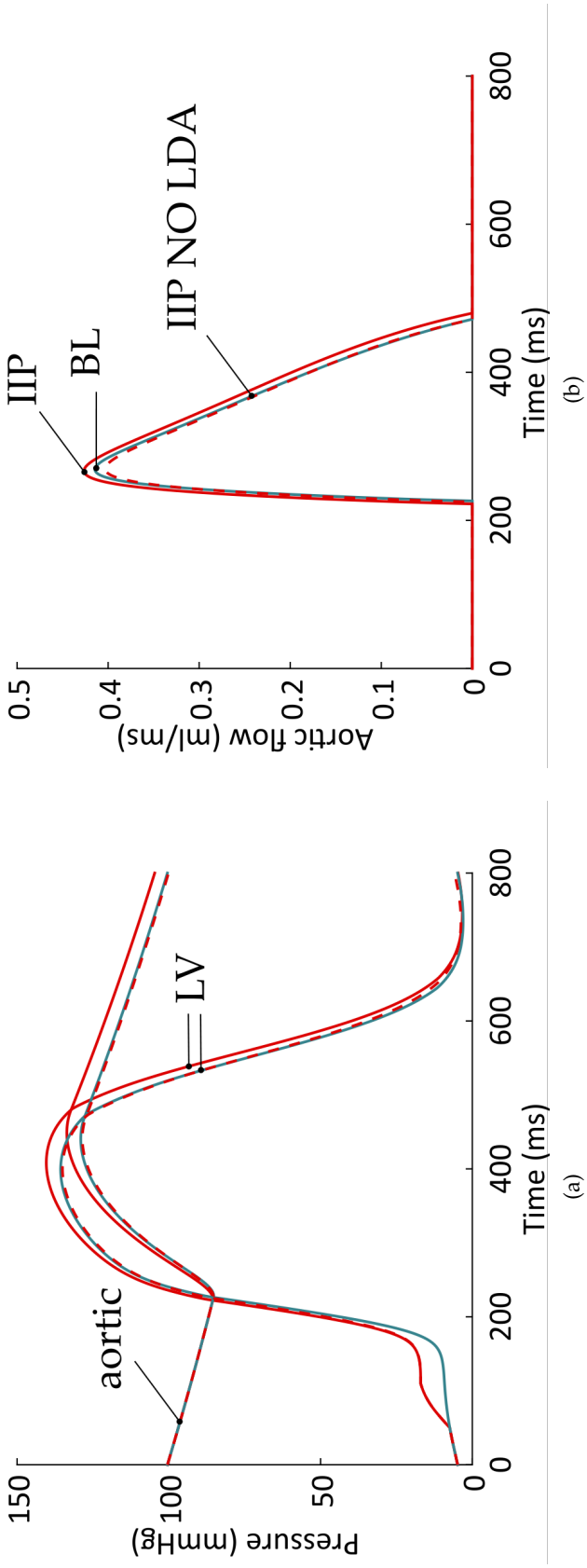

Figure 93: Aortic flow, ventricular and aortic pressures during instantaneous increase in LV preload in the whole CVS model. (a) Ventricular and aortic pressures for the BL (blue), IIP (red) and IIP NO LDA (dashed red). For the IIP case, the increase in ventricular pressure during ejection is followed by an increase in aortic pressure, thus lowering the obtained SV compared to an unchanged afterload situation. (b) Aortic flow increases with IIP (red) compared to the BL case (blue), and slightly decreases for the IIP NO LDA case (dashed red). The ejection duration is greater for IIP. Thus, despite the increased afterload, the increased pressure development following IIP counterbalances the afterload resistance. This leads to an increased aortic flow amplitude and ejection duration.

Here, contrary to the isolated ventricle model, we see that afterload is also affected by the preload increase. The increased "ejecting-capacity" of the ventricle implies a secondary increase in afterload which partially counterbalances the SV increase. In other words, an increase in blood volume ejection capacity actually increases the aortic pressure, as more blood is ejected into the aorta. The afterload thus increases and tends to lower the expected increase in SV [1].

Consequently, we can say that the whole dynamics of contraction is regulated by preload, which sets the initial conditions for contraction, and afterload, which opposes blood ejection. As already pointed out by Katz [42]: "an important factor in the heart's performance is the manner in which the contraction of the heart is accomplished" and "... the characteristics of contraction, which is dependent upon the nature of the arterial pressure variations during the ejection period, help to regulate the performance of the heart beat".

6.9 SUMMARY

The FS mechanism is a global effect induced by an acute increase in preload that results in an increased SV. The common given explanation of this phenomenon is that, as preload increases, LDA, the assumed cellular basis for the FS mechanism, is triggered and the maximal produced force increases, and so does the SV. It is important to remember that LDA is essentially highlighted and defined in isometric experiments (force-tension and force-pCa curves, described in Chapter 3) while cardiac fibers actually undergo auxotonic contractions in a beating heart. In the previous sections, we asked ourselves the following question: is the LDA responsible for the FS mechanism *in vivo*?

To answer this question, we performed an IIP protocol both on a isolated ventricle model and on the whole CVS model. We showed that the mechanism underlying the SV increase following a preload increase can actually be interpreted as follows:

- As preload increases, both maximal developed force and pressure increase, but no to the same extent.
- The increase in maximal force is not enough to predict SV variations, as pressure, the real determinant of SV, is also determined by ventricular dimensions.
- It is the increase in pressure throughout the whole ejection period that increases the pressure gradient ΔP_{vao}. This altered dynamics of contraction and ejection is the result of an altered preload which sets new initial conditions at the beginning of contraction.
- $\Delta P_{vao}(t)$ dictates the aortic flow and the ejection duration. Eventually, SV, which can be calculated as the area under the aortic flow, increases with increasing aortic flow amplitude and Δt_{ej}, both effects being observed following an increase in preload.
- The length-dependence of force developement (LDA) is required to observe an increase in SV following preload alteration. On the other hand,

the velocity-dependence tends to reduce the potential increase in SV, while a completely length-independent biochemistry of CB cycling leads to an inadaptability to preload increase.

- Afterload is secondarily affected by preload alteration and also modulates SV. It actually reduces the expected SV compared to an unchanged afterload situation, like in the isolated ventricle analysis.

In fine, we see that an increase in preload sets new initial conditions at the onset of contraction. This leads to an increase produced force, but this also alters the whole dynamics of length, force and pressure (both for the ventricle and the afterload) developments. As a consequence, amplitude of aortic flow and ejection duration vary. Since they both define SV, the latter varies as well.

To conclude, we can argue that the FS mechanism is a *multiscale and dynamical LDA-driven response to a change in preload*. This response does not only manifest as an increase in produced cellular force, but also as an altered dynamics of contraction.

It is worth pointing out that in one of their founding studies, Patterson, Piper and Starling [7] declared that "the amount of energy set free [...] during each contraction of the ventricles will be determined not merely by the initial length of the fibres composing its walls, but by the length of these fibers throughout the period of contraction. [...] During the whole of this time therefore the influence of length of muscle fibre will be potent in increasing the mechanical stress set up in the muscle." More than 100 years later, De Tombe and Tyberg [19] suggest that the myocardium present an "ejection-history dependence", basing their reasoning on the positive effect of ejection observed experimentally at the cellular [97] and ventricular scales [98] and discussed in Chapter 3. The experimental study of De Tombe and Little [97] concluded that "... conditions set up early in the contraction at the end-diastolic volume may determine contractile state throughout the entire contraction and thus constitute a short-term memory mechanism." These statements confirm our observations and, to our knowledge, this thesis work is the first to analyze in details this relationship between the LDA mechanism (cellular scale) and the FS mechanism (organ scale), and to challenge the consensual definition of the FS mechanism.

6.9.1 *The FS curve*

The schematic curve shown in Fig. 72 is portrayed in many textbooks and in the literature, but the underlying explanation is generally vague or even incorrect. First, the general context is not always clarified. The FS mechanism is an *instantaneous* mechanism that occurs on a beat-to-beat basis when only the preload is varied, all other variables remaining constant. Secondly, the increase in maximal force is not a consistent predictor for SV increase. Finally, there is a secondary increase in afterload following preload alteration. Since all these observations are rarely taken into account regarding the FS mechanism definition, inconsistencies can be found regarding the proposed FS curves, or the proposed PV loops (Fig. 76) in the litterature. On the other hand, and as explained in the

beginning of this chapter, obtaining such curves experimentally is very challenging.

With our model, we can easily build an FS curve which is consistent with the FS mechanism definition, by performing IIP protocols for different Q_{mt} increase (or decrease) values. The obtained SV is reported as a function of preload in Fig. 94, preload being defined as the maximal total half-sarcomere length, $L_m^{\max}$. We see that SV is an increasing linear function of preload, and we do not observe the commonly assumed curvilinear shape or the plateau phase for high preloads.

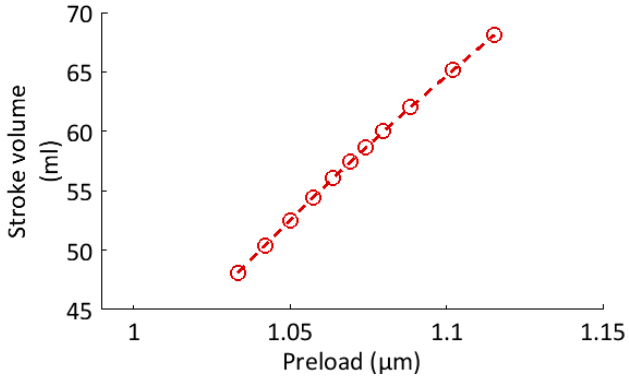

Figure 94: Simulated FS curve with the CVS model. Preload is defined as the maximal total half-sarcomere length $L_m^{\max}$. We observe a linear function, instead of the assumed curvilinear shape. Besides, there is no plateau phase for high preloads.

As noted by Glower *et al.* [182], the shape of the FS curve can go from linear to curvilinear depending on the chosen preload index. In their work, they focused on SW instead of SV (the relevance of both notions will be discussed later in this chapter). They showed that SW is a linear function of EDV, and compared their results to those obtained by Sarnoff *et al.* [43] where SW plotted as a function of EDP resulted in a curvilinear curve, with a plateau phase. They explained that these observations reflected the exponential diastolic pressure-volume curve. So, depending on the chosen preload index, we can expect the FS curve to vary in shape, and the schematic FS curves presented in the literature are more generally drawn considering pressures (either EDP or the atrial pressure) as preload indices, even though sometimes the preload index is not explicitely defined at all.

Besides, the experimental methods used by Glower *et al.* [182] are close to ideal conditions for studying the FS mechanism in vivo: preload is transiently varied with Fogarty protocols (vena cava occlusions and releases) on conscious dogs, whith a pharmacologic attenuation of autonomic reflexes (to limit extrinsic alterations of the cardiac response). Their work focused on SW instead of SV, but in their paper they also provided a curve where SV was reported (see Fig. 95). We see that SV appears as a linear function of EDV, an experimental result similar to our *in silico* result from Fig. 94.

After these general physiological considerations, we can now discuss the FS mechanism with regard to the clinical applications it is associated with. In the next section, we will analyse the basis of vascular filling therapy and challenge its relationship with the FS mechanism.

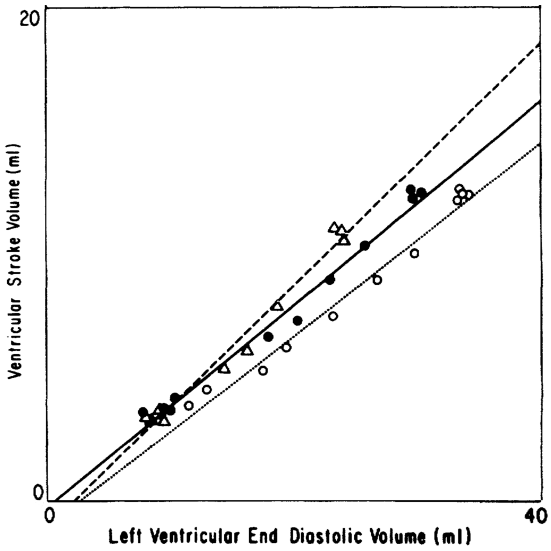

Figure 95: Linearity of the FS curve. SV as a function of EDV in conscious dogs during venal caval releases after occlusions (adapted from [182]). Closed circles: control case. Open circles and triangles: infusions of pharmacological agents to extrinsically modulate blood pressure.

6.10 VASCULAR FILLING

Vascular filling, also called *fluid therapy*, is a commonly used therapy in intensive care units that we described in Chapter 2. As a reminder, it consists in intravenous administration of fluid to a patient in order to increase the cardiac output. The FS mechanism is often considered as a strong basis for fluid therapy, because the increase in circulating blood volume leads to a permanent increase in preload, which is supposed to impacts the SV. Patients operating on the so-called "ascending limb" of the FS curve (Fig. 20, recalled in Fig. 96) are called "fluid-responsive", because the increase in circulating blood volume substantially increases their cardiac output. On the other hand, patient operating on the "saturating part" of the FS curve are not fluid-responsive. There are a lot of discussions about finding the ideal predictor of fluid responsiveness, as explained in Chapter 2. However, the issue that will be addressed here is related to the correlation that is generally assumed between the FS mechanism and fluid-responsiveness, and the relevance of the curve given by Fig. 96.

6.10.1 *Instantaneous versus stabilized behavior*

The FS mechanism occurs on a beat-to-beat basis and is by its very nature an instantaneous effect. But from a clinical perspective, the aim of vascular filling is to increase and *stabilize* the preload so that the SV increase can be maintained and the cardiac output improved. We see that it is delicate to associate the transitory FS mechanism with a stabilized increased cardiac output. We rather introduce the concept of *length-dependent fluid response* (LDFR), which we define as the mechanism underlying the motivations for vascular filling therapy: as circulating blood volume increases, preload increases and a *stabilized* substantial

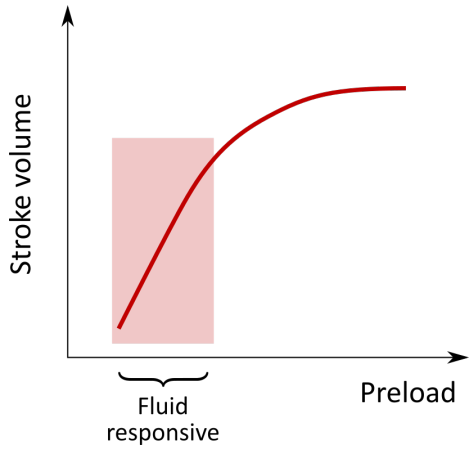

Figure 96: Frank-Starling curve and fluid responsiveness. For a patient operating on the ascending limb of the curve, an increase in circulating blood volume should lead to an increase in preload and to a substantial increase in stroke volume.

increase in SV is expected if the patient is fluid-responsive. Thank to our previous analysis, we can track the markers of the preload effect (not only maximal force and pressure, but also ΔP_{vao} and Δt_{ej}), and determine if LDA is the cellular origin of LDFR. To do so, the CVS model presented in Chapter 4 will be used to perform vascular filling simulations. The presented results come from stabilized simulations, where the system is allowed to reach a new steady-state following the perturbation caused by vascular filling. Note that we will only study the impact of the LDFR mechanism on this new steady-state. *In vivo*, many others mechanisms can take place and also modulate the new steady-state: HR or inotropy may vary, or the autonomic nervous system can adjust the circulating blood volume in response to vascular filling [48]. With that in mind, we can now introduce our vascular filling protocol.

6.10.2 *Stressed blood volume*

To mimick variations in circulating blood volume, the stressed blood volume (SBV) will be varied, and the system will be given enough time to stabilize before assessing the different variables. In our CVS model, SBV is simply defined as follows:

$$SBV = \sum_{chambers} V_i$$

where V_i is the stressed blood volume of chamber i.

The SBV value for the baseline case (described in Chapter 4) is noted SBV_0. In this model, volume filling (and emptying) experiments are associated with an increase (decrease) in SBV.

6.10.3 *Vascular filling simulations*

The results of simulations of volume filling experiments are shown in Fig. 97. Preload and SV in the left ventricle were calculated for a range of SBV values

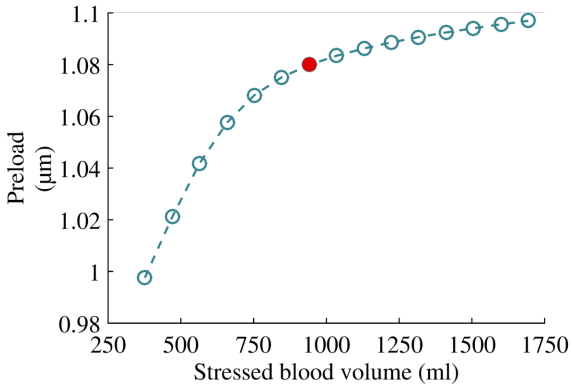

(a)

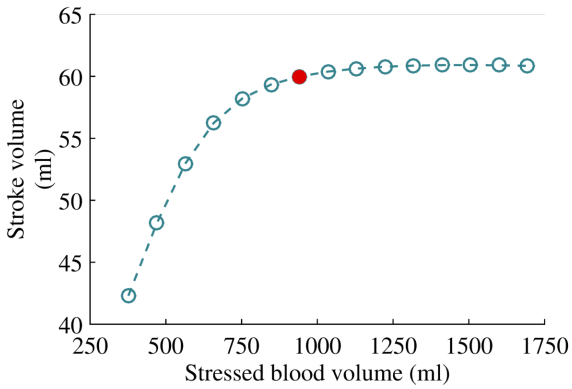

(b)

Figure 97: Vascular filling simulations. Preload (defined as $L_m^{\max}$) (a) and stroke volume (b) as a function of the stressed blood volume. The red marker corresponds to the SBV_0 value (baseline case).

lower and greater than SBV_0. An increase in SBV leads to an increased preload, which is defined here as the maximal total half-sarcomere length, $L_m^{\max}$ (Fig. 97a). For low SBV values, there is a sharp increase in SV, followed by a plateau phase (Fig. 97b). In Fig. 98, SV is plotted as a function of preload. It is important to emphasize that this curve cannot be directly compared to the schematic curve presented in Fig. 96 because the context under which they are obtained are fundamentally different. As already explained previously, the FS mechanism must be considered as an instantaneous effect of preload variation on the CVS, on a beat-to-beat basis. On the other hand, the vascular filling curves are related to a stabilized CVS behavior for a fixed value of SBV, that we introduced as LDFR. Increasing the circulating blood volume indeed increases the preload, but the latter cannot be considered as the only factor regulating the SV when performing vascular filling, as we explain now.

The maximal LV active force increase with SBV, as does the maximal LV pressure and the ejection duration Δt_{ej} (see Fig. 99). This is a manifestation of the LDA-driven dynamics of contraction following preload increase, as observed with the IIP protocols from the previous sections. Note that the increase in ejection duration was also observed experimentally by Braunwald and colleagues [46] who performed blood transfusions on human patients. We however notice that Δt_{ej} saturates for high SBV values, a behavior also observed for SV (Fig. 97b).

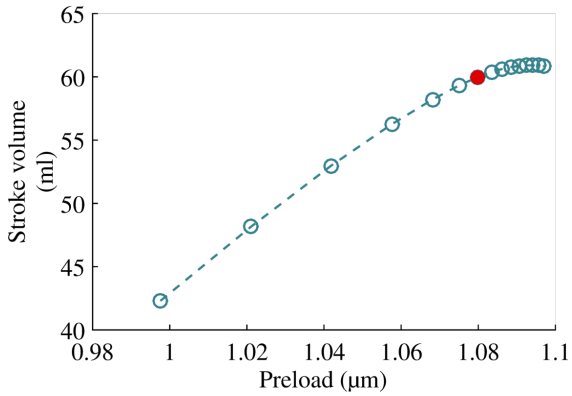

Figure 98: Stroke volume as a function of the preload. Despite it looking like the curve from Fig. 96, it does not represent the CVS behavior for instantaneous variation in preload only. Although the preload is altered by vascular filling, that is not the only changing variable and thus it cannot be solely held reponsible for SV variations.

This indicates that, for high SBV values, the ΔP_{vao} saturates and no subtantial increase in SV can be obtained. Another important factor regulating contraction needs to be adressed to further analyze these results: the afterload.

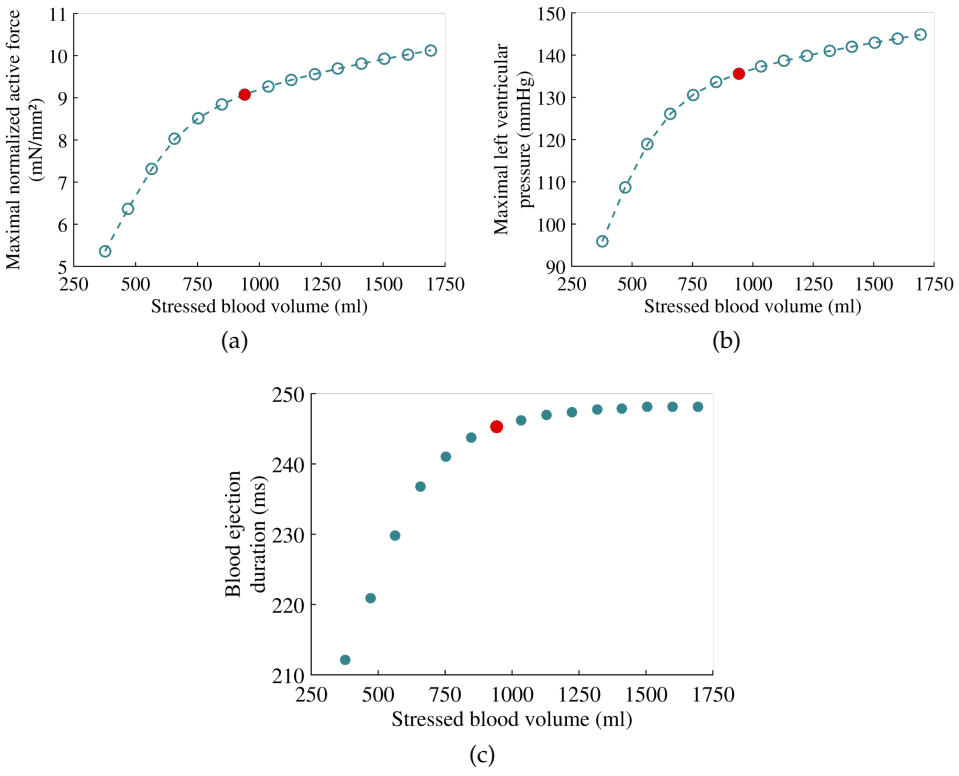

Figure 99: Maximal active force, maximal pressure and ejection duration Δt_{ej} during vascular filling simulations.

As for the IIP simulations in the whole CVS model, the aortic pressure is not an input function, and it will likely be altered by vascular filling. Since the circulating blood volume increases with vascular filling, we can assume that the afterload will increase. If we quantify the afterload by reporting the aortic pres-

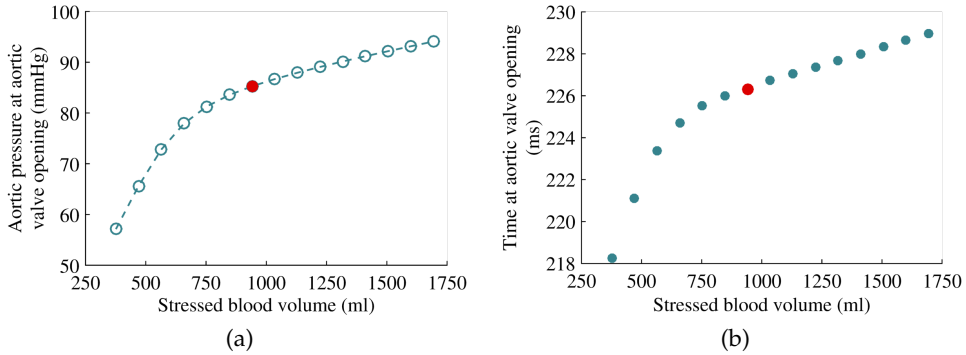

(a) (b)

Figure 100: Afterload and time of aortic valve opening during vascular filling simulations. (a) The afterload is defined as the aortic pressure at aortic valve opening (t_{aoO}). (b) Since the afterload increases with SBV, t_{aoO} increases, as the left ventricle has to overcome a higher value for the aortic valve to open.

sure at aortic valve opening (t_{aoO}), we can see from Fig. 100a that this quantity increases with SBV. Since this pressure represents the pressure the left ventricle has to overcome in order to open the aortic valve and starts ejecting blood,this explains why t_{aoO} increases with increasing SBV (Fig. 100b).

Once the ejection begins, the increased afterload will oppose blood ejection. So following vascular filling, there is a competition between an increased produced pressure (Fig. 99b) and an increased resistance to blood ejection (Fig. 100a). The ejected blood volume might not increase if the left ventricular pressure increase is not large enough compared to the aortic pressure increase. This competition, characterized by ΔP_{vao}, occurs during the whole ejection period, but in order to perform a quantitative analysis, we define ΔP, the numerical difference between the maximal pressure and afterload. ΔP is reported as a function of SBV in Fig. 101a. We see that ΔP saturates for high SBV values, indicating that the LDA-driven increase in pressure developement is not strong enough to couterbalance the afterload increase. This leads to a saturating ejection duration as well (reproduced in Fig. 101b for clarity purposes). As a global result, the SV follows the same tendency, and saturates for high SBV values. We see that, as for the FS mechanism, the LDFR is a deeply multiscale effect. Even if the cellular force increases, hemodynamical variables such a afterload also play a role in the response to vascular filling, and both effects must be considered to describe the global behavior at the CVS scale.

6.10.4 *Vascular filling without LDA*

We also performed the vascular filling simulations with the NO LDA CVS model. The results are presented in Fig. 102 and Fig. 103 and compared to the previous results. We observe a SV decrease with increasing SBV, instead of a saturating part, which is directly related to a decreasing ΔP for high SBV values. In other words, the maximal LV force and pressure do not increase enough compared to the increasing afterload, as LDA is turned off. Consequently, the ejection duration also decreases for high SBV.

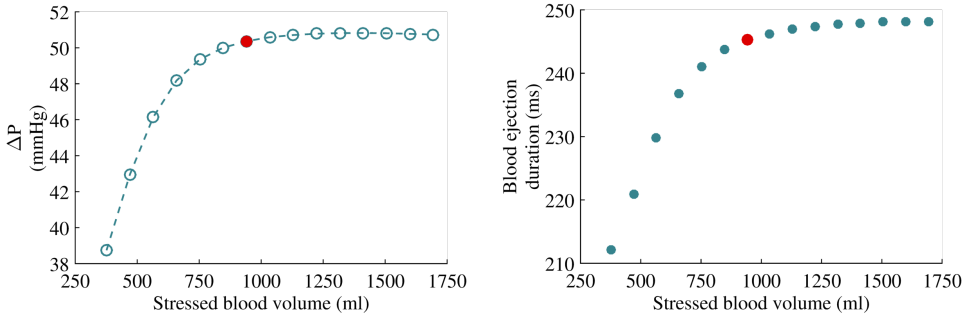

(a) (b)

Figure 101: Analyze of the saturating part of the SV curve. (a) Difference of the two curves from Fig. 99b and 100a (ΔP). For high SBV values, the increase in ventricular pressure is not sufficient to counterbalance the increase in afterload, ΔP saturates. (b) Δt_{ej}, which is dictated by ΔP_{vao}, also saturates for high SBV values.

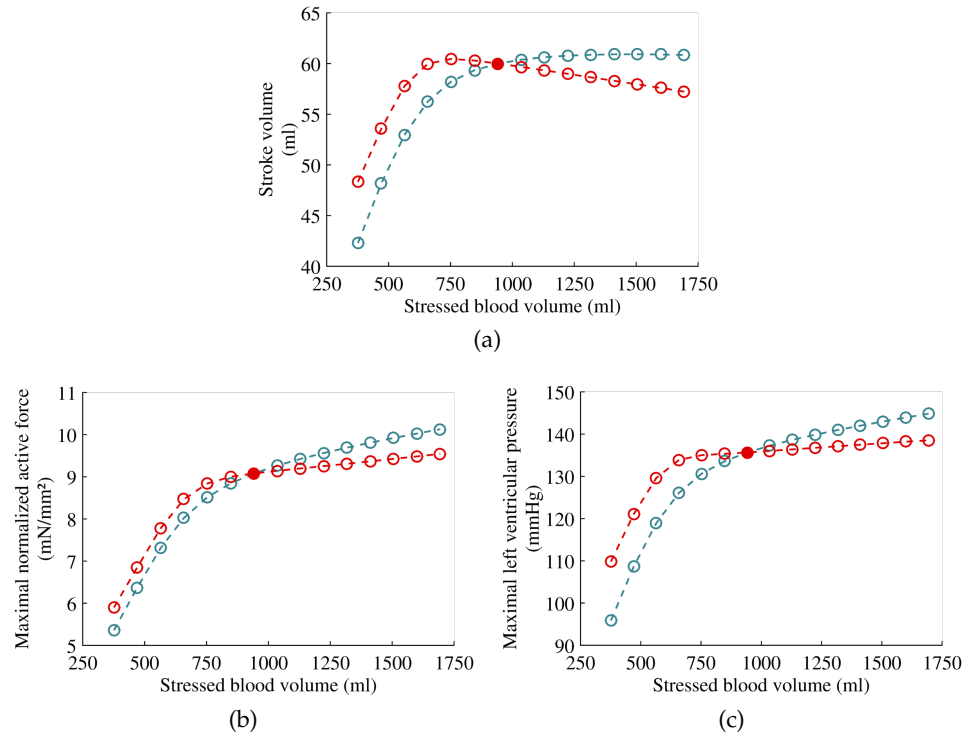

(a) (b) (c)

Figure 102: Vascular filling simulations with the NO LDA CVS model (red) compared to the baseline CVS model (blue).

6.10.5 *Conclusion*

The FS mechanism is regularly presented in the literature as the founding principle for fluid therapy. However, it is an instantaneous effect, while the aim of vascular filling is to increase and stabilize the preload so that the SV increase can be maintained and the cardiac output improved. We instead introduce the concept of length-dependent fluid response (LDFR) to describe the positive CVS response to an increase in circulating blood volume, which underlies the motivations for vascular filling therapy. In this section, we performed vascular filling

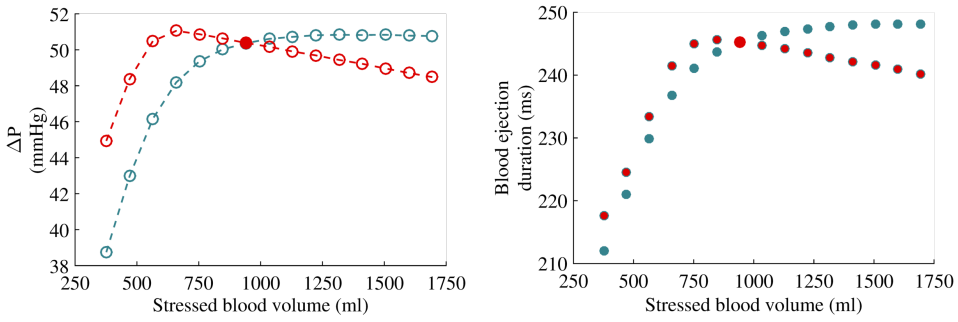

(a) (b)

Figure 103: Vascular filling simulations with the NO LDA CVS model (red) compared to the baseline CVS model (blue). ΔP (a) and ejection duration (b) as a function of SBV.

simulations and studied the impact of LDA on SV variations, in order to elucidate the presumed link between the LDFR and fluid therapy (Fig. 96).

The main consequences of vascular filling, as observed in our numerical simulations, are the following:

- Preload increases. And as preload increases, maximal produced force and pressure increase (LDA).
- The maximal ventricular pressure increases monotonously with SBV. If all other variables would remain constant, this would lead to a monotonous increase in SV, instead of the observed plateau phase for high SBV values.
- Another variable is affected by vascular filling: the afterload, which increases with SBV.
- Since the aortic flow is proportional to the pressure gradient ΔP_{vao}, the SV increase may saturate if the increase in ventricular pressure is not enough to counterbalance the increase in afterload. This happens for high SBV values.
- The timing of aortic valve opening/closing is also affected by the pressure gradient ΔP_{vao}. As SBV increases, the afterload increases. Consequently, the isovolumic contraction duration lasts longer (the ventricular pressure has to reach higher value before the aortic valve opens), and t_{aoO} increases. ΔP_{vao} also dictates the blood ejection duration, which saturates for high SBV values.

We can conclude, that for high SBV values, the increased afterload outweighs the LDA-driven pressure increase. LDFR is thus a multiscale phenomenon where both cellular and hemodynamic variables determine the global CVS behavior. This suggests that attention should not be drawn only to the preload during fluid therapy, because the afterload is also altered and definitely involved in SV changes. Our results indicate that there is in fact a saturating limit for vascular filling procedures.

It is important to emphasize that the saturating part of the vascular filling curve is not equivalent to the saturating part of the schematic FS curves from Fig.

96, as commonly assumed. In the beginning of this section, we challenged the relevance of the assumed correlation between the FS mechanism and vascular filling. To be more assertive, we now compare the simulated FS curve obtained in Section 6.9.1 with the vascular filling curve from Fig. 104. We see that the curves are not similar[5], and that there is a saturating part only for the vascular filling curve. As explained above, this saturating part occurs because the resistance to blood ejection increases highly during vascular filling, and even if the produced force and ventricular pressures continue to increase, a SV saturation is observed. In other words, the LDA effect is overshadowed for high SBV values, but there is still an "LDA reserve".

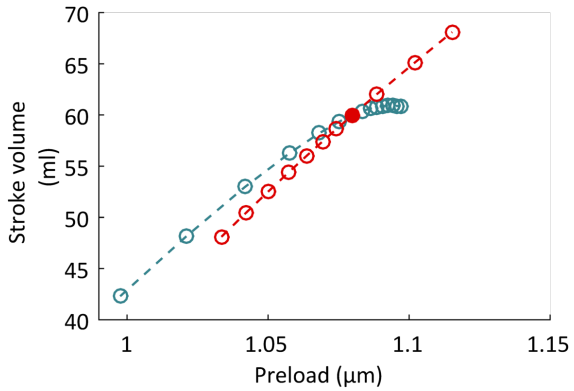

Figure 104: Comparison of the FS curve (red) and the vascular filling curve (blue). The former one is obtained under various instantaneous increases in preload, while the latter is obtained once a steady-state behavior following fluid infusion is achieved. Contrary to what is generally claimed, both curves are not comparable. In particular, the vascular filling curve presents a saturating part, but this saturating part cannot be associated with a saturating FS mechanism. It is rather linked to a high afterload increase for great fluid volume infusions.

6.11 NOTE ON STROKE VOLUME AND STROKE WORK

Stroke volume or cardiac output are generally the measured variables when discussing the FS mechanism. Sometimes however, the preload influence on stroke work is studied instead [43, 182]. We now briefly focus on this subject because SV and SW are commonly addressed without distinction when discussing the FS mechanism. Most of the time, this is not a problem because an increase in SV is positively correlated with an increase in SW. But this is not always the case, and in some situations SW appears to be a more relevant index for assessing the cardiac contractile function.

For instance, regarding the vascular filling simulations from the previous section, we notice that SW does not saturate for high SBV values, it rather still slowly increases (see Fig. 105). This means that the ventricular work production capacity is still increasing for high SBV values (although to a lower extent), even if SV saturates. This SV saturation occurs because the afterload is increasing,

[5]They however obviously cross at the preload value associated with the baseline SBV_0 value (red dot on the figure).

not because the ventricle pumping capacity is depressed. We see that SW better catch the intrinsic pumping ability of the heart.

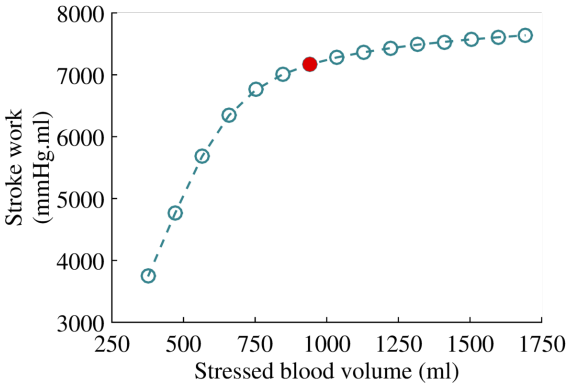

Figure 105: Stroke work as a function of SBV obtained from vascular filling simulations. Contrary to SV, the SW curve does not saturate for the high SBV values.

Furthermore, there may be situations where an increase in SV is not positively correlated with an increase in SW. To theoretically illustrate this, we perform "constant afterload" simulations with our isolated left ventricle model. In these simulations, P_{ao} is set at a constant value for simplicity puposes. Results for two afterload values (60 and 105 mmHg) are shown in Fig. 106 and described quantitatively in Table 12. Although the maximal force and pressure increase with an increased afterload, SV decreased (from 79,3 to 67,08 ml). On the other hand, SW increased (from 6061 to 7861 mmHg·ml). This means that the heart must pump more vigorously to eject blood as afterload increases. However, this increased in produced mechanical work does not automatically correlate with an increase in SV, as more "energy" is spent opposing the increased aortic pressure. This can be observed on the PV loops from Fig. 106b. The "high afterload" PV loop is narrower than the "low afterload" one (less ejected blood), but taller (greater developed pressure). The lesson here is that SV and SW are not interchangeable notions. The intrinsic ventricular pumping ability seems to be better captured by observing SW instead of SV. Indeed, ventricular pressure is used to calculate SW, contrary to SV, and this pressure depends on afterload, as ventricular pressure has to overcome aortic pressure in order to eject blood. However, SV (and cardiac output) is more commonly addressed in research and clinics, as it also represents an essential variable for cardiac function assessement.

	P_{ao} (mmHg)	Δt_{ej} (ms)	Stroke volume (ml)	Stroke work (mmHg · ml)
Low afterload	60	240,8	79,3	6061
High afterload	105	236	67,08	7861

Table 12: Quantitative analysis of the constant afterload protocol.

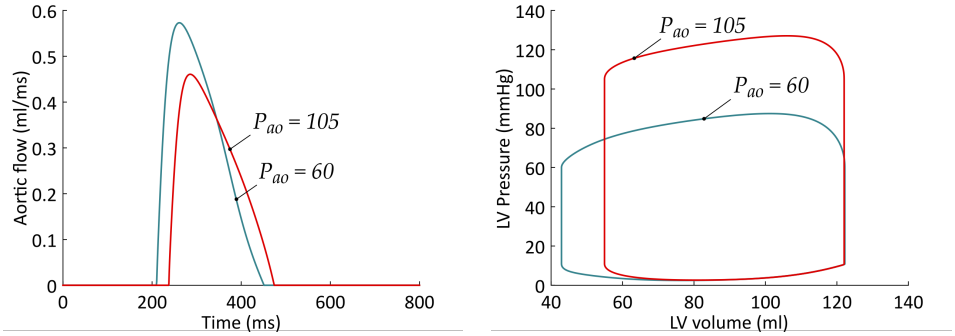

(a) (b)

Figure 106: Constant afterload protocol. The pulmonary pressure is 11 mmHg. The aortic pressure is 60 mmHg (low afterload) and 105 mmHg (high afterload).(a) Aortic flow and the corresponding afterload. (b) PV loop

6.12 SV EQUILIBRIUM

As explained in Chapter 2, it is generally accepted that the FS mechanism is responsible for balancing the right and left ventricular SV [1, 38, 39]. If a perturbation occurs inside the CVS (for instance, an increased venous return in the right ventricle during physical activity), SV equilibrium is suddenly impaired. Indeed, more blood is being ejected by the right ventricle because it received more blood than the left ventricle. The return to a stabilized situation is supposedly achieved through the "FS mechanism" as it is commonly defined in the litterature: an increase in ventricular preload induces an increase in produced force, and more blood is ejected. If more blood enters a ventricle, more blood will be ejected during this beat, so no "stagnant" amount of blood will accumulate inside the cavity. Furthermore, this extra volume of ejected blood will soon reach the other ventricle, where it will also be ejected thanks to the FS mechanism. Therefore, the ouputs of both ventricles are matched over time, and no blood volume accumulates in one circulation. However, one may ask if the FS mechanism, defined as an LDA-driven increase in SV following preload increase, is actually essential for SV equilibrium. That is, if a balance between ventricular outputs could not be achieved without any length-dependent activation of cardiac contraction. To investigate this, we induce a left ventricle IIP inside the whole CVS model, and let the system reach a new steady-state, where SV equilibrium is restored. We keep track of the transitory states by looking at the relative SV difference ΔSV computed at each beat:

$$\Delta SV = \frac{SV_{lv} - SV_{rv}}{SV_{lv}} \tag{6.10}$$

We actually normalize ΔSV relatively to the initial ΔSV_i value, and depict the results in Fig. 107. We see that $\Delta SV / \Delta SV_i$ gets smaller than 0,1 after 89 beats. At this point we can consider that SV equilibrium is indeed restored.

To compare the results in the absence of the FS mechanism, we turn the LDA off on the second beat after the IIP protocol, in order to observe if SV equilibrium can still be restored. We see that $\Delta SV / \Delta SV_i$ gets below 0,1 after 103 beats,

so SV equilibrium is indeed restored, and after a similar time period. These results suggest that the FS mechanism is not essential for SV equilibrium. In other words, only the hemodynamic scale seems to be involved in the restoration of SV equilibrium.

This result seems in contradiction with a study performed by Chaui-Berlinck and Monteiro [189], where they examinated the role of the FS mechanism in ventricular output matching. They could "turn off" the FS mechanism inside their mathematical model by assuming that ventricles produced a constant pressure, independent of ventricular volume, instead of a pressure that increased linearly with ventricular volume. They concluded that the FS mechanism was not necessary to provide stability to the operating point of the CVS, but that it allowed for a much faster return to an operating point after a perturbation [189]. Our results from Fig. 107 do not lead to the same kind of conclusion, but it is worth mentionning that we work with a pressure that still depends on ventricular volume, and is thus not constant within a heartbeat.

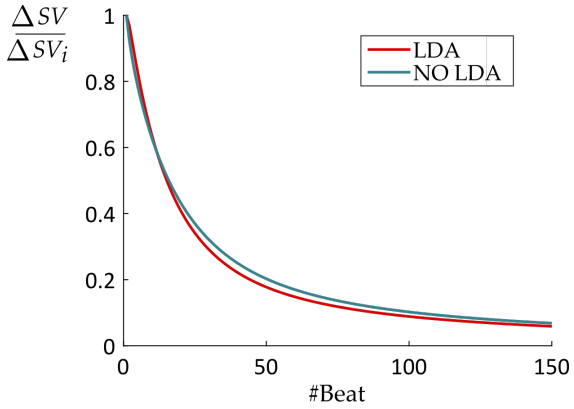

Figure 107: SV equilibrium restoration after a perturbation inside the CVS model. A left ventricular IIP is applied to the CVS model at the first beat. The normalized ΔSV for the CVS model (red) and the NO LDA CVS model (blue) are represented. After 89 beats, SV equilibrium is considered restored in the CVS model, and it is also restored after 103 beats when LDA is turned off

6.13 LINK WITH OTHER WORKS

Niederer and Smith [27] studied the role of the FS mechanism in the efficient transduction of work (ETW) from the cell to the organ, with a multiscale model of the rat left ventricle. Their finite-element model contains an electromechanical rat myocyte model where a filament overlap effect on developed tension and a length-dependent calcium sensitivity are implemented, which make up the FS mechanism. They notably performed simulations with and without these cellular mechanisms (those methods are similar to our "NO LDA", "NO VD" and "FIXED BIOCH" approaches). ETW was quantified by a metric relating the total amount of work performed by the cells to the amount available to pump blood around the body. Their results showed that the FS mechanism was the major determinant for ETW, as ETW decreased substantially in the absence of filament overlap effect and length-dependent calcium sensitivity [27].

Caruel *et al.* [122] proposed a 0D model of left ventricular contraction, associated with a Hill-Maxwell rheological model for sarcomere contraction. They model the kinetics of CBs by using an extension of Huxley's model [148]. The fraction of attached CBs, which determines the force, is modulated by a length-dependent fraction of recruitable CBs. From their results, they suggest that the FS mechanism primarly works by increasing the rate of active force development, thus increasing contraction velocity for a same time-interval, leading to an increased SV. In our study, we also showed that preload variations alter the contraction dynamics and the contraction velocity (see Section 6.4.2), which ultimately impact SV.

A study conducted by Hu and colleagues [190] also concerns the timing of contraction, but instead of looking at the ejection phase, they focused on the ventricular filling phase. They showed in their work that, in order to get an efficient preloading of the ventricle, a proper delay between atrial and ventricular contraction must be achieved. The atrial contraction promotes blood flow into the ventricle. If it occurs too early in the cardiac cycle, ventricular pressure is still too high (from the previous beat) and tends to oppose the blood entry. On the other hand, if atrial contraction occurs too close to ventricular contraction, the ventricular filling time decreases. As a consequence, in both cases, there is less blood to eject, and the resulting SW decreases. Hu *et al.* used a heart model where the atrioventricular (AV) delay could be controlled. Our model does not take into account the atria so it is not possible to exactly reproduce their simulation protocol. However, the simulations where t_0 was varied, in Section 6.6, can "mimick" an atrial contraction occuring at different time. We also showed in these simulations that there was an optimal t_0 value that corresponded to an optimal preload, along with an optimal SV. Hu *et al.* discussed how left atrial and ventricular pressures developement must be optimized over time so that the blood flow entering the left ventricle (the mitral flow) is optimized. This mitral flow is indeed proportional to the pressure gradient $\Delta P_{mt} = P_{la} - P_{lv}$. This way of reasoning shares similarities with our discussion regarding the ΔP_{vao} dynamics during preload increase, and the way this pressure gradient dictates the aortic flow.

7 CONCLUSION

The heart is an elaborated biological pump which continuously adapts its output to hemodynamic conditions and cardiovascular demands. This thesis work aimed at studying the correlation between the cellular determinants of cardiac contraction and the macroscopic observations at the heart scale. A focus was made on the Frank-Starling (FS) mechanism, a cardiac property that is fundamentally multiscale, as it is observed at the heart scale, while it is generally admitted to have a cellular origin. Since it is almost impossible to assess experimentally both microscopic and macroscopic variables together, multiscale mathematical models represent powerful tools to complete and connect the experimental observations. In this thesis, a multiscale model was built in order to relate and study the correlation between cellular (microscopic) and ventricular (macroscopic) variables.

The present chapter summarizes the content of this thesis, and reports the main findings. Then the future perspectives of this work are addressed.

7.1 SUMMARY

Chapter 2 presented a brief description of the cardiovascular system (CVS) and elements of cardiac physiology at the heart scale. Preload and stroke volume (SV) were defined: the former is the initial length of cardiac fibers prior to contraction, and the latter is the amount of blood ejected by the ventricles into the circulatory system at each beat. The FS mechanism was then introduced and defined as an instantaneous cardiac adaptation to preload increase that results in a SV increase. A short history of the experimental validations of the FS mechanism was presented, which showed the variety of experimental protocols and difficulties of measurement techniques. Then, the basis of fluid therapy (or vascular filling) was introduced. This common clinical therapy consists in injecting intravenous fluid to a patient in order to increase its cardiac output (or SV). The FS mechanism being generally presented as the founding principle for this therapy, a vascular filling analysis with a multiscale mathematical model was planned to investigate this statement.

Chapter 3 presented elements of cardiac physiology at the cellular scale. Cardiac cells (or cardiomyocytes) make up the myocardium (cardiac muscle) and have electrical and mechanical properties. These cellular properties naturally contribute to the cardiac behavior observed at the heart scale. Among them, the length-dependent activation (LDA) is of great importance. This property is particularly highlighted in isometric cellular experiments (where the cardiac fiber length is kept constant during the contraction) and is defined as the increased calcium sensitivity upon length increase. This results in an increased cellular produced force with increasing length. LDA is often cited as the cellular basis for the

FS mechanism and the given explanation goes as follows: as preload increases, cardiac cells length increases, so they produce a greater force. A greater pressure is thus generated inside the ventricular cavity and more blood is ejected, hence the increased SV. In this thesis, we wanted to challenge this definition of the FS mechanism as an LDA-based mechanism, because the former is a global (macroscopic) response to an increase in preload, while the latter is essentially defined through cellular (microscopic) isometric experiments that do not correspond to the *in vivo* conditions. Hence, a direct relationship between both mechanisms must be carefully handled.

Since it is of course very difficult to investigate this relationship experimentally, as two very different scales are involved, we built a multiscale CVS model that would allow an *in silico* analysis of the FS mechanism in order to investigate the contribution of LDA. This model was presented in Chapter 4. Our lumped-parameter model of the CVS consists of six chambers: the right and left ventricles, the aorta, the vena cava, the pulmonary vein and artery. In our model, ventricular contraction is described at the cellular scale. The cellular model of contraction consists in a combination of an electrophysiological model and a half-sarcromere contraction model (the sarcomere being the basic contractile unit of a cardiac cell). Then, a spherical ventricular model is assumed, which allows connecting the half-sarcomere length and force (cellular variables) to the chamber volume and pressure (ventricular variables). This multiscale model of ventricular contraction is a simple 0D model, but it presents a low computational cost and is still shown to be able to correctly reproduce the basal behaviors of the CVS system.

Our multiscale model of the CVS was first used to study the relevance of proposed cardiac contractility indices (CIs) in Chapter 5. The contractility (or inotropy) is the intrinsic ability of the heart to contract. It is related to the calcium handling at the cellular scale and mostly regulated by extrinsic factors like the nervous system. In clinics, it is important to assess the contractile state of the heart, which is a property intrinsic to the cardiac muscle, with contractility indices that must be independent of the hemodynamical conditions. We studied the relevance of four proposed left ventricle contractiliy indices by inducing load and inotropic variations to our CVS model.

Then, we used our multiscale model of the CVS to investigate the relationship between LDA and the FS mechanism in Chapter 6. We started by recalling the accepted description of the FS mechanism as an instantaneous adaptation to acute preload increase (decrease) that results in an increased (decreased) SV, provided that all other variables (afterload and inotropy mainly) remain constant. This adaptative response occurs within a single heartbeat, hence the notion of "instantenous", or transitory, mechanism. We thus built an instantaneous increase in preload (IIP) protocol, that we performed first with a left ventricle model extracted from the CVS model, then with the whole CVS model. We could switch LDA "on" and "off" inside the cellular model of contraction. Indeed, since there is an explicit length-dependence inside the biochemical contraction equations, this length-dependence was replaced with an input function of time. We could also switch the velocity-dependence off, by adapting the cellular equations where the time derivative of length appears. We also removed the complete length and velocity dependences from the biochemical equations. This allowed for a direct

analysis of the LDA and velocity-dependence contributions to the FS mechanism. Then, we questionned the relationship between the FS mechanism and vascular filling therapy. The FS mechanism is generally cited as the basis for this therapy, but there is an ambiguity here because it is defined as an *instantaneous* adaptation to preload variations, while vascular filling procedures are associated with a *stabilized* preload increase. We instead introduced the concept of "length-dependent fluid response" (LDFR), a steady-state global phenomenon which really underlies the vascular filling therapy outcomes: an increase in the circulating blood volume leads to an increase in SV. Then we performed vascular filling simulations with our model and studied the contribution of the cellular LDA to the ventricular LDFR. The role of the FS mechanism (or more precisely, of LDA) for SV equilibrium between both ventricles was also investigated.

7.2 MAIN FINDINGS

7.2.1 *The model*

Our multiscale CVS model is able to reproduce a series of physiological results, like the baseline (healthy) behavior, as well as a heart failure condition. Besides, our model correctly portrays the typical shift in the ventricular PV loops following a Fogarty protocol (which induces variations in right ventricular loading conditions). This validates our modeling approach. Note that we use a rather simple multiscale model of cardiac contraction, where the cellular and ventricular variables are connected with a 0D ventricle model. More complex heart models exist, but the one described in this work presents a very low computational cost and still leads to consistent results. Of course, our ventricular model is unable to capture the complexity and spatial heterogeneities of the myocardium. But a mathematical model is always an approximation of reality and the design of it depends on the desired goal. In our case, we were interested in studying the relationship between the length-dependent effects at the cellular scale and the preload-dependent effect at the heart scale (namely, the FS mechanism), while keeping computational tractability.

7.2.2 *Cardiac contractility indices*

The original analysis [116] presented in Chapter 5 shows that the four proposed CIs are indeed dependent on the inotropic state of the left ventricle. An important result is that one of them, the end-systolic elastance (E_{ES}), which is often considered as the gold standard for contractility assessment, was shown to be also load-dependent. This makesthe use of E_{ES} as a reliable CI questionable, as E_{ES} variations could occur because of hemodynamical loading variations, while the inotropic state would actually be unchanged. Two other CIs are also found to be load-dependent, but to a lower extent. Only the last one, the maximal rate of left-ventricular pressure development, $(dP_{lv}/dt)_{max}$, can actually be considered as a reliable CI, truly independent of the load.

7.2.3 *The FS mechanism*

With the isolated ventricle model, we show that the SV increase following preload increase is indeed related to the LDA, because the SV increase vanishes when the LDA is switched off in the model. In other words, LDA is required for the FS mechanism to be observed at the organ scale. But this LDA-driven increase in SV does not manifest itself only as an increase in maximal produced force, as commonly assumed when explaining the FS mechanism. Actually, the maximal produced force is an unreliable index to predict SV evolution. Indeed, an increase in maximal force is also observed when LDA is turned off, while no increase in SV occurs in this case. It is rather the whole dynamics of length, force and pressure development, which are affected by preload and driven by LDA, that leads to an increased aortic flow and ultimately to an increased SV. The same observations are made for the IIP protocol performed with the whole CVS model, which is a simulation more closely related to the FS mechanism occuring *in vivo*. In this case, we show that afterload is also impacted by the preload increase. So the obtained SV is a result of a competition between an LDA-driven increased developed pressure and an increased afterload, this competition occuring during the whole ejection period. The ejection duration is shown to be an interesting marker for preload alterations, more reliable than the maximal produced force or pressure.

When the velocity-dependence is removed, a greater SV increase is observed than for the baseline case. This suggests that the shortening of fibers during ejection is actually detrimental to pressure and force developement, as observed experimentally. When both length and velocity dependences are removed, a severe decrease in SV is observed, suggesting that the length and velocity dependences of the biochemical cycle are actually required for the contractile system to adapt properly to preload variations.

We conclude that the LDA indeed underlies the FS mechanism *in vivo*, but in a way that implies a complex dynamical interaction of cellular and hemodynamical variables. The FS mechanism is thus really a multiscale phenomenon, where the cellular variables (force and sarcomere length) and the hemodynamic variables (pressure and volume) influence each other during the whole heartbeat. Both scales are involved: the cellular length and developed cellular force, respectively affected by preload and LDA, dictate the pressure evolution, which itself determines the blood volume ejection at the ventricular scale, by competing with the aortic pressure which opposes blood ejection. The ventricular volume variations in turn impact the cellular length and developed force, which closes the loop of these multiscale interactions. To our knowledge, this thesis presents the first *in silico* study of the relationship bewteen LDA and the FS mechanism during an instantaneous increase in preload.

7.2.4 *The FS mechanism and vascular filling*

The FS mechanism is often presented as the founding principle for vascular filling therapy. We challenged this theory, because it connects an instantaneous response to preload increase to a procedure that intends to stabilize an increased

preload over time. We thus introduced the concept of *length-dependent fluid response* (LDFR) to describe the observed increase in SV following vascular filling, instead of the FS mechanism. We then studied the relationship between LDA and LDFR. Our model shows that the increase in SV is indeed driven by LDA, which promotes an increase in force and pressure development in response to an increased preload. This preload increase is induced by vascular filling, but we show that an afterload increase is also induced. So, during blood ejection, there is actually a competition between an LDA-driven increase in developed pressure and an increase in the resistance to blood ejection. We observe a saturation limit in the SV increase for large fluid infusions, which occurs because the increase in developed pressure is not strong enough to counterbalance the increase in afterload. We see that preload is not the only factor to consider when performing vascular filling, and the search for reliable preload indices should be handled by keeping that in mind. Besides, the results show that the vascular filling limit is not related to an LDA limit, but to unfavorable hemodynamics ejection conditions. There is still an LDA reserve for large fluid infusions (the developed pressure continues to increase), but it is overshadowed by a larger increase in afterload. Once again, we observe a multiscale adaptative mechanism (LDFR) which mixes cellular and hemodynamical variables.

7.2.5 *The FS mechanism and SV equilibrium*

The SV of both ventricles are equal on average, and the FS mechanism is generally considered as the basis for SV equilibrum management. We investigated how our CVS model responded to a transitory SV equilibrium perturbation, and observed the time it takes to recover its steady-state. We performed an IIP protocol on the left ventricle of the CVS model and waited for the system to go back to its equilibrium point, where right and left ventricular SV were equal again. We performed the same protocol but with LDA turned off. We observe that the system is able to return to its initial steady-state in both cases (with and without LDA), and this return occurs on a similar time scale. This suggests that the FS mechanism is not essential for SV equilibrium. In other words, only the hemodynamic scale seems to be involved for the restoration of SV equilibrium.

7.3 LIMITATIONS AND FUTURE WORK

Limitations

The main limitations regarding this study arise from the assumptions upon which the CVS is built.

The cellular model of contraction consists in an electrophysiological model coupled with a mechanical half-sarcomere contraction model. In contrast to cardiac electrophysiology modeling, there is a lack of consensus on the best modeling framework to simulate the biophysics of the sarcomere [29]. One of the reasons is that our physiological understanding is still limited (the molecular mechanisms underlying LDA are not fully understood yet, for instance), so the relevance of our modeling approach is limited as well. The half-sarcomere con-

traction model is based on many assumptions, as it not possible to describe explicitely all the molecular mechanisms that occur during cellular contraction. The biochemical variables (troponin and calcium concentrations) used to describe the crossbridge cycling are easily associated with a physiological reality. However, the half-sarcomere mechanics is described with an "equivalent crossbridge" model. This a phenomenological approach to describe sarcomere contraction, because there are actually numerous crossbridges which participate in the contractile process. For model simplicity, only two types of "equivalent" crossbridges are assumed to represent all the active crossbridges responsible for contraction and force production. This is the main assumption made with the cellular model of contraction.

A spherical ventricle model is assumed to link the cellular and ventricular variables. Of course, such a simple 0D description of the ventricle is unable to fully capture the sophisticated dynamics of ventricular contraction *in vivo*. The elaborate geometrical structure, along with the spatial and temporal heterogeneities, participates in the complexity and efficiency of cardiac contraction. We are aware that the conclusions presented in this work are thus partly questionable regarding the *in vivo* behavior of the "real" heart. This conclusion could be drawn with all models, since they are, by definition, based on approximations and assumptions. Actually, a model is chosen depending on the aim intended. In our case, we wanted computational tractability and a consistent relationship bewteen cellular and hemodynamics variables, and we achieved both.

Assumptions were also made regarding the CVS model, an even larger and more complex structure, and some limitations are inherent to the lumped-parameter approach we followed. We chose to work with a simple 6-chamber model, which was the minimal requirement to describe the left and right ventricles in a complete loop representing the CVS.

Validation with experimental data

Mathematical models of biological systems are a powerful tool for broadening physiological knowledge, but their utility is limited if they are not used in parallel with experimental studies. In this thesis, we did not have any detailed experimental data to work with, so our results were only qualitatively compared to experimental results found in the literature. For instance, it would be interesting to investigate the timing of contraction during a Fogarty protocol, which is an experimental transitory preload reduction manoeuvre operated on the right ventricle. This experimental protocol is similar to our numerical left ventricular IIP protocol, because the altered right ventricular preload impacts also the left ventricular preload shortly after. If only the first two or three heartbeats following the preload reduction are analyzed, we can reasonably consider that only the preload is varied, while the inotropy and afterload remain unchanged. An experimental recording of the timing of contraction and ventricular pressure development would be very helpful in validating our findings that SV is affected by preload via a profound altered dynamics of contraction. This altered dynamics could for instance be assessed with the ejection duration, that we considered to be a relevant marker of preload alterations. Besides, detailed experimental data

regarding the baseline case (no Fogarty protocol) would allow for a more consistent hemodynamic parameters identification than the one presented in Chapter 4. These experimental data might thus render our numerical study more "quantitative".

CVS model improvements

As stated above, the multiscale ventricular model is voluntarily built to be simple. But the CVS model still can be improved with a more detailed description of important components like the ventricular interaction, which was not taken into account in our model. Since both ventricles share a common wall, volumes variations in one ventricle instantaneously influence the other ventricle, and it would be interesting to study the impact of this interaction regarding preload variations. The modeling of cardiac valves (a simple analogy with electrical diods) could also be improved with more elaborate models. Essentially, the modeling approach is ajustable regarding the study intended. For instance, an atrial model of contraction should be added to the model if the influence of atrioventricular filling on SV needs to be addressed.

Development of the model as a tool for other in silico studies

Our model is still able to reproduce basic behaviors, and its multiscale characteristic is very appealing for any study that aims at linking cellular properties and organ behaviors, especially the study of pathological conditions. Indeed, many pathological conditions observed at the hemodynamic scale originates at the cellular scale, where alterations or remodeling of the electrophysiology or contractile apparatus take place. As a convincing example, a multiscale CVS model similar to the one presented in this work was recently used to study cardiac contractile dysfunction (CD) [119]. The cellular model was modified according to experimental data describing the CD alterations at the cellular scale. This model simulations were in excellent agreement with the hemodynamic experimental data they were compared to. Furthermore, this *in silico* study allowed to inspect the relative impact of each cellular altered component on the global hemodynamic scale, which is a first step to investigate potential targets for medical treatments.

A

EQUATIONS GOVERNING THE CELLULAR ELECTROPHYSIOLOGICAL MODEL

Physical units used: time (t) in ms, membrane potential (V) in mV, transmembrane current densities (I_x) in pA/pF and intracellular and extracellular ionic concentrations (X_i and X_o) in μM (or μmol/L).

TRANSMEMBRANE CURRENTS AND MEMBRANE POTENTIAL [140, 141]

The time evolution of the membrane potential is described as follows:

$$\frac{dV}{dt} + I_{ion} + I_{stim} = 0$$

where I_{ion} is the sum of all transmembrane ionic current densities (see equation and figure below) and I_{stim} is the externally applied stimulus current density.

$$I_{ion} = I_{Na} + I_{K1} + I_{to} + I_{Kr} + I_{CaL} + I_{NaCa} + I_{NaK} + I_{pCa} + I_{pK} + I_{bCa} + I_{bNa}$$

$$I_{stim} = \begin{cases} -9.5 & \text{if } 100 < t < 106 \\ 0 & \text{otherwise} \end{cases}$$

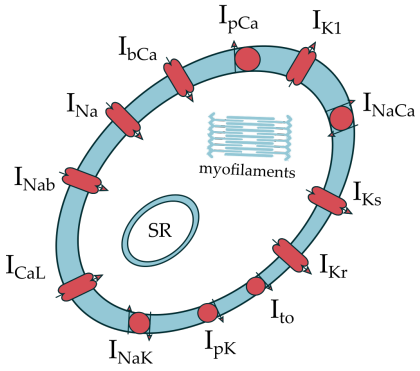

(a) Schematic representation of the transmembrane ionic currents described in the electrophysiological model.

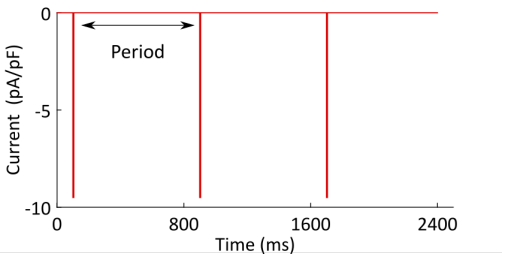

(b) Stimulus current used to trigger the AP. The stimulation period fixes the heart rate.

Nernst potentials

$$E_X = \frac{RT}{zF} \log \frac{[X]_o}{[X]_i} \quad \text{for } X = Na^+, Ca^{2+}, K^+$$

Fast sodium current: I_{Na}

$$m_\infty = \frac{1}{(1+\exp\left(\frac{-56.86-V}{9.03}\right))^2} \qquad \tau_\infty = \alpha_m \beta_m$$

$$\alpha_m = \frac{1}{1+\exp\left(\frac{-60-V}{5}\right)}$$

$$\beta_m = \frac{0.1}{1+\exp\left(\frac{V+35}{5}\right)} + \frac{0.1}{1+\exp\left(\frac{V-50}{200}\right)} \qquad \frac{\mathrm{d}m}{\mathrm{dt}} = \frac{m_\infty - m}{\tau_\infty}$$

$$h_\infty = \frac{1}{(1+\exp\left(\frac{71.55+V}{7.43}\right))^2}$$

$$\alpha_h = \begin{cases} 0.057\exp\left(\frac{-80-V}{6.8}\right) & \text{if V} < 40 \\ 0 & \text{otherwise} \end{cases}$$

$$\beta_h = \begin{cases} 2.7\exp\left(0.079V\right) + 3.1\ 10^5 \exp\left(0.3485V\right) & \text{if V} < 40 \\ \frac{0.77}{0.13(1+\exp\left(\frac{-V-10.66}{11.1}\right))} & \text{otherwise} \end{cases}$$

$$\tau_h = \frac{1}{\alpha_h + \beta_h} \qquad j_\infty = \frac{1}{(1+\exp(\frac{71.55+V}{7.43}))^2}$$

$$\frac{\mathrm{d}h}{\mathrm{dt}} = \frac{h_\infty - h}{\tau_h} \qquad \omega = -2.5428\ 10^4 \exp(0.2444V) - 6.948\ 10^{-6}\exp(-0.04391V)$$

$$\alpha_j = \begin{cases} \frac{\omega(V+37.78)}{1+\exp(0.311(V+79.23))} & \text{if V} < 40 \\ 0 & \text{otherwise} \end{cases}$$

$$\beta_j = \begin{cases} \frac{0.02424\exp(-0.01052V)}{1+\exp(-0.1378(V+40.14))} & \text{if V} < 40 \\ \frac{0.6\exp(0.057V)}{1+\exp(-0.1(V+32))} & \text{otherwise} \end{cases}$$

$$\tau_j = \frac{1}{\alpha_j + \beta_j} \qquad \frac{\mathrm{d}j}{\mathrm{dt}} = \frac{j_\infty - j}{\tau_j}$$

$$I_{\mathrm{Na}} = G_{\mathrm{Na}} m^3 h j (V - E_{\mathrm{Na}})$$

L-type calcium current: I_{CaL}

$$d_\infty = \frac{1}{1 + \exp(\frac{-8-V}{7.5})} \qquad \frac{\mathrm{d}f}{\mathrm{dt}} = \frac{f_\infty - f}{\tau_f}$$

$$\alpha_d = \frac{1.4}{1 + \exp(\frac{-35-V}{13})} + 0.25 \qquad f_{2\infty} = 0.33 + \frac{0.67}{1 + \exp(\frac{35+V}{7})}$$

$$\beta_d = \frac{1.4}{1 + \exp(\frac{5+V}{5})} \qquad \alpha_{f_2} = 562 \exp(-\frac{(V+27)^2}{240})$$

$$\gamma_d = \frac{1}{1 + \exp(\frac{50-V}{20})} \qquad \beta_{f_2} = \frac{31}{1 + \exp(\frac{25-V}{10})}$$

$$\tau_d = \alpha_d \beta_d + \gamma_d \qquad \gamma_{f_2} = \frac{80}{1 + \exp(\frac{30+V}{10})}$$

$$\frac{\mathrm{d}d}{\mathrm{dt}} = \frac{d_\infty - j}{\tau_d} \qquad \tau_{f_2} = \alpha_{f_2} + \beta_{f_2} + \gamma_{f_2}$$

$$f_\infty = \frac{1}{1 + \exp(\frac{20+V}{7})} \qquad \frac{\mathrm{d}f_2}{\mathrm{dt}} = \frac{f_{2\infty} - f_2}{\tau_{f_2}}$$

$$\alpha_f = 1102.5 \exp(\frac{-(27+V)^2}{225}) \qquad f_{\mathrm{cass}\infty} = \frac{0.6}{1 + (\frac{\mathrm{Ca_{ss}}}{50})^2} + 0.4$$

$$\beta_f = \frac{200}{1 + \exp(\frac{13-V}{10})} \qquad \tau_{f\mathrm{cass}} = 2 + \frac{80}{1 + (\frac{\mathrm{Ca_{ss}}}{50})^2}$$

$$\gamma_f = \frac{180}{1 + \exp(\frac{30+V}{10})} + 20 \qquad \frac{\mathrm{d}f_{\mathrm{Ca_{ss}}}}{\mathrm{dt}} = \frac{f_{\mathrm{cass}\infty} - f_{\mathrm{Ca_{ss}}}}{\tau_{f\mathrm{cass}}}$$

$$\tau_f = \alpha_f + \beta_f + \gamma_f$$

$$I_{\mathrm{CaL}} = G_{\mathrm{CaL}} d\, f\, f_2\, f_{\mathrm{Ca_{ss}}}\, 4\frac{(V-15)F^2}{RT} \times \frac{0.25\,\mathrm{Ca_{ss}}\exp(\frac{2(V-15)F}{RT}) - \mathrm{Ca_o}}{1000(\exp(\frac{2(V-15)F}{RT}) - 1)}$$

Transient outward potassium current: I_{to}

$$r_\infty = \frac{1}{1+\exp(\frac{20-V}{6})} \qquad s_\infty = \frac{1}{1+\exp(\frac{20+V}{5})}$$

$$\tau_r = 9.5\exp(-\frac{(V+40)^2}{1800}) + 0.8 \qquad \tau_s = 85\exp(-\frac{(V+45)^2}{320}) + \frac{5}{1+\exp(\frac{V-20}{5})} + 3$$

$$\frac{\mathrm{d}r}{\mathrm{d}t} = \frac{r_\infty - r}{\tau_r} \qquad \frac{\mathrm{d}s}{\mathrm{d}t} = \frac{s_\infty - r}{\tau_s}$$

$$I_{\mathrm{to}} = G_{to} r s (V - E_{\mathrm{K}})$$

Slow delayed rectifier current: I_{Ks}

$$x_{s\infty} = \frac{1}{1+\exp(\frac{-5-V}{14})} \qquad \tau_{xs} = \alpha_{xs}\beta_{xs} + 80$$

$$\alpha_{xs} = \frac{1400}{\sqrt{1+\exp(\frac{-5-V}{6})}}$$

$$\beta_{xs} = \frac{1}{1+\exp(\frac{V-35}{15})} \qquad E_{\mathrm{Ks}} = \frac{RT}{F}\log(\frac{\mathrm{K_o} + p_{\mathrm{KNa}}\mathrm{Na_o}}{\mathrm{K_i} + p_{\mathrm{KNa}}\mathrm{Na_i}})$$

$$I_{Ks} = G_{Ks} x_s^2 (V - E_{\mathrm{Ks}})$$

Rapid delayed rectifier current: I_{Kr}

$$x_{r1\infty} = \frac{1}{1+\exp(\frac{-26-V}{7})} \qquad \alpha_{r1} = \frac{450}{1+\exp(\frac{-45-V}{10})}$$

$$\beta_{r1} = \frac{6}{1+\exp(\frac{30+V}{11.5})} \qquad \alpha_{r2} = \frac{3}{1+\exp(\frac{-60-V}{20})}$$

$$\tau_{r1} = \alpha_{r1}\beta_{r1} \qquad \beta_{r2} = \frac{1.12}{1+\exp(\frac{-60+V}{20})}$$

$$\frac{\mathrm{d}x_{r1}}{\mathrm{dt}} = \frac{x_{r1\infty} - x_{r1}}{\tau_{r1}} \qquad \tau_{r2} = \alpha_{r2}\beta_{r2}$$

$$x_{r2\infty} = \frac{1}{1+\exp(\frac{V+88}{24})} \qquad \frac{\mathrm{d}x_{r1}}{\mathrm{dt}} = \frac{x_{r1\infty} - x_{r1}}{\tau_{r1}}$$

$$I_{Kr} = G_{Kr}\sqrt{\frac{\mathrm{K_o}}{5400}}x_{r1}x_{r2}(V - E_{\mathrm{K}})$$

Inward rectifier potassium current: I_{K1}

$$\alpha_{K1} = \frac{0.1}{1+\exp(0.06(V - E_{\mathrm{K}} - 200))}$$

$$\beta_{K1} = \frac{3\exp(0.0002(V - E_{\mathrm{K}} + 100)) + \exp(0.1(V - E_{\mathrm{K}} - 10))}{1+\exp(-0.5(V - E_{\mathrm{K}}))}$$

$$x_{K1\infty} = \frac{\alpha_{K1}}{\alpha_{K1} + \beta_{K1}}$$

$$I_{K1} = G_{K1}x_{K1\infty}(V - E_{\mathrm{K}})$$

Na/Ca exchanger current: I_{NaCa}

$$I_{\mathrm{NaCa}} = \frac{k_{\mathrm{NaCa}}}{K_{\mathrm{mN}}^3 + \mathrm{Na_o^3}} \times \frac{\exp(\frac{\gamma VF}{RT})\mathrm{Na_i^3Ca_o} - 2.5\exp(\frac{(1-\gamma)VF}{RT})\mathrm{Na_o^3Ca_i}}{(K_{\mathrm{mCa}} + \mathrm{Ca_o})(1 + k_{\mathrm{sat}}\exp(\frac{(\gamma-1)VF}{RT}))}$$

Na/K pump current: I_{NaK}

$$I_{\mathrm{NaK}} = \frac{\mathrm{P_{NaK}K_oNa_i}}{(\mathrm{K_o} + \mathrm{K_{mK}})(\mathrm{Na_i} + \mathrm{K_{mNa}})} \times \frac{1}{(1 + 0.1245\exp(\frac{-0.1VF}{RT}) + 0.0353\exp(\frac{-VF}{RT}))}$$

Sarcolemmal calcium pump current: I_{pCa}

$$I_{pCa} = G_{pCa}\frac{Ca_i}{K_{pCa} + Ca_i}$$

Sarcolemmal potassium pump current: I_{pK}

$$I_{pK} = G_{pK}\frac{V - E_K}{1 + \exp(\frac{25-V}{5.98})}$$

Background currents: I_{bNa} *and* I_{bCa}

$$I_{bNa} = G_{bNa}(V - E_{Na})$$
$$I_{bCa} = G_{bCa}(V - E_{Ca})$$

CALCIUM DYNAMICS

Calcium dynamics is described within three subcellular compartments (see figure): cytoplasm (CYTO), sarcoplasmic reticulum (SR) and diadic subspace (SS). In the following equations, $[Ca]_i$ is free cytoplasmic calcium concentration, $[Ca]_{SR}$ is free SR calcium concentration and $[Ca]_{ss}$ is free diadic subspace calcium concentration (all concentrations expressed in μM). I_{up}, I_{rel}, I_{xfer} and I_{leak} are expressed in μM/ms.

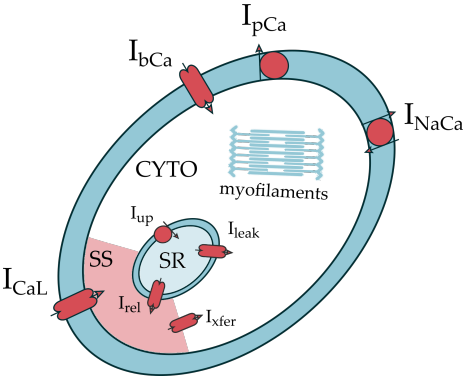

- SERCA (ten Tusscher and Panfilov [141])

$$I_{up} = \frac{V_{up}}{1 + (\frac{K_{up}}{Ca_i})^2}$$

- CICR (Lascano *et al.* [158])

$$u = \max_{sr} - \frac{\max_{sr} - \min_{sr}}{1 + (\frac{EC_{50}}{Ca_{SR}})^2}$$

$$k_1 = \frac{k_1'}{u}, \; k_2 = k_2' u$$

$$
\begin{aligned}
\mathrm{RI} &= 1-\mathrm{R}-\mathrm{O}-\mathrm{I} \\
\frac{\mathrm{dR}}{\mathrm{dt}} &= k_4\mathrm{RI}-k_2\mathrm{RCa_{ss}} \\
&\quad -k_1\mathrm{RCa_i}^2+k_3O \\
\frac{\mathrm{dO}}{\mathrm{dt}} &= k_1\mathrm{RCa_{ss}}^2 \\
&\quad -k_3\mathrm{O}-k_2\mathrm{OCa_{ss}}+k_4\mathrm{I} \\
\frac{\mathrm{dI}}{\mathrm{dt}} &= k_2\mathrm{OCa_{ss}}-k_4\mathrm{I} \\
&\quad -k_3\mathrm{I}+k_1\mathrm{RICa_{ss}^2}
\end{aligned}
$$

$$I_{\mathrm{rel}} = V_{\mathrm{rel}}\mathrm{O}(\mathrm{Ca_{SR}}-\mathrm{Ca_{ss}})+V_{\mathrm{leak(d)}}R(\mathrm{Ca_{SR}}-\mathrm{Ca_{ss}})$$

$$I_{\mathrm{leak}} = V_{\mathrm{leak(c)}}(\mathrm{Ca_{SR}}-\mathrm{Ca_i})$$

$$I_{\mathrm{xfer}} = V_{\mathrm{xfer}}(\mathrm{Ca_{ss}}-\mathrm{Ca_i})$$

- Mechanical feedback (Kosta *et al.* [116])

$$
\begin{aligned}
I_{\mathrm{trop}} &= \frac{1}{2}3\left(\frac{\mathrm{d}[\mathrm{TSCa_3}]_{\mathrm{LV}}}{\mathrm{dt}}+\frac{\mathrm{d}[\mathrm{TS\tilde{Ca}_3}]_{\mathrm{LV}}}{\mathrm{dt}}+\frac{\mathrm{d}[\mathrm{TSCa_3^*}]_{\mathrm{LV}}}{\mathrm{dt}}\right) \\
&\quad +\frac{1}{2}3\left(\frac{\mathrm{d}[\mathrm{TSCa_3}]_{\mathrm{RV}}}{\mathrm{dt}}+\frac{\mathrm{d}[\mathrm{TS\tilde{Ca}_3}]_{\mathrm{RV}}}{\mathrm{dt}}+\frac{\mathrm{d}[\mathrm{TSCa_3^*}]_{\mathrm{RV}}}{\mathrm{dt}}\right)
\end{aligned}
$$

The colored concentrations are obtained from the sarcomere contraction model (see Appendix B).

- Free calcium concentrations in the CYTO, SR and SS compartments

$$
\begin{aligned}
\frac{\mathrm{d}[\mathrm{Ca}]_{\mathrm{i}}}{\mathrm{dt}} &= -\frac{1}{1+\dfrac{K_{\mathrm{buf_i}}\,\mathrm{Buf_i}}{[\mathrm{Ca}]_{\mathrm{i}}+K_{\mathrm{buf_i}}}}\left(C_{m0}\frac{I_{\mathrm{bCa}}+I_{\mathrm{pCa}}-2I_{\mathrm{NaCa}}}{2V_cF}\right. \\
&\quad \left.+\frac{V_{\mathrm{sr}}}{V_c}(I_{\mathrm{leak}}-I_{\mathrm{up}})+I_{\mathrm{xfer}}-I_{\mathrm{trop}}\right)
\end{aligned}
$$

$$
\frac{\mathrm{d}[\mathrm{Ca}]_{\mathrm{SR}}}{\mathrm{dt}} = -\frac{1}{1+\dfrac{K_{\mathrm{bufSR}}\,\mathrm{Buf_{SR}}}{[\mathrm{Ca}]_{\mathrm{SR}}+K_{\mathrm{bufSR}}}}\left(I_{\mathrm{up}}-I_{\mathrm{leak}}-I_{\mathrm{rel}}\right)
$$

$$
\frac{\mathrm{d}[\mathrm{Ca}]_{\mathrm{SS}}}{\mathrm{dt}} = -\frac{1}{1+\dfrac{K_{\mathrm{bufSS}}\,\mathrm{Buf_{SS}}}{[\mathrm{Ca}]_{\mathrm{SS}}+K_{\mathrm{bufSS}}}}\left(-C_{m0}\frac{I_{\mathrm{CaL}}}{2V_{ss}F}+\frac{V_{\mathrm{sr}}}{V_{ss}}I_{\mathrm{rel}}-\frac{V_{\mathrm{c}}}{V_{ss}}I_{\mathrm{xfer}}\right)
$$

SODIUM AND POTASSIUM INTRACELLULAR CONCENTRATIONS

$$
\begin{aligned}
\frac{\mathrm{d}[\mathrm{K}]_{\mathrm{i}}}{\mathrm{dt}} &= -C_{m0}\frac{-2I_{\mathrm{NaK}}+I_{\mathrm{Ks}}+I_{\mathrm{K1}}+I_{\mathrm{to}}+I_{\mathrm{pK}}-I_{\mathrm{stim}}}{V_cF} \\
\frac{\mathrm{d}[\mathrm{Na}]_{\mathrm{i}}}{\mathrm{dt}} &= -C_{m0}\frac{3I_{\mathrm{NaK}}+3I_{\mathrm{NaCa}}+I_{\mathrm{Na}}+I_{\mathrm{bNa}}}{V_cF}
\end{aligned}
$$

Parameter	Units	Value	Parameter	Units	Value
R	J/K/mol	8.314472	K_{mNa}	μM	40 000
F	C/mol	96485.3415	G_{pCa}	nS/pF	0.1238
T	K	310	K_{pCa}	μM	0.5
C_{m0}	μF	$1.84\,10^{-4}$	G_{pK}	nS/pF	0.0146
V_c	mL	$1.6404\,10^{-8}$	V_{up}	μM/ms	6.375
V_{SR}	mL	$1.0941\,10^{-9}$	K_{up}	μM	0.25
V_{SS}	mL	$5.4681\,10^{-11}$	EC_{50}	μM	1500
K_o	μM	5400	k_1'	μM^2/ms	1.5
Na_o	μM	140 000	k_2'	μM/ms	4.5
Ca_o	μM	2000	k_3	ms^{-1}	0.06
G_{Na}	nS/pF	14.838	k_4	ms^{-1}	0.005
G_{CaL}	cm^3/ms/μF	$3.98\,10^{-5}$	V_{rel}	ms^{-1}	0.102
G_{to}	nS/pF	0.294	$V_{\text{leak(d)}}$	ms^{-1}	$1.8\,10^{-5}$
G_{Ks}	nS/pF	0.098	$V_{\text{leak(c)}}$	ms^{-1}	$3.42\,10^{-4}$
p_{KNa}	-	0.03	V_{xfer}	ms^{-1}	0.0038
G_{Kr}	nS/pF	0.153	Buf_i	μM	130
G_{K1}	nS/pF	5.405	K_{buf_i}	μM	1
k_{NaCa}	pA/pF	1000	Buf_{SR}	μM	10^4
K_{mN}	μM	87 500	K_{bufSR}	μM	300
γ	-	0.35	Buf_{SS}	μM	400
k_{sat}	-	0.1	K_{bufSS}	μM	0.25
P_{NaK}	pA/pF	2.724	Period	ms	800
K_{mK}	μM	1000			

Table 13: Electrophysiological parameters

B

EQUATIONS GOVERNING THE SARCOMERE CONTRACTION MODEL

LEFT VENTRICLE

The "LV" indices below designate the left ventricle.

Calcium kinetics

$$[TS]_{LV} = [TS]_{t,LV} - [TSCa_3]_{LV} - [TSCa_3^{\sim}]_{LV} - [TSCa_3^{*}]_{LV} - [TS^{*}]_{LV}$$

$$\begin{aligned}
\frac{d[TSCa_3]_{LV}}{dt} &= Y_b[TS]_{LV}[Ca]_i^3 - Z_b[TSCa_3]_{LV} + g[TSCa_3^{\sim}]_{LV} - f[TSCa_3]_{LV} \\
\frac{d[TSCa_3^{\sim}]_{LV}}{dt} &= f[TSCa_3]_{LV} - g[TSCa_3^{\sim}]_{LV} + Z_p[TSCa_3^{*}]_{LV} - Y_p[TSCa_3^{\sim}]_{LV} \\
\frac{d[TSCa_3^{*}]_{LV}}{dt} &= Y_p[TSCa_3^{\sim}]_{LV} - Z_p[TSCa_3^{*}]_{LV} + Z_r[TS^{*}]_{LV}[Ca]_i^3 - Y_r[TSCa_3^{*}]_{LV} \\
\frac{d[TS^{*}]_{LV}}{dt} &= Y_r[TSCa_3^{*}]_{LV} - Z_r[TS^{*}]_{LV}[Ca]_i^3 - g_d[TS^{*}]_{LV}
\end{aligned}$$

Intracellular calcium concentration ($[Ca]_i$) is obtained from the electrophysiological model (see Appendix A).

$$f = Y_a \exp(-R_{La}(L_{LV} - L_a)^2)$$

$$g = Z_a + Y_h$$

$$Y_h = \begin{cases} Y_v(1 - \exp(-\gamma(h_{w_{LV}} - h_{wr_{LV}})^2)) & \text{if } h_{w_{LV}} < h_{wr_{LV}} \\ 0.1Y_v(1 - \exp(-\gamma(h_{w_{LV}} - h_{wr_{LV}})^2)) & \text{otherwise} \end{cases}$$

$$g_d = Y_d \exp(-Y_c(L_{LV} - L_c))$$

Half-sarcomere length and force

$$\begin{aligned}
h_{w_{LV}} &= L_{LV} - X_{w_{LV}} \\
h_{p_{LV}} &= L_{LV} - X_{p_{LV}}
\end{aligned}$$

$$\begin{aligned}
\frac{dX_{w_{LV}}}{dt} &= B_w(h_{w_{LV}} - h_{wr_{LV}}) \\
\frac{dX_{p_{LV}}}{dt} &= B_p(h_{p_{LV}} - h_{pr_{LV}})
\end{aligned}$$

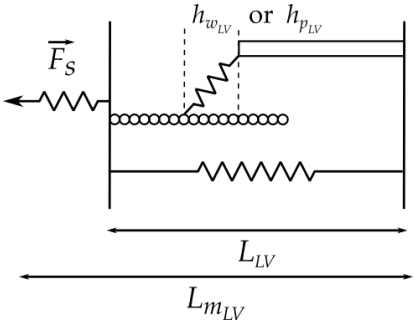

$$
\begin{aligned}
F_a &= A_w \left[\mathrm{TSCa}_3^{\sim}\right]_{\mathrm{LV}} h_{w_{LV}} + A_p \left(\left[\mathrm{TSCa}_3^{*}\right]_{\mathrm{LV}} + \left[\mathrm{TS}^{*}\right]_{\mathrm{LV}}\right) h_{p_{LV}} \\
F_p &= K_e (L_{LV} - L_0)^5 + L_e (L_{LV} - L_0) \\
F &= F_a + F_p \\
F_s &= \alpha(\exp(\beta(L_{m,LV} - L_{LV})) - 1)
\end{aligned}
$$

$L_{m,LV}$ is obtained from the hemodynamic model (see Appendix C) and L_{LV} is calculated for each iteration step by solving $F - F_s = 0$, using the MatLab *fzero* function.

RIGHT VENTRICLE (RV)

The set of equations for RV sarcometric contraction is the same as for LV, where every "*LV*" subscript has to be replaced with "*RV*". The parameters listed below are identical for both ventricles.

Parameter	Units	Value
A_p	$\mathrm{mN/mm^2/\mu m/\mu M}$	2850
A_w	$\mathrm{mN/mm^2/\mu m/\mu M}$	570
α	$\mathrm{mN/mm^2}$	0.15
β	$\mathrm{ms^{-1}}$	80
B_p	$\mathrm{ms^{-1}}$	1.75
B_p	$\mathrm{ms^{-1}}$	1.225
$\mathrm{Y_a}$	$\mathrm{ms^{-1}}$	$2.3\,10^{-3}$
$\mathrm{Y_b}$	$\mu\mathrm{M}^{-3}.\mathrm{ms^{-1}}$	0.1816
$\mathrm{Y_c}$	$\mu\mathrm{M^{-1}}$	4
$\mathrm{Y_d}$	$\mathrm{ms^{-1}}$	0.028
$\mathrm{Y_p}$	$\mathrm{ms^{-1}}$	0.1397
$\mathrm{Y_r}$	$\mathrm{ms^{-1}}$	0.1397
$\mathrm{Y_v}$	$\mathrm{ms^{-1}}$	0.9
$\mathrm{Z_a}$	$\mathrm{ms^{-1}}$	0.0023
$\mathrm{Z_b}$	$\mathrm{ms^{-1}}$	0.1397
$\mathrm{Z_p}$	$\mathrm{ms^{-1}}$	0.2095
$\mathrm{Z_r}$	$\mu\mathrm{M}^{-3}.\mathrm{ms^{-1}}$	7.2626
$[\mathrm{TS}]_\mathrm{t}$	μM	70/3
L_0	μm	0.97
L_a	μm	1.15
R	$\mu\mathrm{m^{-2}}$	15
L_c	μm	1.05
h_{pr}	μm	$6\,10^{-3}$
h_{wr}	μm	10^{-4}
γ	$\mathrm{ms^{-1}}$	$2.8\,10^{-4}$
K_e	$\mathrm{mN/mm^2/\mu m^{-5}}$	$3.15\,10^4$
L_e	$\mathrm{mN/mm^2/\mu m}$	3

Table 14: Mechanical parameters

C

EQUATIONS GOVERNING THE HEMODYNAMIC (6-CHAMBER) MODEL

PASSIVE CHAMBERS PRESSURES

$$
\begin{aligned}
P_{ao} &= E_{ao} \cdot V_{ao} \quad \text{with } E_{ao} = 1/C_{ao} \\
P_{vc} &= E_{vc} \cdot V_{vc} \quad \text{with } E_{vc} = 1/C_{vc} \\
P_{pa} &= E_{pa} \cdot V_{pa} \quad \text{with } E_{pa} = 1/C_{pa} \\
P_{pv} &= E_{pv} \cdot V_{pv} \quad \text{with } E_{pv} = 1/C_{pv}
\end{aligned}
$$

FLOWS

- Pulmonary and systemic flows:

$$
\begin{aligned}
Q_{sys} &= \frac{P_{ao} - P_{vc}}{R_{sys}} \\
Q_{pul} &= \frac{P_{pa} - P_{pv}}{R_{pul}}
\end{aligned}
$$

- Valves flows:

$$
Q_{mt} = \begin{cases} \dfrac{P_{pv} - P_{lv}}{R_{mt}} & \text{if } P_{PV} > P_{LV} \\ 0 & \text{otherwise} \end{cases}
$$

$$
Q_{av} = \begin{cases} \dfrac{P_{lv} - P_{ao}}{R_{av}} & \text{if } P_{LV} > P_{AO} \\ 0 & \text{otherwise} \end{cases}
$$

$$
Q_{tc} = \begin{cases} \dfrac{P_{vc} - P_{rv}}{R_{tc}} & \text{if } P_{VC} > P_{RV} \\ 0 & \text{otherwise} \end{cases}
$$

$$
Q_{pv} = \begin{cases} \dfrac{P_{rv} - P_{pa}}{R_{pv}} & \text{if } P_{RV} > P_{PA} \\ 0 & \text{otherwise} \end{cases}
$$

VOLUMES

$$\frac{dV_{lv}}{dt} = Q_{mt} - Q_{av}$$
$$\frac{dV_{ao}}{dt} = Q_{av} - Q_{sys}$$
$$\frac{dV_{vc}}{dt} = Q_{sys} - Q_{tc}$$
$$\frac{dV_{rv}}{dt} = Q_{tc} - Q_{pv}$$
$$\frac{dV_{pa}}{dt} = Q_{pv} - Q_{pul}$$

$$V_{pv} = SBV - V_{lv} - V_{ao} - V_{vc} - V_{rv} - V_{pa}$$

ACTIVE CHAMBERS PRESSURES

LV (RV) ventricle is assimilated to a thick walled sphere (see figure below) with a wall volume $V_{w_{LV}}$ ($V_{w_{RV}}$). The reference (and variable) radius R_{LV} (R_{RV}) corresponds to the position of the N_{LV} (N_{RV}) sarcomeres of length $L_{m,LV}$ ($L_{m,RV}$) assembled in circle inside the ventricular wall. The volume included between $r_{in_{LV}}$ and R_{LV} ($r_{in_{RV}}$ and R_{RV}) is noted $V_{r_{LV}}$ ($V_{r_{RV}}$).

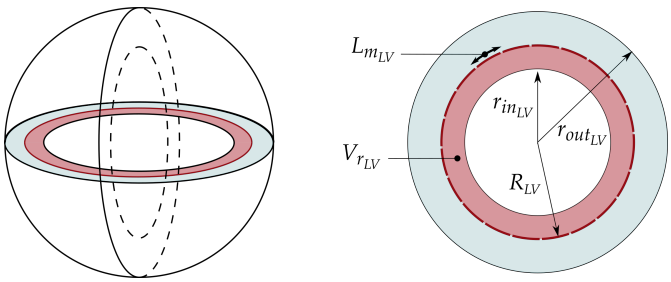

$$\frac{4}{3}\pi r_{in_{LV}}^3 = V_{LV} \Rightarrow r_{in_{LV}} = \sqrt[3]{\frac{3}{4\pi}V_{LV}}$$
$$\frac{4}{3}\pi r_{out_{LV}}^3 = V_{LV} + V_{w_{LV}} \Rightarrow r_{out_{LV}} = \sqrt[3]{\frac{3}{4\pi}V_{LV} + V_{w_{LV}}}$$
$$\frac{4}{3}\pi R_{LV}^3 = V_{LV} + V_{r_{LV}} \Rightarrow R_{LV} = \sqrt[3]{\frac{3}{4\pi}V_{LV} + V_{r_{LV}}}$$
$$N_{LV}\, L_{m,LV} = 2\,\pi\, R_{LV} \Rightarrow L_{m,LV} = \frac{2\pi R_{LV}}{N_{LV}}$$

$$P_{LV} = 7.5\, F_{LV}\, \frac{L_{m,LV}}{L_r} \left((\frac{r_{out_{LV}}}{r_{in_{LV}}})^2 - 1 \right) + \lambda\, (V_{LV} - V_0)$$

F_{LV} is obtained from the sarcomere contraction model (see Appendix B).

Parameter	Units	Value
SBV	ml	940.86 (identified)
R_{sys}	10^3 mmHg $\cdot$ ms/ml	1.38 (identified)
R_{pul}	mmHg $\cdot$ ms/ml	109.57 (identified)
R_{mt}	mmHg $\cdot$ ms/ml	22.09 (identified)
R_{tc}	mmHg $\cdot$ ms/ml	11.56 (identified)
R_{av}	mmHg $\cdot$ ms/ml	47.96 (identified)
R_{pv}	mmHg $\cdot$ ms/ml	3.51 (identified)
C_{ao}	mmHg/ml	0.9550 (identified)
C_{vc}	mmHg/ml	79.10 (identified)
C_{pa}	mmHg/ml	2.43 (identified)
C_{pv}	mmHg/ml	23.34 (identified)
V_{lvw}	ml	334.86 (identified)
V_{rvw}	ml	48.31 (identified)
λ	mmHg/ml^3	$5\ 10^{-5}$ [118]
V_0	ml	80 [118]

Table 15: Hemodynamic parameters.

The same reasoning for the RV gives:

$$P_{RV} = 7.5\, F_{RV}\, \frac{Lm_{RV}}{L_r} \left((\frac{r_{out_{RV}}}{r_{in_{RV}}})^2 - 1 \right) + \lambda\, (V_{RV} - V_0)$$

BIBLIOGRAPHY

[1] R. E. Klabunde, *Cardiovascular physiology concepts*. Lippincott Williams & Wilkins, 2005, p. 235, ISBN: 078175030X.

[2] G. J. Crystal, S. I. Assaad, and P. M. Heerdt, "Cardiovascular physiology: integrative function," *Pharmacol. Physiol. Anesth.*, pp. 473–519, 2019.

[3] J. E. J. E. Hall and A. C. Guyton, *Guyton and Hall textbook of medical physiology*. Saunders Elsevier, 2011, ISBN: 1437726747.

[4] H. Shiels and E. White, "The Frank-Starling mechanism in vertebrate cardiac myocytes.," *J. Exp. Biol.*, vol. 211, no. Pt 13, pp. 2005–2013, 2008, ISSN: 0022-0949.

[5] O. Frank, "On the dynamics of cardiac muscle," *Am. Heart J.*, vol. 58, no. 2, pp. 282–317, 1959, ISSN: 0002-8703.

[6] S. W. Patterson and E. H. Starling, "On the mechanical factors which determine the output of the ventricles.," *J. Physiol.*, vol. 48, no. 5, pp. 357–79, 1914, ISSN: 0022-3751.

[7] S. W. Patterson, H Piper, and E. H. Starling, "The regulation of the heart beat.," *J. Physiol.*, vol. 48, no. 6, pp. 465–513, 1914, ISSN: 0022-3751.

[8] E. H. Starling and M. B. Visscher, "The regulation of the energy output of the heart.," *J. Physiol.*, vol. 62, no. 3, pp. 243–61, 1927, ISSN: 0022-3751.

[9] E. H. Starling, "The linacre lecture on the law of the heart given at cambridge, 1915," *Nature*, vol. 101, no. 2525, pp. 43–43, 1918, ISSN: 0028-0836.

[10] H.-G. Zimmer, "Who discovered the Frank-Starling mechanism?" *Physiology*, vol. 17, no. 5, pp. 181–184, 2002, ISSN: 1548-9213.

[11] A. M. Katz, "Ernest henry Starling, his predecessors, and the "law of the heart"," *Circulation*, vol. 106, no. 23, pp. 2986–2992, 2002, ISSN: 0009-7322.

[12] H. Huxley and J. Hanson, "Changes in the cross-striations of muscle during contraction and stretch and their structural interpretation," *Nature*, vol. 173, no. 4412, pp. 973–976, 1954, ISSN: 0028-0836.

[13] A. F. Huxley and R. Niedergerke, "Structural changes in muscle during contraction: interference microscopy of living muscle fibres," *Nature*, vol. 173, no. 4412, pp. 971–973, 1954, ISSN: 0028-0836.

[14] A. M. Gordon, E Homsher, and M Regnier, "Regulation of contraction in striated muscle," *Physiol. Rev.*, vol. 80, no. 2, pp. 853–924, 2000.

[15] A Fabiato and F Fabiato, "Dependence of the contractile activation of skinned cardiac cells on the sarcomere length.," *Nature*, vol. 256, no. 5512, pp. 54–6, 1975, ISSN: 0028-0836.

[16] F. Fuchs and S. H. Smith, "Calcium, cross-bridges, and the Frank-Starling relationship," *News Physiol Sci*, vol. 16, no. 1, pp. 5–10, 2001.

[17] J. P. Konhilas, T. C. Irving, and P. P. De Tombe, "Frank-Starling law of the heart and the cellular mechanisms of length-dependent activation," *Pflugers Arch. Eur. J. Physiol.*, vol. 445, no. 3, pp. 305–310, 2002, ISSN: 00316768.

[18] P. P. de Tombe, R. D. Mateja, K Tachampa, Y Ait Mou, G. P. Farman, and T. C. Irving, "Myofilament length dependent activation," *J Mol Cell Cardiol*, vol. 48, no. 5, pp. 851–858, 2010.

[19] P. P. de Tombe and J. V. Tyberg, "Frank's law of the heart: found in translation," *J. Mol. Cell. Cardiol.*, vol. 121, pp. 33–35, 2018, ISSN: 0022-2828.

[20] V. Sequeira and J. van der Velden, "Historical perspective on heart function: the Frank–Starling law," *Biophys. Rev.*, vol. 7, no. 4, pp. 421–447, 2015, ISSN: 1867-2450.

[21] ——, "The Frank–Starling law: a jigsaw of titin proportions," *Biophys. Rev.*, vol. 9, no. 3, pp. 259–267, 2017, ISSN: 1867-2450.

[22] J. Feher and J. Feher, "The cardiac function curve," *Quant. Hum. Physiol.*, pp. 486–494, 2012.

[23] F Michard and J. L. Teboul, "Using heart-lung interactions to assess fluid responsiveness during mechanical ventilation.," *Crit. Care*, vol. 4, no. 5, pp. 282–9, 2000, ISSN: 1364-8535.

[24] K. Bendjelid and J.-A. Romand, "Fluid responsiveness in mechanically ventilated patients: a review of indices used in intensive care.," en, *Intensive Care Med.*, vol. 29, no. 3, pp. 352–60, 2003, ISSN: 0342-4642.

[25] X. Monnet and J.-L. Teboul, "Volume responsiveness.," *Curr. Opin. Crit. Care*, vol. 13, no. 5, pp. 549–553, 2007, ISSN: 1070-5295.

[26] P. E. Marik, X. Monnet, and J.-L. Teboul, "Hemodynamic parameters to guide fluid therapy.," En, *Ann. Intensive Care*, vol. 1, no. 1, p. 1, 2011, ISSN: 2110-5820.

[27] S. A. Niederer and N. P. Smith, "At the heart of computational modelling," *J. Physiol.*, vol. 590, no. 6, pp. 1331–1338, 2012, ISSN: 1469-7793.

[28] N. A. Trayanova and J. J. Rice, "Cardiac electromechanical models: from cell to organ," *Front Physiol*, vol. 2, p. 43, 2011.

[29] S. A. Niederer, K. S. Campbell, and S. G. Campbell, "A short history of the development of mathematical models of cardiac mechanics," *J. Mol. Cell. Cardiol.*, vol. 127, pp. 11–19, 2019, ISSN: 0022-2828.

[30] *Wiggers diagram - wikimedia commons*. [Online]. Available: https://commons.wikimedia.org/wiki/File:Wiggers{_}Diagram{_}2.svg (visited on 05/20/2019).

[31] V. M. Sitzer, "Physiologic framework of extrinsic controls.," *J. Cardiovasc. Nurs.*, vol. 5, no. 4, pp. 1–9, 1991, ISSN: 0889-4655.

[32] D. M. Bers, *Excitation-Contraction Coupling and Cardiac Contractile Force*. Springer Netherlands, 2001, p. 452, ISBN: 9789401006583.

[33] A. M. Gordon, M. Regnier, and E. Homsher, "Skeletal and cardiac muscle contractile activation: tropomyosin "rocks and rolls"," *Physiology*, vol. 16, no. 2, pp. 49–55, 2001, ISSN: 1548-9213.

[34] J. Feher and J. Feher, "The cellular basis of cardiac contractility," *Quant. Hum. Physiol.*, pp. 477–485, 2012.

[35] H. E. Cingolani, N. G. Pérez, O. H. Cingolani, and I. L. Ennis, "The anrep effect: 100 years later," *Am. J. Physiol. Circ. Physiol.*, vol. 304, no. 2, H175–H182, 2013, ISSN: 0363-6135.

[36] H. Schotola, S. T. Sossalla, A. Renner, J. Gummert, B. C. Danner, P. Schott, and K. Toischer, "The contractile adaption to preload depends on the amount of afterload.," *ESC Hear. Fail.*, vol. 4, no. 4, pp. 468–478, 2017, ISSN: 2055-5822.

[37] K. S. Campbell, "Impact of myocyte strain on cardiac myofilament activation.," *Pflugers Arch.*, vol. 462, no. 1, pp. 3–14, 2011, ISSN: 1432-2013.

[38] J. Feher, "Integration of cardiac output and venous return," in *Quant. Hum. Physiol.* Elsevier, 2012, pp. 529–537.

[39] R Jacob, B Dierberger, and G Kissling, "Functional significance of the Frank-Starling mechanism under physiological and pathophysiological conditions," *Eur.Heart J.*, vol. 13 Suppl E, pp. 7–14, 1992, ISSN: 0195-668X.

[40] D. A. Berlin and J. Bakker, "Starling curves and central venous pressure," *Crit. Care*, vol. 19, no. 1, p. 55, 2015, ISSN: 1364-8535.

[41] J. P. Holt, J. Allensworth, J. Diana, D. Collins, and H. Kines, "Effects of plethora and hemorrhage on left ventricular volume and pressure.," *Circ. Res.*, vol. 5, no. 3, pp. 273–80, 1957, ISSN: 0009-7330.

[42] L. N. Katz, "Analysis of the several factors regulating the performance of the heart," *Physiol. Rev.*, vol. 35, no. 1, pp. 91–106, 1955, ISSN: 0031-9333.

[43] S. J. Sarnoff and E. Berglund, "Ventricular function. i. Starling's law of the heart studied by means of simultaneous right and left ventricular function curves in the dog.," *Circulation*, vol. 9, no. 5, pp. 706–718, 1954, ISSN: 00097322.

[44] S. J. Sarnoff, "Myocardial contractility as described by ventricular function curves; observations on Starling's law of the heart.," *Physiol. Rev.*, vol. 35, no. 1, pp. 107–22, 1955, ISSN: 0031-9333.

[45] E. Braunwald, R. L. Frye, M. M. Aygen, J. W. Gilbert, and Jr., "Studies on Starling's law of the heart. iii. observations in patients with mitral stenosis and atrial fibrillation on the relationships between left ventricular end-diastolic segment length, filling pressure, and the characteristics of ventricular contrac," *J. Clin. Invest.*, vol. 39, no. 12, p. 1874, 1960.

[46] E Braunwald, C. J. Frahm, J Ross, and Jr., "Studies on Starling's law of the heart. v. left ventricular function in man.," *J. Clin. Invest.*, vol. 40, no. 10, pp. 1882–90, 1961, ISSN: 0021-9738.

[47] B. William, "Starling ' s law of the heart and stroke volume in man with observations on the," vol. XXV, no. May, 1962.

[48] J Ross and E Braunwald, "Studies on Starling's law of the heart. ix. the effects of impeding venous return on performance of the normal and failing human left ventricle.," *Circulation*, vol. 30, no. 5, pp. 719–27, 1964, ISSN: 0009-7322.

[49] E Braunwald, "The control of ventricular function in man.," *Br. Heart J.*, vol. 27, pp. 1–16, 1965, ISSN: 0007-0769.

[50] P. E. Marik, "The physiology of volume resuscitation," *Curr. Anesthesiol. Rep.*, vol. 4, no. 4, pp. 353–359, 2014, ISSN: 2167-6275.

[51] K. R. Walley, "Left ventricular function: time-varying elastance and left ventricular aortic coupling," *Crit. Care*, vol. 20, no. 1, p. 270, 2016, ISSN: 1364-8535.

[52] D. Burkhoff, I. Mirsky, and H. Suga, "Assessment of systolic and diastolic ventricular properties via pressure-volume analysis: a guide for clinical, translational, and basic researchers," *Am. J. Physiol. Circ. Physiol.*, vol. 289, no. 2, H501–H512, 2005, ISSN: 0363-6135.

[53] A. Pironet, "Model-based prediction of the response to vascular filling therapy," PhD thesis, Université de Liège, Liège, Belgique, 2016.

[54] F. Michard and J.-L. Teboul, "Predicting fluid responsiveness in icu patients," *Chest*, vol. 121, no. 6, pp. 2000–2008, 2002, ISSN: 00123692.

[55] D. W. Fawcett and N. S. McNutt, "The ultrastructure of the cat myocardium: i. ventricular papillary muscle," *J. Cell Biol.*, vol. 42, no. 1, pp. 1–45, 1969, ISSN: 0021-9525.

[56] J. P. Keener and J. Sneyd, *Mathematical physiology*. Springer, 2009, ISBN: 0387793887.

[57] D. M. Bers, "Cardiac excitation–contraction coupling," *Nature*, vol. 415, no. 6868, pp. 198–205, 2002, ISSN: 0028-0836.

[58] P. P. de Tombe, "Cardiac myofilaments: mechanics and regulation," *J. Biomech.*, vol. 36, no. 5, pp. 721–730, 2003, ISSN: 00219290.

[59] R. J. Solaro, "Integration of myofilament response to ca2+ with cardiac pump regulation and pump dynamics.," *Adv. Physiol. Educ.*, vol. 277, no. 6, S155, 1999, ISSN: 1043-4046.

[60] R. J. Adams and A. Schwartz, "Comparative mechanisms for contraction of cardiac and skeletal muscle," *Chest*, vol. 78, no. 1, pp. 123–139, 1980, ISSN: 0012-3692.

[61] A. M. Gordon, A. F. Huxley, and F. J. Julian, "The variation in isometric tension with sarcomere length in vertebrate muscle fibres.," *J. Physiol.*, vol. 184, no. 1, pp. 170–92, 1966, ISSN: 0022-3751.

[62] D. G. Allen and J. C. Kentish, "The cellular basis of the length-tension relation in cardiac muscle.," *J. Mol. Cell. Cardiol.*, vol. 17, no. 9, pp. 821–40, 1985, ISSN: 0022-2828.

[63] F. Kobirumaki-Shimozawa, T. Inoue, S. A. Shintani, K. Oyama, T. Terui, S. Minamisawa, S. Ishiwata, and N. Fukuda, "Cardiac thin filament regulation and the Frank-Starling mechanism.," *J. Physiol. Sci.*, vol. 64, no. 4, pp. 221–32, 2014, ISSN: 1880-6562.

[64] R. L. Moss and D. P. Fitzsimons, "Frank-Starling relationship: long on importance, short on mechanism," *Circ. Res.*, vol. 90, no. 1, pp. 11–13, 2002.

[65] J. Feher, "Contractile mechanisms in skeletal muscle," in *Quant. Hum. Physiol.* Elsevier, 2017, pp. 305–317.

[66] J. S. Walker, X. Li, and P. M. Buttrick, "Analysing force–pca curves," *J. Muscle Res. Cell Motil.*, vol. 31, no. 1, pp. 59–69, 2010, ISSN: 0142-4319.

[67] Y.-B. Sun and M. Irving, "The molecular basis of the steep force-calcium relation in heart muscle.," *J. Mol. Cell. Cardiol.*, vol. 48, no. 5, pp. 859–65, 2010, ISSN: 1095-8584.

[68] K. D. Varian, S. Raman, and P. M. L. Janssen, "Measurement of myofilament calcium sensitivity at physiological temperature in intact cardiac trabeculae," *Am. J. Physiol. Circ. Physiol.*, vol. 290, no. 5, H2092–H2097, 2006, ISSN: 0363-6135.

[69] B. R. MacIntosh, "Role of calcium sensitivity modulation in skeletal muscle performance," *Physiology*, vol. 18, no. 6, pp. 222–225, 2003, ISSN: 1548-9213.

[70] Y. Ait mou, J.-Y. le Guennec, E. Mosca, P. P. de Tombe, and O. Cazorla, "Differential contribution of cardiac sarcomeric proteins in the myofibrillar force response to stretch," *Pflügers Arch. - Eur. J. Physiol.*, vol. 457, no. 1, pp. 25–36, 2008, ISSN: 0031-6768.

[71] J.-H. Chung, B. J. Biesiadecki, M. T. Ziolo, J. P. Davis, and P. M. L. Janssen, "Myofilament calcium sensitivity: role in regulation of in vivo cardiac contraction and relaxation.," *Front. Physiol.*, vol. 7, p. 562, 2016, ISSN: 1664-042X.

[72] D. G. Stephenson and D. A. Williams, "Effects of sarcomere length on the force-pca relation in fast- and slow-twitch skinned muscle fibres from the rat.," *J. Physiol.*, vol. 333, pp. 637–53, 1982, ISSN: 0022-3751.

[73] E White, J. Y. Le Guennec, J. M. Nigretto, F Gannier, J. A. Argibay, and D Garnier, "The effects of increasing cell length on auxotonic contractions; membrane potential and intracellular calcium transients in single guinea-pig ventricular myocytes," *Exp. Physiol.*, vol. 78, no. 1, pp. 65–78, 1993.

[74] F. Fuchs and D. A. Martyn, "Length-dependent ca2+ activation in cardiac muscle: some remaining questions," *J. Muscle Res. Cell Motil.*, vol. 26, no. 4-5, pp. 199–212, 2005, ISSN: 0142-4319.

[75] L. M. Hanft, F. S. Korte, and K. S. McDonald, "Cardiac function and modulation of sarcomeric function by length," *Cardiovasc. Res.*, vol. 77, no. 4, pp. 627–636, 2007, ISSN: 0008-6363.

[76] P. P. de Tombe and H. E. ter Keurs, "Cardiac muscle mechanics: sarcomere length matters," *J. Mol. Cell. Cardiol.*, vol. 91, pp. 148–150, 2016, ISSN: 00222828.

[77] D. Amiad Pavlov and A. Landesberg, "The cross-bridge dynamics is determined by two length-independent kinetics: implications on muscle economy and Frank–Starling law," *J. Mol. Cell. Cardiol.*, vol. 90, pp. 94–101, 2016, ISSN: 0022-2828.

[78] J. P. Konhilas, T. C. Irving, and P. P. de Tombe, "Length-dependent activation in three striated muscle types of the rat.," *J. Physiol.*, vol. 544, no. Pt 1, pp. 225–36, 2002, ISSN: 0022-3751.

[79] R. J. Solaro, "Mechanisms of the Frank-Starling law of the heart: the beat goes on.," *Biophys. J.*, vol. 93, no. 12, pp. 4095–6, 2007, ISSN: 1542-0086.

[80] K. S. McDonald and R. L. Moss, "Osmotic compression of single cardiac myocytes eliminates the reduction in ca2+ sensitivity of tension at short sarcomere length.," *Circ. Res.*, vol. 77, no. 1, pp. 199–205, 1995, ISSN: 0009-7330.

[81] O Herzberg and M. N. James, "Refined crystal structure of troponin c from turkey skeletal muscle at 2.0 a resolution.," *J. Mol. Biol.*, vol. 203, no. 3, pp. 761–79, 1988, ISSN: 0022-2836.

[82] J. P. van Eerd and K Takahshi, "Determination of the complete amino acid sequence of bovine cardiac troponin c.," *Biochemistry*, vol. 15, no. 5, pp. 1171–80, 1976, ISSN: 0006-2960.

[83] Z. Yang, M. Yamazaki, Q. W. Shen, and D. R. Swartz, "Differences between cardiac and skeletal troponin interaction with the thin filament probed by troponin exchange in skeletal myofibrils.," *Biophys. J.*, vol. 97, no. 1, pp. 183–94, 2009, ISSN: 1542-0086.

[84] N Piroddi, C Tesi, M. A. Pellegrino, L. S. Tobacman, E Homsher, and C Poggesi, "Contractile effects of the exchange of cardiac troponin for fast skeletal troponin in rabbit psoas single myofibrils.," *J. Physiol.*, vol. 552, no. Pt 3, pp. 917–31, 2003, ISSN: 0022-3751.

[85] J. P. Konhilas, T. C. Irving, B. M. Wolska, E. E. Jweied, A. F. Martin, R. J. Solaro, and P. P. de Tombe, "Troponin i in the murine myocardium: influence on length-dependent activation and interfilament spacing.," *J. Physiol.*, vol. 547, no. Pt 3, pp. 951–61, 2003, ISSN: 0022-3751.

[86] F. S. Korte and K. S. McDonald, "Sarcomere length dependence of rat skinned cardiac myocyte mechanical properties: dependence on myosin heavy chain," *J. Physiol.*, vol. 581, no. 2, pp. 725–739, 2007, ISSN: 00223751.

[87] T. Kobayashi and R. J. Solaro, "Calcium, thin filaments, and the integrative biology of cardiac contractility," *Annu. Rev. Physiol.*, vol. 67, no. 1, pp. 39–67, 2005, ISSN: 0066-4278.

[88] T. Longyear, S. Walcott, and E. P. Debold, "The molecular basis of thin filament activation: from single molecule to muscle," *Sci. Rep.*, vol. 7, no. 1, p. 1822, 2017, ISSN: 2045-2322.

[89] L. J. Dupuis, J. Lumens, T. Arts, and T. Delhaas, "Mechano-chemical interactions in cardiac sarcomere contraction: a computational modeling study," *PLOS Comput. Biol.*, vol. 12, no. 10, A. D. McCulloch, Ed., e1005126, 2016, ISSN: 1553-7358.

[90] J. J. Rice, R. L. Winslow, and W. C. Hunter, "Comparison of putative cooperative mechanisms in cardiac muscle: length dependence and dynamic responses," *Am. J. Physiol. Circ. Physiol.*, vol. 276, no. 5, H1734–H1754, 1999, ISSN: 0363-6135.

[91] D. P. Dobesh, J. P. Konhilas, and P. P. de Tombe, "Cooperative activation in cardiac muscle: impact of sarcomere length," *Am. J. Physiol. Circ. Physiol.*, vol. 282, no. 3, H1055–H1062, 2002, ISSN: 0363-6135.

[92] E White, "Length-dependent mechanisms in single cardiac cells," *Exp. Physiol.*, vol. 81, no. 6, pp. 885–897, 1996, ISSN: 09580670.

[93] S. Nishimura, S.-i. Yasuda, M. Katoh, K. P. Yamada, H. Yamashita, Y. Saeki, K. Sunagawa, R. Nagai, T. Hisada, and S. Sugiura, "Single cell mechanics of rat cardiomyocytes under isometric, unloaded, and physiologically loaded conditions," *Am. J. Physiol. Circ. Physiol.*, vol. 287, no. 1, H196–H202, 2004.

[94] J. K. Leach, A. J. Brady, B. J. Skipper, and D. L. Millis, "Effects of active shortening on tension development of rabbit papillary muscle," *Am. J. Physiol. Circ. Physiol.*, vol. 238, no. 1, H8–H13, 1980, ISSN: 0363-6135.

[95] E White, M. R. Boyett, and C. H. Orchard, "The effects of mechanical loading and changes of length on single guinea-pig ventricular myocytes.," *J. Physiol.*, vol. 482 (Pt 1, pp. 93–107, 1995, ISSN: 0022-3751.

[96] C. Bollensdorff, O. Lookin, and P. Kohl, "Assessment of contractility in intact ventricular cardiomyocytes using the dimensionless 'Frank–Starling gain' index," *Pflügers Arch. - Eur. J. Physiol.*, vol. 462, no. 1, pp. 39–48, 2011, ISSN: 0031-6768.

[97] P. P. De Tombe and W. C. Little, "Inotropic effects of ejection are myocardial properties," *Am. J. Physiol. Circ. Physiol.*, vol. 266, no. 3, H1202–H1213, 1994, ISSN: 0363-6135.

[98] W. C. Hunter, "End-systolic pressure as a balance between opposing effects of ejection.," *Circ. Res.*, vol. 64, no. 2, pp. 265–275, 1989, ISSN: 0009-7330.

[99] D. Burkhoff, P. P. de Tombe, W. C. Hunter, and D. A. Kass, "Contractile strength and mechanical efficiency of left ventricle are enhanced by physiological afterload," *Am. J. Physiol. Circ. Physiol.*, vol. 260, no. 2, H569–H578, 1991, ISSN: 0363-6135.

[100] M. I. Noble, "The Frank–Starling curve.," *Clin. Sci. Mol. Med.*, vol. 54, no. 1, pp. 1–7, 1978, ISSN: 0301-0538.

[101] A. J. Brady, "Length-tension relations in cardiac muscle," vol. 7, pp. 603–610,

[102] G Elzinga and N Westerhof, "How to quantify pump function of the heart. the value of variables derived from measurements on isolated muscle.," *Circ. Res.*, vol. 44, no. 3, pp. 303–308, 1979, ISSN: 0009-7330.

[103] L. M. Hanft, M. L. Greaser, and K. S. McDonald, "Titin-mediated control of cardiac myofibrillar function," *Arch. Biochem. Biophys.*, vol. 552-553, pp. 83–91, 2014, ISSN: 0003-9861.

[104] J. J. Rice, F Wang, D. M. Bers, and P. P. de Tombe, "Approximate model of cooperative activation and crossbridge cycling in cardiac muscle using ordinary differential equations," *Biophys J*, vol. 95, no. 5, pp. 2368–2390, 2008.

[105] R. Kerckhoffs, S. Healy, T. Usyk, and A. McCulloch, "Computational methods for cardiac electromechanics," *Proc. IEEE*, vol. 94, no. 4, pp. 769–783, 2006, ISSN: 0018-9219.

[106] R. C. P. Kerckhoffs, O. P. Faris, P. H. M. Bovendeerd, F. W. Prinzen, K Smits, E. R. McVeigh, and T Arts, "Electromechanics of paced left ventricle simulated by straightforward mathematical model: comparison with experiments.," *Am. J. Physiol. Heart Circ. Physiol.*, vol. 289, no. 5, H1889–97, 2005, ISSN: 0363-6135.

[107] K. D. Costa, J. W. Holmes, and A. D. Mcculloch, "Modelling cardiac mechanical properties in three dimensions," *Philos. Trans. R. Soc. London. Ser. A Math. Phys. Eng. Sci.*, vol. 359, no. 1783, P. Kohl, D. Noble, and P. J. Hunter, Eds., pp. 1233–1250, 2001, ISSN: 1471-2962.

[108] M. P. Nash, M. P. Nash, and P. J. Hunter, "Computational mechanics of the heart - from tissue structure to ventricular function," *J. Elast.*, 2000.

[109] P. M. Nielsen, I. J. Le Grice, B. H. Smaill, and P. J. Hunter, "Mathematical model of geometry and fibrous structure of the heart.," *Am. J. Physiol.*, vol. 260, no. 4 Pt 2, H1365–78, 1991, ISSN: 0002-9513.

[110] P. J. Hunter, A. J. Pullan, and B. H. Smaill, "Modeling total heart function," *Annu. Rev. Biomed. Eng.*, vol. 5, no. 1, pp. 147–177, 2003, ISSN: 1523-9829.

[111] S. A. Niederer and N. P. Smith, "The role of the Frank-Starling law in the transduction of cellular work to whole organ pump function: a computational modeling analysis," *PLoS Comput. Biol.*, vol. 5, no. 4, 2009, ISSN: 1553734X.

[112] X. Zhang, Z.-Q. Liu, K. S. Campbell, and J. F. Wenk, "Evaluation of a novel finite element model of active contraction in the heart," *Front. Physiol.*, vol. 9, p. 425, 2018, ISSN: 1664-042X.

[113] H. Suga, K. Sagawa, and A. A. Shoukas, "Load independence of the instantaneous pressure-volume ratio of the canine left ventricle and effects of epinephrine and heart rate on the ratio," *Circ. Res.*, vol. 32, no. 3, pp. 314–322, 1973, ISSN: 0009-7330.

[114] E. B. Shim, C. H. Leem, Y. Abe, and A. Noma, "A new multi-scale simulation model of the circulation: from cells to system.," *Philos. Trans. A. Math. Phys. Eng. Sci.*, vol. 364, no. 1843, pp. 1483–500, 2006, ISSN: 1364-503X.

[115] A. Pironet, T. Desaive, S. Kosta, A. Lucas, S. Paeme, A. Collet, C. G. Pretty, P. Kolh, and P. C. Dauby, "A multi-scale cardiovascular system model can account for the load-dependence of the end-systolic pressure-volume relationship," *Biomed. Eng. Online*, vol. 12, no. 1, p. 8, 2013, ISSN: 1475-925X.

[116] S. Kosta, J. Negroni, E. Lascano, and P. Dauby, "Multiscale model of the human cardiovascular system: description of heart failure and comparison of contractility indices," *Math. Biosci.*, vol. 284, pp. 71–79, 2017, ISSN: 0025-5564.

[117] T. Arts, T. Delhaas, P. Bovendeerd, X. Verbeek, and F. W. Prinzen, "Adaptation to mechanical load determines shape and properties of heart and circulation: the circadapt model.," *Am. J. Physiol. Heart Circ. Physiol.*, vol. 288, no. 4, H1943–54, 2005, ISSN: 0363-6135.

[118] J. A. Negroni and E. C. Lascano, "Concentration and elongation of attached cross-bridges as pressure determinants in a ventricular model," *J. Mol. Cell. Cardiol.*, vol. 31, no. 8, pp. 1509–1526, 1999, ISSN: 0022-2828.

[119] E. C. Lascano, J. I. Felice, S. Wray, S. Kosta, P. C. Dauby, E. I. Cabrera-Fischer, and J. A. Negroni, "Experimental assessment of a myocyte-based multiscale model of cardiac contractile dysfunction," *J. Theor. Biol.*, vol. 456, pp. 16–28, 2018, ISSN: 0022-5193.

[120] D. Burkhoff, "Explaining load dependence of ventricular contractile properties with a model of excitation-contraction coupling," *J. Mol. Cell. Cardiol.*, vol. 26, no. 8, pp. 959–978, 1994, ISSN: 00222828.

[121] K. B. Campbell, A. M. Simpson, S. G. Campbell, H. L. Granzier, and B. K. Slinker, "Dynamic left ventricular elastance: a model for integrating cardiac muscle contraction into ventricular pressure-volume relationships," *J. Appl. Physiol.*, vol. 104, no. 4, pp. 958–975, 2008, ISSN: 8750-7587.

[122] M. Caruel, R. Chabiniok, P. Moireau, Y. Lecarpentier, and D. Chapelle, "Dimensional reductions of a cardiac model for effective validation and calibration," *Biomech. Model. Mechanobiol.*, vol. 13, no. 4, pp. 897–914, 2014, ISSN: 1617-7959.

[123] P. Nardinocchi, L. Teresi, and V. Varano, "A simplified mechanical modeling for myocardial contractions and the ventricular pressure–volume relationships," *Mech. Res. Commun.*, vol. 38, no. 7, pp. 532–535, 2011, ISSN: 0093-6413.

[124] R. Beyar, S. Sideman, and U. Dinnar, "Cardiac assist by intrathoracic and abdominal pressure variations: a mathematical study," *Med. Biol. Eng. Comput.*, vol. 22, no. 6, pp. 507–515, 1984, ISSN: 0140-0118.

[125] D. Burkhoff, P. P. De Tombe, and W. C. Hunter, "Impact of ejection on magnitude and time course of ventricular pressure-generating capacity," *Am. J. Physiol. Circ. Physiol.*, vol. 265, no. 3, H899–H909, 1993, ISSN: 0363-6135.

[126] B. W. Smith, J. Chase, R. I. Nokes, G. M. Shaw, and G. Wake, "Minimal haemodynamic system model including ventricular interaction and valve dynamics," *Med. Eng. Phys.*, vol. 26, no. 2, pp. 131–139, 2004, ISSN: 13504533.

[127] C. Hann, J. Chase, and G. Shaw, "Efficient implementation of non-linear valve law and ventricular interaction dynamics in the minimal cardiac model," *Comput. Methods Programs Biomed.*, vol. 80, no. 1, pp. 65–74, 2005, ISSN: 0169-2607.

[128] E. B. Shim, A. Amano, T. Takahata, T. Shimayoshi, and A. Noma, "The cross-bridge dynamics during ventricular contraction predicted by coupling the cardiac cell model with a circulation model," *J. Physiol. Sci.*, vol. 57, no. 5, pp. 275–285, 2007, ISSN: 1880-6546.

[129] N. Westerhof, N. Stergiopulos, and M. I. M. Noble, *Snapshots of hemodynamics : an aid for clinical research and graduate education*. Springer, 2010, p. 271, ISBN: 1441963634.

[130] J. K.-J. Li, *Dynamics of the vascular system*. World Scientific, 2004, p. 257, ISBN: 9810249071.

[131] C. F. Babbs, "Noninvasive measurement of cardiac stroke volume using pulse wave velocity and aortic dimensions: a simulation study.," *Biomed. Eng. Online*, vol. 13, p. 137, 2014, ISSN: 1475-925X.

[132] D. Burkhoff, S. Sugiura, D. T. Yue, and K. Sagawa, "Contractility-dependent curvilinearity of end-systolic pressure-volume relations," *Am. J. Physiol. Circ. Physiol.*, vol. 252, no. 6, H1218–H1227, 1987, ISSN: 0363-6135.

[133] D. A. Kass, R Beyar, E Lankford, M Heard, W. L. Maughan, and K Sagawa, "Influence of contractile state on curvilinearity of in situ end-systolic pressure-volume relations.," *Circulation*, vol. 79, no. 1, pp. 167–78, 1989, ISSN: 0009-7322.

[134] T. E. Claessens, D. Georgakopoulos, M. Afanasyeva, S. J. Vermeersch, H. D. Millar, N. Stergiopulos, N. Westerhof, P. R. Verdonck, and P. Segers, "Nonlinear isochrones in murine left ventricular pressure-volume loops: how well does the time-varying elastance concept hold?" *Am. J. Physiol. Circ. Physiol.*, vol. 290, no. 4, H1474–H1483, 2006, ISSN: 0363-6135.

[135] W. L. Maughan, A. A. Shoukas, K Sagawa, and M. L. Weisfeldt, "Instantaneous pressure-volume relationship of the canine right ventricle.," *Circ. Res.*, vol. 44, no. 3, pp. 309–315, 1979, ISSN: 0009-7330.

[136] S. G. Shroff, J. S. Janicki, and K. T. Weber, "Evidence and quantitation of left ventricular systolic resistance," *Am. J. Physiol. Circ. Physiol.*, vol. 249, no. 2, H358–H370, 1985, ISSN: 0363-6135.

[137] S. R. Vaartjes and H. B. Boom, "Left ventricular internal resistance and unloaded ejection flow assessed from pressure-flow relations: a flow-clamp study on isolated rabbit hearts.," *Circ. Res.*, vol. 60, no. 5, pp. 727–37, 1987, ISSN: 0009-7330.

[138] J.-W. Lankhaar, F. A. Rövekamp, P. Steendijk, T. J. C. Faes, B. E. Westerhof, T. Kind, A. Vonk-Noordegraaf, and N. Westerhof, "Modeling the instantaneous pressure–volume relation of the left ventricle: a comparison of six models," *Ann. Biomed. Eng.*, vol. 37, no. 9, pp. 1710–1726, 2009, ISSN: 0090-6964.

[139] S. M. Davidson, D. O. Kannangara, C. G. Pretty, S. Kamoi, A. Pironet, T. Desaive, and J. G. Chase, "Modelling of the nonlinear end-systolic pressure-volume relation and volume-at-zero-pressure in porcine experiments," in *2015 37th Annu. Int. Conf. IEEE Eng. Med. Biol. Soc.*, vol. 2015, IEEE, 2015, pp. 6544–6547, ISBN: 978-1-4244-9271-8.

[140] K. H. W. J. ten Tusscher, D. Noble, P. J. Noble, and A. V. Panfilov, "A model for human ventricular tissue," *Am. J. Physiol. Circ. Physiol.*, vol. 286, no. 4, H1573–H1589, 2004, ISSN: 0363-6135.

[141] K. H. W. J. ten Tusscher and A. V. Panfilov, "Alternans and spiral breakup in a human ventricular tissue model.," *Am. J. Physiol. Heart Circ. Physiol.*, vol. 291, no. 3, H1088–100, 2006, ISSN: 0363-6135.

[142] J. A. Negroni and E. C. Lascano, "A cardiac muscle model relating sarcomere dynamics to calcium kinetics," *J. Mol. Cell. Cardiol.*, vol. 28, no. 5, pp. 915–929, 1996, ISSN: 0022-2828.

[143] ——, "Simulation of steady state and transient cardiac muscle response experiments with a huxley-based contraction model," *J. Mol. Cell. Cardiol.*, vol. 45, no. 2, pp. 300–312, 2008, ISSN: 00222828.

[144] J. A. Negroni, S. Morotti, E. C. Lascano, A. V. Gomes, E. Grandi, J. L. Puglisi, and D. M. Bers, "Beta-adrenergic effects on cardiac myofilaments and contraction in an integrated rabbit ventricular myocyte model," *J. Mol. Cell. Cardiol.*, vol. 81, pp. 162–175, 2015, ISSN: 00222828.

[145] J. Keener and J. Sneyd, "Cellular homeostasis," in, Springer, New York, NY, 2009, pp. 49–119.

[146] J. M. Nerbonne, "Molecular basis of functional voltage-gated k+ channel diversity in the mammalian myocardium.," *J. Physiol.*, vol. 525 Pt 2, no. Pt 2, pp. 285–98, 2000, ISSN: 0022-3751.

[147] H. Schmidt, "Calcium buffering: models of ca2+ dynamics and steady-state approximations," in *Encycl. Comput. Neurosci.* New York, NY: Springer New York, 2013, pp. 1–6.

[148] A. F. Huxley, "Muscle structure and theories of contraction.," *Prog. Biophys. Biophys. Chem.*, vol. 7, pp. 255–318, 1957, ISSN: 0096-4174.

[149] S. A. Bruce, S. K. Phillips, and R. C. Woledge, "Interpreting the relation between force and cross-sectional area in human muscle.," *Med. Sci. Sports Exerc.*, vol. 29, no. 5, pp. 677–83, 1997, ISSN: 0195-9131.

[150] M. L. Munro, X. Shen, M. Ward, P. N. Ruygrok, D. J. Crossman, and C. Soeller, "Highly variable contractile performance correlates with myocyte content in trabeculae from failing human hearts," *Sci. Rep.*, vol. 8, 2018.

[151] I. Colorado Cervantes, V. Sansalone, and L. Teresi, "The heart function as a motor-brake system," *J. Theor. Biol.*, vol. 467, pp. 23–30, 2019, ISSN: 00225193.

[152] J. A. Shaw, K. Dasharathi, A. S. Wineman, and M.-S. Si, "A simple model for myocardial changes in a failing heart," *Int. J. Non. Linear. Mech.*, vol. 68, pp. 132–145, 2015, ISSN: 0020-7462.

[153] T Arts, P. H. Bovendeerd, F. W. Prinzen, and R. S. Reneman, "Relation between left ventricular cavity pressure and volume and systolic fiber stress and strain in the wall.," *Biophys. J.*, vol. 59, no. 1, pp. 93–102, 1991, ISSN: 0006-3495.

[154] E. K. Rodriguez, W. C. Hunter, M. J. Royce, M. K. Leppo, A. S. Douglas, and H. F. Weisman, "A method to reconstruct myocardial sarcomere lengths and orientations at transmural sites in beating canine hearts.," *Am. J. Physiol.*, vol. 263, no. 1 Pt 2, H293–306, 1992, ISSN: 0002-9513.

[155] H. M. Spotnitz, "Macro design, structure, and mechanics of the left ventricle," *J. Thorac. Cardiovasc. Surg.*, vol. 119, no. 5, pp. 1053–1077, 2000, ISSN: 00225223.

[156] *Lidco - normal hemodynamic parameters*. [Online]. Available: http://www.lidco.com/clinical/hemodynamic.php.

[157] T. Shannon, "Integrated calcium management in cardiac myocytes," in, Springer, Berlin, Heidelberg, 2005, pp. 63–95.

[158] E. C. Lascano, M. Said, L. Vittone, A. Mattiazzi, C. Mundiña-Weilenmann, and J. A. Negroni, "Role of camkii in post acidosis arrhythmias: a simulation study using a human myocyte model.," *J. Mol. Cell. Cardiol.*, vol. 60, pp. 172–83, 2013, ISSN: 1095-8584.

[159] S. Land, S.-J. Park-Holohan, N. P. Smith, C. G. dos Remedios, J. C. Kentish, and S. A. Niederer, "A model of cardiac contraction based on novel measurements of tension development in human cardiomyocytes," *J. Mol. Cell. Cardiol.*, vol. 106, pp. 68–83, 2017, ISSN: 0022-2828.

[160] *Edwards lifesciences: normal hemodynamic parameters and laboratory values.*

[161] A. Pironet, P. C. Dauby, J. G. Chase, P. D. Docherty, J. A. Revie, and T. Desaive, "Structural identifiability analysis of a cardiovascular system model," *Med. Eng. Phys.*, vol. 38, no. 5, pp. 433–441, 2016, ISSN: 13504533.

[162] J. A. Revie, D. J. Stevenson, J. G. Chase, C. E. Hann, B. C. Lambermont, A. Ghuysen, P. Kolh, G. M. Shaw, S. Heldmann, and T. Desaive, "Validation of subject-specific cardiovascular system models from porcine measurements," *Comput. Methods Programs Biomed.*, vol. 109, no. 2, pp. 197–210, 2013, ISSN: 01692607.

[163] L. K. Waldman, Y. C. Fung, and J. W. Covell, "Transmural myocardial deformation in the canine left ventricle. normal in vivo three-dimensional finite strains.," *Circ. Res.*, vol. 57, no. 1, pp. 152–163, 1985, ISSN: 0009-7330.

[164] Y. Wang and J. A. Hill, "Electrophysiological remodeling in heart failure.," *J. Mol. Cell. Cardiol.*, vol. 48, no. 4, pp. 619–32, 2010, ISSN: 1095-8584.

[165] D. J. Beuckelmann, M. Nabauer, and E. Erdmann, "Intracellular calcium handling in isolated ventricular myocytes from patients with terminal heart failure," *Circulation*, vol. 85, no. 3, pp. 1046–1055, 1992, ISSN: 0009-7322.

[166] ——, "Alterations of k+ currents in isolated human ventricular myocytes from patients with terminal heart failure," *Circ. Res.*, vol. 73, no. 2, pp. 379–385, 1993, ISSN: 0009-7330.

[167] C.-H. Chen, M. Nakayama, E. Nevo, B. J. Fetics, W. Maughan, and D. A. Kass, "Coupled systolic-ventricular and vascular stiffening with age," *J. Am. Coll. Cardiol.*, vol. 32, no. 5, pp. 1221–1227, 1998, ISSN: 07351097.

[168] G. M. Shaw, J. G. Chase, C. Starfinger, B. W. Smith, C. E. Hann, T. Desaive, and A. Ghuysen, "Modelling the cardiovascular system.," *Crit. Care Resusc.*, vol. 9, no. 3, pp. 264–9, 2007, ISSN: 1441-2772.

[169] R. C. P. Kerckhoffs, M. L. Neal, Q. Gu, J. B. Bassingthwaighte, J. H. Omens, and A. D. McCulloch, "Coupling of a 3d finite element model of cardiac ventricular mechanics to lumped systems models of the systemic and pulmonic circulation.," *Ann. Biomed. Eng.*, vol. 35, no. 1, pp. 1–18, 2007, ISSN: 0090-6964.

[170] H. Watanabe, S. Sugiura, H. Kafuku, and T. Hisada, "Multiphysics simulation of left ventricular filling dynamics using fluid-structure interaction finite element method," *Biophys. J.*, vol. 87, no. 3, pp. 2074–2085, 2004, ISSN: 00063495.

[171] S. G. Campbell, E. Howard, J. Aguado-Sierra, B. A. Coppola, J. H. Omens, L. J. Mulligan, A. D. McCulloch, and R. C. P. Kerckhoffs, "Effect of transmurally heterogeneous myocyte excitation-contraction coupling on canine left ventricular electromechanics," *Exp. Physiol.*, vol. 94, no. 5, pp. 541–552, 2009, ISSN: 09580670.

[172] S. A. Niederer and N. P. Smith, "A mathematical model of the slow force response to stretch in rat ventricular myocytes," *Biophys. J.*, vol. 92, no. 11, pp. 4030–4044, 2007, ISSN: 0006-3495.

[173] J. Sainte-Marie, D. Chapelle, R. Cimrman, and M. Sorine, "Modeling and estimation of the cardiac electromechanical activity," *Comput. Struct.*, vol. 84, no. 28, pp. 1743–1759, 2006, ISSN: 0045-7949.

[174] S. Land, S. A. Niederer, and N. P. Smith, "Efficient computational methods for strongly coupled cardiac electromechanics," *IEEE Trans. Biomed. Eng.*, vol. 59, no. 5, pp. 1219–1228, 2012, ISSN: 0018-9294.

[175] P. Nardinocchi, L. Teresi, and V. Varano, "Myocardial contractions and the ventricular pressure–volume relationship," 2010. arXiv: 1005.5292.

[176] D. A. Kass and W. L. Maughan, "From 'emax' to pressure-volume relations: a broader view.," *Circulation*, vol. 77, no. 6, pp. 1203–1212, 1988, ISSN: 0009-7322.

[177] P. Morimont, B. Lambermont, T. Desaive, N. Janssen, G. Chase, and V. D'Orio, "Arterial dp/dtmax accurately reflects left ventricular contractility during shock when adequate vascular filling is achieved.," En, *BMC Cardiovasc. Disord.*, vol. 12, no. 1, p. 13, 2012, ISSN: 1471-2261.

[178] D. A. Kass, W. L. Maughan, Z. M. Guo, A Kono, K Sunagawa, and K Sagawa, "Comparative influence of load versus inotropic states on indexes of ventricular contractility: experimental and theoretical analysis based on pressure-volume relationships.," *Circulation*, vol. 76, no. 6, pp. 1422–36, 1987, ISSN: 0009-7322.

[179] D. Adler, E. Scott Monrad, E. H. Sonnenblick, O. M. Hess, and H. P. Krayenbuehl, "Time to dp/dt max , a useful index for evaluation of contractility in the catheterization laboratory," *Clin. Cardiol.*, vol. 19, no. 5, pp. 397–403, 1996, ISSN: 01609289.

[180] A. J. Drake-Holland, C. J. Mills, M. I. Noble, and S Pugh, "Responses to changes in filling and contractility of indices of human left ventricular mechanical performance.," *J. Physiol.*, vol. 422, pp. 29–39, 1990, ISSN: 0022-3751.

[181] A. M. Gosselink, P. K. Blanksma, H. J. Crijns, I. C. Van Gelder, P.-J. de Kam, H. L. Hillege, M. G. Niemeijer, K. I. Lie, and F. L. Meijler, "Left ventricular beat-to-beat performance in atrial fibrillation: contribution of Frank-Starling mechanism after short rather than long rr intervals," *J. Am. Coll. Cardiol.*, vol. 26, no. 6, pp. 1516–1521, 1995, ISSN: 07351097.

[182] D. D. Glower, J. A. Spratt, N. D. Snow, J. S. Kabas, J. W. Davis, C. O. Olsen, G. S. Tyson, D. C. Sabiston, and J. S. Rankin, "Linearity of the Frank-Starling relationship in the intact heart: the concept of preload recruitable stroke work.," *Circulation*, vol. 71, no. 5, pp. 994–1009, 1985, ISSN: 0009-7322.

[183] D. T. Mangano, D. C. Van Dyke, and R. J. Ellis, "The effect of increasing preload on ventricular output and ejection in man. limitations of the Frank-Starling mechanism.," *Circulation*, vol. 62, no. 3, pp. 535–41, 1980, ISSN: 0009-7322.

[184] K Komamura, R. P. Shannon, T Ihara, Y. T. Shen, I Mirsky, S. P. Bishop, and S. F. Vatner, "Exhaustion of Frank-Starling mechanism in conscious dogs with heart failure.," *Am. J. Physiol.*, vol. 265, no. 4 Pt 2, H1119–31, 1993, ISSN: 0002-9513.

[185] J. V. Nixon, R. G. Murray, P. D. Leonard, J. H. Mitchell, and C. G. Blomqvist, "Effect of large variations in preload on left ventricular performance characteristics in normal subjects.," *Circulation*, vol. 65, no. 4, pp. 698–703, 1982, ISSN: 0009-7322.

[186] J. M. Norton, "Toward consistent definitions for preload and afterload," *Adv. Physiol. Educ.*, vol. 25, no. 1, pp. 53–61, 2001, ISSN: 1043-4046.

[187] P. LaCombe and S. L. Lappin, *Physiology, Afterload Reduction*. StatPearls Publishing, 2019.

[188] Y. A. Mou, C. Bollensdorff, O. Cazorla, Y. Magdi, and P. P. de Tombe, "Exploring cardiac biophysical properties," *Glob. Cardiol. Sci. Pract.*, vol. 2015, no. 1, p. 10, 2015, ISSN: 2305-7823.

[189] J. G. Chaui-Berlinck and L. H. A. Monteiro, "Frank-Starling mechanism and short-term adjustment of cardiac flow.," *J. Exp. Biol.*, vol. 220, no. Pt 23, pp. 4391–4398, 2017, ISSN: 1477-9145.

[190] Y. Hu, V. Gurev, J. Constantino, and N. Trayanova, "Efficient preloading of the ventricles by a properly timed atrial contraction underlies stroke work improvement in the acute response to cardiac resynchronization therapy.," *Hear. Rhythm*, vol. 10, no. 12, pp. 1800–6, 2013, ISSN: 1556-3871.